

Formation and Avoidance of Surface Defects During Casting and Heat- Treatment of Single-Crystal Nickel- Based Superalloys

Thesis submitted for the degree of Doctor of Philosophy
at the University of Leicester

By

Scott Simmonds
Department of Engineering
University of Leicester

2013

Abstract

Formation and Avoidance of Surface Defects during Casting and Heat-Treatment of Single-Crystal Nickel-Based Superalloys

Scott Simmonds

Nickel-based superalloys are a class of materials that have been specifically developed for high temperature applications for use in aero-engines and power generation. The evolution of superalloy chemistry and solidification structure has made the control and prevention of defect formation in single-crystal components increasingly challenging. This study examines the formation and avoidance of Surface Scale and Surface Melting, both of which are detrimental to the production cost and the performance of single-crystal turbine components.

Surface Scale is a defect found on the surface of as-cast single-crystal components identified as a region of discolouration. A systematic analysis reveals that Surface Scale forms in the solid-state during casting due to the combined effects of (1) differential thermal contractions between mould and metal and (2) transient oxidation of the exposed metal casting surface at temperature below $\sim 1300^{\circ}\text{C}$. The resultant transient oxide film is $0.5\text{-}1\mu\text{m}$ thick whilst the remaining surface undergoes a mould-metal reaction during the initial stages of casting, at temperatures above the liquidus, producing a $1\text{-}2\mu\text{m}$ thick protective layer of Al_2O_3 .

Surface Melting is identified on the heat-treated blade surface as an area of localised melting within the Scaled surface area. Through an in-depth analysis of the microstructural evolution it was found that Surface Melting is a consequence of elemental evaporation of γ -phase stabilisers. The subsequent change in chemistry results in the transformation of the γ phase to γ' and TCPs and a concomitant occurrence of incipient melting at the surface during solution heat treatment.

This thesis concludes that the prevention of Surface Scale is made possible by the use of an inert atmospheric gas, such as Argon, within the casting furnace. However, the subsequent formation of Surface Melting during heat-treatment can only be prevented by pre-oxidising the as-cast components, thus forming Al_2O_3 in order to form a protective barrier to evaporation.

List of Publications

1. G. Brewster, N. D'Souza, K. S. Ryder, S. Simmonds, H. B. Dong, "Mechanism for Formation of Surface Scale during Directional Solidification of Ni-Base Superalloys", *Metallurgical and Materials Transactions A*, Vol. 43, Issue 4, pp. 1288-1302, April 2012.
2. N. D'Souza, S. Simmonds, G. D. West, H. B. Dong, "Role of Elemental Sublimation during Solution Heat Treatment of Ni-Based Superalloys", *Metallurgical and Materials Transactions A*, Vol. 44, Issue 10, pp. 4764-4773, Oct 2013.
3. S. Simmonds, N. D'Souza, K. S. Ryder and H. B. Dong, "Analysis of surface scale on the Ni-based superalloy CMSX-10N and proposed mechanism of formation", *IOP Conference Series: Materials Science and Engineering*, Vol. 27, 2011.

Acknowledgements

First of all I would like to thank my academic supervisor Prof. Hongbiao Dong (University of Leicester) for his guidance and support throughout my PhD. He has given me some unforgettable opportunities to present my work at conferences at home and abroad and has been an inspiration for my future career choices.

I would also like to thank Dr Neil D'Souza (Rolls-Royce plc), who has been like a second supervisor for me, for his invaluable advice and discussions throughout my PhD. His experience and knowledge has been crucial to my successful completion and has been a continued source of motivation.

Special appreciation should be given to Dr Karl S. Ryder (University of Leicester), Dr Geoff West and Dr Gary Critchlow (University of Loughborough), Dr Shu-Yan Zhang and Dr Joe Kelleher (Rutherford Appleton Laboratory) and Peter Cranmer (University of Birmingham) for their insight and assistance. Their combined expertise and skill in much of the analytical microscopy and experimentation critical to this thesis was invaluable.

My thanks are also extended to all the fantastic staff within the Department of Engineering at the University of Leicester. Especially to the Heads of Department Prof. Helen Atkinson and Prof. John Fothergill who have both been a great source of support and a friendly face to talk to throughout my studies.

Acknowledgements

The technical staff within the Department deserve a special mention for their hard-work. They always have time for a chat, to help with last-minute requests and their contribution to my successful completion is greatly appreciated.

I should like to thank all my fantastic friends for their encouragement and understanding. Tom, Beckett, Simon, Alex, Jack, Helen, Jo, Tris, Mike, Adam, Yu, Ben, everyone from Leicester, Thursday Club and especially all of you back home in Suffolk, you are all ace!

My family, as always, have been there for me at all times and for that they forever have my love and gratitude.

Last, but by no means least, I would like to thank my girlfriend Marion Pluskota without whose love, support and belief over the last 3 years I could not have completed this thesis.

Table of Contents

Chapter 1. Introduction to Gas Turbines and Nickel-Based Superalloys for Gas Turbine Applications	1
1.1 Introduction	1
1.2 The Gas Turbine Engine	2
1.2.1 Turbojet vs. Turbofan	4
1.2.2 Modern Engine Requirements.....	6
1.3 Nickel-Based Superalloys used in Aero-Engine Turbine Blades.....	8
1.3.1 Superalloy Chemistry and Microstructure.....	9
1.3.2 Alloy Elemental Additions.....	12
1.3.3 Topologically Close-Packed Phases.....	18
1.3.4 Superalloy Mechanical Properties	21
1.4 Investment Casting and Directional Solidification	23
1.4.1 Investment Casting	24
1.4.2 Directional Solidification.....	27
1.5 Solidification of Nickel-Based Superalloys	28
1.5.1 Grain Structure Evolution during Casting	28
1.5.2 Primary Dendrite Arm Spacing and Micro-Segregation	31
1.6 Heat-Treatment of Nickel-Based Superalloys.....	33
Chapter 2. Defect Formation during Casting and Heat-Treatment of Nickel-Based Superalloys.....	37
2.1 Casting Defects.....	37
2.1.1 Stray Grain Formation and Freckling	37
2.1.2 Cracking and Hot Tearing.....	39
2.1.3 Surface Scale	39

2.2 Heat-Treatment Defects	45
2.2.1 Surface Melting.....	45
2.2.1 Recrystallization.....	49
2.3 High Temperature Oxidation	51
2.3.1 Thermodynamics of Oxidation	51
2.3.2 Ellingham Diagram	52
2.3.3 Pilling-Bedworth Ratio	55
2.3.4 Oxide Growth Mechanisms	55
2.3.5 Oxidation Kinetics	58
2.3.6 Oxidation of Alloys.....	61
2.3.7 Oxide Volatilisation.....	63
Chapter 3. Mechanism of Surface Scale Formation	66
3.1 Introduction	66
3.2 Experimental Methods.....	67
3.2.1 Investment Casting	67
3.2.2 Optical Microscopy (OM) and Scanning Electron Microscopy (SEM)	68
3.2.3 X-Ray Photoelectron Spectroscopy (XPS)	69
3.2.4 Auger Electron Spectroscopy (AES)	71
3.2.5 Preparation of Transmission Electron Microscopy (TEM) Foils Using Focused Ion-Beam (FIB) Extraction.....	73
3.3 Results	75
3.3.1 Appearance of the Scaled and Unscaled As-Cast Surfaces.....	75
3.3.2 Chemical Analysis of the Scaled and Unscaled Surfaces	77
3.3.3 Surface Analysis using Auger Electron Spectroscopy	83
3.3.4 TEM/EDX Analysis of the Surface Scale Oxides	85

3.4 Discussion.....	90
3.4.1 Mould-Metal Reaction during Casting.....	90
3.4.2 Mould-Metal Separation	96
3.4.3 Surface Scale Formation	102
3.5 A Model for Surface Scale Formation	111
Chapter 4. Characterisation of the Surface Melt Blister formed during Heat-Treatment	113
4.1 Introduction	113
4.2 Experimental Methods.....	115
4.2.1 Investment Casting and Heat-Treatment	115
4.2.2 Optical Microscopy and Scanning Electron Microscopy (SEM)	116
4.3 Results	117
4.3.1 Microstructural Analysis of the Heat-Treated Surface	117
4.3.2 Microstructural Analysis of the Pre-Oxidised Test-Bars	122
4.4 Discussion.....	125
4.4.1 Stabilisation of the γ' Phase at the Surface during Solutioning	125
4.4.2 Discontinuous Cellular Recrystallization during Ramp-Up.....	129
4.4.3 Classical Strain-Induced Recrystallization.....	131
4.4.4 Diffusion-Induced Recrystallization of the γ' Surface Layer.....	133
4.4.5 Discontinuous Precipitation during Subsequent Ageing	141
4.5 Conclusions	142
Chapter 5. Elemental Evaporation from the Scaled Casting Surface during Solution Heat-Treatment.....	144
5.1 Introduction	144
5.2 Experimental Methods.....	145
5.2.1 Investment Casting and Heat-Treatment	146

5.2.2 Scanning Electron Microscopy (SEM) and Focused Ion-Beam (FIB)	147
5.2.3 Thermo-Calc Phase Calculations.....	149
5.3 Results	152
5.3.1 SEM Analysis of the Solutioned Test-Bar Surface.....	152
5.3.2 FIB/SEM Analysis of the Solutioned Alumina Crucible Surface	156
5.3.3 Thermodynamic Modelling of the Surface Phase Instability.....	161
5.4 Discussion.....	165
5.4.1 Surface Evaporation during Solution Heat-Treatment.....	165
5.4.2 Diffusion Interactions in the Near-Surface Region	170
5.4.3 Vapour Condensate Analysis	173
5.4.4 Oxidation during Solution Heat-Treatment.....	175
5.5 Conclusions	178
Chapter 6. Exploring the use of Neutron Diffraction for Tracking the Formation of the γ' Surface Layer during Heat-Treatment.....	179
6.1 Introduction	179
6.2 Research on Neutron Diffraction in the Open Literature	180
6.3 Experimental Methods.....	182
6.3.1 Investment Casting and Heat-Treatment	182
6.3.2 Neutron Diffraction and <i>in-situ</i> Heat-Treatment.....	183
6.3.3 Optical Microscopy (OM) and Scanning Electron Microscopy (SEM)	187
6.4 Results	188
6.4.1 Optical Microscopy and SEM of the As-Cast CMSX-10N and Solutioned CMSX-4 Test-bars.....	188
6.4.2 Neutron Diffraction Analysis of As-Cast CMSX-10N	194
6.4.3 Neutron Diffraction Analysis of Solutioned CMSX-4	197

Table of Contents

6.5 Discussion.....	203
6.5.1 Microstructural Analysis	203
6.5.2 Neutron Diffraction Analysis.....	205
6.6 Conclusions	214
Chapter 7. Overall Conclusions and Further Work.....	216
7.1 Conclusions	216
7.2 Further Work.....	218
Chapter 8. References	221

Table of Figures

Figure 1.1 The Pressure-Volume thermodynamic cycle for a simple gas-turbine [1].....	2
Figure 1.2 Schematic diagram of a Rolls-Royce single-shaft Turbojet [3]	3
Figure 1.3 Air pressure changes through the jet engine. Spare pressure is left to provide thrust [2]	3
Figure 1.4 Diagram of a Rolls-Royce Trent 884 High-Bypass Turbofan [1]	5
Figure 1.5 Relationship between thrust and fuel consumption for increasing jet velocity [2]	6
Figure 1.6 Rolls-Royce Trent family 3-shaft turbofan [Picture courtesy of Rolls-Royce plc]	7
Figure 1.7 Evolution of TET during take-off since 1940 [4]	7
Figure 1.8 (a) Internal cooling passages through an HP turbine blade [7] and (b) cross-section of a typical TBC [9]	9
Figure 1.9 Diagram of (a) the FCC γ crystal structure and (b) the ordered $L1_2 \gamma'$ crystal structure.....	10
Figure 1.10(a) Al-Ni binary phase diagram [14] and (b) Ni superalloy γ/γ' microstructure [15].....	11
Figure 1.11 Major alloying elements in Ni-based superalloys and where they partition to during solidification [5]	13
Figure 1.12 Compositional trends in Ni-based superalloy chemistry [6].....	18
Figure 1.13 (a) Schematic image of a typical SRZ formed under an Aluminide TBC [24] (b) Micrograph of the SRZ formed on the single-crystal superalloy MC544 [26]	20
Figure 1.14 (a) Variation of yield stress for some typical single-crystal (SX) Ni-based superalloys [4] (b) Variation of yield stress with temperature of the SX alloy Mar-M200 and SX Ni ₃ Al equivalent to a γ' particle (taken from [4] [27]).....	21
Figure 1.15 (a) Conventionally cast equiaxed grain (b) DS and (c) Single-crystal turbine blades (taken from [8]).....	24
Figure 1.16 Main stages in the investment casting of turbine blades [4] including a wax blade assembly (left) [7]	25
Figure 1.17 Secondary-electron image of the ceramic; (A) colloidal binder (B) refractory filler (C) stucco [34].....	26
Figure 1.18 (a) Bridgman type induction furnace for DS casting [37] and (b) schematic diagram of competitive grain growth during directional solidification, grains A and B are favourable and unfavourable respectively [38]	27
Figure 1.19 (a) Columnar to equiaxed transition and (b) columnar dendritic heat field [10][37][41]	29
Figure 1.20 Scanning electron microscopy image of the dendrite morphology of a Nickel-based superalloy along (a) transverse and (b) longitudinal directions [43]	31
Figure 1.21 Dendrite characteristic length scales [37].....	31

Table of Figures

Figure 1.22 Transverse secondary electron image of a dendritic Nickel-based superalloy with segregation of alloy elements to the inter-dendritic and dendrite core regions [43]	32
Figure 1.23(a) Optical micrograph of the as-cast dendrite network γ/γ' with ID eutectic [52] (b) CMSX-10N as-cast segregated microstructure with increased fraction of ID eutectic (in white) [17]	33
Figure 1.24 Diffusion rates of key alloying elements within pure Ni as a function of inverse temperature [54]	35
Figure 1.25 Secondary electron imaging of the Ni-base superalloy CMSX-4 after (a) solutioning and (b) ageing [52]	36
Figure 2.1 (a) Trail of small equiaxed grains to form a freckle defect and (b) a single, mis-orientated stray grain [60].....	38
Figure 2.2(a) Surface scale after casting and (b) after subsequent heat-treatment [7][19].....	40
Figure 2.3 Proposed formation mechanism of Surface Scale from Brewster [7]	42
Figure 2.4 Surface melt blister on a solutioned Intermediate-Pressure (IP) Trent 800 turbine blade [67].....	46
Figure 2.5 OM image of melt blister cross-section from a heat-treated SX turbine blade.....	48
Figure 2.6(a) Surface RX formed on a SX superalloy after solutioning at 1300°C for 1hr [81] (b) Surface RX formed on a SX CMSX-2 superalloy after solutioning at 1315°C for 3hrs and ageing at 1050°C for 16hrs and at 850°C for 48hrs [82]	50
Figure 2.7 The Ellingham diagram for a variety of oxidation reactions taken from [86] (a solid dot on the reaction line indicates where a phase change has occurred and there is usually a corresponding change in the line's slope).....	54
Figure 2.8 PBR values for common oxides and their protectiveness. P=protective, NP=non-protective [8][89]	55
Figure 2.9 Diagrammatic representation of (a) cation mobile and (b) anion mobile oxide growth [85].....	57
Figure 2.10 Concept of activation energy during oxidation of a Ni-Al alloy [87]	59
Figure 2.11 Rate constants of parabolic oxidation vs. temperature [5].....	60
Figure 2.12 Binary alloy oxidation with component B more reactive than A [5][87]	61
Figure 2.13 Binary alloy oxidation with A and B forming stable oxides. BO is more stable than AO [5][87]	62
Figure 2.14 Cr-O system of volatile species at 1250°K [96].....	65
Figure 3.1 Scaled SX turbine blades a) LP SRR99 alloy turbine blade [7] and b) IP RR3000 alloy turbine blade [67]	67
Figure 3.2 Auger Electron Emission (a) Incident electron beam displays a core electron (b) electron from the 2s level drops to fill the vacancy, releasing 'spare' energy to the Auger electron in the 2p level, which is ejected [106]	72

Table of Figures

Figure 3.3 FIB SEI of the scaled region selected for TEM foil extraction. The Pt deposited strip is outlined in red.....	75
Figure 3.4 TEM sample foil extraction (a) Ion beam mills trenches either side of Pt strip (b) Sample is rotated and ion beam mills beneath sample. A micro-probe is moved into position and affixed to the sample (c) Sample is released from substrate and moved to TEM grid (d) Ion beam is finally used to thin the sample TEM transparency.	75
Figure 3.5 (a) Scaled surface of a turbine blade solidified from CMSX-4 and (b) CMSX-10N.....	76
Figure 3.6 SEI of the scaled/unscaled interface region. Insert A shows the magnified unscaled region and Insert B shows the magnified scaled region. Red cross indicates spectra location for Figure 3.7(c).....	77
Figure 3.7 EDX spectra for (a) the unscaled region (b) the scaled region and (c) the unscaled particles in Figure 3.6.....	78
Figure 3.8 (a) SEM of unscaled surface and (b-f) corresponding EDX maps of Al, Ni, O, Si and Zr	79
Figure 3.9 High-resolution XPS compositional analysis of scaled and unscaled surfaces as-cast surfaces. (a) Ni(2p) spectrum (b) Al(2p) and Ni(3p) spectra, (c) Zr(3d) spectra (d) Re, W, Ta(4f) spectra.	81
Figure 3.10 Optical photograph of detached mould prime-coat surface showing scaled-facing surface (smooth) on the left and the unscaled-facing side (rough) on the right. XPS spectra locations A and B are also shown	82
Figure 3.11 XPS spectrum collected from the mould wall adjacent to the scaled region (a) Al (2p) and (b) O (1s)	82
Figure 3.12 AES depth profiles of the as-cast CMSX-10N turbine blade in (a) scaled and (b) unscaled regions	84
Figure 3.13(a) FIB micrograph of TEM extraction area and (b) TEM image of scale oxide cross-section.....	85
Figure 3.14 EDX maps of oxide layers a) Al K α b) Ni K α c) Co K α d) Cr K α e) O K α f) EDX locations in Figure 3.15	86
Figure 3.15 EDX spectra from the scale oxide (a) (Ni,Co)O outer scale oxide, (b-d) Mixed oxide subscale rich in Cr, Al, Ti, W and Ta. NB: Cu is detected as contamination from the TEM grid	86
Figure 3.16 TEM micrograph of the scaled region of alloy CMSX-10N with EDX spectra locations for Figure 3.18.....	88
Figure 3.17 EDX maps of oxide layers a) Al K α b) Ni K α c) Co K α d) Cr K α e) O K α f) Pt L α	89
Figure 3.18 EDX spectra from the scaled region locations in Figure 3.16 (a) NiO layer (b) Al ₂ O ₃ particle (c) Al, Cr oxide layer (d) porous subscale layer	89
Figure 3.19 BSE image of the ceramic mould layered structure. The Primary coat is in intimate contact with the metal casting, whilst the Back-up coats impart strength to the mould. Porosity is between 15-20%. [Image courtesy of Dr Neil D'Souza, Rolls-Royce plc.].....	91
Figure 3.20 Graphical representation of Raoult's law for ideal solutions [86]	92

Table of Figures

Figure 3.21 Ellingham diagram of standard free energies for oxide formation. Al and Si oxides are highlighted in blue and red respectively [86].....	96
Figure 3.22 Optical images of the border between the scaled and unscaled regions.....	97
Figure 3.23 Temperature and displacement contour plots calculated using ProCAST™ for the bottom section (a-b) and for the top section (c-d) at 900°C.	99
Figure 3.24 Temperature and displacement contour plots calculated using ProCAST™ for the bottom section (a-b) and for the top section (c-d) at 1100°C.	100
Figure 3.25 Gibbs free-energy for the reduction of SiO ₂ by Al, Ni and Ti within the liquid alloy	103
Figure 3.26 Calculated Ellingham diagrams for CMSX-4 and -10N (Legend in Figure 3.27) [126].....	106
Figure 3.27 Equilibrium partial pressure of oxygen versus temperature for CMSX-4 NB: Same as CMSX-10N	106
Figure 3.28 Ion and electron transport schematic for (a) cation diffusion controlled oxide film (e.g. NiO) and (b) anion diffusion controlled oxide film (e.g. Al ₂ O ₃). Adapted from [131].....	108
Figure 3.29 The transient oxidation process of a Ni-15Cr-6Al alloy at 1000°C in 0.1 atm oxygen [137].....	110
Figure 3.30 Schematic diagram of the model for the formation of surface scale during directional solidification (adapted from the original diagram by Brewster [7])	112
Figure 4.1 Surface wrinkle melt blister on the aerofoil of an IPTB cast from CMSX-10N [68]	113
Figure 4.2 OM image of melt blister cross-section from a heat-treated SX turbine blade.....	114
Figure 4.3 As-cast test-bar surface after grit-blasting. There is no remaining oxides or eutectic, except for small channels of inter-dendritic eutectic that intersects with the surface	117
Figure 4.4 (a) OM image of the fully heat-treated test-bar surface with surface layer and (b) higher magnification BSI of the same surface area with EDX spectral locations highlighted for Figure 4.5	118
Figure 4.5 EDX spectra from the surface layer (red) and the substrate (black)	118
Figure 4.6 BSI's showing (a-b) close-up of the γ' surface layer porosity and DP reaction (c) γ' coarsening in the substrate adjacent to the γ' surface layer and (d) the interface with the γ' layer and γ RX grains below.....	119
Figure 4.7 Crystallographic analysis of the surface region (a) BSI of γ' surface layer and RX γ grains and (b) EBSD derived inverse pole figure map of same area showing polycrystalline nature of the surface (where colour variation indicates different crystallographic orientations).....	121
Figure 4.8(a) BSI of the solutioned test-bar with characteristic γ' surface layer and RX γ grains but no DP at interfaces (b) RX γ grain/substrate interface showing coarse γ' precipitates on the grain-boundary and an absence of DP (c) close-up of the γ' surface layer/RX grain interface showing formation of some discrete TCP's	122
Figure 4.9 Pre-oxidised test-bar surface prior to subsequent solutioning with Al ₂ O ₃ surface oxide (black)	123

Table of Figures

Figure 4.10 Pre-oxidised and solutioned test-bar surface (a) OM and (b) BSI of the surface morphology showing the outer Al_2O_3 layer (plus internal oxidation), RX γ grains and no γ' layer. Insert shows no PFZ below oxide	124
Figure 4.11 EDX spectra for the surface oxide layer, the γ RX grains and the substrate of the pre-oxidised and solutioned test-bar sample	125
Figure 4.12(a) Vapour pressure vs. temperature plots for Ni, Co and Cr (b) Evaporative rate from the sample surface into vacuum using the Langmuir equation	127
Figure 4.13(a) Schematic of the classical recrystallization process and final solutioned structure (adapted from [145]) (b) OM of the final solutioned surface with RX grains grown into the substrate	132
Figure 4.14 Schematic diagram showing sequence of cellular RX grain transformation to classical RX and its subsequent growth into the substrate during solutioning ($\gamma' =$ black, $\gamma =$ grey and TCPs = white).....	133
Figure 4.15 Schematic diagram of the microstructure of a polycrystalline material that has undergone DIGBM transformation. The initial grain-boundary location is shown by the dotted-line [adapted from [153]]	136
Figure 4.16 Diagram of the mechanism of DIGBM induced by grain-boundary diffusion of solute. A thin, inter-diffusion area exists ahead of the moving GB which is stressed due to size mismatch between A & B atoms (adapted from [155]).....	137
Figure 4.17 (a) Schematic representation of the Kirkendall effect. The diffusion coefficient of metal A is greater than for metal B resulting in the net flux of vacancies, j_v , towards metal A and the production of a porosity zone [adapted from [162]] (b) Representation of the diffusion and evaporation fluxes from the surface of an A(B) alloy in the presence of a vacuum. Both the diffusion coefficient and vapour pressure of A is greater than that for B.....	139
Figure 5.1 (a) University of Birmingham's solution heat-treatment furnace (b) solutioned test-bar inside the alumina crucibles used to trap the evaporated material on its interior surface, these were subsequently analysed	147
Figure 5.2 Image of the heat-treated test-bar sat inside the top half of the Al_2O_3 crucible. Around the crucible edges are silvery deposits whilst the rest of the crucible remains white.....	153
Figure 5.3 OM of the central portion of the solutioned test-bar surface. The evolution of the γ' surface layer is evident, as are the γ RX grains below.....	153
Figure 5.4 OM of the end of the solutioned test-bar. Cross-section shows the silvery deposits seen in Figure 5.2	154
Figure 5.5 BSI of the central portion of the solutioned test-bar surface showing the typical γ' surface layer + TCPs and γ RX grains below	154
Figure 5.6 SEI of the end of the test-bar. Cross-section showing the silvery deposits above the original surface	155
Figure 5.7 BSI of the end of the test-bar. Cross-section showing the silvery deposits above the γ' surface layer. EDX spectrum locals are highlighted by dotted line for Figure 5.8.....	156
Figure 5.8 EDX spectra collected at 15kV from the upper silvery deposit and compared to the bulk.....	156
Figure 5.9 SEI of the heat-treated crucible surface (a) white area and (b) grey area	157

Table of Figures

Figure 5.10 Close-up of the blocky deposits found in the grey area of the heat-treated crucible surface	157
Figure 5.11 Grey area of the heat-treated crucible surface (a) 3kV and (b) 20kV SEI of the surface cross-section	158
Figure 5.12 FIB image showing the milled cross-section face with metal deposits on top of the Al ₂ O ₃ substrate.....	159
Figure 5.13 EDX 10kV maps of the grey area cross-section (a) 20kV SEI (b) Al (c) Co (d) Ni (e) O (f) Pt.....	160
Figure 5.14 EDX point spectra (10kV) from the Ni,Co particles and the Al ₂ O ₃ area surrounding them. Ga and Pt peaks are present due to contamination from the Ga ion beam and Pt deposit respectively	160
Figure 5.15 White area cross-section of the heat-treated crucible surface (a) 10kV SEI and (b) Ion beam image	161
Figure 5.16 Phase evolution of the surface layer calculated using Thermo-Calc for elemental vapour losses (a) 5% Langmuir Ni, Co loss (b) 8% Langmuir Ni, Co loss (c) 10% Langmuir Ni, Co loss (d) 15% Langmuir Ni, Co loss. Cr losses are at 0.5% Langmuir in (a)-(d).....	164
Figure 5.17(a) Langmuir evaporative rate into vacuum (b) Mass loss (g) of Ni, Cr and Co for different %'s of total Langmuir loss to vacuum (during 8 hours solution at 1312°C)	167
Figure 5.18(a) Comparison of Al, Ni, Cr & Co vapour pressures and (b) corresponding Langmuir evaporative rates.....	168
Figure 5.19 Mass losses (g) of Ni, Cr, Co and Al for different %'s of total Langmuir loss to vacuum (during 8 hours solution at 1312°C)	168
Figure 5.20(a) Diffusion rates of key alloying elements within pure Ni as a function of 1/T [54] (b) Self-diffusion rate of Ni within pure, SX Ni as a function of 1/T [179]. The solutioning temperature, 1312°C, is marked to highlight the relative diffusion coefficients acting to replenish metal evaporative losses.....	172
Figure 5.21 EDX mapping of the Al ₂ O ₃ surface oxide formed during solution heat-treatment (a) SEI (b) Al and (c) O	176
Figure 5.22 Calculated Ellingham diagram for the alloy CMSX-4 with solutioning temperature indicated by red line.....	176
Figure 6.1 (200) γ/γ' peak de-convolution. (200) peak is constrained by the γ' (100) d-spacing (adapted from [194])	182
Figure 6.2 Engin-X neutron beam line experimental setup for in-situ heat-treatment. (a) Schematic diagram of experimental setup and gauge volume and (b) photo of experimental stage with furnace installed	184
Figure 6.3 Sample holder layout. Sample is suspended at the bottom with Ta wire and insulated with Al ₂ O ₃ ceramic. Thermocouples are placed against the sample to provide temperature feedback for the furnace control	185
Figure 6.4 Diffraction spectra of a single-crystal test-bar obtained by TOF neutron diffraction	186
Figure 6.5 OM image of the as-received CMSX-10N test-bar surface.....	188

Table of Figures

Figure 6.6 (a) OM image (b) SEI and (c) BSI of the ISIS tested CMSX-10N test bar surface. The γ' surface layer is shown in detail in (b) & (c). Of note are the TCP needles fanning out from the substrate within the γ' layer (white).....	189
Figure 6.7 SEI of the ISIS tested CMSX-10N test bar surface detailing the lack of TCP phases within the γ' surface layer adjacent to the inter-dendritic eutectic region.....	190
Figure 6.8 (a) OM and (b) SE images of the CMSX-4 test-bar surface prior to ISIS heat-treatment, showing the complete removal any remnant γ' surface layer. RX γ grains due to grit-blast/solutioning are highlighted in (b)	191
Figure 6.9 OM of the ISIS test-bar surface. The γ' surface layer is clearly visible in white above the γ RX grains.....	192
Figure 6.10 (a) SEM image of the ISIS solutioned test-bar surface and (b) close-up of the interface with the γ RX grain below. The γ' surface layer is clearly visible, as are the TCPs formed within this layer. Of note is the way the γ' layer has grown into the substrate, consuming the γ RX grains where possible	192
Figure 6.11 (a) SEM image of the ISIS solutioned test-bar surface and (b) close-up of an area where the γ' layer has consumed the RX γ grain up to the border with the substrate	193
Figure 6.12 Room temperature ND spectra of the as-cast CMSX-10N bulk alloy	194
Figure 6.13 Dissolution of the (100) γ' peak from room temperature to 1350°C+1hr; (a) dissolution begins ~525°C (b) final stage of dissolution occurs ~1345°C after which dissolution of the γ' stops	195
Figure 6.14 Dissolution of the (200) γ/γ' peak from room temperature to 1350°C+1hr	196
Figure 6.15 ND spectra from the near-surface region of as-cast CMSX-10N after heat-treatment at 1350°C for 18hrs	196
Figure 6.16 Room temperature ND spectra from the centre of the solutioned CMSX-4 test-bar	197
Figure 6.17 (a) Room temperature ND spectra from the surface of solutioned CMSX-4 (b) zoom of left-hand region	198
Figure 6.18 Dissolution of bulk γ' from room temperature to 1000°C; (a) (200) γ/γ' peak (b) (100) γ' peak.....	199
Figure 6.19 Final stages of bulk γ' dissolution; (a) (200) γ/γ' peak from 1000-1305°C (b) (100) γ' peak from 1000-1285°C, showing final dissolution at 1285°C.....	199
Figure 6.20 Dissolution of surface γ' from room temperature to 1000°C; (a) (200) γ/γ' peak (b) (100) γ' peak	200
Figure 6.21 Final stages of surface γ' dissolution; (a) (200) γ/γ' peak from 1000-1305°C+7hr hold (b) (100) γ' peak from 1000-1305°C+7hr hold, final dissolution of γ' noted at 1289°C	200
Figure 6.22 (a) Evolution of the (100) γ' peak through isothermal hold at 1305°C for 8 hours (b) Offset (+0.5) spectra	201
Figure 6.23 Offset (+0.5) spectra of the (300) and RX grain peaks showing evolution from room temperature to 1305°C	202
Figure 6.24 Offset (+0.5) spectra of the (300) and RX grain peaks showing evolution during 1305°C hold	202

Table of Figures

<i>Figure 6.25 Offset (+0.5) spectra of the (300) and RX grain peaks showing evolution during cooling from 1305°C.....</i>	<i>203</i>
<i>Figure 6.26 (a) Illustration of the Nominal Gauge Volume (red) and Instrument Gauge Volume (blue). (b) 3-dimensional illustration of the IGV arising from the scattering of the incident and diffracted neutron beams, defined by the scattering angle, $\alpha_{in,det}^{x,y,z}$ (adapted from [199])</i>	<i>205</i>
<i>Figure 6.27 Example contour map of the ENGIN-X IGV taken from [199]. Measured by scanning a 0.25mm thin nylon thread across the horizontal plane (x,z).....</i>	<i>206</i>
<i>Figure 6.28 Illustration of SGV (dark) partially filling the nominal gauge volume (NGV) as the sample is translated into the NGV. The distance between the dot and the cross shows the variation in the geometric centroid of the SGV and NGV, resulting in a shift in the measured d-spacing's (illustration adapted from [182])</i>	<i>207</i>
<i>Figure 6.29 Schematic diagram of the two experimental positions used in this Chapter, (a) the bulk measurement position and (b) the surface measurement position, detailing the intersecting SGV with the test-bar radius</i>	<i>207</i>
<i>Figure 6.30 Calculated equilibrium phase diagram for CMSX-4 using Thermo-CALC</i>	<i>212</i>
<i>Figure 6.31(a) Vapour pressure vs. temperature plots for Ni, Co and Cr (b) Evaporative rate from the sample surface into vacuum using the Langmuir equation (taken from Chapter 4)</i>	<i>213</i>

List of Tables

<i>Table 1.1 Composition of some commercially available superalloys (wt%) [adapted from 7,10]</i>	<i>14</i>
<i>Table 3.1 Nominal composition (wt.%) of alloying elements in the Ni-base superalloys CMSX-4 and CMSX-10N</i>	<i>67</i>
<i>Table 3.2 Mould slurry constituent materials</i>	<i>68</i>
<i>Table 3.3 Composition (at.%) of the mould face-coat (adjacent to the scaled region of the blade surface) for the two analysis areas, A and B, determined by integration of the XPS spectral data</i>	<i>83</i>
<i>Table 3.4 Nominal composition and element activities for CMSX-4 and 10N</i>	<i>94</i>
<i>Table 4.1 Nominal composition (wt.%) of alloying elements</i>	<i>115</i>
<i>Table 5.1 Nominal composition and mole fraction of alloying elements in the Nickel-based superalloy CMSX-4</i>	<i>146</i>
<i>Table 5.2 Calculated compositions (wt.%) within 20µm surface layer following Ni and Co vapour losses of varying fractions of the total Langmuir loss to vacuum. Cr is maintained at 0.5%Langmuir. The composition due to mass losses of Ni and Cr to form oxides 0.5µm thick are also considered</i>	<i>151</i>
<i>Table 5.3 Calculated transition temperatures using Thermo-Calc (Equilibrium condition) for fractions of Langmuir loss, as well as NiO+Cr₂O₃ losses and nominal composition for comparison</i>	<i>161</i>
<i>Table 5.4 Phases (mole %) calculated at 1312°C solution and after quench. Scheil condition applied to liquid fraction at 1312°C to ascertain final solidified phases. Nominal composition phases shown for comparison</i>	<i>162</i>
<i>Table 6.1 Nominal composition (wt.%) of alloying elements in the Ni-based superalloys CMSX-4 and CMSX-10N</i>	<i>182</i>

Chapter 1. Introduction to Gas Turbines and Nickel-Based Superalloys for Gas Turbine Applications

1.1 Introduction

The introduction and development of Nickel-based superalloys for use in gas turbine aero-engines has allowed the progressive achievement of higher engine efficiencies and greater performance. These superalloys exhibit enhanced performance at high temperatures, such as improved strength, creep and fatigue resistance, even at temperatures approaching their melting points. Because of this improved performance they are used extensively for the production of high-temperature rotating components, such as high-pressure turbine blades and nozzle guide vanes, used in gas turbine engines. These components have to operate in the hottest, most demanding sections of the gas turbine. Further performance gains have been achieved with the introduction of new thermal barrier coatings and internal cooling channels as well as the change of solidification structure from multi-grained to single-crystal castings. However, controlling the solidification structure, and therefore the resultant material properties, has become increasingly challenging due to the formation of defects during casting and heat-treatment.

The proposed research program, based at the University of Leicester and in collaboration with Rolls-Royce plc., aimed to study the formation and microstructural evolution of two inter-related surface defects that form during casting and subsequent heat-treatment of single-crystal Nickel-based superalloy turbine blades. It is seen that

there is a spatial correlation to the location of the casting defect Surface Scale (an area of discolouration on the blade surface, discussed in Chapter 3) and the heat-treatment defect Surface Melting (a wrinkled area of localised melting on the surface of heat-treated blades, discussed in Chapters 4 and 5), the cause of which was unknown. The impetus for this research project is the continuing problem of these surface defects on the cost and production through-put of turbine blades and it is hoped that, through understanding of their formation, proposals can be made that will result in their removal or abatement from the production process.

1.2 The Gas Turbine Engine

The gas turbine is used in a variety of power applications, from domestic electricity generation to naval propulsion, but due to its high power to weight ratio it has revolutionised the aviation industry and allowed worldwide air travel to flourish. All gas turbines run on the Brayton thermodynamic cycle, Figure 1.1, which involves 3 stages; compression, combustion and expansion.

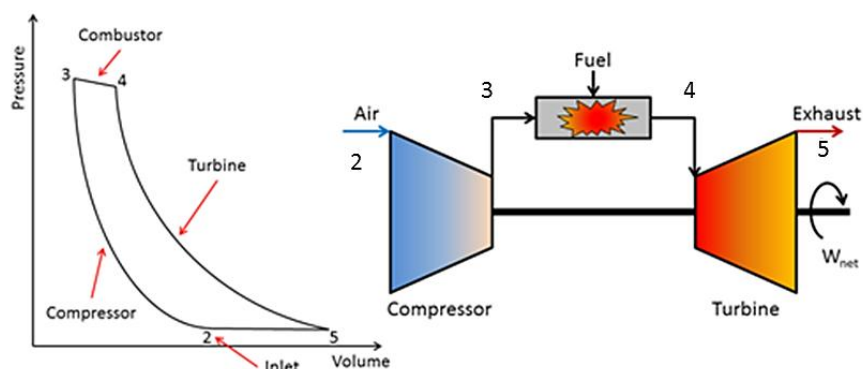


Figure 1.1 The Pressure-Volume thermodynamic cycle for a simple gas-turbine [1]

The gas turbine aero-engine, or 'jet engine', is used to accelerate air rearwards, taken in at the front and forced out the back at a higher speed. In doing so an equal and opposite force is transmitted through the engine and engine-mounts to the aircraft

providing forward thrust (F). Newton's second law states that force is equal to the rate of change in momentum therefore an equation for thrust can be given as:

$$F = W(V_J - V_0) \quad \text{Equation 1.1}$$

Where V_0 is the intake jet velocity, V_J is the exit jet velocity and W is the mass of air flowing through the engine (see Figure 1.2).

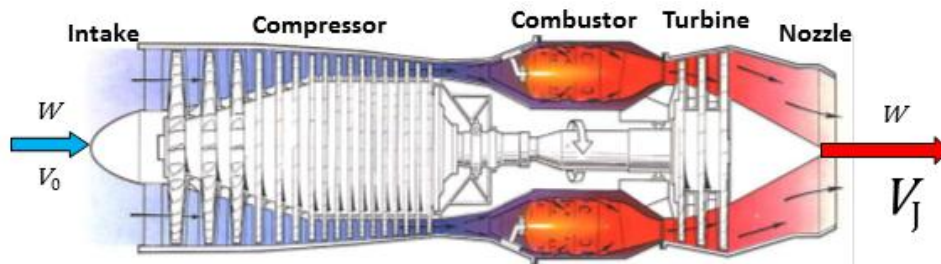


Figure 1.2 Schematic diagram of a Rolls-Royce single-spool Turbojet [3]

By increasing the jet velocity, V_J , and/or the mass of air flow through the engine, W , then greater thrust can be achieved [2]. The jet engine has many variants and components however they all share the same basic core known as a 'Turbojet' (Figure 1.2). The turbojet consists of an intake, compressor, combustion chamber, turbine and nozzle. Pressure changes inside the aero-engine are schematically shown in Figure 1.3.

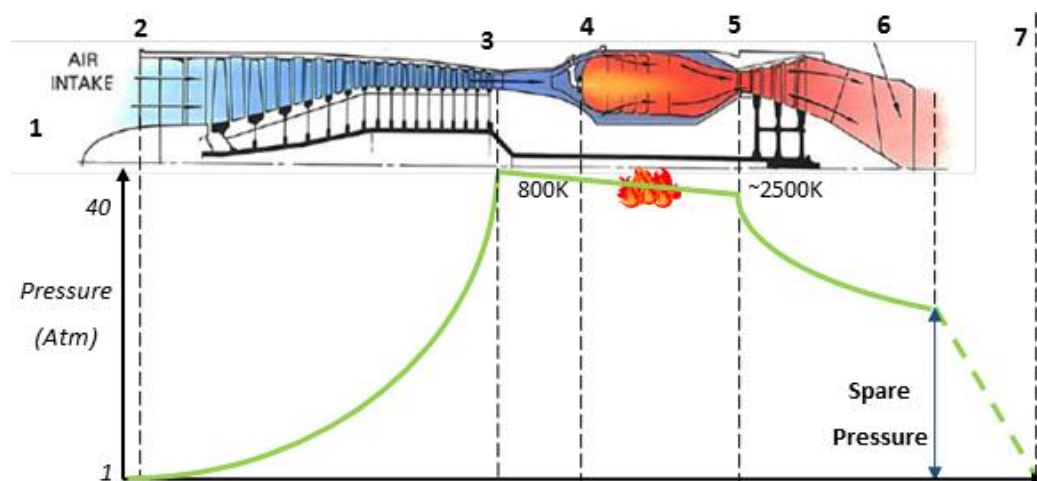


Figure 1.3 Air pressure changes through the jet engine. Spare pressure is left to provide thrust [2]

As shown in Figure 1.3, air enters the turbojet intake (position 1) at velocity V_0 before passing through several compression stages (positions 2-3) which squash the air and

raise its pressure by around 40:1 and temperature to 800K [2]. The hot gas then enters the combustion chamber (position **4**) where it is mixed with fuel and burnt at near constant pressure to raise its temperature to around 2500K (Note: This is unlike an internal combustion engine where fuel and air is combusted at constant volume). Combustion at constant pressure ensures that the airflow continues to accelerate rearwards, through the engine, and not 'surge' back through the front. It should be noted that there is a slight drop in pressure over the combustor (~5%) due to the restriction of the combustor geometry. The hot gas is now expanded through the turbine section (position **5**) where a portion of its energy is used to rotate the turbine and thus drive the compressor, therefore sustaining its operation. The pressure drop over the turbine (position **5-6**) is less than the pressure rise over the compressor (position **2-3**) which leaves spare pressure left for useful work to accelerate the air to a high V_j and produce thrust [1][2][4].

1.2.1 Turbojet vs. Turbofan

In civil aviation the most common jet engine is the high-bypass turbofan. The turbofan consists of a turbojet core but with the addition of a large fan at the front of the engine. The fan is driven by an additional, low-pressure, turbine stage and is designed to bypass a large portion of the incoming airflow around the outside of the engine core (Figure 1.4). The remaining air is forced through the core, as in a turbojet, which produces the power to drive the fan and compressor and create some added core-thrust.

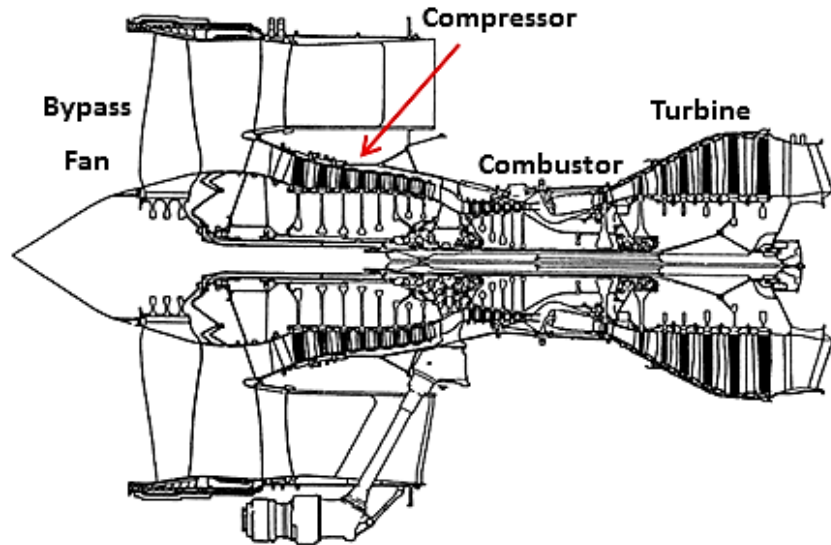


Figure 1.4 Diagram of a Rolls-Royce Trent 884 High-Bypass Turbofan [1]

This arrangement results in a relatively low jet velocity, but much higher mass flow rate of air, as the spare pressure, that was left in the case of a turbojet, is now used to rotate the fan instead of accelerating the flow to high exit velocities. This design reduces engine noise since the noise is strongly related to the jet velocity; therefore any reduction in V_j results in a significant reduction in jet noise and is therefore more attractive to aircraft operators flying over populated areas [1].

The amount of thrust produced by a jet engine varies not only with V_j but also with W as shown by Equation 1.1. The turbofan produces thrust by increasing W , accelerating a large amount of air to a relatively low velocity. The added benefit of this arrangement is an increase in fuel efficiency because the amount of fuel that is turned into useful jet kinetic energy varies with V_j^2 whilst the thrust produced from that V_j varies linearly. As illustrated in Figure 1.5, as thrust increases (black curve), the fuel consumed to achieve that thrust (red curve) increases at a greater rate. So for an engine with a high jet velocity, like a turbojet, the fuel consumption will be high [2].

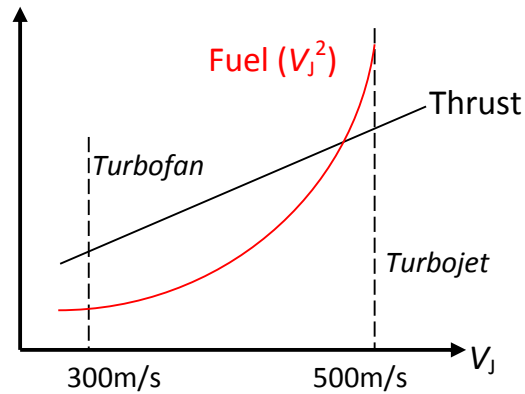


Figure 1.5 Relationship between thrust and fuel consumption for increasing jet velocity [2]

The propulsive efficiency (a measure of the amount of engine power transferred to kinetic energy, thrust) is also improved by using a Turbofan jet engine since the jet velocity is lower than for an equivalent Turbojet, thus according to:

$$\eta_{prop} = \frac{F \cdot V_0}{\frac{W}{2}(V_j^2 - V_0^2)} \quad \text{Equation 1.2}$$

By lowering the jet velocity to a value closer to the velocity of the surrounding air, the propulsive efficiency increases [4]. A compromise still needs to be made however, since increasing W also means increasing the fan size and thus the frontal area of the engine becomes bigger, increasing the drag of the aircraft and posing ground-clearance design issues.

1.2.2 Modern Engine Requirements

The Turbine Entry Temperature (TET) is an important design consideration of an aero-engine and is defined as the temperature of the gas flow, after combustion, as it enters the first stage of the turbine section (Figure 1.6). The TET is important since a higher TET improves the thermal efficiency of the engine and therefore has a positive effect on the specific fuel consumption. Over the last 50 years the TET on commercial turbojets has risen by $\sim 700\text{K}$ to 1800K due to greater fuel efficiency and power

requirements (Figure 1.7) [4]. This has had the benefit of a corresponding increase in thrust by a factor of 80 [5] compared to Frank Whittle’s early engines of the 1940’s [1].

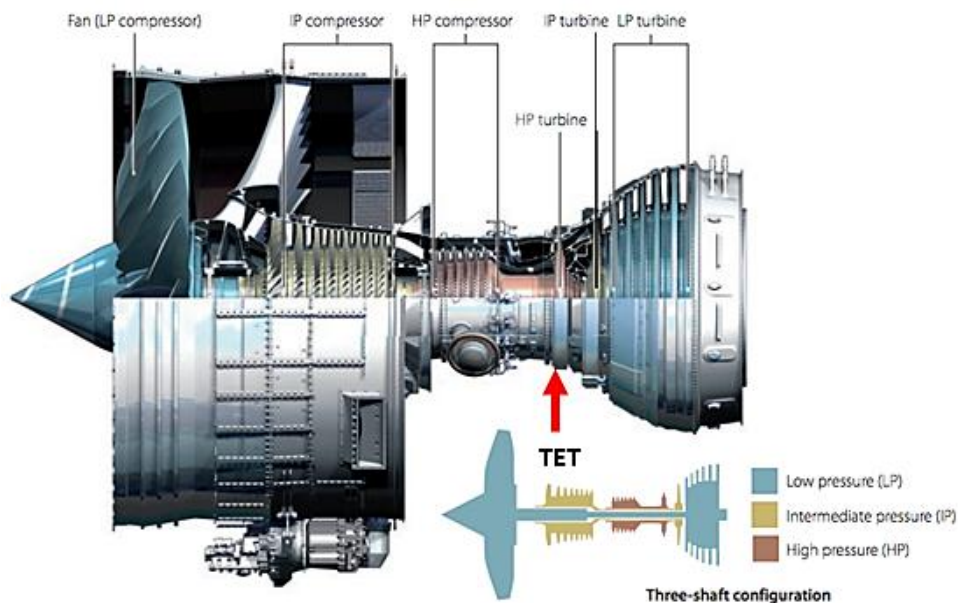


Figure 1.6 Rolls-Royce Trent family 3-shaft turbofan [Picture courtesy of Rolls-Royce plc]

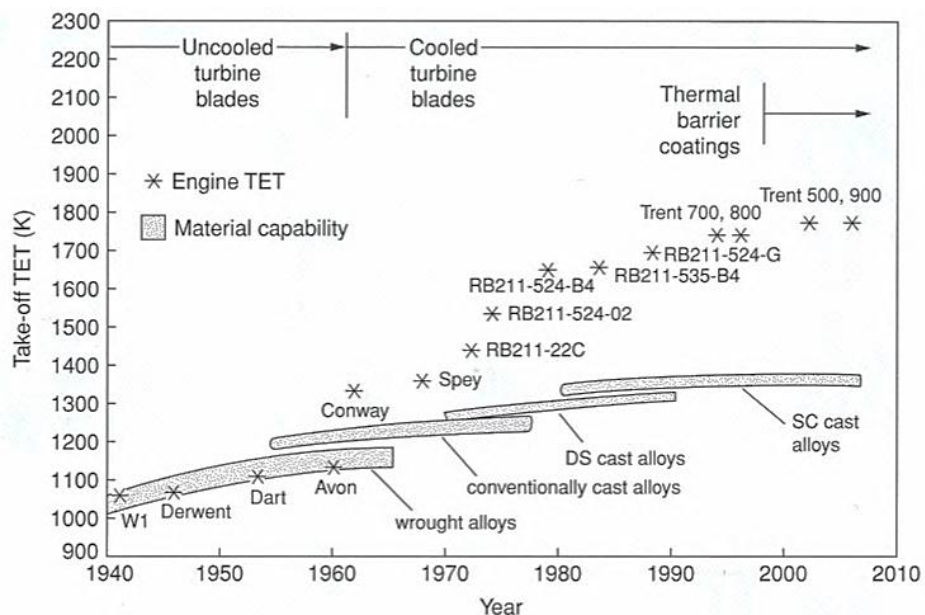


Figure 1.7 Evolution of TET during take-off since 1940 [4]

The thermal efficiency (and power) that a jet engine generates is dependent on the difference in temperature between the cold source (the atmosphere) and the hot source (TET). It is therefore beneficial in the case of a jet engine to increase the temperature of the gas stream entering the turbine. This aim has been the biggest factor in driving the evolution and introduction of new materials, with greater

temperature capabilities, as well as the introduction of thermal barrier coatings and internal cooling passages to turbine blades.

1.3 Nickel-Based Superalloys used in Aero-Engine Turbine Blades

As discussed in the previous section, when designing a jet engine choosing a suitable TET is critical in order to achieve the required performance and efficiency. However, as TET is increased, the choice of materials capable of surviving in such hot, corrosive environments decreases. This directly affects the turbine blades, as they are located in the turbine section where they extract work from the hot combustion gases to drive the compressor and fan at the front of the engine. Superalloys are extremely significant to modern-day aviation, in 1950 around 10% of an aircraft's jet engine weight was from superalloys whereas in 1985 that had risen to about 50% [6].

The high-pressure (HP) turbine blade operates in the harshest environment, directly after the combustion chamber, in gas temperatures in excess of 1600°C, which is above the melting point of the metal alloy [7]. As well as extreme temperature, the turbine blade has to withstand centripetal forces of approximately 18 tonnes (at take-off), cyclic operation over many years, long service intervals (of approximately 5 million miles), high-temperature oxidation/corrosion, thermal expansion and creep and impact damage from foreign objects [8]. Added to this are weight considerations of the turbine blades, since their weight adds stress to the whole rotor/shaft assembly and therefore is detrimental to fuel efficiency.

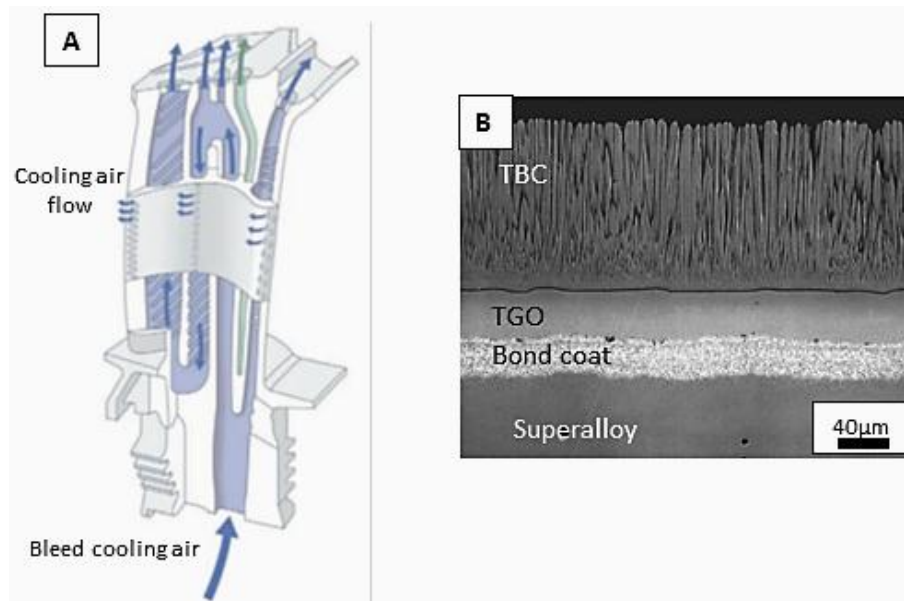


Figure 1.8 (a) Internal cooling passages through an HP turbine blade [7] and (b) cross-section of a typical TBC [9]

The melting temperatures of superalloys are typically below that of the TET for example, the 3rd generation alloy CMSX-10 has a solidus temperature of 1366°C which is ~250°C lower than the gas-stream temperature around it. In order to prevent the blades from melting designers use internal cooling channels (with cooler, compressor bleed air) and external ceramic thermal barrier coatings (TBC) to lower the surface temperature of the blade to an acceptable level of ~1000°C (Figure 1.8) [1].

1.3.1 Superalloy Chemistry and Microstructure

A superalloy is a complex alloy-system that can be defined as:

“An alloy developed for elevated temperature service, usually based on group VIII A elements, where relatively severe mechanical stressing is encountered, and where high surface stability is frequently required” [5].

Most superalloys can be divided into three classes: nickel-based superalloys, cobalt-based superalloys and iron-based superalloys [5]. However, Nickel-based superalloys are the class of high temperature superalloys used extensively in the production of

critical jet engine components and are discussed in this work. They are characterised by their ability to withstand creep deformation at elevated temperatures (up to 80-90% of their melting point) [10] and exhibit a greater resistance to fatigue, thermal shock and have high strength that remains stable over a larger temperature range than other alloy systems, especially when operating at temperatures above 800°C.

When rotating at extremely high speeds in a hot, corrosive environment turbine blades are particularly vulnerable to creep deformation and thermo-mechanical fatigue stresses, as well as a higher degree of oxidation and corrosion caused by the reactive combustion gases. Turbine blades can therefore quickly fail unless adequately protected. The need to increase engine TET, reduce the risk of blade failure and maintain a useful service life has resulted in the drive to better understand the alloy chemistry and the processes involved during manufacture.

Some of the first Ni-based superalloys, like Inconel 600, consisted of a single nickel face-centred cubic phase with additions of chrome, copper, cobalt and iron. When compared to other materials of the time, such as stainless steels, these alloys had superior mechanical properties and were the basis on which newer generations of Ni-based superalloys were developed [5] [11] [12].

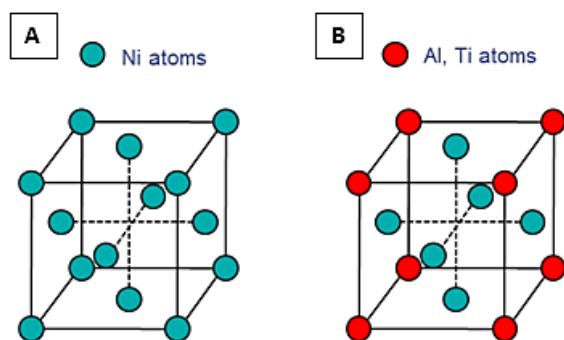


Figure 1.9 Diagram of (a) the FCC γ crystal structure and (b) the ordered L1₂ γ' crystal structure

An important step in superalloy evolution was the addition of aluminium (around 6 wt%) in order to improve some of the above performance requirements by creating a two-phase microstructure. A binary Ni-Al phase diagram (Figure 1.10) is commonly used to simplistically illustrate the phase changes in Ni-based superalloys. At room temperature, the alloy has two equilibrium phases, γ and γ' . The γ phase is a disordered solid solution containing elements that make up the face-centred cubic crystal lattice (FCC) whilst the γ' phase prefers an $L1_2$ structure [13] containing nickel atoms at the face centres and aluminium atoms at the corners (Figure 1.9) [5]. This facilitates the formation of coherent, ordered cuboid intermetallic γ' precipitates (Ni_3Al) arranged within the γ matrix (Figure 1.10).

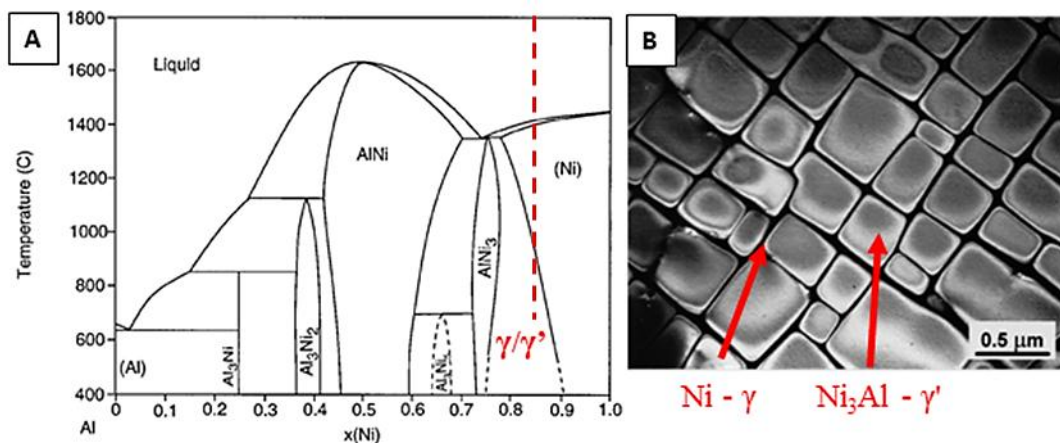


Figure 1.10(a) Al-Ni binary phase diagram [14] and (b) Ni superalloy γ/γ' microstructure [15]

The fine, ordered distribution of the γ' phase hinders the movement of dislocations, even at high temperatures. It is the combination of these two phases, with a large volume fraction of γ' precipitates (~70%), that contributes to the high material strength and creep resistance of Ni-based superalloys [6] [10] [16].

1.3.2 Alloy Elemental Additions

Ni-based superalloys are complex alloy systems usually consisting of at least 10-12 different elements which must be carefully controlled so as to achieve the desired material properties. As well as controlling the main elemental constituents it is also necessary to limit the concentration of undesirable impurities (such as silicon, oxygen and sulphur), which may be present in the elemental additions or revert material, if there is not appropriate melting and casting practice. These impurities can cause deleterious effects on material strength and oxidation resistance, in particular, sulphur is renowned for weakening the adherence of protective surface oxide scales and reducing stress rupture life [5].

During solidification the alloying elements segregate to either the solid γ phase, the liquid phases or to the grain boundaries. As the metal cools, (and during subsequent solution heat-treatment) the γ' phase precipitates out within the γ phase matrix, creating the γ/γ' structure. During the precipitation, elements that preferentially partition to the γ' or γ phase are summarised in Figure 1.11, below. Aluminium, titanium, niobium and tantalum partition to the γ' whilst nickel, cobalt, iron, chromium and tungsten partition to the γ phase. Finally, elements such as boron, carbon and zirconium partition to the grain boundaries, impeding dislocation movement. Another important group of elements are those that form surface oxides (like aluminium and chromium), which have beneficial effects on corrosion and in-service oxidation resistance.

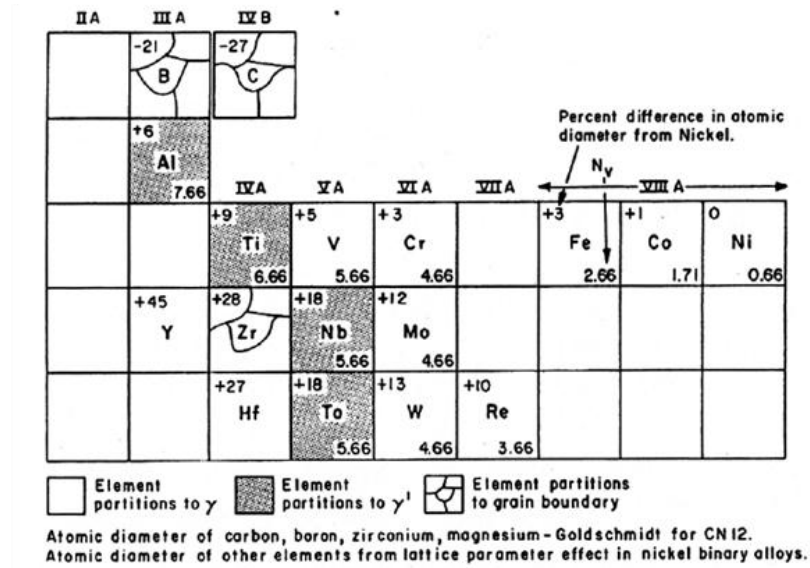


Figure 1.11 Major alloying elements in Ni-based superalloys and where they partition to during solidification [5]

The size and volume fraction of the γ' precipitates is critical to the alloys creep and fatigue strength properties. The morphology of the precipitates is dependent on properties such as the lattice misfit, elastic anisotropy, precipitate elastic modulus and temperature, whilst the volume fraction is dependent on the Al + Ti additions. The γ' precipitates typically range in size from 0.2 - 0.5 μm , with a volume fraction of >60% in most Nickel superalloys [8] [10]. For comparison, the compositions of some commercially available single-crystal γ/γ' superalloys are shown in Table 1.1 below.

Alloy	Cr	Co	Mo	W	Ta	Al	Ti	Hf	Re	Ru	other
1st Generation											
PWA1480	10	5	0	4	12	5	1.5	0			
Rene N4	9.8	7.5	1.5	6	4.8	4.2	3.5	0	0.15		0.5 Nb 0.05 C
SRR99	8	5	0	10	3	5.5	2.2	0			
CMSX-2	8	5	0.6	8	6	5.6	1	0			
CMSX-3	8	5	0.6	8	6	5.6	1	0.1			
CMSX-6	10	5	3	0	2	4.8	4.7	0.1			
2nd Generation											
CMSX-4	6.5	9	0.6	6	6.5	5.6	1	0.1	3		
PWA1484	5	10	2	6	9	5.6	0	0.1	3		0.05 C
Rene N5	7	7.5	1.5	5	6.5	6.2	0	0.15	3		0.05
3rd Generation											
CMSX-10	2	3	0.4	5	8	5.7	0.2	0.03	6		
Rene N6	4.2	12.5	1.4	6	7.2	5.75	0	0.15	5.4		0.1 Nb
TMS75	3	12	2	6	6	6	0	0.1	5		
4th Generation											
MX4/PWA1487	2.5	16.5	2	6	8.25	5.55	0	0.15	5.95	3	0.03 C
TMS138	2.9	5.8	2.9	5.9	5.6	5.9	0	0.1	4.9	2	

Table 1.1 Composition of some commercially available superalloys (wt%) [adapted from 7,10]

There exists much work in the literature about how each element behaves within the alloy and the contributions it has on the material properties. An explanation of the main effects each element addition has is detailed below [4] [7]:

Ni – Nickel is the main constituent of any Nickel-based superalloy, it provides the FCC crystal matrix to which the other elements are added and results in the γ/γ' microstructure key to the alloys high temperature properties. It has a relatively high melting point, 1455°C, a low thermal expansion coefficient and a density of 8.907g/cm³.

Al – Aluminium additions are typically ~6wt% and are vital in order for the γ' phase to develop. Additionally it also forms a stable, protective alumina (Al₂O₃) oxide on the

blade surface which protects the blade from further oxidation and corrosion. Al does however act as a melting point depressant for Ni.

Cr – Chromium is a solid solution strengthening element within the γ phase that also improves hot corrosion/oxidation resistance. However Cr is also prone to form the brittle Topologically Close Packed (TCP) phases and has therefore been reduced in recent alloy generations [5].

Co – The optimum amount of Cobalt has yet to be determined, and its concentrations vary considerably due to its contradictory effects. It has been shown to improve creep resistance and prevent TCP phase formation but also to lower the γ' solvus and reduce TBC compatibility [7]. However, it has been shown to aid the homogenisation of the γ' phase, within the γ matrix during heat-treatment, due to the lowered γ' solvus.

Mo – Molybdenum is a good solid solutioning element, strengthening both the γ and γ' phases but negatively affects the alloys corrosion resistance properties and promotes TCP phase formation.

W – Tungsten is also a good solid solutioning element, added to Ni-based superalloys to improve their high temperature strength due to its large atomic size. However, it also freely segregates to the γ phase and, with increasing concentrations, increases the risk of TCP phase formation and the nucleation of grain defects.

Re – Rhenium is a relatively new and important addition, first appearing in the 2nd generation Ni-based superalloys, due to its ability to improve high temperature strength as a solid-solution strengthener. It is characterised with an extremely slow diffusion rate in Ni, which makes it good at resisting high temperature creep. It does

however come at a cost of increased density, micro-structural instability and a significant financial cost.

Nb and Ta – Niobium and Tantalum are added to strengthen the γ' precipitates, improving high temperature strength, by substituting for aluminium atoms in the lattice. Too much of these elements can make an alloy prone to the formation of brittle TCP phases. Ta also aids castability by reducing the formation of freckle defects [17].

Ti – Titanium is added to strengthen γ' precipitates but is also prone to forming brittle TCP phases. Ti is known to exacerbate the rate of oxidation and negatively affect the adherence of thermal barrier coating's and is therefore less common, or absent, in the later generation superalloys [18].

Hf – Hafnium improves the alloy coatability, oxidation resistance and, in non-single crystal superalloys, inhibits crack propagation caused by excessive grain boundary carbides [5].

C – Carbon additions are not normally found in single-crystal superalloys due to their lack of grain boundaries and because it lowers the γ phase solvus, restricting the time window available for heat-treatment [7]. It can be found in multi-grained components where it positively contributes to the casting process and strengthens grain boundaries by forming grain boundary carbides.

B, Zr – Both Boron and Zirconium strengthen grain boundaries however they also lower the incipient melting point. Absent in Single-Crystal superalloys [19].

Y – Yttrium will improve the adhesion of beneficial alumina oxides formed at high temperature as well as contributing positively to oxidation resistance [6].

Ru – Ruthenium improves the stability of the alloy microstructure and reduces TCP formation, thus increasing strength, although at a high price due to its considerable expense. Ru partitions preferentially to the γ phase, where it allows higher levels of solid-solution strengthening elements, such as Re and W, without promoting the formation of TCP phases.

Reed [4] produced a figure detailing the broad trends in the use of individual elements for Ni-based superalloys (Figure 1.12) following the transition from 1st generation single crystal superalloys to today's 3rd and 4th generation single crystal superalloys. The 1st generation single crystal superalloys are marked by an increase in solid solution strengthening elements like Cr and Co and the ability to homogenise the microstructure with a single high temperature solution heat-treatment [15]. The transition from the 2nd generation to 3rd generation superalloys is characterised by an increase in rhenium content from around 3wt% to around 6wt% whilst the 4th generation superalloys have increased amounts of ruthenium. The increase in rhenium improved the high temperature capability of the superalloys but left them more prone to the formation of TCP phases. The addition of ruthenium to the latest 4th gen alloys is due to its ability to prevent TCP phase formation but at an increased cost due to its significant market price [7] [15].

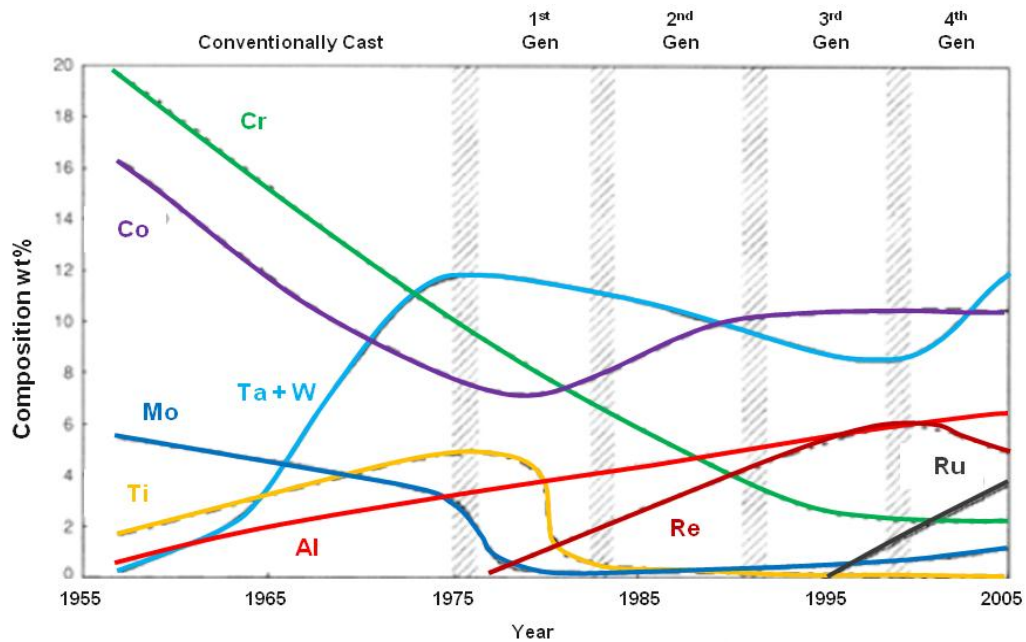


Figure 1.12 Compositional trends in Ni-based superalloy chemistry [6]

The marked drop in Cr content over the years can be explained by the introduction and increased use of thermal barrier coatings. As stated earlier Cr is added to improve high temperature oxidation and corrosion resistance properties but is also susceptible to TCP formation. With the introduction of thermal barrier coatings, a ceramic layer added to the blade surface after casting, the need for Cr was removed.

1.3.3 Topologically Close-Packed Phases

Some important, but undesirable, phases to discuss briefly are the brittle, intermetallic Topologically Close-Packed (TCP) phase's σ , μ and Laves. These are brittle phases that can form during long heat-treatments or during extended in-service high temperatures in alloys containing a high concentration of Co, Cr, Mo, W or Re [5][6][20][21]. TCP phases have closely packed atoms arranged in layers separated by relatively large inter-atomic distances and modern superalloys are increasingly prone to TCP phase formation due to an increase in the concentration of solid-solution refractory elements [22]. These phases typically have low ductility, causing a loss in mechanical strength, as

well as a reduction in corrosion resistance if present in significant quantities. They are commonly identified as long plates/sheets or globular precipitates, often nucleating on grain boundaries [6].

The sigma TCP phase is particularly detrimental to superalloys since its high hardness and plate morphology make it a point for crack initiation to occur, leading to brittle failure at low temperatures. It also adversely affects the alloys high temperature creep strength as it 'sucks' solid-solutioning refractory elements like W and Re from the γ matrix [5].

The precipitation of TCPs is slow and usually requires long hold and high temperatures to compensate for the slow diffusivities of the constituent elements, W and Re. However they are also seen to develop, at lower temperatures and holds, between the superalloy surface and the latest generation of thermal barrier coatings (Pt-aluminide and aluminide [23][24]) in what is termed the 'secondary-reaction zone' or SRZ. Walston *et al* [25] summarised this particular instability and described the formation of the SRZ, as well as the related instability 'cellular colonies' which are formed at grain boundaries and within dendrite cores. The discontinuous nature of the precipitation of the TCPs is a result of the transformation of a supersaturated α' phase into a structurally identical α phase and the lamellar β phase, similar to a eutectoid decomposition [25].

Rae *et al* [23] investigated the effect of the substrate composition on the formation of the SRZ and found that the alloy CMSX-4 preferentially formed μ TCPs whilst the alloy

RR3000 preferentially formed σ TCPs. It was also found that, due to differences in morphology, the σ and μ phases give different diffusion path lengths, σ having a shorter path in RR3000 than μ in CMSX-4. This limits the rate at which the substrate is transformed. In a later paper [24] Suzuki and Rae stated that the formation of the SRZ microstructure was due to the transformation of the metastable Al-enriched substrate (due to inward diffusion of Al from the coating) into an equilibrium mix of γ , γ' and TCPs. The TCPs are aligned perpendicular to the growth direction, facilitated by the rapid diffusion path of the surrounding high-angle grain boundary, and are therefore associated with a grain boundary with high mobility and diffusivity (Figure 1.13). Finally, Suzuki and Rae showed that Ru is effective in inhibiting TCP formation but has a detrimental effect on SRZ formation, promoting it rather than suppressing it [24].

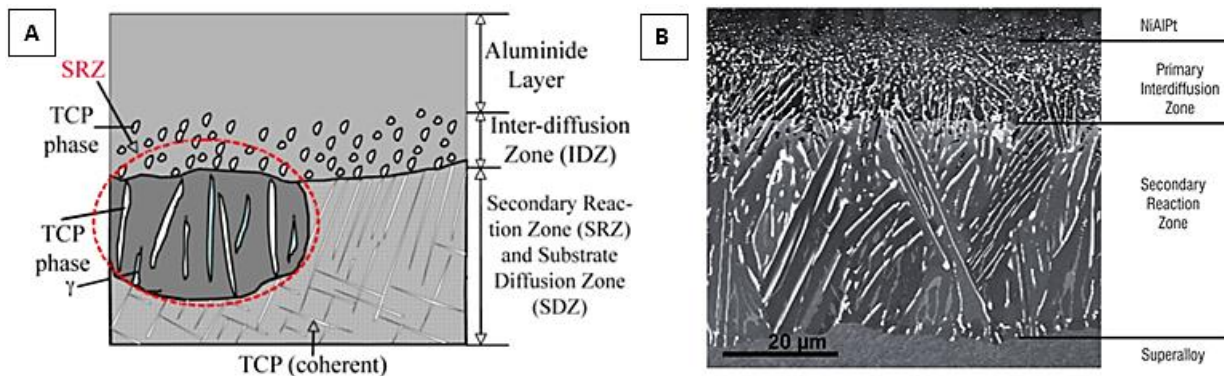


Figure 1.13 (a) Schematic image of a typical SRZ formed under an Aluminide TBC [24] (b) Micrograph of the SRZ formed on the single-crystal superalloy MC544 [26]

1.3.4 Superalloy Mechanical Properties

The mechanical properties of Nickel-based superalloys should be briefly discussed since it is these properties, at high temperatures, which make them stand out from other alloy systems such as steels and titanium alloys. Through a combination of solid-solution strengthening, precipitation-hardening and, in multi-grained components, carbide strengthening, these alloys exhibit high strengths and creep resistance at temperatures approaching their melting point. In fact, the yield strength of many Nickel-based superalloys actually increases initially with temperature before falling at $\sim 800^\circ\text{C}$ [4].

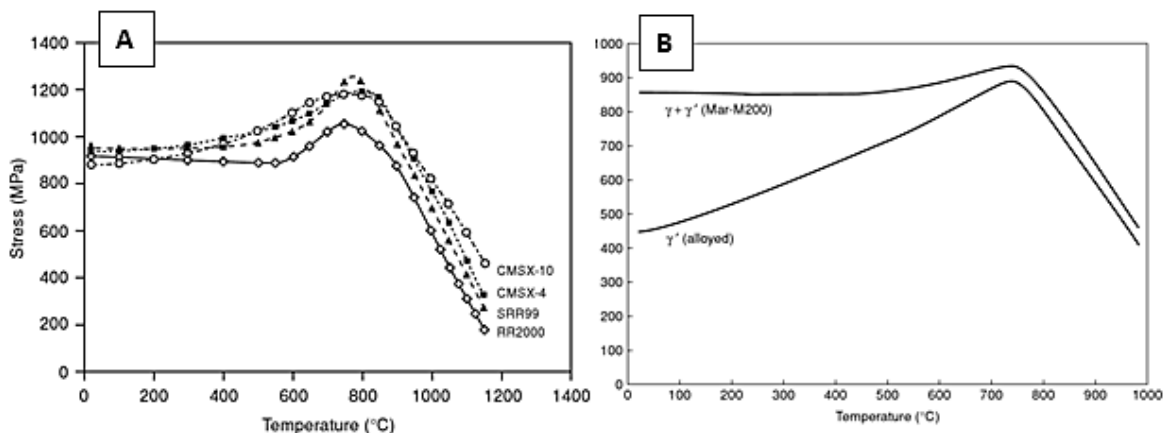


Figure 1.14 (a) Variation of yield stress for some typical single-crystal (SX) Ni-based superalloys [4] (b) Variation of yield stress with temperature of the SX alloy Mar-M200 and SX Ni_3Al equivalent to a γ' particle (taken from [4] [27])

Work by Pearcey *et al* [27] investigated the role of γ' in the strength of Nickel-based superalloys by comparing the yield stress of the SX superalloy Mar-M200 to that of the constituent γ' particle. They showed that the γ' precipitates impart an increasing degree of strength to the superalloy from room temperature and that at and above the peak stress, the superalloy strength is determined solely by the γ' precipitates and not the γ matrix [4] [25]. The method by which the γ' deforms in relation to the γ phase, and its interaction with dislocations, is key to the strength of the superalloy. The paper by Pollock and Argon [28] showed the initial microstructure contains

dislocations within the γ matrix, with the γ' precipitates dislocation-free. Once loaded, the dislocations initially move through the γ matrix (hindered by solute atoms), passing against the γ/γ' interfaces and leaving a trail of dislocations. However, once the stress is high enough, the dislocations can begin to penetrate the γ' precipitates [29].

The most common method by which slip occurs within the γ' precipitates is by shear due to anti-phase boundary (APB) dislocation pairs [30]. These 'superdislocations' are formed of pairs of $\frac{1}{2}\langle 110 \rangle$ dislocations separated by an APB. The APB is formed by the leading dislocation as it destroys the $L1_2$ order (due to a Ni atom moving onto an energetically unfavourable Al site) whilst the trailing dislocation restores the $L1_2$ order after the APB has passed. This process exerts a drag stress on the superdislocation, preventing its penetration further into the precipitate, however the opposite is true for a second trailing dislocation which can then enter the precipitate under a lower applied stress [31].

The characteristic increase in strength with temperature seen in Nickel-based superalloys is explained by this method of dislocation movement through the γ' precipitates. The APB (formed by the lead passing dislocation) has a higher energy on the $\{100\}$ plane than on the $\{110\}$ plane and so, as temperature rises, the dislocations can cross-slip onto this plane resulting in one of the dislocation pairs on a different plane, effectively pinning them and making further slip difficult. This is known as 'Kear-Wilsdorf locking'. This hardening effect is reduced once the temperature is increased to a point where diffusion is enabled, allowing rapid rearrangement of the atoms and making dislocations more mobile [7], [31]. The impressive high-temperature

mechanical properties of Nickel-based superalloys are thus a composite of the strength of its constituent phases and their interactions.

The chemistry and composition of the Nickel-based superalloys has consistently evolved with the drive to improve the material properties, in particular creep and fatigue strength. At the same time, the manufacture and processing of turbine blades has also evolved, with the aim of improving the properties of the finished blade. The processes involved in the manufacture of a single-crystal turbine blade, and some of the advances made, will be discussed in the next Section.

1.4 Investment Casting and Directional Solidification

Gas turbine blades are manufactured using an investment casting process, allowing the production of equiaxed grain, columnar grain or single-crystal turbine blades (Figure 1.15). Directionally solidified (DS) and single-crystal (SX) Ni-based superalloys have enhanced high-temperature capabilities, compared to equiaxed grain components, which can be explained in part by the alignment (or elimination) of grain boundaries with the primary stress direction [32]. This has dramatically improved the thermal fatigue resistance, cyclic strain life, intermediate temperature ductility and creep resistance of high-temperature turbine blades. At the same time, removing grain boundaries allowed optimisation of the alloy chemistry, by removing strengtheners like carbon and hafnium, facilitating further improvements to high-temperature strength and creep properties [33].

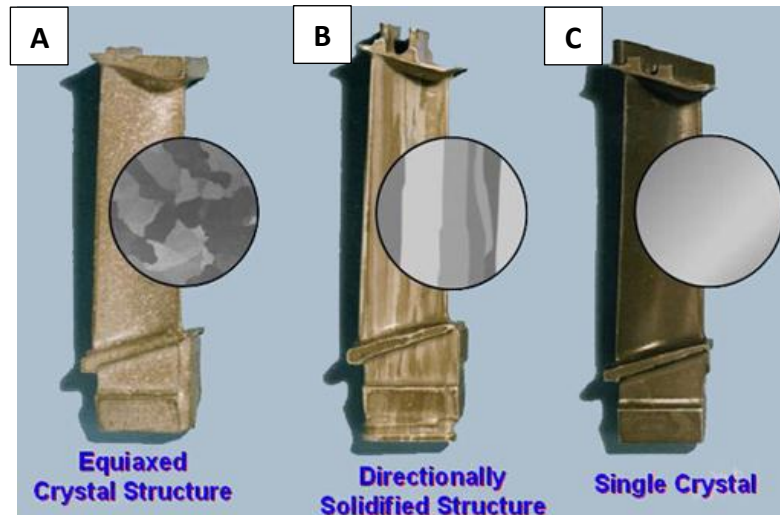


Figure 1.15 (a) Conventionally cast equiaxed grain (b) DS and (c) Single-crystal turbine blades (taken from [8])

1.4.1 Investment Casting

Figure 1.16 illustrates the stages involved in the investment casting process. A wax model of the turbine blade is first made using a metal die. To increase production rates several wax blades are assembled together, with wax runners and risers, allowing multiple blades to be cast at once. The wax assembly can now be coated in alternate layers of ceramic slurry (mixes of zircon, alumina, and silica) and larger, stuccoing particles to create a strong, heat/shock resistant ceramic mould. The ceramic layers are built up until the required thickness is achieved depending on the strength required for casting. After melting out the wax assemblies in a steam oven the ceramic mould is fired to increase its strength so that the molten alloy can be introduced to the mould without it cracking [34].

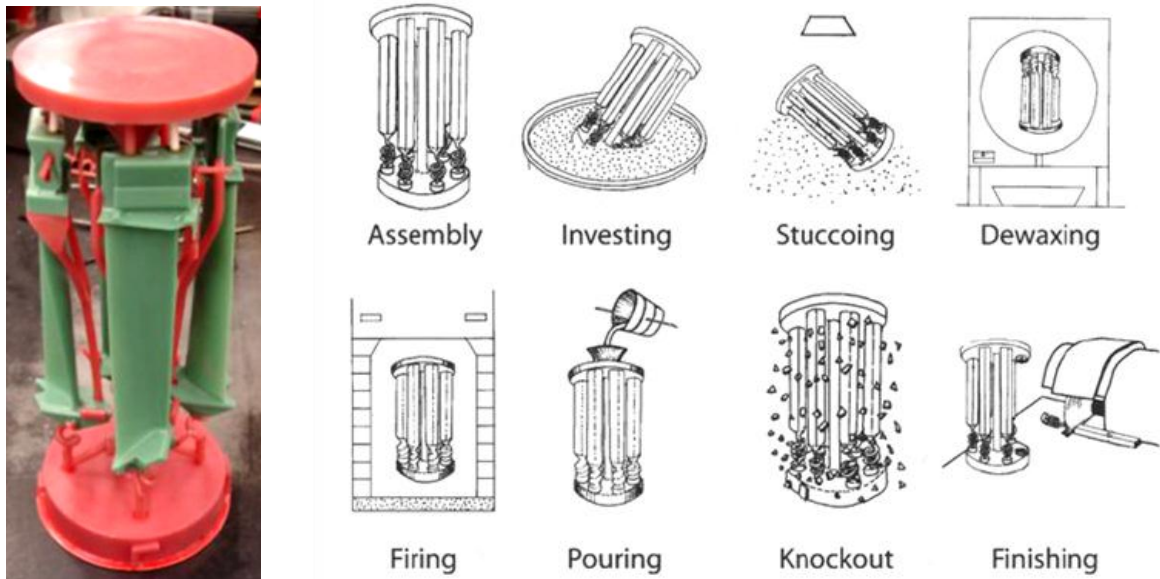


Figure 1.16 Main stages in the investment casting of turbine blades [4] including a wax blade assembly (left) [7]

The casting furnace operates under vacuum, to prevent reactions between the furnace atmosphere and the molten alloy, and melts a superalloy 'charge' (usually via induction heating) which is poured into the ceramic mould via the runners and risers. The molten superalloy is introduced from the top down a central channel but fills the turbine blade cavities from the bottom via the runners and risers. The mould assembly is in contact with a copper chill-plate at the bottom, the purpose of which is to initiate solidification by the formation of equiaxed grains which can subsequently be transformed into DS or SX parts.

It is possible during the wax assembly stage to create internal cooling channels, within the turbine blades, by inserting ceramic cores into the die before introducing the liquid wax. These ceramic cores remain until after casting has finished, imparting their shape to the interior of the turbine blade, and are subsequently removed by a chemical leaching process.

The ceramic mould constituents are a complex system in their own right, developed to have enough strength to resist thermal shock during casting but have enough ductility to allow the solidifying blades to contract without imparting significant strain. Jones *et al* [34] listed the key requirements for a successful ceramic mould and investigated possible future developments for mould design, including the use of organic fibres in the binder to reduce shell production times and improve performance. The typical slurries used for turbine blade manufacture are composed of fine-mesh refractory filler and a colloidal binder, such as water-based colloidal silica. A secondary-electron image of the ceramic is shown in Figure 1.17 detailing the binder, filler and stucco (ceramic particles used between slurry layers to aid binding) materials.

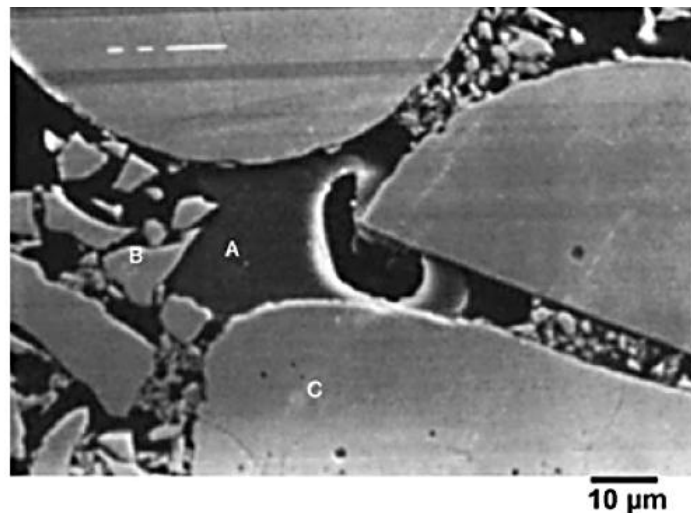


Figure 1.17 Secondary-electron image of the ceramic; (A) colloidal binder (B) refractory filler (C) stucco [34]

The filler material used tends to be 200 mesh sized oxides such as zircon, Al_2O_3 , silica, yttria or mullite on the primary ceramic coats (which allows a fine surface finish to be achieved on the as-cast component) with larger filler material used on the subsequent back-up coats to achieve the desired mould strength. The stucco particles are typically alumina-silicate for economy and are used to minimise drying stresses and provide a rough surface between ceramic layers, assisting in the bond between them [34].

1.4.2 Directional Solidification

To produce DS or SX gas turbine blades the directional solidification technique was developed to create a positive thermal gradient parallel to the growth direction of the solidifying blade [32]. During directional solidification, the liquid alloy is introduced into the mould before the mould/chill-plate assembly is lowered out of the furnace at a controlled rate, producing the required vertical temperature gradient. Equiaxed grains nucleate on the chill-plate, at the bottom of the mould, with essentially random orientations [35][36].

Competitive grain growth occurs as the solidifying metal is continuously withdrawn from the furnace, favouring the grains whose $\langle 001 \rangle$ orientation most closely match the thermal gradient (Figure 1.18(b)); those grains not aligned along the thermal gradient grow at a slower rate (vertically) than those dendrites that are aligned. Because of the slower growth velocity of the mis-aligned dendrites, their growth front is retarded, allowing the aligned $\langle 001 \rangle$ dendrites to overtake and block their growth.

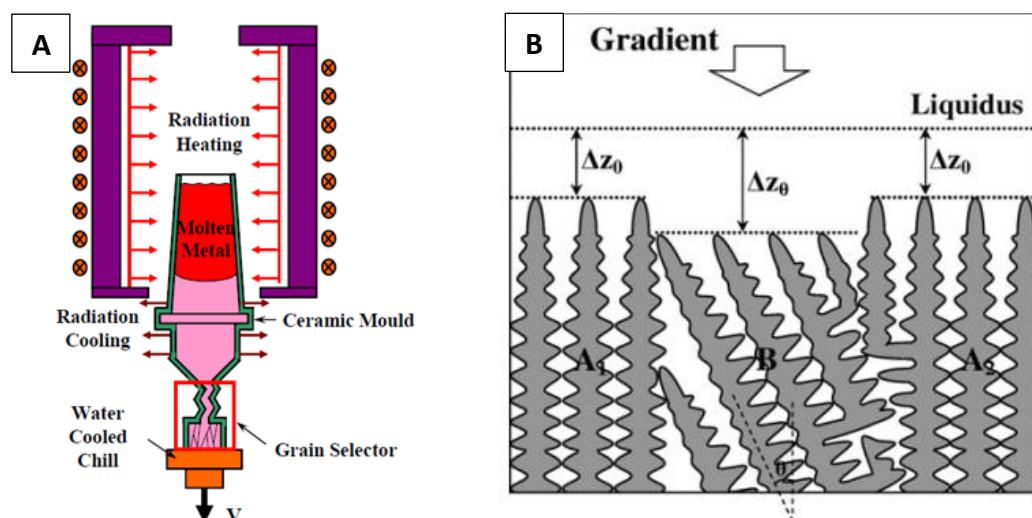


Figure 1.18 (a) Bridgman type induction furnace for DS casting [37] and (b) schematic diagram of competitive grain growth during directional solidification, grains A and B are favourable and unfavourable respectively [38]

In order to produce a single-crystal (SX) turbine blade it is necessary to introduce either a grain selector or a seed to the bottom of the casting. The grain selector, or 'pig-tail', is a helical section of the starter block, above the initial solidification region and chill plate but below the turbine blade body. This acts as a filter, allowing only a single grain of the correct crystal orientation to pass into the blade cavity [35][37].

Another method involves the insertion of a 'seed' of pre-cast alloy, with the desired crystal orientation, on the chill-plate. The seed is pre-heated to partially melt-back the top of the seed before molten superalloy is poured onto the seed, so that the molten superalloy will solidify with the same crystal orientation as the seed crystal. The main advantage of using a seed is that any crystal orientation can be selected, simply by changing the seed, making it possible to cast blades with specific crystal orientations and anisotropic properties [39].

1.5 Solidification of Nickel-Based Superalloys

1.5.1 Grain Structure Evolution during Casting

In order to design and manufacture a casting component, with the aim of improving its mechanical properties, it is important to understand the structural change that occurs during the solidification process. It is well known that by changing the grain structure or crystallographic orientation of a metal it is possible to improve, or deteriorate, the material properties. Coupled with this, the segregation of alloying elements during solidification to different regions within the melt can also have dramatic effects, desirable or undesirable, on the final material properties.

There are many forms that the structure of a solidifying alloy or pure metal can take; cellular and planar amongst others but the most important to this scope of study, and the one most common in Nickel-based superalloys, is the ‘tree-like’ dendrite. The formation of dendrites is initiated by the breakdown of an unstable planar solid/liquid interface and usually the dendritic growth of a solidifying alloy will be either columnar or equiaxed. Columnar dendrites occur when the growth direction is orientated parallel with the direction of heat flux, but in the opposite direction (Figure 1.19(b)). Equiaxed dendrite growth occurs when the direction of heat flux is the same as the direction of growth, heat being extracted radially through the undercooled melt [40].

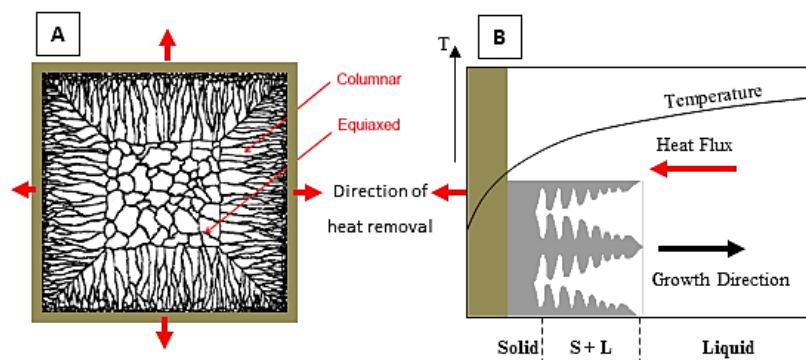


Figure 1.19 (a) Columnar to equiaxed transition and (b) columnar dendritic heat field [10][37][41]

In conventional metallic casting conditions, columnar to equiaxed transition (CET) can occur. As the temperature falls below the liquidus, grains nucleate at heterogeneous sites on, or near to, the mould wall. This produces a thin outer wall of equiaxed grains however, since heat is being removed through the mould walls, there is directionality to the heat flux which causes competitive dendrite growth to occur in the opposite direction. This favours those dendrites most closely aligned to the direction of heat flux, forming the columnar zone. As the dendrites reach a critical stage branches of the dendrite lobes can become detached and grow independently due to the slight undercooling existing within the remaining liquid. These form a centre region of equiaxed

grains with their heat being removed radially rather than parallel to the growth direction. The degree to which this occurs is strongly related to the amount of convection/stirring within the melt [40]. This transition is particularly important to Ni-base superalloy turbine blade production as the mechanical properties of the blade are strongly dependant on the grain orientation (and the elimination of high-angle grain boundaries which are grains whose orientation is greater than 10° from the desired bulk crystal orientation) [42].

As stated earlier, it is important to create and maintain the correct grain structure in order to optimise the mechanical properties of the final cast item. Methods such as adding grain refiners (which remain solid during casting and act as heterogeneous nucleation sites) and directional solidification were developed in order to 'tune' the microstructure to achieve the desired material properties. Figure 1.20 shows the dendritic microstructure of a single-crystal Nickel-based superalloy used for turbine blade manufacture. For this purpose it can be seen that all the dendrites have been aligned along the same axis (parallel to the direction of greatest stress) with no high angle grain boundaries or equiaxed regions. This is one of the contributing factors to the high creep resistance and tensile strength of directionally solidified Nickel-based superalloys [43].

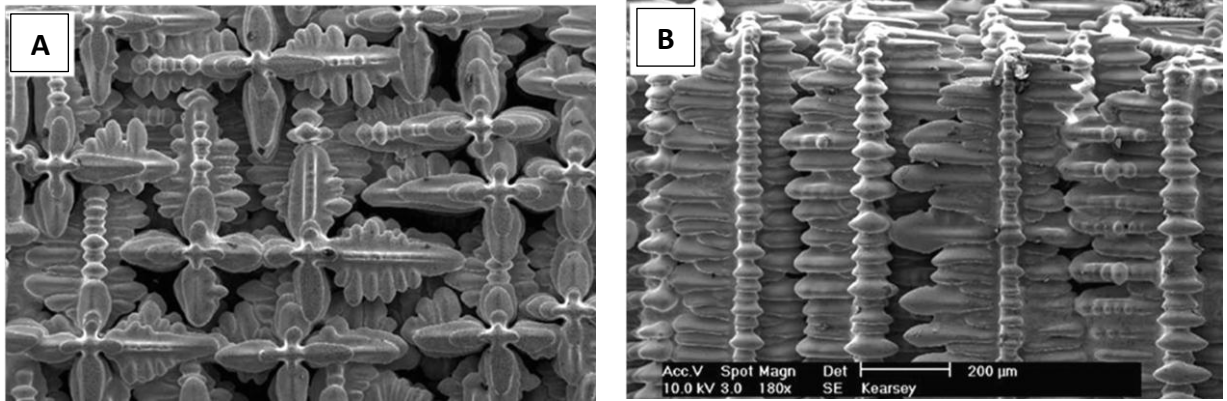


Figure 1.20 Scanning electron microscopy image of the dendrite morphology of a Nickel-based superalloy along (a) transverse and (b) longitudinal directions [43]

1.5.2 Primary Dendrite Arm Spacing and Micro-Segregation

Dendrites can be described by characteristics such as the dendrite tip radius, primary arm spacing and the secondary arm spacing (Figure 1.21).

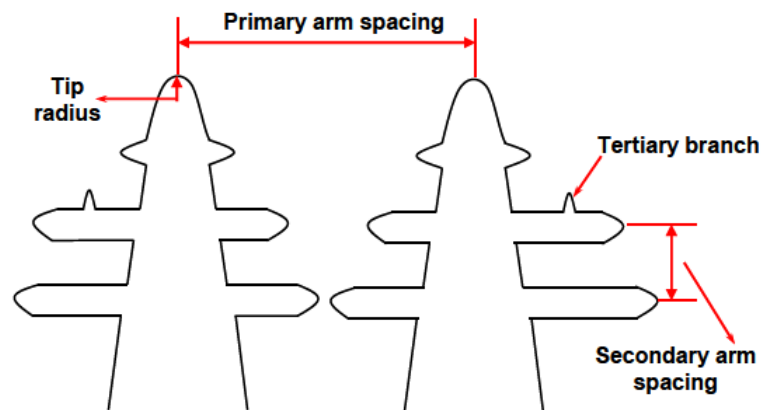


Figure 1.21 Dendrite characteristic length scales [37]

Dendrite length scales are usually given the notation, λ_1 , for primary arm spacing, λ_2 , for secondary arm spacing and so on. Usually as the cooling rate is increased so the primary dendrite arm spacing becomes finer. Since during directional solidification the dendritic growth is predominantly columnar the primary arm spacing defines the maximum length scale over which micro-segregation of alloying elements can occur, that is elements preferentially moving from one location to another [44]. Figure 1.22

shows a transverse secondary electron image of columnar dendrites with darker inter-dendritic (ID) regions.

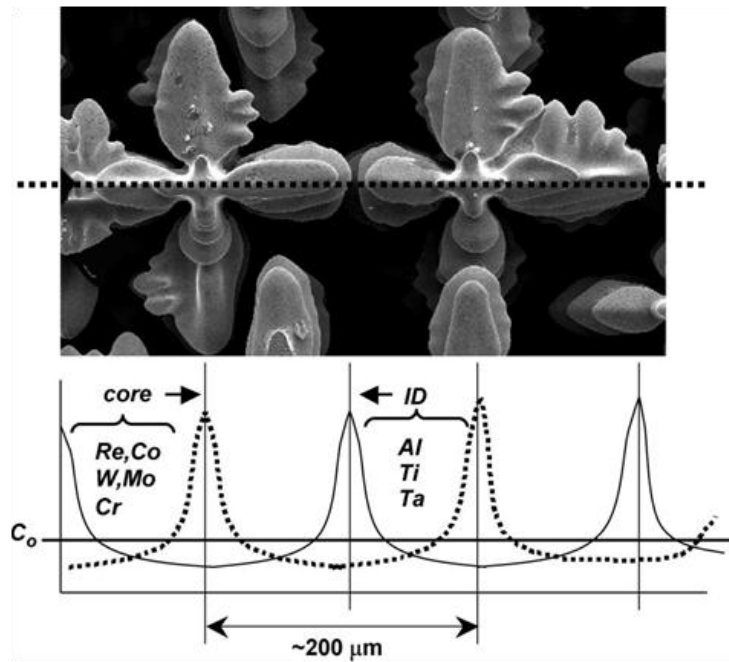


Figure 1.22 Transverse secondary electron image of a dendritic Nickel-based superalloy with segregation of alloy elements to the inter-dendritic and dendrite core regions [43]

During solidification some elements will preferentially partition to the dendrite cores, such as Co, Cr, Re and W, whereas other elements will partition to the ID regions, such as Al and Ti. This is known as solute micro-segregation. It arises due to the preferential partitioning of elements to either the solid or liquid during solidification. As the dendrites form, those elements that partition to the solid become enriched and ‘frozen’ within, likewise those elements that partition to the liquid are rejected and enrich in the liquid, where they can diffuse easily. This results in a concentration gradient from the dendrite core to the ID regions and as the final stages of solidification proceed, the ID regions can freeze as pools of eutectic γ/γ' phases [7][10][43][45].

The scale of primary arm spacing will affect the distances over which these elements must diffuse, and subsequently will affect the solution heat-treatment time (and cost) needed to homogenise the segregated as-cast microstructure [44][46]. It is generally considered that a finer as-cast primary arm spacing leads to higher mechanical properties, lower heat-treatment times (since solutioning time is proportional to the square of the primary arm spacing) and reduced risk of casting defects [37][42][47].

1.6 Heat-Treatment of Nickel-Based Superalloys

Superalloys are heat-treated in order to homogenise the as-cast γ/γ' microstructure and strengthen the alloy by refining the γ' precipitate size upon cooling [48]. These can typically be divided into 3 classes: solution heat-treatment, ageing heat-treatment and coating heat-treatment. A suitable solution heat-treatment is used to remove the inter-dendritic eutectic phases and homogenise the local solidus temperatures thus significantly improving the superalloy mechanical and high-temperature properties [49][50][51].

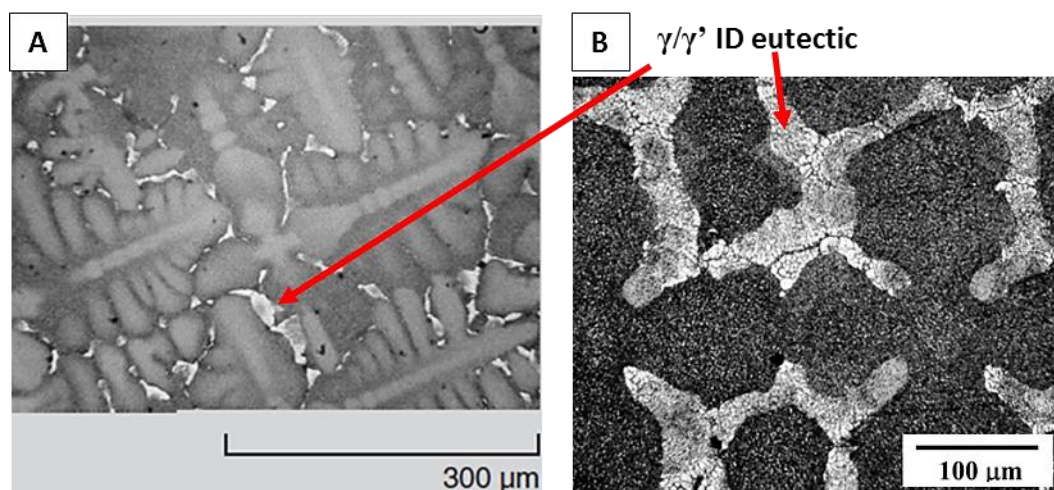


Figure 1.23(a) Optical micrograph of the as-cast dendrite network γ/γ' with ID eutectic [52] (b) CMSX-10N as-cast segregated microstructure with increased fraction of ID eutectic (in white) [17]

When designing a suitable solution heat-treatment cycle it is necessary to find a temperature within the γ single phase field where the γ' solvus temperature is reached before incipient melting of the alloy can occur, this is known as the heat-treatment 'window' [15]. In order to reduce the cost of solutioning, the maximum solutioning temperature is desired to be as high as possible (to facilitate fast diffusion of segregated elements) and the hold time as short as possible, however if localised melting is encountered this will result in rework or scrapping of the component. It is therefore useful to know the temperature at which γ' solutioning is complete, the eutectic phases have fully dissolved and homogenisation of the microstructure is achieved [49]. Because of this the design of an adequate heat-treatment window is always a key factor in new alloy design and development

To ensure that localised incipient melting does not occur during the final hold temperature, a series of ramps/holds are employed to partially homogenise the alloy and remove the eutectic phases, via solid-state diffusion, before reaching the final hold temperature. As can be seen from Figure 1.24 the rates of diffusion for the segregation prone refractory additions, Re and W are very slow within the Ni matrix and this has had a huge impact on the development of heat-treatment cycles and resulted in an increase in the typical heat-treatment time from a few hours at 1300°C, for 1st generation superalloys [7][15], to 30-35 hours at 1366°C for the 3rd generation superalloy CMSX-10 [53].

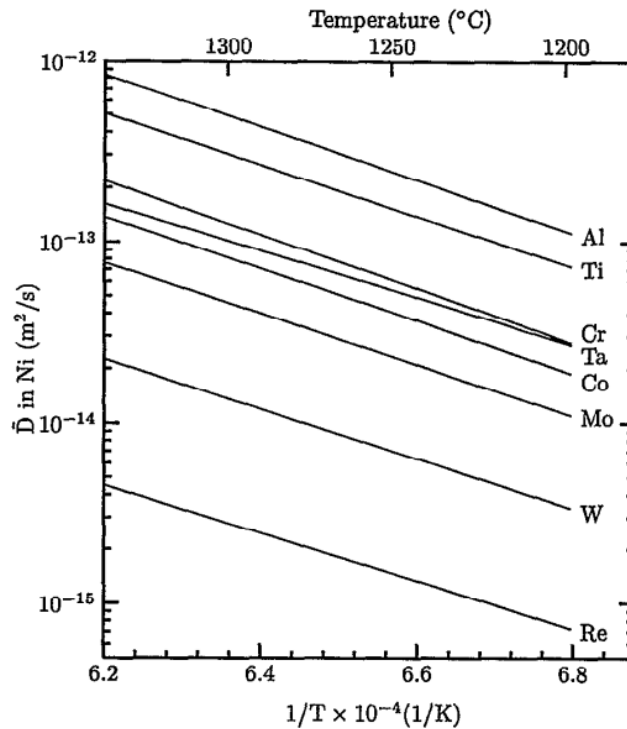


Figure 1.24 Diffusion rates of key alloying elements within pure Ni as a function of inverse temperature [54]

Once the final solutioning hold has been completed the components are quenched, typically with argon gas circulated using fans to maximise the cooling and minimise hot/cool spots within the furnace. The solutioned microstructure subsequently consists of a homogenised γ matrix with irregular γ' particles precipitated during cooling. These are then grown into regular, cuboidal γ' precipitates during the following ageing heat-treatments [7][52].

Once solution heat-treatment has been completed subsequent ageing heat-treatments may be applied to modify the morphology of the γ' precipitates to regular, cuboids in order to improve mechanical properties such as creep life [55] (or in the case of DS and equiaxed castings, the ageing heat-treatments will precipitate grain boundary carbides). Ageing heat-treatments are typically done at lower temperatures than solutioning but for longer hold times for example, the SX superalloy CMSX-4 has a

primary ageing at 1080°C for 4 hours followed by a secondary age at 870°C for 16 hours [56].

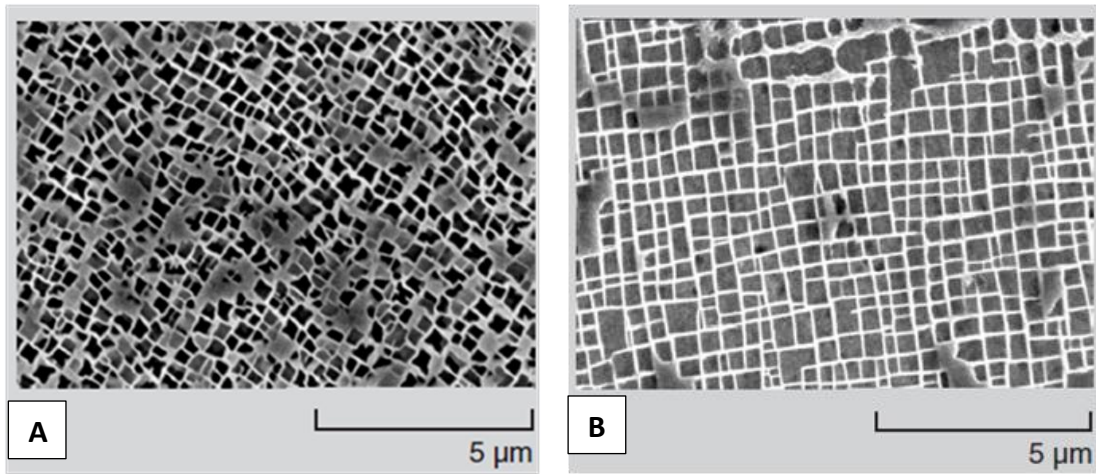


Figure 1.25 Secondary electron imaging of the Ni-base superalloy CMSX-4 after (a) solutioning and (b) ageing [52]

Chapter 2. Defect Formation during Casting and Heat-

Treatment of Nickel-Based Superalloys

The following Chapter introduces some typical casting and heat-treatments defects, and their formation, found on Nickel-based superalloys. The process of oxidation, and in particular high-temperature oxidation, is also discussed in detail due to its importance to many of the discussions in this Thesis.

2.1 Casting Defects

A casting defect is any imperfection or irregularity in the as-cast product that is either tolerable or intolerable (in which case it must be removed, repaired or scrapped). For turbine blades, it is vital to the final strength that casting parameters are adequately controlled in order to minimise the risk of casting defects. Due to the inherent high cost of the production of turbine blades it is necessary to minimise/remove these detrimental defects (in order to maximise profit) by understanding their formation. It is for this reason that considerable research has been, and continues to be, conducted on casting (and processing) defects. Some intolerable casting defects that have negative effects on the material properties of Nickel-based turbine blades are discussed below.

2.1.1 Stray Grain Formation and Freckling

Misaligned or 'stray' grains can form during the solidification process of SX components in areas around complex geometric features like platforms and shrouds, nucleating with random crystallographic orientations and hence may form high-angle

grain boundaries ($>10^\circ$ from the bulk crystal orientation). They are known to act as favourable locations for crack initiation and are deleterious to creep life, resulting in possible in-service failure [57][58].

Freckling is identified as a thin chain of randomly nucleated stray grains associated with localised variations in concentrations of alloying elements and is particularly prevalent in 3rd and 4th generation superalloys rich in Re. The presence of stray grains and freckling is therefore extremely detrimental to the mechanical properties of the turbine blade [59]. The formation of stray grains is typically a result of localised changes in the thermal gradient due to the geometry of the casting, or improper casting parameters. However, freckling is seen to additionally be a product of increasing concentrations of refractory elements, causing convective instabilities in the melt due to dendritic segregation and gravitational forces on the denser refractory solutes [59].

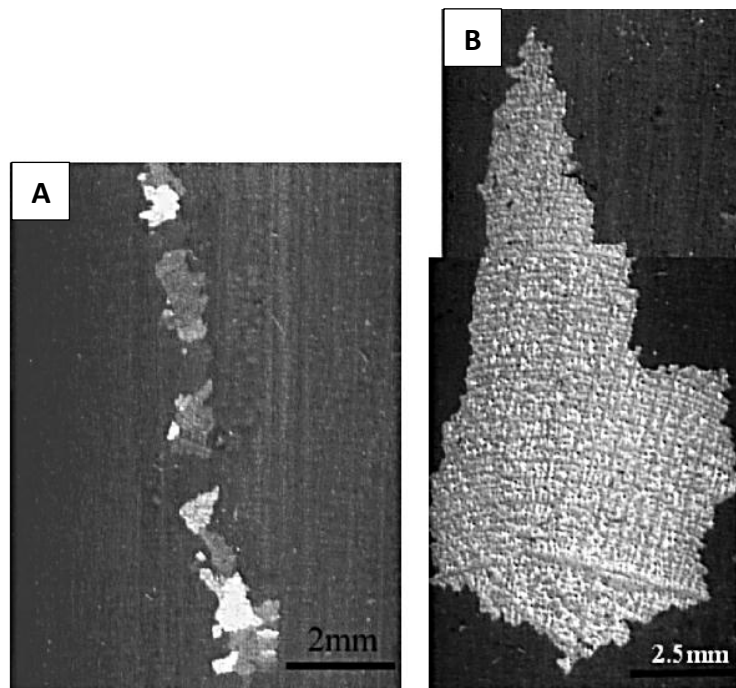


Figure 2.1 (a) Trail of small equiaxed grains to form a freckle defect and (b) a single, mis-orientated stray grain [60]

2.1.2 Cracking and Hot Tearing

Columnar grained components can be prone to grain boundary cracking during solidification and when cooling around ceramic cores, used to provide internal cooling passages, due to differences in thermal expansion in the final stages of solidification. Some directionally solidified alloys (DS) such as IN792 are well-known to be particularly susceptible to hot tearing during the latter stages of solidification [61]. As the alloy and ceramic cores cool, large hoop stresses can be created causing cracks to form at the grain boundaries. This can be alleviated by adding 0.75-2% Hf to the alloy [5][62][63]. Unfortunately Hf additions have two key detrimental effects, (1) Hf is a reactive element that can react with the mould to form brittle inclusions within the alloy and (2) it lowers the incipient melting temperature of the alloy, making solutioning of the γ' without melting the component difficult [61][53][54][66].

2.1.3 Surface Scale

Surface scale is a particularly common casting defect identified as an area of the as-cast turbine blade surface that exhibits a 'fish-scale' like discolouration and roughness. It is usually multi-coloured in the as-cast condition and after subsequent heat-treatment becomes a darker grey (Figure 2.2) [67][68]. It is seen that the area of the turbine blade that exhibits surface scale is the upper aerofoil section (that is withdrawn last from the furnace) and that single crystal Nickel-based turbine blades are particularly prone to this defect [7][19].

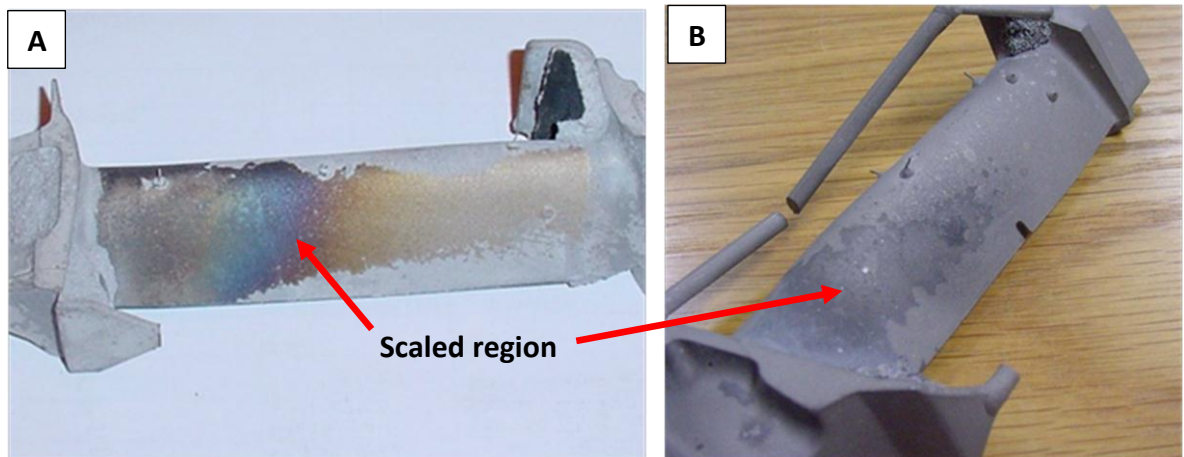


Figure 2.2(a) Surface scale after casting and (b) after subsequent heat-treatment [7][19]

Surface scale is a commonly occurring casting defect on SX Nickel-based superalloy turbine blades but has been little reported in the open literature, most notably however in the thesis by Dr G. Brewster [7] who conducted the first research into the chemistry, nature and factors affecting the formation of surface scale found on the 1st generation superalloy, SRR99. The term 'scale' is commonly used in oxidation studies whilst 'surface scale' is an in-house term used within the Precision Casting Facility (PCF) at Rolls-Royce plc to refer to this particular surface defect. All other areas of the scaled turbine blade are subsequently referred to as 'unscaled'.

Surface scale has a significant impact on the post-processing of turbine components following heat-treatment. The scaled regions must be mechanically abraded using a blasting operation with grit media before the component can be etched to visually assess the for grain structure defects like freckling and mis-orientated grains. The adherence of the surface scale to the parent substrate therefore determines the intensity of the mechanical ablation and it follows that three scenarios can arise:

- i. For a less aggressive blast, the scale remains adhered to the surface and, because the scale is not attacked by the etch reagent, this region is consequently “opaque” and cannot be inspected for grain defects.
- ii. For an aggressive blast, whilst it is possible to “peel” off the surface scale layer, there is also an appreciable removal of metal from beneath the scale, as well as from the unscaled surface and this can lead to a distortion of the aerofoil geometry or a thinning of the blade surface beyond specified limits.
- iii. The grit-blasting action will impart residual strain into the turbine blade surface, this strain can result in the formation of re-crystallised grains which reduce the strength of the component and necessitate its scrapping.

All of these scenarios will result in an increase in production costs due to blade scrappages, re-work and lost time. It is difficult to know the exact cost of surface scale to the casting facility, since it has not been evaluated individually. In 2010 a cost analysis of the total effects of surface scale (and the related surface melting) was estimated at £1.2m per annum [67] in a modern casting foundry.

The most notable research into surface scale to date was produced by Dr G. Brewster [7], who investigated the factors affecting the formation of surface scale on the 1st generation alloy, SRR99, including its composition and chemistry. Brewster showed that the blue/gold discolouration of the scaled area is an optical effect caused by thin film interference effects and that a layer of eutectic, ~20µm thick, is present along the blade surface in the scaled areas, due to shrinkage of the dendrite network and the subsequent flow of inter-dendritic liquid to the surface of the casting. This only occurred at higher solidification heights due to stresses imparted on the mushy zone

from the contracting solid below. It was also shown that, on the alloy SRR99, surface scale constitutes a thin oxide film (~ 150nm thick) of predominantly Al, Ti and Cr and he proposed that the formation of these oxides were driven by mould-metal separation allowing oxidation of the solid alloy during the latter stages of solidification. Brewster's mechanism of scale formation is shown in Figure 2.3 and forms the basis of the revised formation mechanism diagram proposed in Chapter 3.

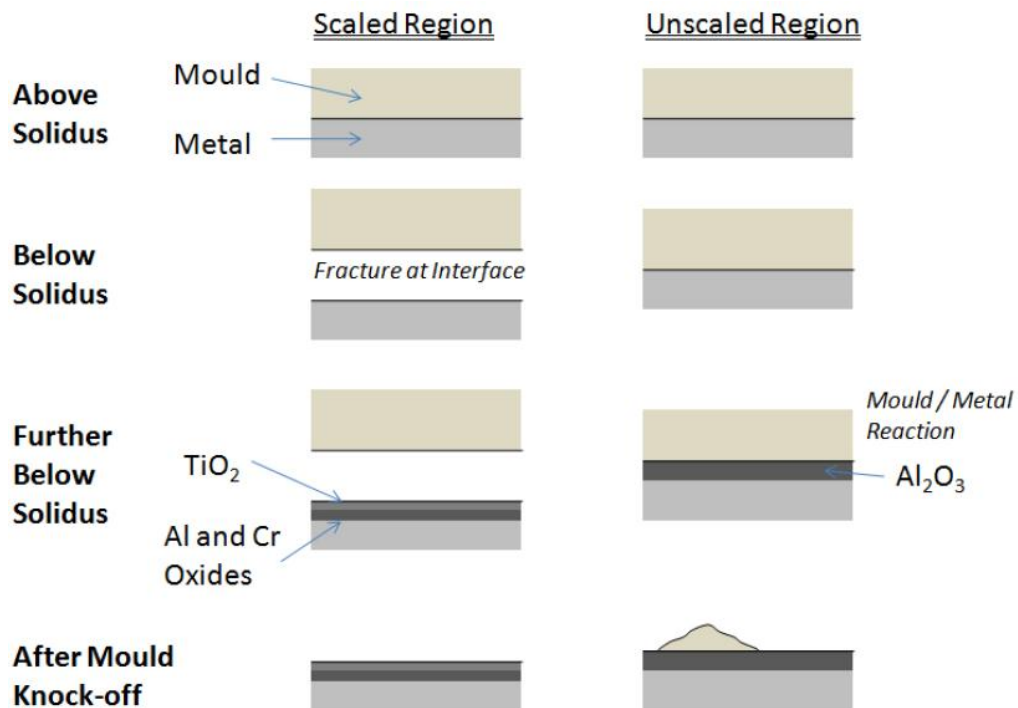


Figure 2.3 Proposed formation mechanism of Surface Scale from Brewster [7]

2.1.3.1 Surface Scale on Rolls-Royce's Single-Crystal Components

Surface scale is an important defect to the PCF and has therefore been subject to internal investigations, although no correlations were made that could prevent surface scale formation. The internal report by Grindley [67] showed that surface scale is seen post-cast when the ceramic mould shell is removed and it always occurs across the upper aerofoil, under the shoulder of the turbine blade (TB) and the extent of surface coverage varies with the geometry of the blade. In the case of low-pressure (LP) and intermediate-pressure (IP) TB's, having an appreciably greater length of aerofoil

compared with the high-pressure TB's, the extent of surface scale coverage across the length of the aerofoil is more severe. It is the convex portion of the blade aerofoil that is affected by surface scale with little or no scale found on the reverse, concave side.

Several casting parameters were also investigated for their effect on surface scale formation and these are concluded below [67]:

- i. Faster mould withdrawal rates from the furnace hot-zone during casting were shown to increase the severity of surface scale coverage.
- ii. A trial to test whether blade orientation within the casting furnace affected the spatial location of surface scale was conducted on blades cast root-up (standard orientation) and root-down. This showed that surface scale always formed on the last part of the blade to solidify, irrespective of orientation, although the localised mould shape affected the spatial dimensions of the scale.
- iii. The feeder and continuator designs (the parts that direct the liquid metal into each blade cavity in an even manner) were investigated and it was found that a Y-shaped continuator increased the scale severity.

2.1.3.2 Research on Surface Scale and Mould-Metal Reactions in the Literature

There is little literature on the formation of surface scale; although limited experimental evidence exists that cites the beneficial role of carbon additions ≤ 450 ppm in suppressing the formation of surface scale [69][70]. A possible reason for the occurrence of surface scale can be related to a mould-metal reaction, since the metal and the ceramic mould are in intimate contact, at high temperature, during

casting. Frye *et al.* [71] have classified possible mould-metal reactions that involve an oxide at the mould interface (M_xO_y) reacting with an element in the liquid alloy (N) to form a new oxide (N_xO_y) and dissolution of the displaced element, M, which then dissolves in the liquid metal/alloy. These reactions are particularly prevalent in alloy systems with additions, like Al, that form stable oxides with large negative free energies of formation and are therefore important considerations for Ni-base superalloys due to their relatively high Al content. These mould-metal reactions are, however, classified as occurring over the entire casting surface whereas surface scale is clearly relegated to certain areas.

Most notable alloy examples where such mould-metal reactions occur are: steels [72], Ti and TiAl alloys [73], Mg alloys [74], and NiTaC systems [75]. A key feature of these mould-metal reactions is that the reaction product is responsible for the existence of a strong adherence between the mould prime-coat and the surface of the casting.

Reports in the literature of mould-metal reactions in Ni-base superalloys are sparse; the most notable being the study of Piwonka [76], which reports the reaction between the Ni-base superalloy, Rene 80 and a zirconia/silica base ceramic mould. It was argued that Al, Ti and Hf from the liquid alloy can react with the silica (SiO_2) to form alumina (Al_2O_3), which can account for an Al denuded zone identified in the vicinity of the casting surface. A key aspect of this type of reaction is that it occurs across the entire casting surface since the reaction occurs when the alloy is liquid.

2.2 Heat-Treatment Defects

The as-cast microstructure of modern Nickel-based superalloys is increasingly segregated due to the rising addition of refractory elements and therefore requires complex heat-treatment processes, which are both time consuming and expensive. Solution heat-treatments involve a series of ramps and lower temperature isothermal holds before a final isothermal hold at the solutioning temperature. This is done to achieve part-homogenising of the as-cast alloy before reaching the final solutioning temperature and thus avoiding incipient melting. However, this process is made challenging due to the narrow heat-treatment window (Solidus temperature - γ' Solvus) of these alloys and the high temperatures required for adequate homogenisation [49][52][54]. The following heat-treatment defects, Surface Melting and Recrystallization, are described here due to their importance to this Thesis.

2.2.1 Surface Melting

An undesirable side-effect of solution heat-treatment is the formation of surface melt blisters/wrinkles. The melt blister is an area of the blade surface (10's mm²) that has incipiently melted during solution heat-treatment, resulting in a raised re-solidified defect with a characteristic darker appearance than the rest of the blade (Figure 2.4). This defect is directly linked with surface scale because it is in the areas that previously exhibited surface scale that the melt blisters appear during subsequent heat-treatment. This melted and re-frozen layer has to be mechanically abraded before the components surface can be visually assessed for grain structure defects such as recrystallisation, freckles and high-angled grain boundaries. It is also more likely that the

blade will be scrapped due to excess material removal (resulting in exceeded dimensional tolerances) or if the part requires too many rework stages.

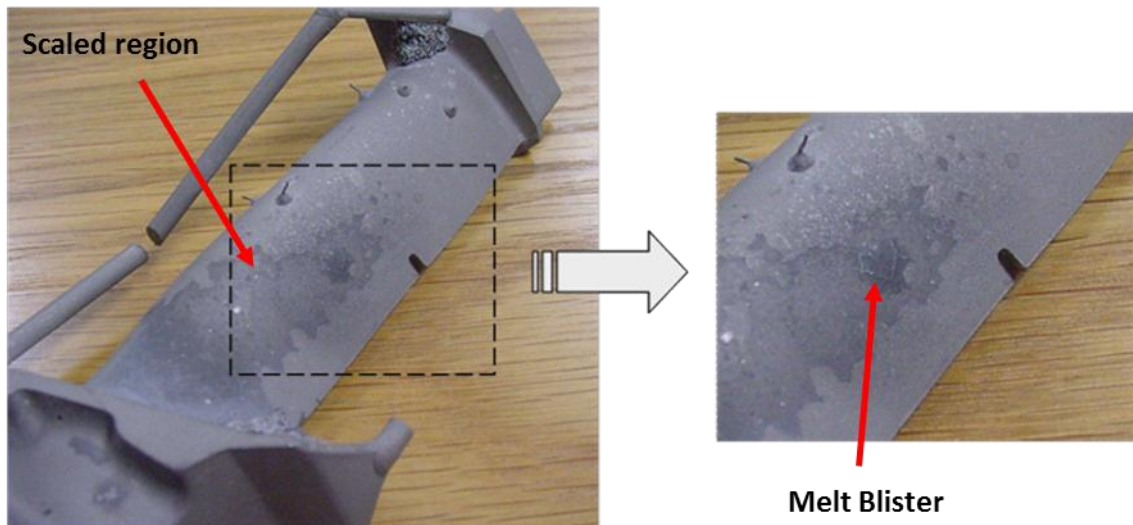


Figure 2.4 Surface melt blister on a solutioned Intermediate-Pressure (IP) Trent 800 turbine blade [67]

It is particularly common on the SX Nickel-based superalloys CMSX-10K and CMSX-10N due to their very limited solution heat-treatment windows, where they are taken very close to their melting temperatures (it should be noted that surface melting is also seen on CMSX-4 components as well). It is also seen however that these melting defects are commonly found on under-solutioned components and is therefore a result of significant localised melting temperature suppression, not bulk over-heating [7]. The cause of the formation of this particular defect during solutioning forms the basis of the investigations in Chapter's 4 and 5.

2.2.1.1 Surface Melting Experience at the PCF, Rolls-Royce plc

Surface melting is a commonly occurring surface defect on SX Nickel-based superalloy turbine blades at Rolls-Royce plc. and has therefore been subject to internal investigations to try and minimise the impact on productivity. It is particularly prevalent on the SX alloys CMSX-10K and CMSX-10N; however other alloys such as CMSX-4 are also affected. Two key Rolls-Royce internal reports by Jackson *et al* [68]

and Grindley [67] aimed to track the causes and influential factors of surface melt defects by means of investigating each variable along the casting and heat-treatment process cycle. These included casting and heat-treatment furnace variables (for example: temperature variation, power spikes and withdrawal rates), mould shell material affects and alloy bar-stock composition. Achieving statistically relevant results for many of these variables proved difficult however, due to the complexity of the processes involved and the sporadic nature of the surface melting defect. A statistical analysis of the occurrence of surface melting was conducted for two different alloys (CMSX-10K and CMSX-10N) on sample sizes of 4,428 and 6,135 respectively, which found the percentage of affected blades to be 33% and 53% respectively and the associated cost (due to rework) was estimated to be between £100K-200K per annum in 2005 [67]. There is therefore a significant financial incentive towards minimising the occurrence of this surface defect.

Grindley's investigation noted that the occurrence of surface melting could be eliminated from the majority of the CMSX-10K/N components by using an alternate heat-treatment furnace in Woodford. The cause of this was not fully understood but the main differences between the Woodford furnace and the standard production furnace at Bodycote plc in Derby is that Woodford uses Molybdenum heating elements and liners whereas the Bodycote furnace uses graphite. The Bodycote furnace was also more prone to temperature overshoots and power spikes due to temperature lag on the insulated thermocouples and inaccurate temperature readings. To counter this problem, a number of trials have been conducted to attempt to achieve complete homogenisation of the bulk microstructure, whilst preventing surface melting, by

changing the heat-treatment profile. These results showed however that complete homogenisation, within an adequate time-scale, was difficult to achieve without encountering surface melting.

2.2.1.2 Research on Surface Melting in the Open Literature

The most recent work reported so far is the thesis by Brewster [7] who investigated the bulk solutioning and melting properties of some key SX Nickel-based superalloys, as well as analysing the surface melt blister morphology in detail. Brewster showed that the surface melt blister is not necessarily a product of bulk over-heating during solution heat-treatment since it was evident on under-solutioned samples, but rather due to localised depression of the incipient melting temperature. He also noted that there was a significant increase in the levels of Si within the melt blister region (~5 wt.%), which acts as a melting point depressant. The most likely source of the Si is the $ZrSiO_4$ and SiO_2 within the mould shell used during casting which reacts with the Al in the melt during casting to form Al_2O_3 and elemental Si. This is one of the key stages during the formation of Surface Scale, occurring in the unscaled regions, and is discussed in Chapter 3.



Figure 2.5 OM image of melt blister cross-section from a heat-treated SX turbine blade

A recent paper by D'Souza *et al* [77] studied the microstructure and composition of a typical melt blister cross-section found on the scaled region of a solutioned CMSX-10N SX turbine blade. The surface melt blister was shown to be an area of significant microstructural instability with both incipient melting and solid-state transformations

occurring during solutioning. The morphologies that evolved along the surface cross-section of the melt blister were (in order of appearance along the cross-section):

- (i) SX γ' grains with fine TCPs precipitated within.
- (ii) Polycrystalline γ' cells with large needle-like TCP sheets.
- (iii) SX banded cellular structure of alternating γ and γ' phase which has incipiently melted and re-frozen with the orientation of the substrate. The γ' bands show γ channels and TCPs whilst the γ bands precipitate out the γ' phase.

It was shown that the composition in all three regions was significantly enriched in Al and Si which was identified as the cause of the incipiently melted banded cellular region; however the cause of this enrichment was not identified. The morphology of the melt-blister was shown to be characteristic of the discontinuous precipitation reaction and secondary-reaction zone (SRZ) (a γ' matrix with TCP precipitates and γ -lamellae) which is typically found beneath the diffusion zone of thermal barrier coatings [25]. The findings of this paper showed that the melt-blister is an area of significant microstructural instability, where it is possible for the stable γ phase (matrix) to be transformed to the non-equilibrium γ' phase in the near-surface region of the casting during solutioning.

2.2.1 Recrystallization

A particularly undesirable defect found on directionally solidified turbine blades, due to its detrimental impact on creep and fatigue properties, is recrystallization (RX). This is the formation of randomly orientated grains, during heat-treatment, as a result of cold work done on the as-cast component. This could be grinding/blasting operations to remove casting defects such as surface scale, or due to differential thermal

contraction between mould, metal and internal ceramic cores [78]. Porter and Ralph [79] reviewed the mechanisms of recrystallization on four wrought Nickel-based superalloys; particularly investigating the effect of γ' distribution on the motion of the recrystallization front. It was shown that the recrystallization front is characterised by high diffusivity and solubility which causes, in low γ' fraction alloys, complete dissolution of the γ' ahead of the recrystallization front followed by re-precipitation behind it. In high γ' fraction alloys the re-precipitation of γ' occurs discontinuously at the recrystallization front due to the front becoming supersaturated by the dissolved γ' solute. The severity and depth to which the recrystallized grains penetrate is dependent on the imparted strain, the solutioning temperature and hold duration as well as the degree of retardation imparted by precipitates [80][81].

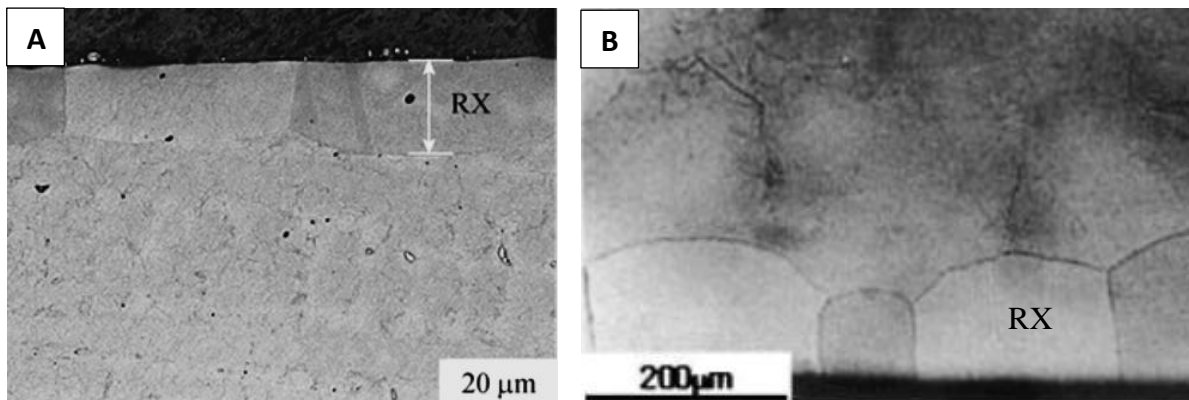


Figure 2.6(a) Surface RX formed on a SX superalloy after solutioning at 1300°C for 1hr [81] (b) Surface RX formed on a SX CMSX-2 superalloy after solutioning at 1315°C for 3hrs and ageing at 1050°C for 16hrs and at 850°C for 48hrs [82]

At temperatures below the γ' solvus, recrystallization occurs via a discontinuous cellular precipitation process whereas above the γ' solvus normal recrystallization occurs, at a much faster rate [80]. This is because the γ' precipitates act to 'pin' the recrystallization front below the γ' solvus temperature, resulting in a slower migration rate [83][84]. Recrystallization is an important phenomenon to discuss as many of the factors affecting its formation, and the mechanisms by which it grows, are pertinent to

the discussions in Chapter 4 in order to explain the formation of the surface melt blister defects.

2.3 High Temperature Oxidation

High temperature oxidation occurs when a metal is exposed to an oxygen rich atmosphere (like air) at elevated temperatures and is usually detrimental to components such as turbine blades. Oxidation can cause depletion of key strengthening elements, particularly γ' precipitates through the loss of aluminium to the oxide, loss of mechanical properties, and internal void formation. Many Nickel-based superalloys are designed to form protective alumina or chromia oxide surface layers to maximise their resistance to further oxidation and hot corrosion. In order to do this a firm understanding of how these oxides form, and how they perform during service is essential [8]. High temperature oxidation also affects Nickel-based superalloys during their manufacture, particularly during casting and heat-treatment, and its consideration therefore forms a backbone of this research project.

2.3.1 Thermodynamics of Oxidation

The general equation for the oxidation of a pure metal is given by [86]:



Where M is the oxidised metal and $M_x O_y$ the oxide product. The driving force for the oxidation reaction to occur is defined by the Gibbs free-energy equation, which must be negative in order for the reaction to proceed (if it is positive then the reverse reaction becomes more favourable). Using the above reaction, the Gibbs free-energy is defined as:

$$\Delta G = \Delta G^\circ + RT \ln \left(\frac{a_{M_x O_y}^{2/y}}{a_M^{2x/y} \cdot a_{O_2}} \right) = \Delta G^\circ - RT \ln P_{O_2} \quad \text{Equation 2.2}$$

Where ΔG is the Gibbs free-energy change for the reaction, ΔG° is the standard free-energy change, R is the gas constant, T is temperature, a is the thermodynamic activity of the species (taken as unity for solid phases at standard conditions) and P_{O_2} is the partial pressure of oxygen (taken to be equal to a_{O_2}). At equilibrium, the free-energy change is zero (since there are equal amounts of oxide being produced as there are dissociated), therefore the partial pressure of oxygen in which the oxide and metal are in equilibrium can be found from:

$$\begin{aligned} \Delta G = 0 &= \Delta G^\circ - RT \ln P_{O_2} \\ \Delta G^\circ &= RT \ln P_{O_2} \end{aligned} \quad \text{Equation 2.3}$$

This P_{O_2} must be exceeded for oxidation to occur and therefore this equation has become important in describing the likelihood that an oxidation reaction will occur, given the temperature and oxygen partial pressure. ΔG° is defined by the relationship:

$$\Delta G^\circ = \Delta H^\circ - T \Delta S^\circ \quad \text{Equation 2.4}$$

Where ΔH° and ΔS° are the standard changes in enthalpy and entropy respectively. This relationship enables the plotting of temperature versus ΔG° for each oxide reaction, where the gradient of each line is equal to $-\Delta S^\circ$ and the y-axis intercept is equal to ΔH° . This type of plot is known as an Ellingham Diagram and when combined with Equation 2.4 it allows the determination of the conditions under which an oxide reaction will occur [8][85].

2.3.2 Ellingham Diagram

The Ellingham diagram is a useful and fast method to determine which oxides may form and in what order. This is because the free-energy change is negative for most

oxidation reactions, thus the most thermodynamically favourable reactions are located at the lower end of the diagram and it is these metal elements that have the greatest affinity for oxygen. Caution is needed however, since it is not only thermodynamic stability that affects which oxides will form but also growth kinetics (i.e. less stable oxides can typically grow faster than the stable ones, resulting in their appearance first) [8].

For each reaction on the Ellingham diagram the oxidation is normalised to occur at 1 atmosphere of P_{O_2} and to consume 1 mole of oxygen. The majority of reaction lines slope upwards because they are reacting a condensed phase (solid or liquid) with a gas phase (oxygen) to produce another condensed phase (the oxide), which results in a reduction in the reaction entropy. However, a notable exception is the oxidation of carbon ($C+O_2=CO_2$) which involves the reaction of a solid with a mole of gas (oxygen) to produce a mole of gas (CO_2), therefore there is little net change in entropy and the reaction line stays near-horizontal. Likewise, for the production of carbon monoxide ($2C+O_2=2CO$) there is a solid reacting with a mole of gas (oxygen) to produce 2 moles of gas ($2CO$), which results in a net increase in entropy, thus the reaction line slopes downwards. The Ellingham diagram has three main uses:

- i. Determine the relative ease of reducing a given metallic oxide to metal;
- ii. Determine the partial pressure of oxygen (P_{O_2}) that is in equilibrium with a metal oxide at a given temperature (using the nomographic scale on the outside of the diagram) and;
- iii. Determine the ratio of carbon monoxide to carbon dioxide (CO/CO_2) that will be able to reduce the metallic oxide to pure metal at a given temperature. The more

stable the oxide that is to be reduced, the greater the amount of CO is needed in relation to the amount of CO_2 .

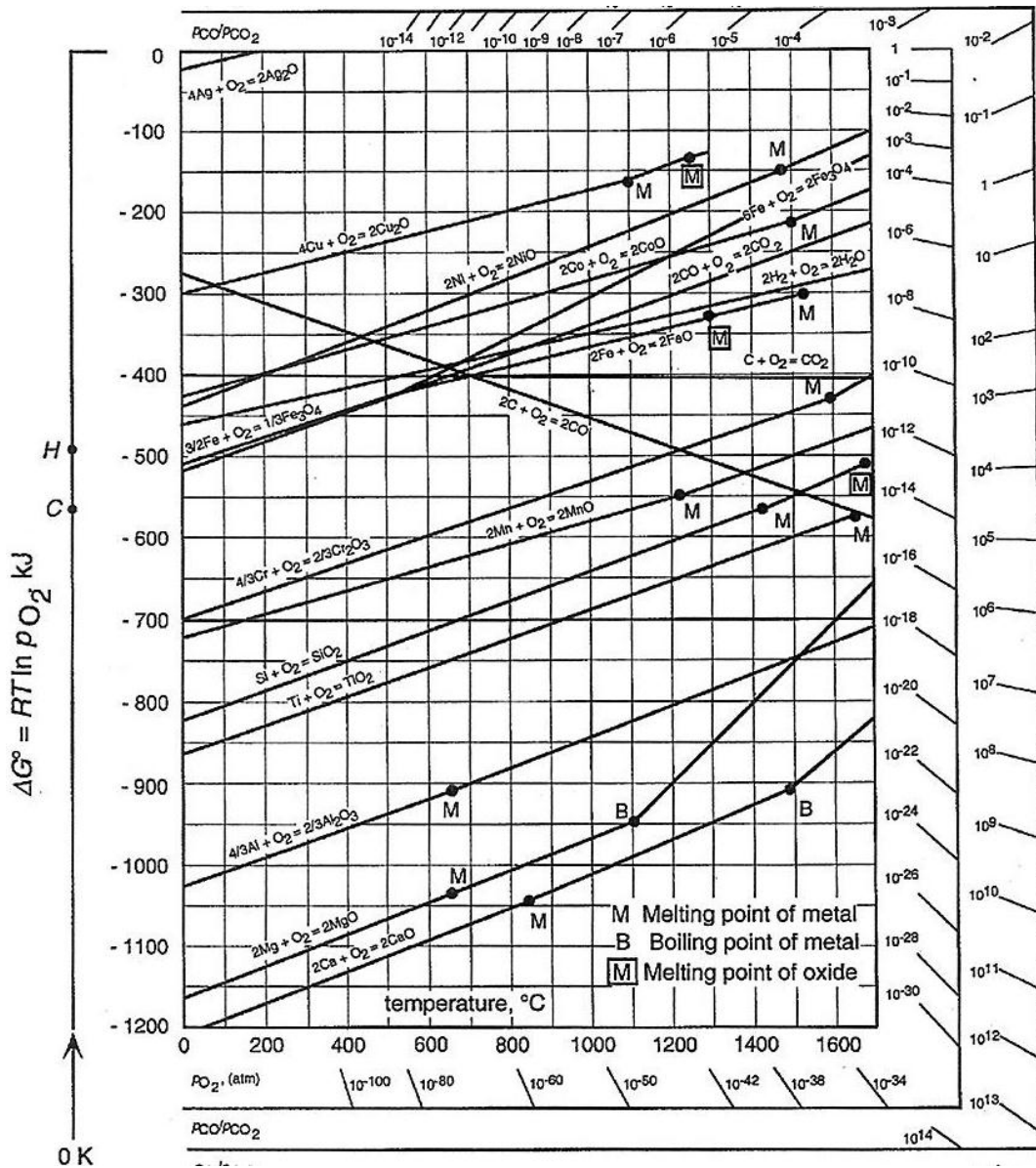


Figure 2.7 The Ellingham diagram for a variety of oxidation reactions taken from [86] (a solid dot on the reaction line indicates where a phase change has occurred and there is usually a corresponding change in the line's slope)

The lower down the diagram, the more thermodynamically stable the oxide and the harder it is to reduce the oxide back to pure metal. A given metal can reduce the oxides of all other metals that lie above it on the Ellingham diagram, so Al, Mg and Ca can easily reduce the oxides of Ni, Co and Cu for example. The same is true of carbon at high temperatures however; it cannot reduce the oxides of Al or Mg [8][86].

2.3.3 Pilling-Bedworth Ratio

The Pilling-Bedworth ratio (PBR) is the ratio of the volume of the metal oxide produced to the volume of the metal consumed and is used as an indicator for whether an oxide will be protective (i.e. prevent further oxidation) or not. If the PBR value is $\ll 1$, the volume of the oxide formed is lower than the amount of metal consumed thus for the oxide to conform to the surface of the metal, the oxide will be porous and un-protective. If the PBR is ~ 1 then the oxide is usually protective. However, if the PBR is $\gg 1$ then the oxide volume is greater than the metal consumed and the oxide will buckle and spall away due to high compressive stresses, this is therefore an un-protective oxide too. This is only a general rule however, and there are exceptions. The protectiveness of the oxide will also depend on the adherence of the oxide to the substrate, the difference in thermal expansion coefficients, the oxides melting point or volatility and any chemical effects due to alloying [87].

Metal Oxide	PBR	Protectiveness
Al/Al ₂ O ₃	1.29	P
Cr/Cr ₂ O ₃	2.07	P
Si/SiO ₂	2.15	P
Ca/CaO	0.64	NP
Ta/Ta ₂ O ₅	2.47	NP
Ni/NiO [88]	1.65	NP

Figure 2.8 PBR values for common oxides and their protectiveness. P=protective, NP=non-protective [8][89]

2.3.4 Oxide Growth Mechanisms

The driving force for oxidation is the minimisation of Gibbs free-energy between the separate reactants and the final product. However, in order for the reaction to occur, the reactants must first come into contact. The first stage of oxidation involves the adsorption of oxygen onto the surface of the metal which can occur by chemical

adsorption (chemisorption) or physical adsorption (physisorption). Chemisorption is the chemical bonding of the oxygen molecules to the metal surface whilst physisorption involves the physical attraction of oxygen molecules to the metal surface by Van der Waals forces [90]. Physisorption occurs without any need to overcome an activation energy and is only dependant on the flux of oxygen atoms striking the metal surface whilst chemisorption is more complex, requiring the activation energy to be overcome. The activation energy is the energy required to be input into the system in order to overcome the 'height' of the potential energy barrier, separating the two minima of potential energy for the initial state and the final state of the reaction (detailed in Figure 2.10 below). Chemisorption is affected by factors such as crystallographic orientation, the number of active sites at the surface, the number of defects and the surface preparative history.

Initial islands of oxide are the first to form, followed by growth laterally to form a continuous oxide monolayer. Subsequent growth of the oxide is an electro-chemical process and is dependent on the transport of anions (negatively charged oxygen ions), cations (positively charged metal ions) and electrons, through the oxide layer, to either the metal/oxide or oxide/gas interface. Figure 2.9 is a diagrammatic representation of this concept and shows that, for cation mobile growth the oxide forms at the oxide/gas interface whilst for anion mobile growth the oxide forms at the oxide/metal interface. The rate at which this ionic transport occurs will ultimately control the kinetics of oxide growth [8][85][90].

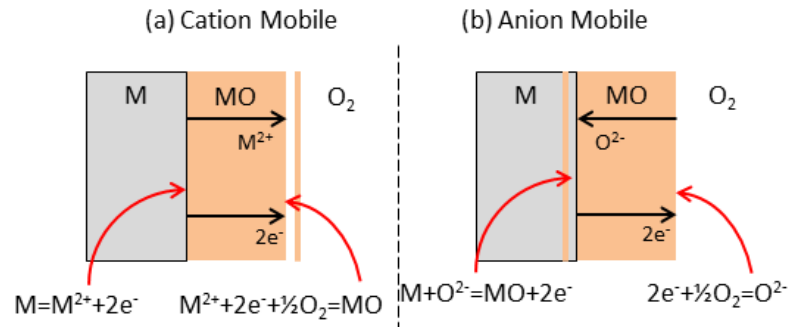


Figure 2.9 Diagrammatic representation of (a) cation mobile and (b) anion mobile oxide growth [85]

The transport of ions from the metal, through the oxide layer is a solid-state diffusion process which is dependent on the imperfections or defects within the crystal structure. Point defects exist when there is either missing or displaced atoms from the crystal lattice and the most prominent point defects are 'Vacancy', 'Interstitial' and 'Impurity' defects. Vacancies are the result of missing metal ions or oxygen anions from the lattice whilst Interstitials are a result of displaced ions from the lattice. Impurities arise when cations are substituted by a foreign cation. In addition to bulk-diffusion controlling point defects, crystal lattice defects (e.g. dislocations, grain boundaries, stacking faults and anti-phase boundaries) are an important consideration to the transport of ions during oxidation since they act as 'short-circuit' diffusion paths therefore increasing the rate of diffusion/oxidation.

Most oxides are non-stoichiometric, i.e. they contain an excess or deficit of metal or oxygen ions, and are therefore classified as semi-conductors [85]. An oxide that contains an excess of metal cations is known as an N-type semiconductor and can have either excess interstitial metal cations or oxygen anion vacancies, resulting in electrical conduction via excess excited electrons. The interstitial metal ions must be small enough to fit within the interstitial sites and can diffuse through the lattice by jumping from one site to another. Alternatively, oxygen anion vacancies can dominate (in

oxides with highly charged cations or of large size [8]), moving from one vacancy to another, resulting in a net metal excess. Charge is neutralised in both cases via an excess of electrons. Examples of oxides exhibiting N-type semiconductor behaviour are ZnO, α -Al₂O₃, Ta₂O₅ and SiO₂ [8][85][90].

An oxide that is deficient in metal cations is known as a P-type semiconductor and is a result of cation vacancies on the crystal lattice, together with electron holes, resulting in electrical conduction. Metal cations diffuse in this case by movement between vacancies, which has a corresponding energy penalty which is why diffusion is thermally activated. Examples of oxides exhibiting P-type semiconductor behaviour are NiO, Cr₂O₃ and CoO [8][85][90].

2.3.5 Oxidation Kinetics

The thermodynamics of oxidation give an indication as to whether a reaction can occur given factors such as temperature, P_{O_2} and thermodynamic activity support the minimisation of Gibbs free-energy as per Equation 2.2. However, as discussed previously, the formation of an oxide layer is rate-dependant on the ability for ions and electrons to diffuse to the reaction interface. In addition to this, the activation energy of the transformation from one state to another must be overcome. These considerations are not included in the thermodynamics of oxidation and are instead determined by the oxidation kinetics.

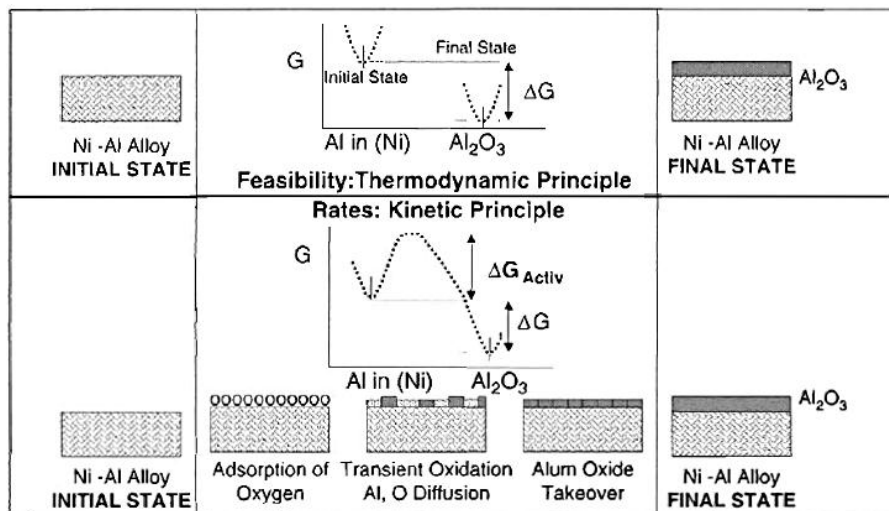


Figure 2.10 Concept of activation energy during oxidation of a Ni-Al alloy [87]

The example proposed in Figure 2.10 shows the difference between pure thermodynamic considerations and by taking reaction kinetics into account. In the top row, the initial Ni-Al alloy is exposed to an oxidation environment that favours Al_2O_3 growth which is evident by the negative change in Gibbs free-energy between the initial (un-oxidised) state and the final (oxidised) state. In the bottom row the kinetics of the same oxidation reaction are considered. The absolute change in Gibbs free-energy is still negative; however there is now a significant 'hill' of energy that must be overcome in order to progress from the initial state to the final state. The intermediate steps that create this 'hill' of energy include the dissociation of molecular O_2 into atomic O_2 and its adsorption to the metal surface, motion of the adsorbed O_2 to low-energy sites, the formation of transient oxides (such as NiO in this example), the diffusion of Al to the reaction interface and the conversion of the transient oxides to the final Al_2O_3 oxide state. Thermal energy from the surroundings provides the energy to overcome this 'hill' which is why high-temperature oxidation is usually a faster occurring process than low-temperature oxidation, despite the associated climb in

Gibbs free-energy to a less negative value (see Ellingham diagram Figure 2.7). An expression for the rate of oxidation can therefore be defined as [87]:

$$k = k_1 \exp(-\Delta G_{Activ}/RT) \quad \text{Equation 2.5}$$

Where k is the rate constant, k_1 is a constant and ΔG_{Activ} is the free-energy of activation. Using this equation it is possible to plot the rate constant against temperature for multiple oxides, allowing a comparison of their speed of formation (Figure 2.11).

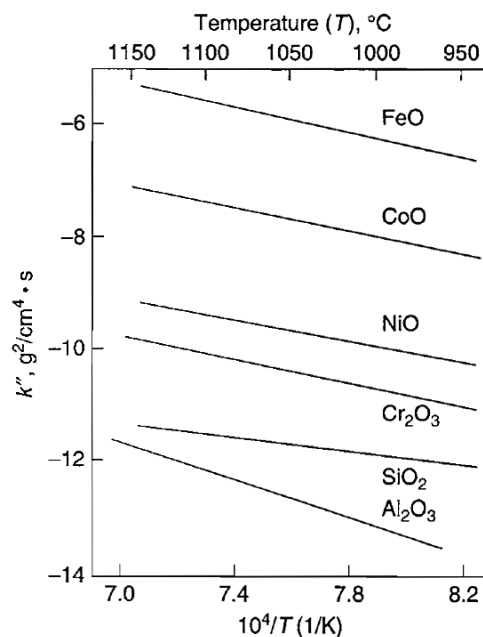


Figure 2.11 Rate constants of parabolic oxidation vs. temperature [5]

The initial stages of oxidation usually obey a linear rate law, however once the oxide layer becomes continuous, the subsequent growth rate can either remain linear or, more commonly, follow a (sub)parabolic or logarithmic rate law. The transition is due to a reducing ionic flux across the oxide layer as it becomes increasingly thick, acting as a barrier to ionic transport [85].

2.3.6 Oxidation of Alloys

It is pertinent to discuss the oxidation of alloys since the focus of this research is on Nickel-based superalloys which contain ~10 different alloying elements, many of which can affect the oxidation properties. The relative concentrations of the individual alloying elements within the bulk alloy will have a large impact on the subsequent oxide formation since there will be a difference in the reactivity (based on kinetics and thermodynamics) between each element. The simplest way to consider this is to look at a binary system with one element, A, the major alloying component and B, the minor alloying component. It follows that two scenarios can arise, (1) that A is less reactive than B and (2) that A and B are reactive but BO is more stable than AO.

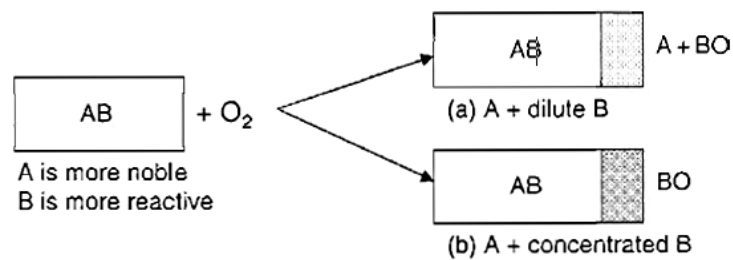


Figure 2.12 Binary alloy oxidation with component B more reactive than A [5][87]

For the first scenario (Figure 2.12), the P_{O_2} is too low for A to form an oxide, but B can form BO. If the concentration of B within the alloy is high enough then a continuous layer of BO is the result. Conversely, if the concentration of B is low, then internal oxidation will form particles of BO within the alloy, enriching A at the surface and not forming a continuous oxide layer. Clearly this would not result in a protective oxide layer.

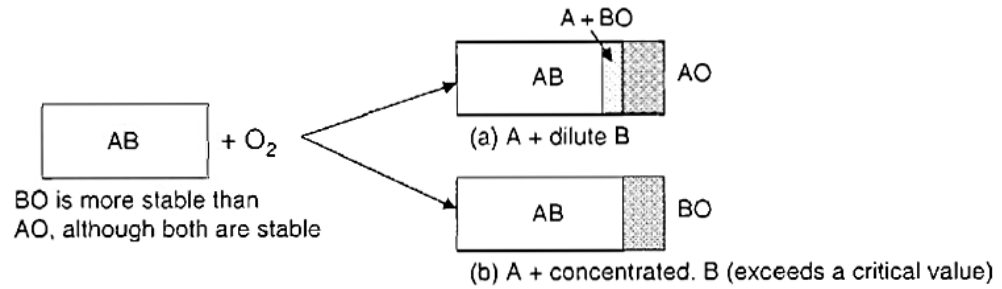


Figure 2.13 Binary alloy oxidation with A and B forming stable oxides. BO is more stable than AO [5][87]

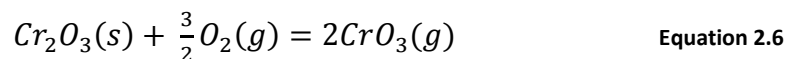
In the second scenario (Figure 2.13), the P_{O_2} is sufficient that both A and B are reactive to form oxides, but BO is more stable than AO. In this case, if the alloy has a low concentration of B then an outer layer of AO oxide forms below which the P_{O_2} is sufficiently reduced (by the oxide above) that only BO is stable and therefore discrete particles of BO form within the A enriched alloy. Alternatively, if the concentration of B is high enough, then the outer oxide layer will be BO, preventing any further formation of AO. There will however usually be some AO formed, due to initial growth kinetics, before the BO oxide becomes continuous and this is known as 'transient' oxidation [5].

This final scenario (Figure 2.13(b)) is the desired state for alloys whose oxidation resistance depends on the growth of a stable, protective oxide such as Nickel-based superalloys. In the case of superalloys, the component A is usually representative of Ni or Co whilst component B is representative of Al, Cr or Ti. In order for Ni-Al based alloys to form an outer oxide layer of protective Al₂O₃, with a sufficient reservoir of Al to replenish the depleted near-surface zone, it is necessary to have >17 wt.% Al. Between 6 – 17 wt.% Al, there will be insufficient Al to replenish the depleted zone and NiO will then form at the oxide/metal interface (solid-state reactions between NiO and Al₂O₃ will also produce NiAl₂O₄ spinels). If the Al concentration is <6 wt.% then an outer NiO layer will dominate, with internal oxidation of Al producing Al₂O₃ and

NiAl₂O₄ spinels (as in Figure 2.13(a)). Finally, addition of at least 5 wt.% Cr to the Ni-Al alloy reduces the concentration of Al needed to produce an outer Al₂O₃ layer from 17 wt.% to as low as 5 wt.% by acting as an oxygen ‘getter’ to form an initial Cr₂O₃ sub-oxide layer, which subsequently transforms to Al₂O₃ via Al substitution of Cr atoms [5][87].

2.3.7 Oxide Volatilisation

In order to assess the long-term oxide protectiveness it is necessary to understand the volatility of the oxides employed which requires knowledge of the oxides vapour pressure (the pressure of the vapour that is in equilibrium with the solid/liquid). It is well known that Cr₂O₃ forming alloys are susceptible to degradation at temperatures exceeding 1000°C due to vaporisation of the oxide and are therefore usually limited to operating temperatures below this value [5][85]. The vaporisation of Cr₂O₃ usually proceeds as follows (although reactions involving Cr(g), CrO and CrO₂ are also possible [91]):



This reaction results in thinning of the oxide layer which increases the rate of diffusion of metal ions to the surface; directly affecting the oxidation kinetics of the alloy. Initially the effect of vaporisation is minimal, since diffusion of metal ions to the surface is rapid enough to replenish the lost oxide. As the oxide layer thickens however, the transport rate of vaporisation becomes comparable and then equal to the rate of ion diffusion, creating a limiting factor for oxide thickness. This would imply that the oxide layer would become protective, however Tedmon [92] showed that as the scale thickness reaches steady-state, the rate of metal consumption to retain that

thickness increases [85]. This places a limit on the usability of Cr_2O_3 as a high-temperature protective oxide and is why Al_2O_3 is instead the oxide of choice at the moment for high-temperature Nickel-based superalloys.

Other elemental additions to the Nickel-based superalloys are of significance to oxide volatility, for example Re, Ru, Mo and W all form potentially volatile oxides [93][94][95][96], and even though they are not employed as protective oxides formers, their formation and volatility during transient oxidation conditions can have detrimental effects on the subsequent formation of protective oxides such as Al_2O_3 . Unlike the vaporisation of Cr_2O_3 , the oxides of Mo and W are known to experience complete vaporisation, resulting in significantly higher rates of oxidation. In order to graphically represent the vapour pressure data for metal oxides, Gulbransen and Jansson [97] developed the approach of using the graph of $\log P_{M_xO_y}$ vs. $\log P_{O_2}$, at constant temperature, to show the influence of P_{O_2} on the equilibrium pressures of the volatile oxide species. Likewise, the same data can be displayed for constant P_{O_2} at varying temperature. The vapour pressure diagram for Cr at 1250°K is shown in Figure 2.14 and it is seen that only one solid oxide forms, Cr_2O_3 , during high temperature oxidation (for a full list of thermochemical data the reader is directed to [85][96]). The vapour pressures are calculated for each species in equilibrium with either Cr(s) or Cr_2O_3 (s), depending on the calculated equilibrium P_{O_2} boundary (vertical line) between Cr(s) and Cr_2O_3 (s). From the graphical representation it is clear that, at low P_{O_2} , the vapour pressure of Cr(g) is significant and independent of P_{O_2} which corresponds to potential conditions at the metal/oxide interface. Conversely at high P_{O_2} , the vapour

pressure of $\text{CrO}_3(\text{g})$ is high resulting in the loss of Cr_2O_3 oxide at the oxide/gas interface via vaporisation.

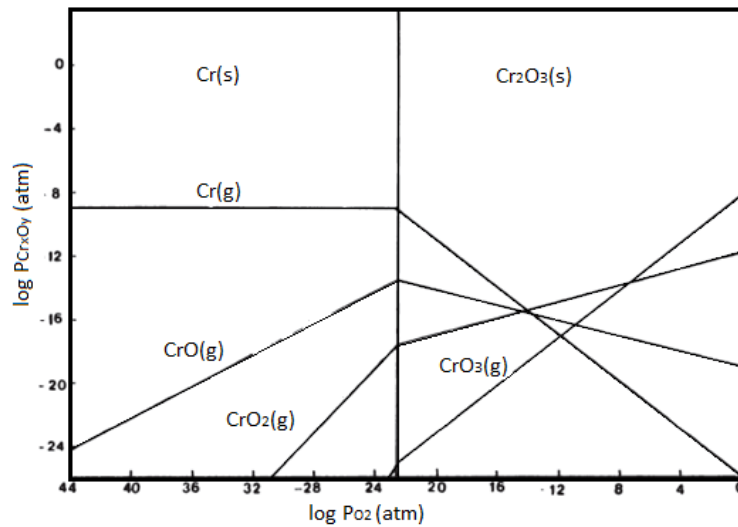


Figure 2.14 Cr-O system of volatile species at 1250°K [96]

In summary, surface defect formation has become one of the most important factors during casting and heat-treatment of Nickel-based superalloys and, whilst progress has been made in recent years, a systematic study of the mechanisms of defect formation is needed in order to provide further understanding and propose methods of prevention. Working in collaboration with the Precision Casting Facility (PCF) at Rolls-Royce plc., this research project has been carried out to provide answers to the root-causes of the casting defect Surface Scale and the heat-treatment defect Surface Melting. This work is presented in the following Chapters.

Chapter 3. Mechanism of Surface Scale Formation

3.1 Introduction

Superalloy chemistry has evolved over the last four decades, primarily characterised by the increasing addition of refractory metals such as Ta, W and Re in order to improve solid solution hardening and to enhance microstructural stability at elevated temperatures [4][52][98][99]. Simultaneously, innovations in materials processing routes have resulted in the casting of single crystal (SX) turbine blades, where the primary orientation of the single crystal is aligned along the turbine blade or stress axis [19][100][101]. However, these advances in alloy chemistry and solidification have made the control of the crystal orientation and the prevention of defect formation during casting in modern turbine components increasingly challenging. In this Chapter a detailed investigation into one such casting defect, known as ‘surface scale’, is discussed. Figure 3.1 shows two representative scaled SX turbine blades cast at the Precision Casting Facility (PCF) at Rolls-Royce plc. Derby.

The aim is to report on the structure and chemistry of the Surface Scale formed on the commonly used 2nd generation SX Nickel-based superalloy, CMSX-4 as well the 3rd generation alloy, CMSX-10N; with the aim of producing a complete understanding of the mechanism driving Surface Scale formation. Finally, suggestions for reducing, or eliminating, scale formation will be proposed.

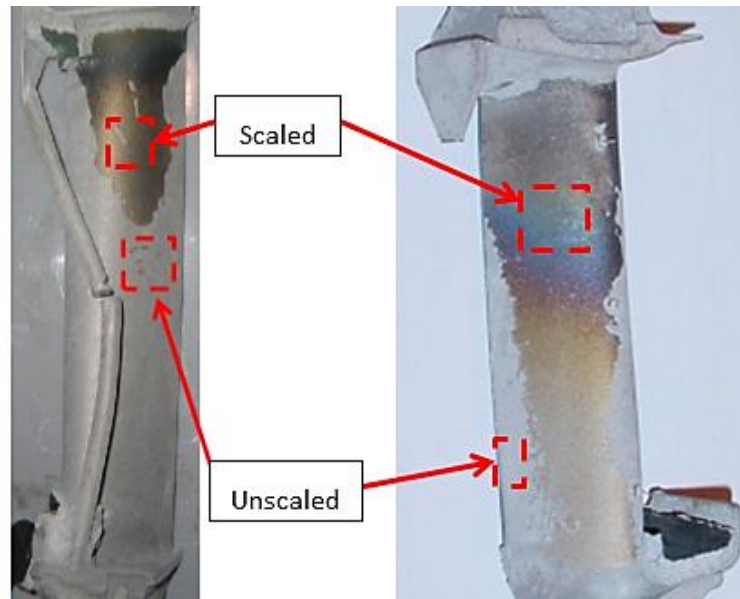


Figure 3.1 Scaled SX turbine blades a) LP SRR99 alloy turbine blade [7] and b) IP RR3000 alloy turbine blade [67]

3.2 Experimental Methods

Two commonly used Ni-based superalloys were used in this study, the 2nd generation alloy CMSX-4 and the 3rd generation CMSX-10N. The main difference between them is the increased addition of Re at the expense of Ti, Co and Cr in CMSX-10N. Nominal compositions (wt.%) are given in Table 3.1.

Alloy	Al	Co	Cr	Ti	Mo	Ta	W	Re	Ni
CMSX-4	5.8	9.5	6.5	1.1	0.6	6.5	6.5	3	Bal
CMSX-10N	5.9	3.1	1.6	0.1	0.45	8.5	5.5	6.8	Bal

Table 3.1 Nominal composition (wt.%) of alloying elements in the Ni-base superalloys CMSX-4 and CMSX-10N

3.2.1 Investment Casting

Turbine blades were cast using the lost-wax (investment casting) process at the Precision Casting Facility, Rolls-Royce plc, Derby, UK. The furnace heater temperature used for casting the turbine blades was nominally 1500°C and a withdrawal rate of around $5 \times 10^{-5} \text{ m.s}^{-1}$ was used. As per standard operation, a reasonably flat thermal gradient of $\sim 5 \text{ K.mm}^{-1}$ was ensured at the solid/liquid interface. The ceramic mould

slurry consists of a binder and a refractory material with additions of wetting and antifoaming agents to improve the slurry properties. Details of the slurry constituents are indicated in Table 3.2.

Mould Slurry Binder	Mould Slurry Refractory	Mould Stucco
Colloidal Silica	200 mesh (75µm) Zirconium Silicate	Alumina

Table 3.2 Mould slurry constituent materials

3.2.2 Optical Microscopy (OM) and Scanning Electron Microscopy (SEM)

A FEI Sirion Field-Emission Gun SEM (FEGSEM) was used throughout this research project, coupled with a PGT Spirit Energy-Dispersive X-ray Spectroscopy (EDX) system, at the University of Leicester. The FEGSEM is a type of electron microscope that produces a high-magnification, high-quality image by scanning the surface of the sample with a focused beam of electrons, exciting the atoms within the sample and producing various different emitted electrons and X-rays that can be detected to form an image and/or analyse the surface chemistry. The FEGSEM differs from the standard SEM in the design of the electron gun that produces the beam of electrons. In an SEM the electron gun is a thermionic emitter which uses electrical current to heat an element, typically Tungsten or Lanthanum Hexaboride (LaB_6), causing the release of electrons. Compared to a FEGSEM, this produces a wider beam of relatively low brightness. In a FEGSEM, electrons are produced using a cold-cathode Field-emission source which is not heated but instead held at a large electrical potential relative to an anode. The cathode is usually made of a single-crystal of tungsten, sharpened to a fine point with a tip radius of $\sim 100\text{nm}$ in order to concentrate the electric field to the magnitude needed to release electrons. The principle benefit of the cold-cathode

Field-emission source is that it gives a very fine beam, so can achieve higher resolution imaging than the SEM [102].

Back-scattered electron imaging (BSI) and Secondary electron imaging (SEI) were performed at a working distance (WD) of 5mm, spot size 5 and an accelerating voltage of 15-20 kV. EDX spectra were collected with an accelerating voltage varied between 10-15kV, depending on the flux of emitted X-rays and the dead-time of the detector.

Turbine blade surfaces were initially analysed with an Olympus BX-51 optical microscope at various magnifications to select appropriate areas for further analysis. Transverse sections were subsequently cut in the regions of interest using either a diamond tipped rotary bench saw or by wire erosion EDM. Samples were mounted in conducting Bakelite resin and progressively polished with grit/SiC papers, followed by a final 1/4 μm diamond polish for metallographic examination. Where necessary, samples were chemically etched with a Nimonic etchant of 50ml HNO_3 , 200ml HCl, 12.5g CuCl_2 and 12.5g FeCl_2 made up to 500ml with distilled water.

3.2.3 X-Ray Photoelectron Spectroscopy (XPS)

XPS is an analytical technique that allows the user to identify a materials composition, chemical and electrical state and empirical formula (empirical formula is the simplest whole number ratio of atoms). It does this using photo-ionisation and analysis of the kinetic energy distribution of emitted photoelectrons from the top 1-10nm of the material surface [103]. XPS was used as a complimentary technique to Auger-electron spectroscopy (AES) since it is able to analyse a larger surface-area than AES (mm^2

versus $\sim 100\mu\text{m}^2$) negating the effects of local compositional inhomogeneities. Due to the near-surface nature of the analysis technique, it was also utilized to study the formation of oxide reaction layers on the surface of mould pieces retrieved from the unscaled portion of the as-cast turbine blade (see Section 4.5.3).

In an XPS machine, X-rays are accelerated towards the sample surface in an ultra-high vacuum, with an energy $h\nu$, and when they hit the sample surface photoelectrons are ejected from the inner shell orbital of the atoms. The kinetic energy, E_k , of each ejected photoelectron is related to the energy of the incident X-ray and the binding energy, E_b , of the electron by:

$$E_k = h\nu - E_b - \phi_{SP} \quad \text{Equation 3.1}$$

Where, ϕ_{SP} is a work function of the spectrometer.

Every element has a characteristic binding energy that allows it to be identified from the kinetic energy of the ejected photoelectron. XPS provides a quantitative analysis of the surface composition by counting the number of photoelectrons at different energies and plotting an energy peak spectrum [103]. In addition, Auger electrons are also produced by sample interactions with the incident X-ray and can aid in the identification of elements and compounds. They are produced in the same way as is described in Section 3.2.4 however, instead of an incident electron being responsible for the initial electron ejection, it is an X-ray.

XPS data was acquired using the Scienta ESCA300 instrument at the National Centre for Electron Spectroscopy and Surface Analysis (NCESS), Daresbury Laboratory UK. This uses mono-chromated Al $K\alpha$ (1486.7 eV) radiation, a slit width of 0.8mm and a take-off

angle of 90°. Samples were subjected to Ar ion etching by filling the sample preparation chamber of the Scienta instrument with Ar gas to a pressure of approximately 2×10^{-6} Torr. The sample was then exposed to the Ar ion beam for a time period of typically several minutes using an accelerator voltage of 5 kV resulting in a beam current of ca. 200 mA.

3.2.4 Auger Electron Spectroscopy (AES)

AES is a popular technique for obtaining chemical analyses of solid surfaces, its main advantages are a high sensitivity in the near-surface range ($\sim 2\text{-}5\text{nm}$ [104]), fast data acquisition rate, fine spatial resolution (due to a small electron beam size) and an ability to detect all elements above helium (although some elements, like Ta and W, are hard to distinguish due to similar energy signatures) [105]. The Jeol Jamp-7100 AES at the University of Loughborough was used to analyse the surface scale oxide composition by performing depth-sensitive scans in both scaled and unscaled regions. This technique is advantageous as the loosely adhered scale oxides require no prior polishing or preparation, ensuring they are not damaged or spall away. Since the scale oxides are typically $\sim 0.5\mu\text{m}$ in thickness, the depth sensitivity of AES also allows the accurate distinction of the individual oxide layers.

AES uses an incident electron beam, of sufficient energy, to excite an atom, displacing a core electron and leaving a vacancy in the 1s (k) energy level. This vacancy is filled by an electron from the 2s level releasing 'spare' energy ($E_{1s} - E_{2s}$) to an electron in the 2p level. This process ejects the 2p electron as an *Auger Electron* (Figure 3.2(b)) with energy, E , defined as:

$$E = E_{1s} - E_{2s} - E_{2p} \quad \text{Equation 3.2}$$

The energy of the Auger electron is therefore characteristic of the atom that emitted it, and not of the incident electron beam, allowing the identification of the parent atom [103]. Only Auger electrons from the very near-surface are emitted from the sample without energy loss, contributing to the Auger peaks for each element detected. However, some Auger electrons that have escaped the surface but have lost energy will also contribute to the signal in the form of background noise, particularly at the lower kinetic energies.

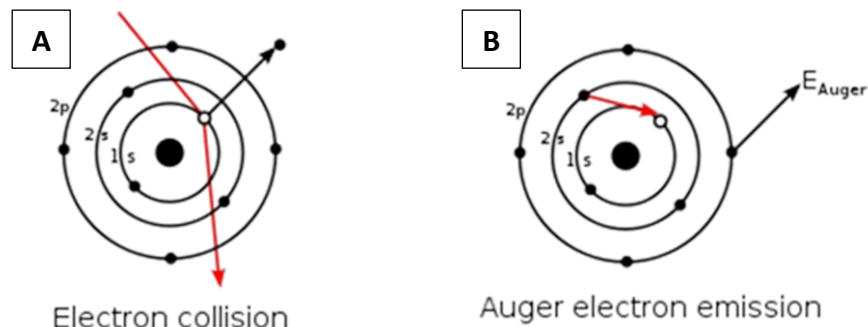


Figure 3.2 Auger Electron Emission (a) Incident electron beam displays a core electron (b) electron from the 2s level drops to fill the vacancy, releasing 'spare' energy to the Auger electron in the 2p level, which is ejected [106]

Depth-sensitive compositional scans are made possible by the coupling of an ion sputtering source, which bombards the sample surface with Ar (or other inert gases) ions to destructively remove material from the sample surface. The Ar ions are accelerated in an ion gun to $\sim 3\text{keV}$, as they strike the sample energy is transferred and atoms from the sample are sputtered away. After each sputtering, the remaining surface is analysed by AES, before additional ion sputtering is conducted and so on.

AES depth profiles were obtained from regions on the turbine blade samples selected using SEI. The AES operates at $\sim 2 \times 10^{-9}$ Torr with a primary electron beam energy of 10 keV focussed into a spot approximately 10 μm in diameter with a current of $\sim 0.5 \times 10^{-7}$

nA. Depth profiles were performed by sputtering with Ar⁺ ions with an energy of 3 keV and current density of 50 $\mu\text{A cm}^{-2}$. This resulted in a theoretical etch rate of $\sim 10\text{nm min}^{-1}$. Quantitative analysis was performed using experimentally derived relative sensitivity factors based on NiO and Al₂O₃ reference samples, with an estimated error of $\pm 15\%$ of the calculated value.

3.2.5 Preparation of Transmission Electron Microscopy (TEM) Foils Using Focused Ion-Beam (FIB) Extraction

TEM is another analytical technique based on the utilization of an electron beam to probe the specimen's atomic structure and composition. In a TEM the beam of electrons is accelerated and focused by a series of high-voltage apertures and electrostatic lenses, to a point on a very thin sample (a few 100nm's or thinner). The electrons are transmitted through the sample and in doing so reveal crystallographic and compositional information. By focussing the electron beam to a fine point and rastering it across the sample surface, Scanning Transmission Electron Microscopy (STEM) can be conducted. This is similar to the principles of SEM, and can be used to collect the secondary and back-scattered electrons as well as EDX; however the transmission of electrons through the sample makes available the collection of complementary images from bright-field (BF) and dark-field (DF) detectors. The BF detector is positioned directly in the beam path, under the sample and image-forming lenses, which results in images where holes appear bright and gives phase related contrast. The DF detector on the other hand is positioned annularly, out of the beam path, resulting in images where holes appear dark and contrast is related to the atomic number of the interacted atom [107][108].

The Tecnai F20 FEG TEM at the University of Birmingham was used in STEM mode with the High-Angle Annular Dark Field (HAADF) detector at 200kV to analyse the surface scale oxide's cross-section in finer detail. This detector gives the best Z-based contrast, making the distinction between different phases and oxides much clearer. The imaging resolution of this TEM system is 0.12nm (line) and 0.24nm (point). This TEM system is also coupled with an Oxford Instruments Xmax 80 EDS detector, allowing the creation of elemental maps.

TEM samples were prepared via Focused Ion-Beam (FIB) extraction using the FEI Nova 600 Nanolab FIB at the University of Loughborough as follows:

- (i) The area of interest was selected using the secondary-electron detector. A Pt strip is deposited on this area to protect the surface oxides from damage/spallation during the extraction process (red oblong in Figure 3.3).
- (ii) Vertical trenches are milled either side of the Pt strip, using the Ga⁺ beam, into the sample. The sample is then rotated by 45° to allow the ion beam to mill beneath the sample resulting in a 'U' shaped under-cut (Figure 3.4(a)).
- (iii) A micro-probe is moved into position and affixed to the top of the Pt strip, using extra Pt deposits. The final cut is made and the sample is lifted out and positioned on the copper TEM sample grid (Figure 3.4(b-c)).
- (iv) The sample is 'glued' to the copper TEM grid using more Pt. Finally, the sample is thinned to ~200nm with the ion beam for TEM transparency (Figure 3.4(d)).

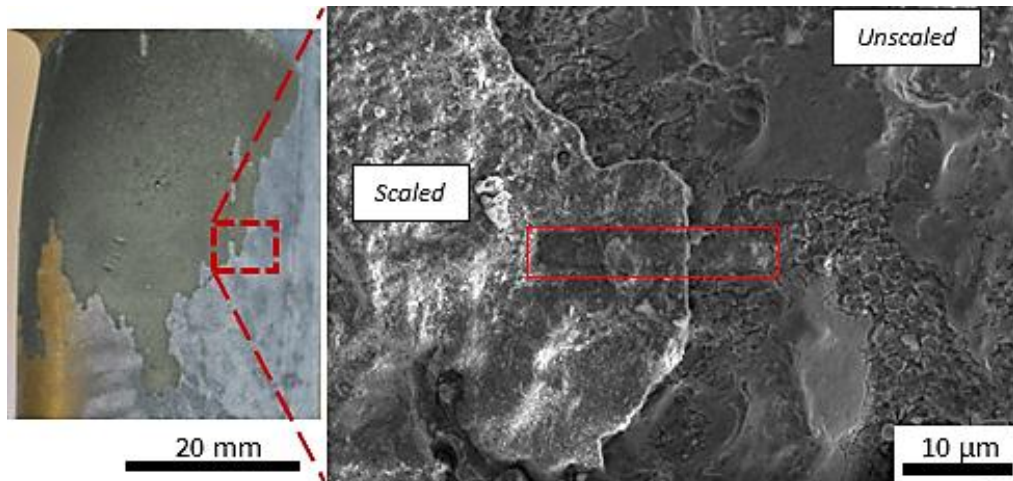


Figure 3.3 FIB SEI of the scaled region selected for TEM foil extraction. The Pt deposited strip is outlined in red

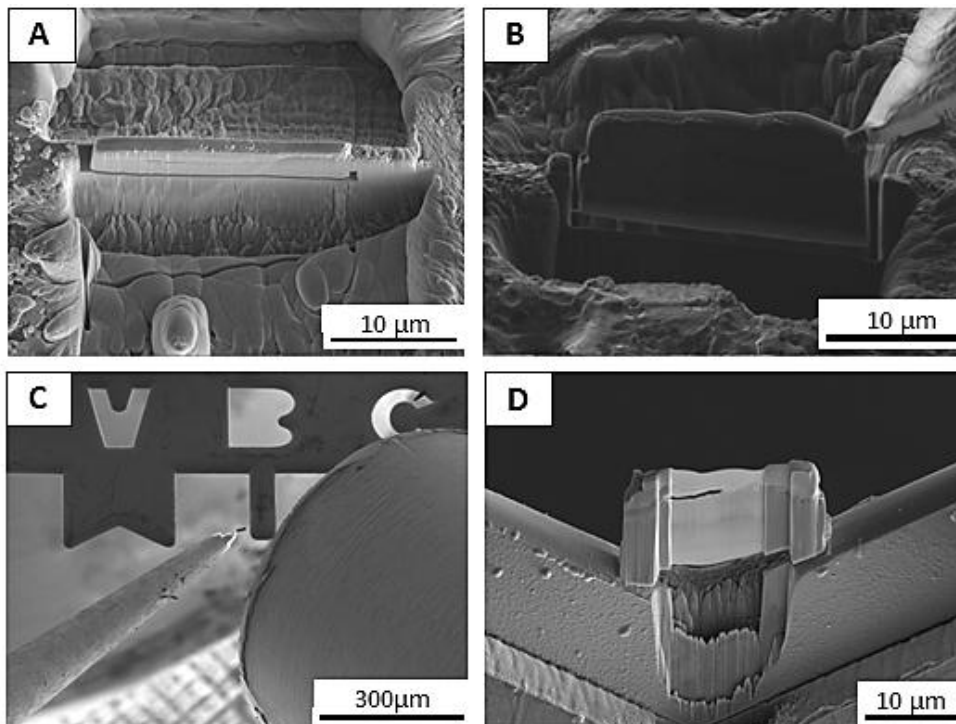


Figure 3.4 TEM sample foil extraction (a) Ion beam mills trenches either side of Pt strip (b) Sample is rotated and ion beam mills beneath sample. A micro-probe is moved into position and affixed to the sample (c) Sample is released from substrate and moved to TEM grid (d) Ion beam is finally used to thin the sample TEM transparency.

3.3 Results

3.3.1 Appearance of the Scaled and Unscaled As-Cast Surfaces

The occurrence of surface scale on the aerofoil of two typical turbine blades is shown in Figure 3.5. The turbine blade in Figure 3.5(a) was directionally solidified using the 2nd

generation Ni-base superalloy, CMSX-4, whilst that in Figure 3.5(b) was cast using the 3rd generation alloy, CMSX-10N.

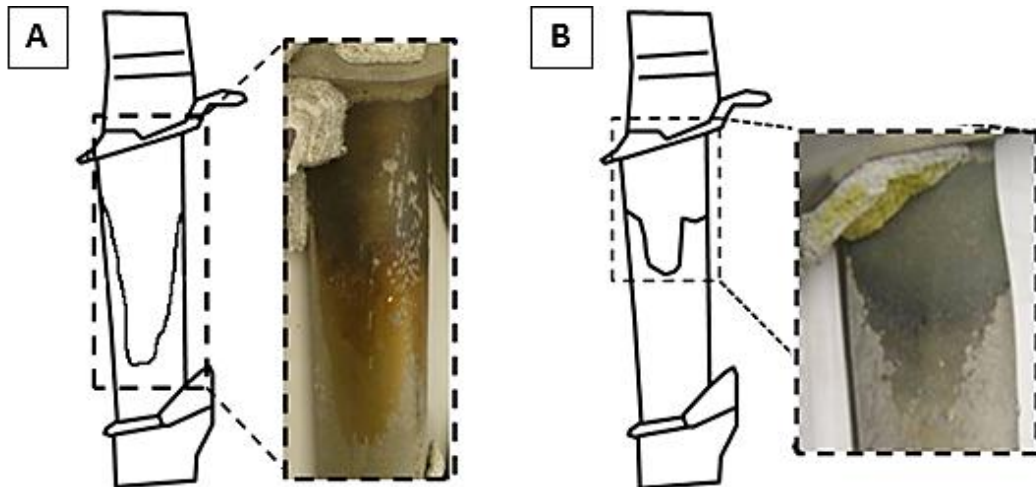


Figure 3.5 (a) Scaled surface of a turbine blade solidified from CMSX-4 and (b) CMSX-10N

From Figure 3.5 the following conclusions can be made:

- CMSX-4 – The scale is coloured in a hue from blue to gold and occurs over a large portion of the aerofoil length on the upper, convex portion of the aerofoil. It has a “tongue-shaped” appearance, originating from a point and then fanning out.
- CMSX-10N - The scale is, in this case, pale green in appearance and its spatial location and shape is similar to that of CMSX-4.

To characterise the morphology of the surfaces associated with scaled and the unscaled regions secondary electron imaging (SEI) was performed on the corresponding surfaces. The SEI images are presented in Figure 3.6, these sections were taken from a blade cast using the alloy CMSX-10N and similar observations were made for CMSX-4. From both figures it can be seen that there is a marked presence of adhered particles sitting on the surface of the unscaled aerofoil which appear as bright patches in the SEI (Figure 3.6 Insert A), indicating that these are insulative, or loosely

adhered, material prone to electron charging in the SEM due to poor conductance with the alloy substrate. These bright particles vary in size and shape and are not found in the scaled region and, further to this, the transition from the scaled to the unscaled regions is abrupt in nature.

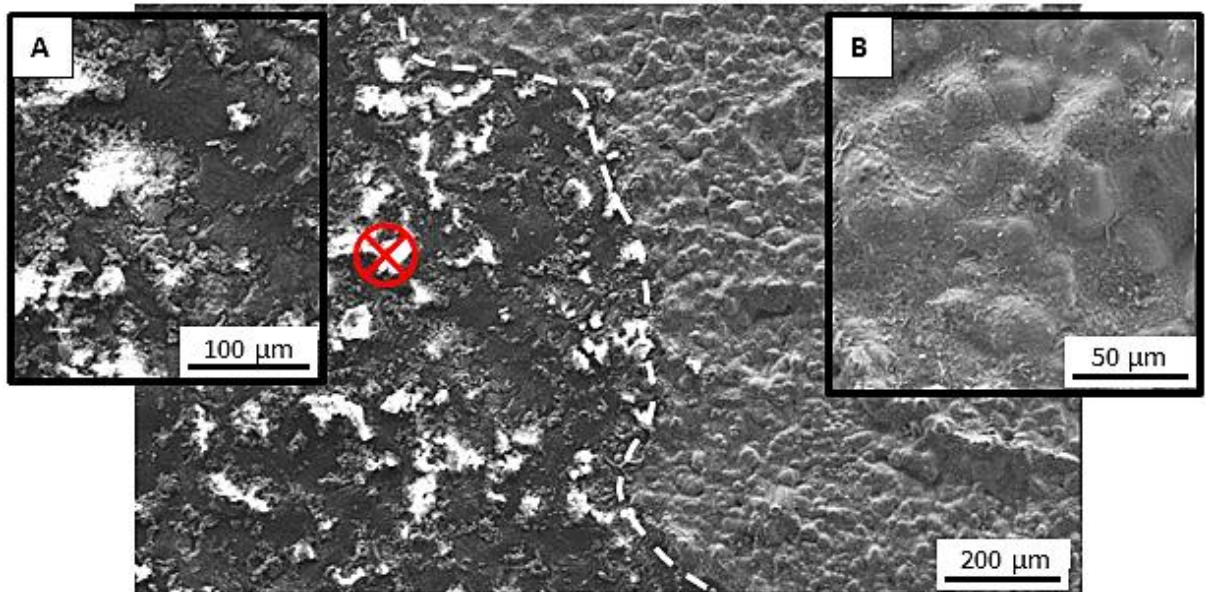


Figure 3.6 SEI of the scaled/unscaled interface region. Insert A shows the magnified unscaled region and Insert B shows the magnified scaled region. Red cross indicates spectra location for Figure 3.7(c)

3.3.2 Chemical Analysis of the Scaled and Unscaled Surfaces

3.3.2.1 EDX surface analysis

Figure 3.7 shows the EDX spectra obtained for the unscaled and scaled regions shown in Figure 3.6. Of note are the large Zr and Si peaks in the unscaled region which are missing in the scaled, as well as the large Ni peak that is present only in the scaled region. In both spectra there is an appreciable oxygen peak which suggests the surface is covered in an oxide layer. This data initially supports the hypothesis that the unscaled region is covered with remaining mould material (since Zr and Si are not present within the alloy but are found as the main constituents of the mould ceramic) and that the scaled region is most likely covered by a nickel oxide.

The elemental composition of a typical particle retained on the unscaled surface was determined using EDX by looking at the cross-section of an unscaled blade. The back-scattered image is shown in Figure 3.8(a), with the corresponding EDX maps also shown. From this it is clear that the particles are refractory (ceramic) in nature and enriched in Zr, Si and O, the main constituents of the ceramic mould (and not found in the metal alloy). There is also a thin Al oxide layer sandwiched between the mould particles and the metal substrate that is continuous along the surface periphery and of a thickness of $\sim 2\mu\text{m}$.

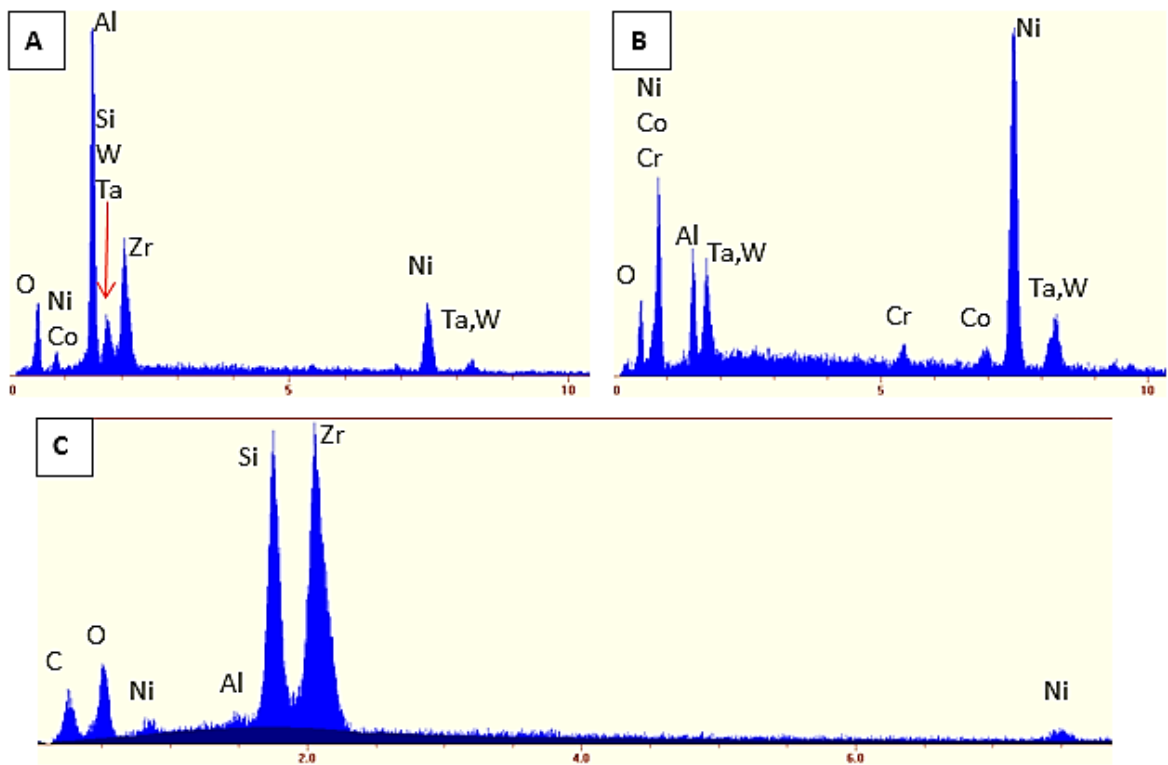


Figure 3.7 EDX spectra for (a) the unscaled region (b) the scaled region and (c) the unscaled particles in Figure 3.6

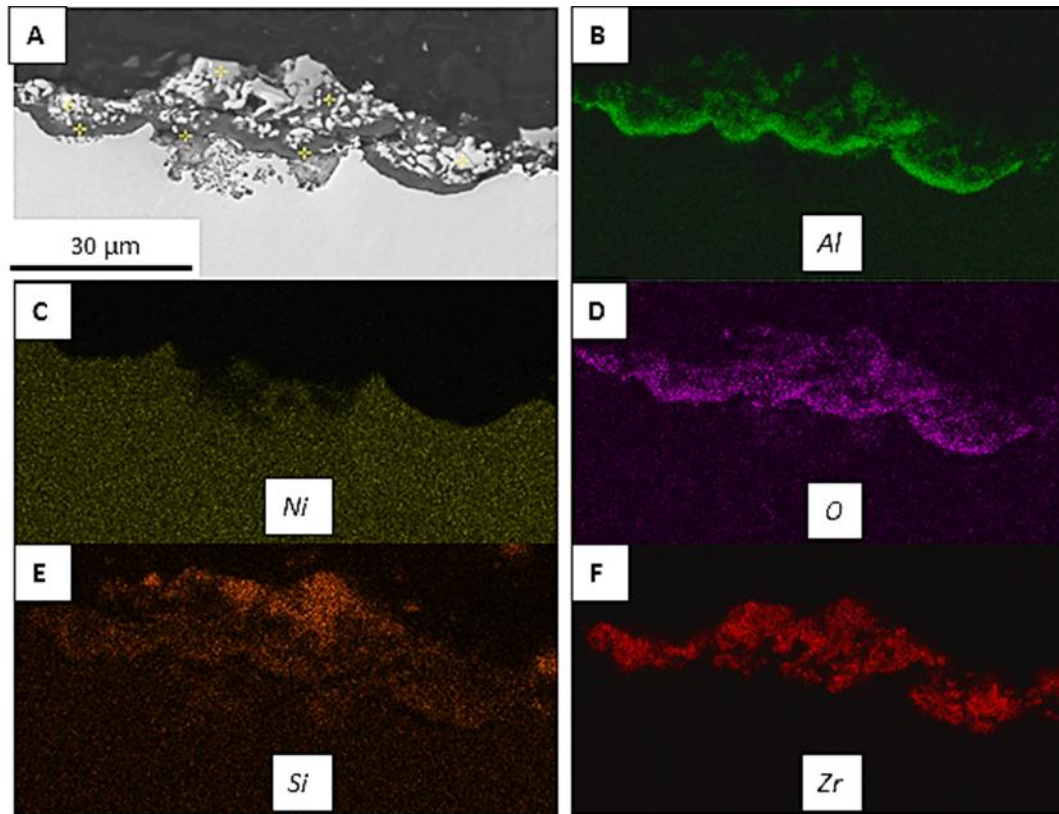


Figure 3.8 (a) SEM of unscaled surface and (b-f) corresponding EDX maps of Al, Ni, O, Si and Zr

The adhered mould patches and sandwiched alumina layer were also observed by Brewster for the Ni-based superalloy SRR99 [7] which shows that this is not an alloy specific occurrence but rather, a characteristic of turbine blade casting.

The EDX analysis performed here was isolated to small areas of the scaled and unscaled regions and is unable to give accurate quantitative compositions due to the peak overlap of key alloying elements, especially W and Ta. In order to sample a larger surface area, and to give accurate compositional measurements, X-ray photoelectron spectroscopy (XPS) was subsequently used to look at the scaled and unscaled surfaces.

3.3.2.2 XPS surface analysis

XPS surface analysis data was acquired for the Ni (2p), Al (2p), Zr (3d), Re (4f), W (4f) and Ta (4f) spectral regions for samples cut from the as-cast scaled and unscaled areas.

The use of XPS gives compositional data from a large surface area (mm^2) but small depth (nm^2) resulting in data that is not point-specific. One would expect to see strong peaks for Ni (2p), since this element comprises the bulk of the alloy; however Figure 3.9 shows that in the unscaled region (black) this was not the case. Similarly the rare earth components W, Ta and Re also showed very weak and poorly defined spectral features in the unscaled region despite their significant presence within the bulk alloy. In addition to this, strong signals were observed in both the Zr (3d) and Al (2p) spectrums for the unscaled area.

Following these measurements the unscaled region was subjected to Ar^+ ion plasma etching (Blue lines on Figure 3.9) for a period of 90 minutes and then returned to the analysis chamber for repeat measurements. These measurements showed both a marked increase in the intensity of Ni and rare earth elements with a decrease in the intensity of Zr. Quantification of these spectra showed Ni:Al:Zr ratios of 1:84:149 in the unscaled region before Ar^+ ion etching compared to the equivalent ratios of 1:24:83 afterwards.

In contrast, XPS data from the surface of the scaled sample showed intense and well defined spectra for nickel and the rare earth elements whilst there was no evidence of any zirconium (Figure 3.9(c)). Interestingly there is an additional signal (at a binding energy of ~ 27 eV) in the rare earth spectra for the scaled sample that is absent in the unscaled etched spectrum, (Figure 3.9(d)). This is most likely an oxide species of Ta, for example Ta_2O_5 which has a binding energy at 26 eV [109][110]. Due to the low penetrating depth of XPS the next step was to use Auger electron spectroscopy (AES)

to perform depth-sensitive compositional analysis, coupled with calibration standards to allow accurate depth quantification.

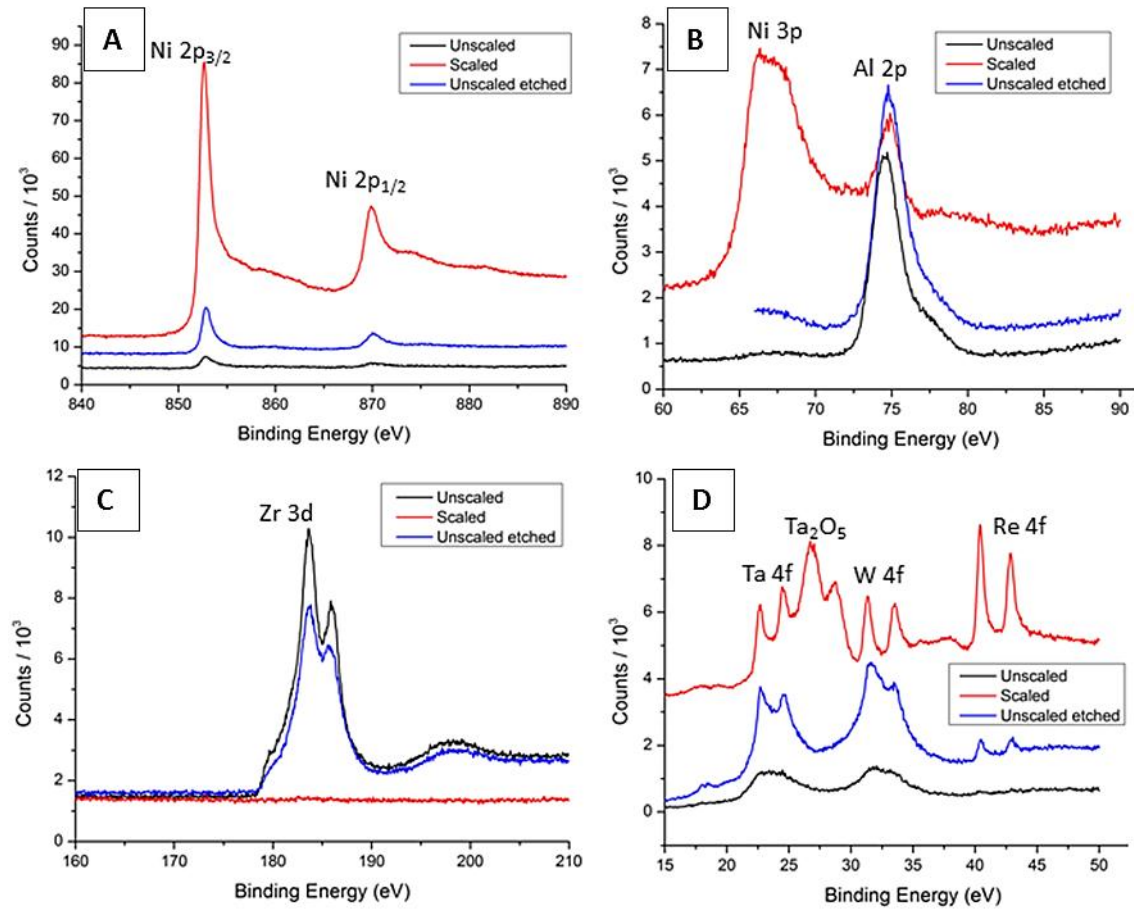


Figure 3.9 High-resolution XPS compositional analysis of scaled and unscaled surfaces as-cast surfaces. (a) Ni(2p) spectrum (b) Al(2p) and Ni(3p) spectra, (c) Zr(3d) spectra (d) Re, W, Ta(4f) spectra.

3.3.2.3 XPS surface analysis of the mould face-coat

It was also decided to use the XPS facility to analyse the mould face-coat corresponding to the scaled region. This was in order to locate any mould-metal reaction products that should have formed during the initial stages of casting, between the liquid alloy and the mould. It is expected therefore that this analysis should find the resultant Al₂O₃ layer sitting on the surface of the mould face-coat. In order to discount localised anomalies XPS spectra were taken in two areas of the mould adjacent to the scaled region; these are shown in Figure 3.10 as area A (near the centre of the mould) and area B (near the edge)

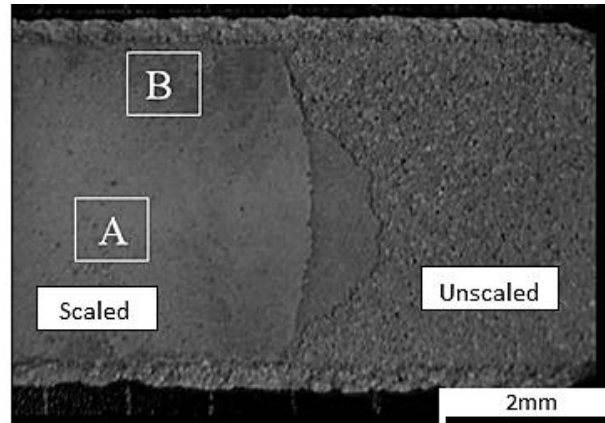


Figure 3.10 Optical photograph of detached mould prime-coat surface showing scaled-facing surface (smooth) on the left and the unscaled-facing side (rough) on the right. XPS spectra locations A and B are also shown

Figure 3.11 shows the XPS data for the Al (2p) and O (1s) spectral regions respectively for area A. The integrated analytical data from both areas A and B are summarised in Table 3.3. The XPS spectra shows the distinct presence of Al and O on the mould prime-coat, although the presence of oxygen is to be expected from the SiO₂ binder and Zircon filler in the face-coat, the corresponding presence of a strong signal in the Al (2p) region is strong evidence for the existence of Al₂O₃ on the mould face-coat surface.

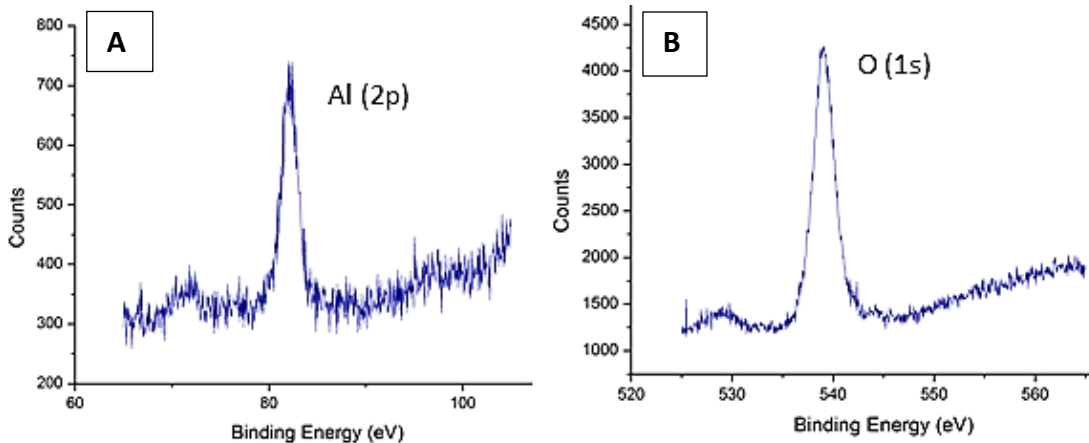


Figure 3.11 XPS spectrum collected from the mould wall adjacent to the scaled region (a) Al (2p) and (b) O (1s)

Looking at Table 3.3, both areas A and B show evidence of an Al₂O₃ layer, however in area A there clearly exists some sampling of the exposed face-coat (colloidal SiO₂ and some ZrSiO₄) in addition to the Al₂O₃ surface layer. In area B there is a distinct lack of Si

and Zr, despite these being the main constituents of the mould, which, coupled with the strong Al and O peaks, shows that the XPS beam was sampling only the Al₂O₃ surface layer adhered to the mould face-coat and not the mould constituents below. It can be discounted that the Al signal in these XPS results is a result of the Al₂O₃ stucco particles in the primary + 1 and Back-up coats of the mould, since they are located at least 100 µm from the mould surface and are therefore beyond the penetration depth of the XPS beam.

Analysis area	Al	Si	Zr	C	N	Ca	O	Na	Hf
A	6.5	10.1	1.5	43.5	1.7	2.6	33.1	1.0	0.0
B	18.5	0.0	0.8	39.7	2.0	0.0	37.5	1.2	0.3

Table 3.3 Composition (at.%) of the mould face-coat (adjacent to the scaled region of the blade surface) for the two analysis areas, A and B, determined by integration of the XPS spectral data

3.3.3 Surface Analysis using Auger Electron Spectroscopy

The XPS data collected in Section 4.5.3 for the scaled and unscaled regions is sampled over a large surface area of ~10mm². Complementary localised AES depth profiles were also carried out at representative locations within the scaled and unscaled regions in order to acquire depth-sensitive composition profiles. These are presented in Figure 3.12. In the case of the unscaled region the depth scans were chosen between the adhered ceramic particles so that they were not included in the analysis.

In the scaled region the strongest metallic peaks proceeding inwards from the surface were Ni, Co and Al in that order. There is a strong O peak of ~50 at.% indicating that the scale is an oxide and the typical thickness beyond which the O reduces and Ni from the substrate begins to dominate is ~800 nm. In the unscaled region, the most prominent peaks were Al (30 at.%) and O (60 at.%), which indicate the presence of

Al_2O_3 (52wt.% O, 48wt.% Al), which was also observed in Figure 3.8. The thickness of the Al_2O_3 layer is thicker than the oxide in the scaled region but greater than the AES sample depth. The carbon peak in both samples is likely due to contamination from the casting furnace carbon heating elements, as well as oil from the SEM vacuum pump.

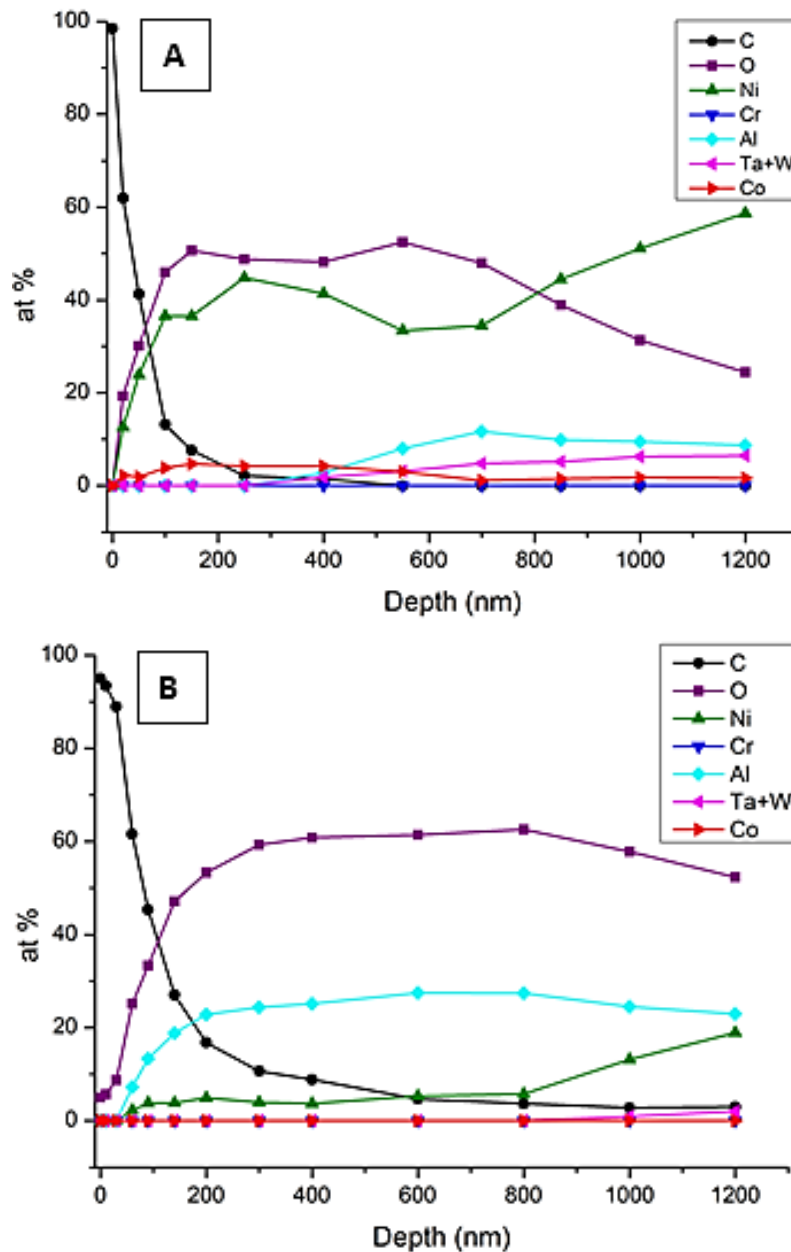


Figure 3.12 AES depth profiles of the as-cast CMSX-10N turbine blade in (a) scaled and (b) unscaled regions

The AES data from the scaled region (Figure 3.12(a)) suggests that the scale oxide may in fact be multi-layered, and not a single thin oxide film as initially thought. This is evident from the corresponding dip in the Ni concentration and rise in the Al at

600nm. To investigate this further the next step was to take a TEM sample foil from the scaled region and conduct EDX mapping of the oxide layers.

3.3.4 TEM/EDX Analysis of the Surface Scale Oxides

FIB/TEM gives one the ability to select a specific area of interest and then remove a TEM sample, whilst protecting any surface oxides which are normally characterised by low adherence to the substrate. Once extracted, the samples can then be visually investigated in the TEM and, coupled with EDX, compositional mapping can be performed. Figure 3.13 shows the location of the TEM foil extraction and the TEM image from the scaled region.

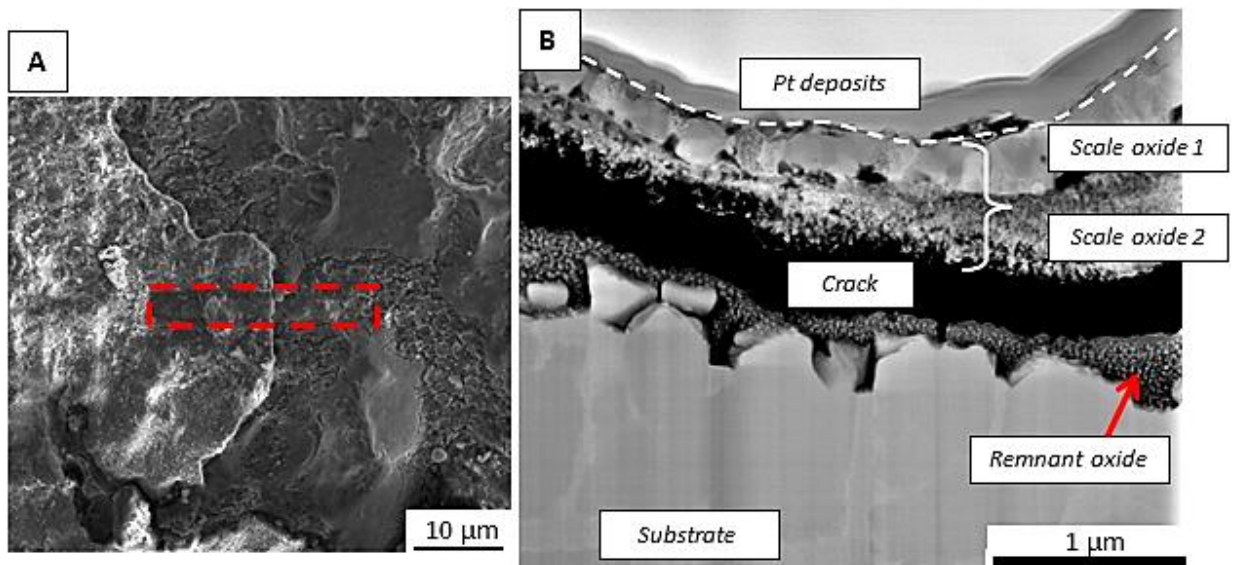


Figure 3.13(a) FIB micrograph of TEM extraction area and (b) TEM image of scale oxide cross-section

The complete scale oxide has a total thickness of between 0.5 - 1μm and consists of an outer Ni, Co rich oxide (Figure 3.14(b-c)). The outer oxide layer has a coarse-grained, blocky microstructure that is typical of a (Ni,Co)O solid-solution [85][111] and is ~0.5μm thick. Below the NiO layer is a finer grained and porous mixed oxide of predominantly Al and Cr with traces of Ta/W and Ti (Figure 3.15(b-d)). The TEM image shows the presence of crack between the oxide and the substrate below. This is likely

formed due to the low adherence of the oxide to the substrate, combined with the relief of internal stresses, within the oxide, during FIB extraction.

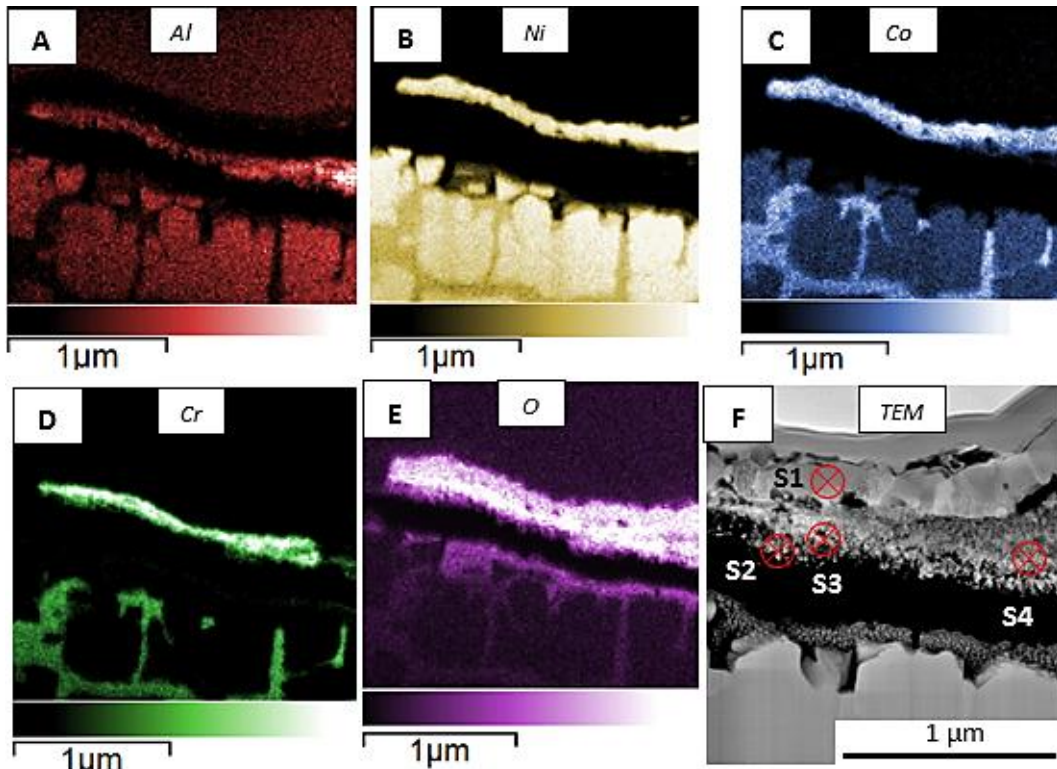


Figure 3.14 EDX maps of oxide layers a) Al K α b) Ni K α c) Co K α d) Cr K α e) O K α f) EDX locations in Figure 3.15

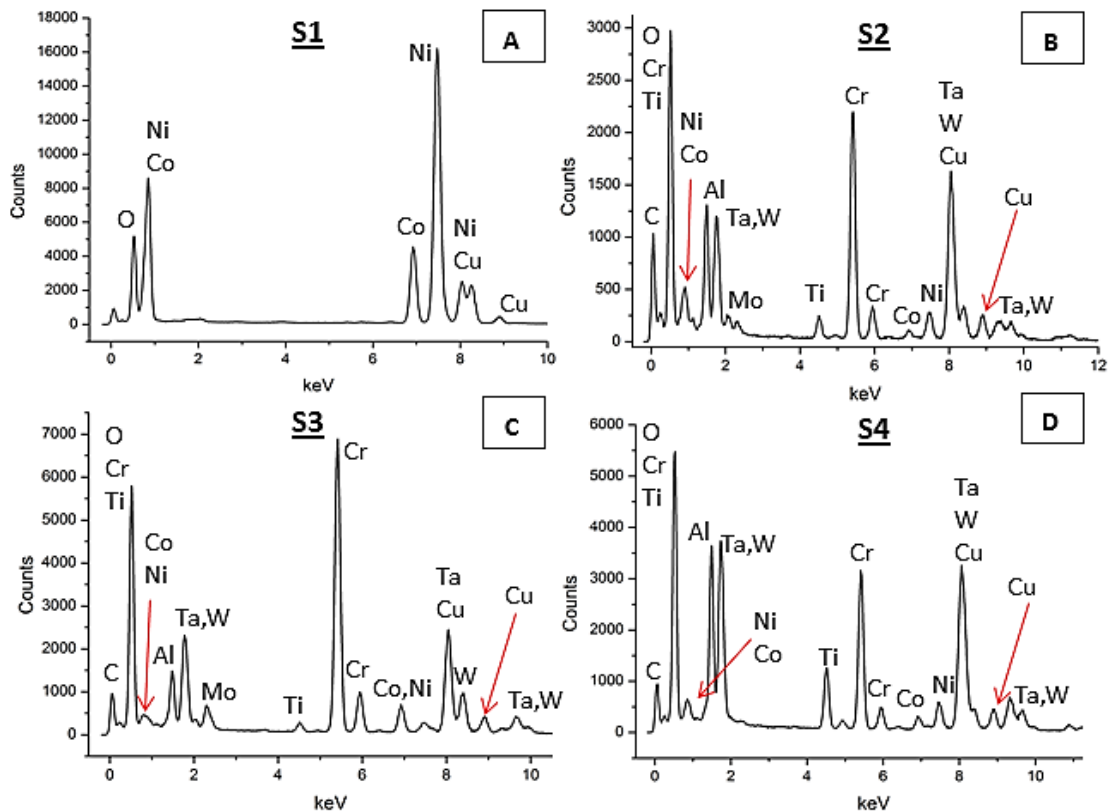


Figure 3.15 EDX spectra from the scale oxide (a) (Ni,Co)O outer scale oxide, (b-d) Mixed oxide subscale rich in Cr, Al, Ti, W and Ta. NB: Cu is detected as contamination from the TEM grid

Between these two layers there is evidence of small pores, seen in black in Figure 3.13, between the upper and lower oxide layers. However, there was no evidence of a continuous Al_2O_3 layer at the oxide/alloy interface or of any γ' denuded layer in the substrate, which is typically seen after isothermal/cyclic oxidation studies on these alloys [94][112][113]. The separation of Ta and W compositional measurements is not possible using this technique because of their $\text{L}\alpha$ and M peak overlaps, as well as the added overlap with Ni $\text{K}\beta$ at 8.2keV, so for this reason they are grouped together.

TEM analysis is, by its very nature, representative of only a very small sample of the bulk material due to its high magnification. However, these results obtained by TEM are complimentary to the other microstructural and chemical analyses in this Chapter (i.e. XPS, AES and SEM) and support their findings; therefore it can be stated with confidence that these results are representative of the bulk surface.

Further to this TEM investigation of the scale oxides found on CMSX-4 it was decided to repeat the analysis on the alloy CMSX-10N to check that the oxides formed were universal across alloy types. Figure 3.16 is a TEM micrograph of the extracted scaled cross-section and shows a series of oxide layers sitting above the alloy substrate, similar to those found on CMSX-4. This sample highlighted the complexity of extracting a TEM sample as there is evidence of porosity between the platinum deposited layers, as well as fragmentation of some of the oxide (seen as 'needle-like' fragments between the NiO layer and the Pt deposits and as a thick, porous layer above the substrate).

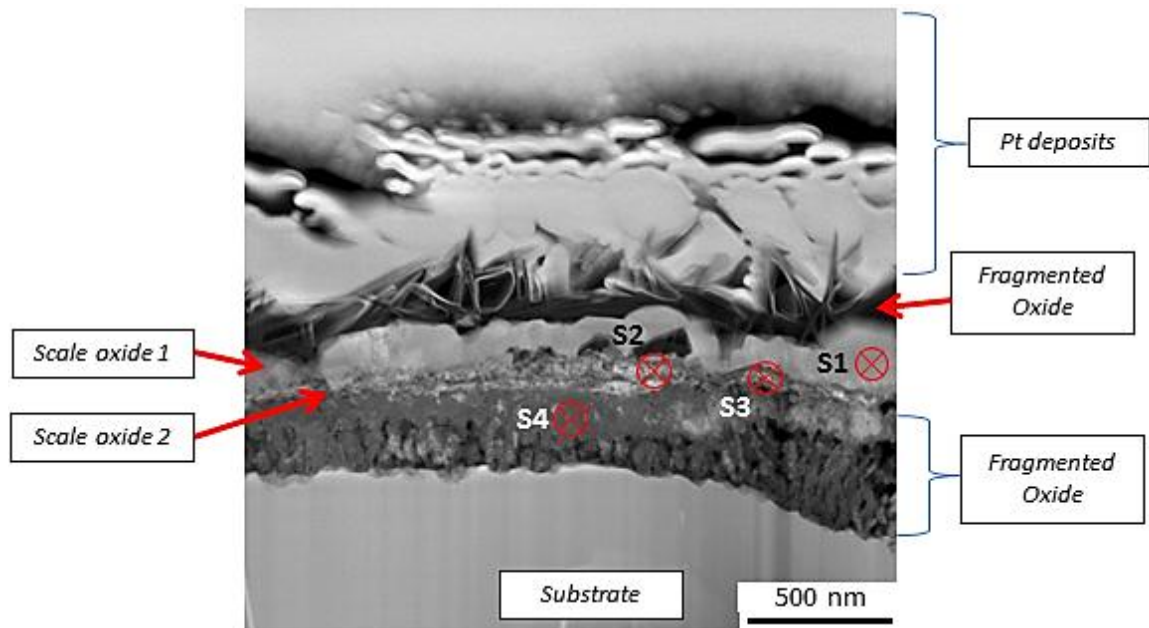


Figure 3.16 TEM micrograph of the scaled region of alloy CMSX-10N with EDX spectra locations for Figure 3.18

The whole oxide layer has a thickness of $\sim 0.5 \mu\text{m}$ and, like CMSX-4, consists of an outer Ni, Co rich oxide which is $\sim 150\text{-}200 \text{ nm}$ thick. The NiO layer is roughly half the thickness of the same layer found on alloy CMSX-4 but has a similar morphology. Below the NiO layer is the porous mixed oxide rich in Al and Cr, as well as Ta and W, which was also seen on CMSX-4. This layer is most visible in the Al and Cr EDX maps in Figure 3.17(a) and (d) but also evident in the EDX spectra in Figure 3.18(b) and (c).

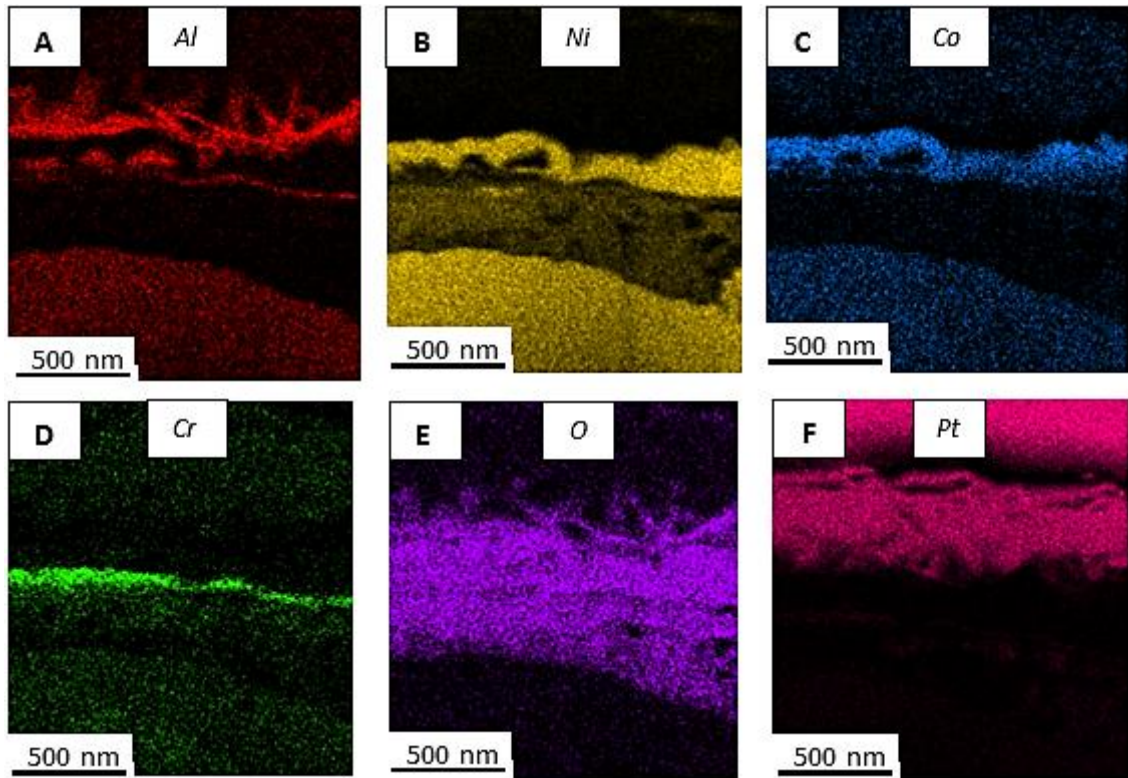


Figure 3.17 EDX maps of oxide layers a) Al K α b) Ni K α c) Co K α d) Cr K α e) O K α f) Pt La

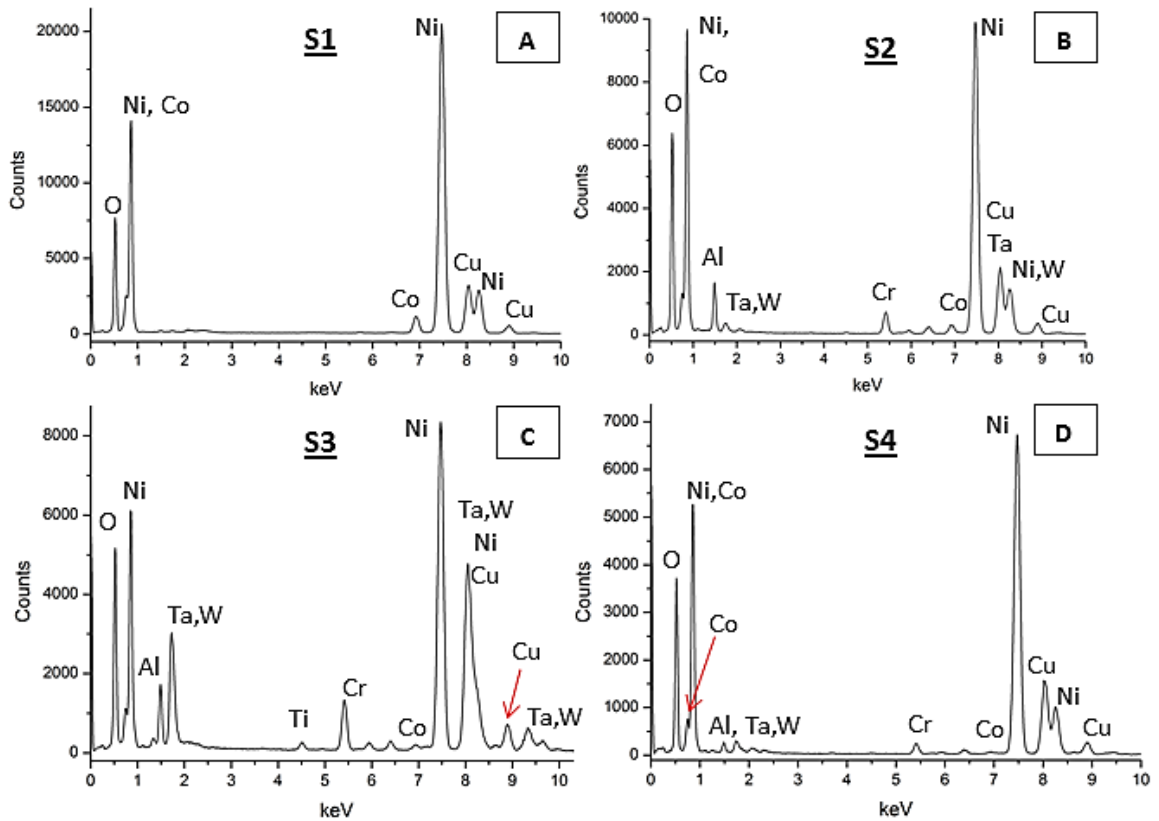


Figure 3.18 EDX spectra from the scaled region locations in Figure 3.16 (a) NiO layer (b) Al₂O₃ particle (c) Al, Cr oxide layer (d) porous subscale layer

3.4 Discussion

3.4.1 Mould-Metal Reaction during Casting

Since the metal turbine blades are cast at a temperature around 1500°C from the liquid state and in contact with a ceramic mould, it is pertinent to consider the role of possible mould-metal reactions. The ceramic mould is comprised of a layered structure, whose respective morphologies and microstructures can be seen in Figure 3.19 (below), which is a back-scattered electron image of a cross-section of a typical mould wall. Three distinct layers can be identified which refer to the prime-coat (the layer in contact with the casting), prime+1 coat and the back-up coats. The prime-coat has a typical thickness of 100-800µm and is comprised of 18wt.% colloidal silica (SiO_2) and 82wt.% of the refractory filler, ZrSiO_4 (Zircon). There are no alumina stucco particles within the prime-coat; instead the fine-grained fused alumina stucco is located within the prime+1 coat and the backup coats. Any mould-metal reaction would therefore occur between the liquid alloy and the $\text{SiO}_2/\text{ZrSiO}_4$ within the mould prime-coat.

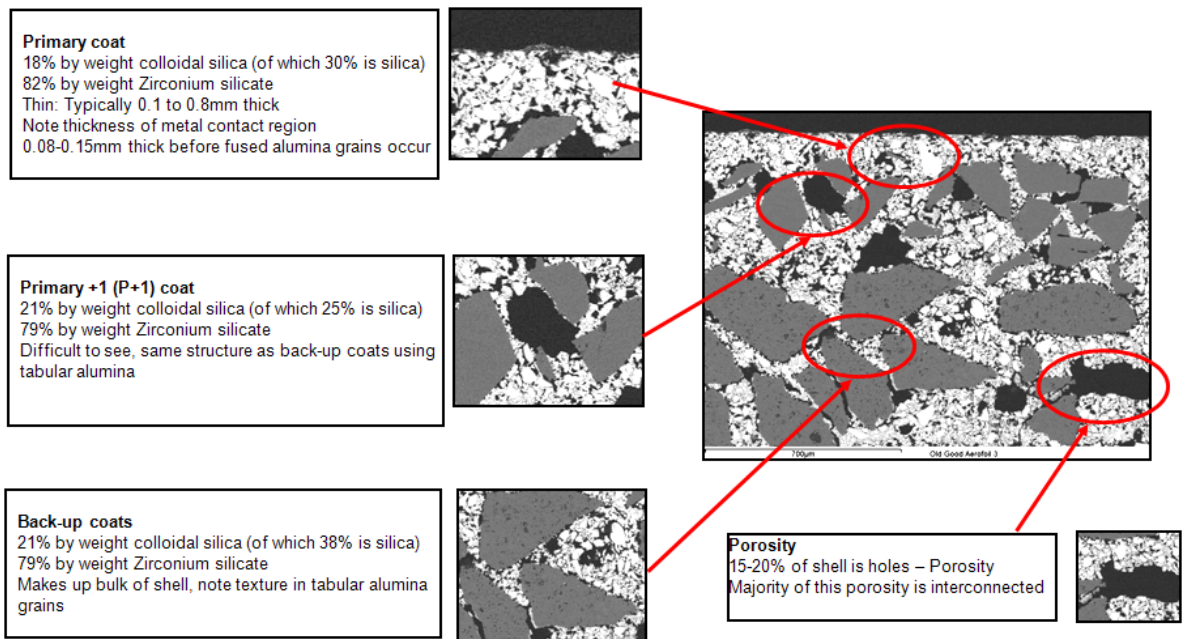


Figure 3.19 BSE image of the ceramic mould layered structure. The Primary coat is in intimate contact with the metal casting, whilst the Back-up coats impart strength to the mould. Porosity is between 15-20%. [Image courtesy of Dr Neil D’Souza, Rolls-Royce plc.]

The reduction of SiO_2 by Al to form Al_2O_3 is made possible due to alumina’s greater thermodynamic stability (appearing lower on the Ellingham diagram than SiO_2) and is well-documented [114][115][116][117]. Using thermodynamics, one can calculate the necessary partial pressure of oxygen, or p_{O_2} , and the temperature range over which the reaction can occur. In order to do so however, the activity (i.e. the effective concentration of a species within a mixture) is needed. By assuming that a component, i , within a solution behaves ideally, then the activity of i can be expressed as:

$$a_i = X_i$$

Where a_i is the activity of component i and X_i is its mole fraction within the solution.

This is an expression of Raoult’s law which is graphically represented in Figure 3.20 for the example of the component Cr within the Fe-Cr system. As the concentration of Cr (X_{Cr}) increases, the activity of Cr increases proportionally, with the corresponding activity of iron (a_{Fe}) reducing linearly, in order to maintain the overall activity ($a=1$).

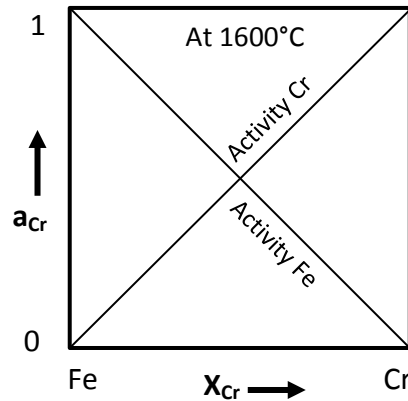


Figure 3.20 Graphical representation of Raoult's law for ideal solutions [86]

Since the SiO_2 in the mould prime-coat is solid, and distinct from the ZrSiO_4 , it can be assumed to be pure with activity = 1. However, Al is dissolved in the liquid alloy and the Si produced as a product of the reaction also dissolves in the liquid alloy, therefore their activities will be less than one ($a < 1$). The reduction of SiO_2 by Al can thus be represented by their two constituent reactions:



$$\Delta G_{3.3}^0 = [0.22(T-273) - 1065] \text{ kJ/Mole O}_2 \text{ [126]}$$



$$\Delta G_{3.4}^0 = [0.176(T-273) - 843] \text{ kJ/Mole O}_2 \text{ [126]}$$

Where T = temperature in Kelvin.

By assuming an ideal solution and Raoult's law, the mole fraction is taken to represent the activity of Al and Si. Therefore:

$$a = N = \frac{\left(\frac{w}{At.wt}\right)_i}{\sum \left(\frac{w}{At.wt}\right)_i}$$

Where i refers to i^{th} species, w is weight and $At.wt$ is atomic weight, a is activity and N is the mole fraction.

The Gibbs free energy change, ΔG , defines the driving force for the reaction and must be negative for it to proceed in the forward direction.

$$\Delta G = \Delta G^0 + RT \ln \left(\frac{a_{M_x O_y}^{2/y}}{a_M^{2x/y} a_{O_2}} \right) \quad \text{Equation 3.5}$$

Where ΔG^0 is the standard free energy change when all species are in their standard states, R is the molar gas constant, T is temperature, a is the activity of each species and a_{O_2} is the activity of oxygen (taken as the same as P_{O_2}) [85][86].

At equilibrium, $\Delta G = 0$ and the partial pressure of oxygen can therefore be expressed as:

$$\Delta G^0 = -RT \ln(K) \quad \text{Equation 3.6}$$

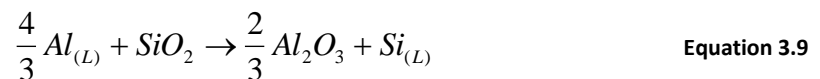
Where K is the equilibrium constant, a description of the equilibrium state of the system. If the constituents Al_2O_3 and SiO_2 appear in their standard, pure states, then their activity is expressed as 1. The Gibbs free energy change for oxidation of Al is therefore:

$$\Delta G_{3.3} = \Delta G_{3.3}^0 + RT \ln \left[\frac{1}{p_{O_2} * a_{Al}^{4/3}} \right] \quad \text{Equation 3.7}$$

And for Si:

$$\Delta G_{3.4} = \Delta G_{3.4}^0 + RT \ln \left[\frac{1}{p_{O_2} * a_{Si}} \right] \quad \text{Equation 3.8}$$

Combination of the two half-reactions describes how the reduction of SiO_2 by Al proceeds:



It can therefore be shown that the Gibbs free-energy for the reduction of SiO_2 by Al is:

$$\Delta G_{3.9} = \Delta G_{3.3} - \Delta G_{3.4} = [\Delta G_{3.3}^0 - \Delta G_{3.4}^0] + RT \ln \left[\frac{a_{Si}}{a_{Al}^{4/3}} \right] \quad \text{Equation 3.10}$$

For the reduction to be spontaneous $\Delta G_{3.9} < 0$. In the case of Al, the mole fraction (and therefore activity) can be obtained from the nominal alloy composition (Table 3.4)

CMSX-4	Al	Co	Cr	Ti	Ta	W	Re	Mo	Ni
wt%	5.8	9.5	6.5	1.1	6.5	6.5	3.0	0.6	60.5
at%	13.04	9.78	7.58	1.39	2.18	2.15	0.98	0.38	62.53
activity, a	0.13	0.01	0.08	0.014	0.022	0.021	0.01	0.004	0.63
CMSX-10N									
wt%	5.9	3.1	1.6	0.1	8.5	5.5	6.8	0.45	68.05
at%	13.83	3.33	1.95	0.13	2.97	1.89	2.31	0.30	73.30
activity, a	0.14	0.03	0.02	0.001	0.03	0.019	0.023	0.003	0.73

Table 3.4 Nominal composition and element activities for CMSX-4 and 10N

The activity of Si can be estimated from an elementary mass balance based on the thickness of the resulting Al_2O_3 layer and taking into consideration the stoichiometry of Equation 3.9. By considering a unit volume of the turbine blade ($1cm^3$), with a $2\mu m$ thick Al_2O_3 layer on the single, external surface (Figure 3.8), and assuming the Al_2O_3 mould-metal reaction layer forms across the entire blade surface (both scaled and unscaled areas), the mass of the Al_2O_3 formed on the blade surface and the mass of Si dissolved in the liquid are given by:

$$m_{Al_2O_3} = [A_{Cross-section} l] \rho_{Al_2O_3} = 7.9 \times 10^{-5} g \quad \text{Equation 3.11}$$

$$m_{Si} = \left[\frac{At.wt_{Si}}{\left(\frac{2}{3}\right) MW_{Al_2O_3}} \right] m_{Al_2O_3} = 3.3 \times 10^{-5} g \quad \text{Equation 3.12}$$

Where l is the Al_2O_3 thickness, ρ is the density of alumina, $At.wt$ is the atomic weight and MW is the molecular weight.

The densities of CMSX-4 and CMSX-10N are 8.7 and $9.05g/cm^3$ respectively and therefore the unit masses are 8.7 and $9.05g$ respectively. By assuming that the reduction reaction occurs whilst the alloy is liquid and that the Si produced is dissolved within the liquid, the mass of Si produced can be added to the unit mass and the

activities calculated from their mole fractions. For the temperature range where the alloy is liquid ($1400 < T < 1500^{\circ}\text{C}$) the activity of Si is 8×10^{-6} .

Using the Al and Si activities and Equation 3.10, the free energy change for the reduction of SiO_2 by aluminium can be calculated and shown to be negative for the temperature range $1400 < T < 1500^{\circ}\text{C}$:

$$-286.6 \text{ kJ/mole O}_2 \leq \Delta G \leq -289.7 \text{ kJ/mole O}_2 \quad (\text{CMSX-10N})$$

$$-285.5 \text{ kJ/mole O}_2 \leq \Delta G \leq -288.6 \text{ kJ/mole O}_2 \quad (\text{CMSX-4})$$

Therefore because the Gibbs free-energy for this reaction is negative, the reduction of SiO_2 by Al in the liquid will occur spontaneously. In the case of Equation 3.3 (the oxidation of aluminium) the equilibrium partial pressure of oxygen can be taken from the Ellingham diagram (Figure 3.21 purple line) as $P_{\text{O}_2} \approx 10^{-23}$ at 1500°C and $\approx 10^{-25}$ at 1400°C , whilst the casting furnace $P_{\text{O}_2} \approx 10^{-6}$. Therefore, this reaction is spontaneous and Al in the melt will also form an oxide with the residual O_2 within the furnace as well as reaction with the SiO_2 in the mould Prime-coat, resulting in a continuous oxide layer across the liquid alloy at the mould-metal interface.

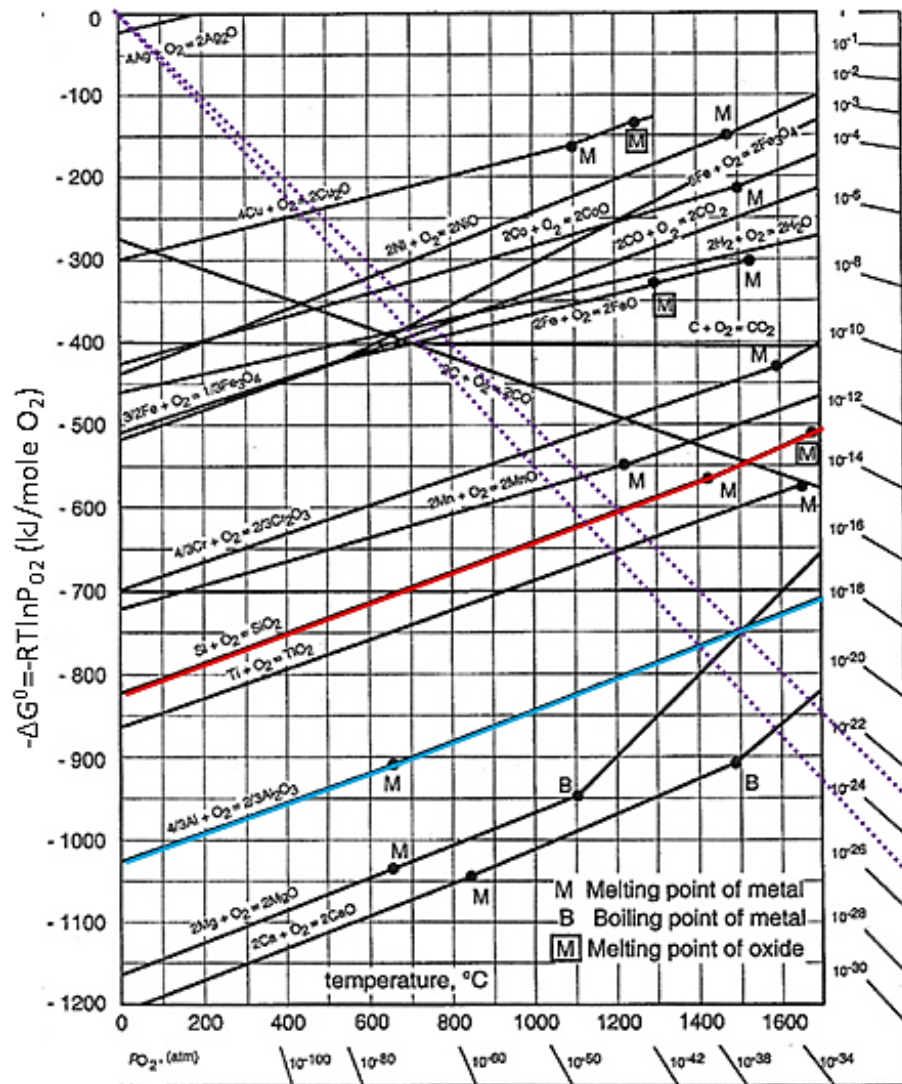


Figure 3.21 Ellingham diagram of standard free energies for oxide formation. Al and Si oxides are highlighted in blue and red respectively [86]

For Equation 3.4 (oxidation of Si) the standard free energy of formation between 1400-1500°C is also negative and the equilibrium P_{O_2} is $10^{-18} < T < 10^{-19}$. However, the activity of Si is very low ($\sim 10^{-6}$), therefore the low activity of Si decreases the spontaneity of Equation 3.4; rather favouring the reverse reaction, reduction of SiO_2 by Al.

3.4.2 Mould-Metal Separation

The mould surfaces in contact with the scaled and unscaled as-cast surfaces are shown in Figure 3.22. There is a clear boundary between the scaled and unscaled mould surfaces which matches the corresponding boundary seen on the turbine blade

surface, between the scaled and unscaled areas. It is also evident that, whilst the mould surface corresponding to the scaled surface is macroscopically smooth, in the unscaled case the mould surface is much rougher and 'grainy' in texture.

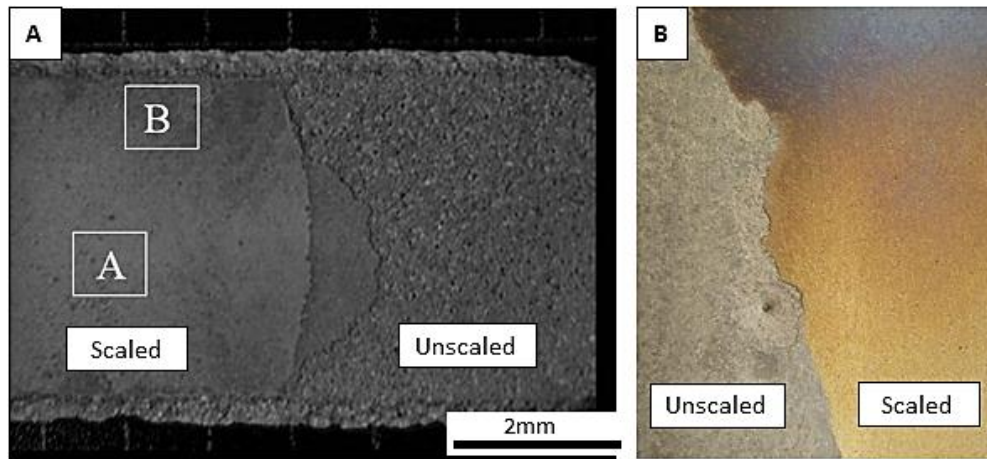


Figure 3.22 Optical images of the border between the scaled and unscaled regions

From Figure 3.8, the presence of a continuous Al_2O_3 layer which is in intimate contact with the mould prime-coat and the unscaled blade surface is clear. Therefore, when the casting is separated from the mould during knock-off, this Al_2O_3 layer remains adhered to the metal surface and furthermore, pulls off patches of the mould prime-coat with it. However, in the scaled regions, no such continuous alumina layer is seen on the blade surface after knock-off, nor is there any evidence of zircon/ SiO_2 ceramic from the mould. The thermodynamic analysis in Section 3.4.1 proves that the Al_2O_3 layer is a mould-metal reaction product whilst the XPS analysis in Figure 3.11 of the mould prime-coat adjacent to the scaled regions showed that the missing Al_2O_3 layer is adhered to the prime-coat. The difference in surface texture, and the removal of Al_2O_3 , suggests that the mould and metal are being pulled apart in the scaled regions.

During the last stage of casting the blade/mould assembly is cooled and during this process both the solid metal and the ceramic mould contract with a differential

thermal contraction existing between them. Since the metal contraction is greater ($1.4 \times 10^{-5} \text{K}^{-1}$ versus $5.4 \times 10^{-6} \text{K}^{-1}$ [118]) a gap will form between the metal casting surface and the mould wall.

The commercial software package, ProCAST™, was used at Rolls-Royce as part of this research project to predict the separation between mould and metal during investment casting [119]. Due to the complex nature of modelling such a system it was assumed that radiation is the dominant heat transfer mode and appropriate heat transfer coefficients were applied to the mould/metal interface, which have been validated using instrumented moulds with thermocouples [120]. Since casting is performed under vacuum it is a reasonable assumption to ignore conduction and convection heat transfer modes.

The calculated temperature profiles were then used as input for a 3D mechanical model, which calculates the local stress and the accompanying strain from which local displacement is determined. Consequently, the gap between the mould and metal is determined from this nodal displacement for any given temperature. To facilitate the run-time, some further simplifying assumptions were made in the calculation:

- The metal is assumed to deform elastically up to its yield point beyond which only plastic deformation occurs. The mould is considered to be perfectly elastic. No creep is considered and fracture is not considered in the ceramic.
- No mechanical interaction is considered between the mould and metal at the interface. This ignores any effects of 'sticking' due to the Al_2O_3 layer sandwiched between the two surfaces.

Because the surface scale is prevalent on the upper, convex portion of the blade aerofoil, two typical transverse sections were examined at the lower end of the casting (termed “bottom” or unscaled) and the other at the top end of the casting (termed “top” or scaled). The calculated temperature contour plots and displacement are shown in Figure 3.23 for 900°C whilst Figure 3.24 shows the same for 1100°C.

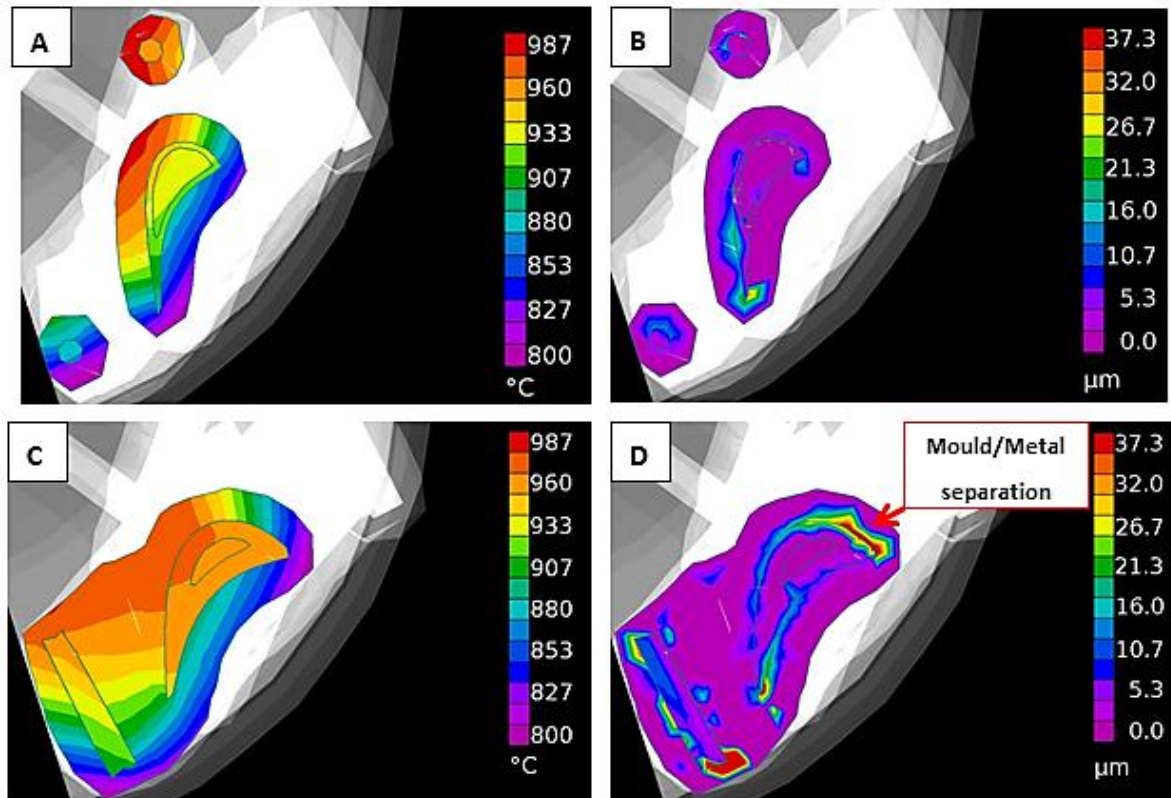


Figure 3.23 Temperature and displacement contour plots calculated using ProCAST™ for the bottom section (a-b) and for the top section (c-d) at 900°C.

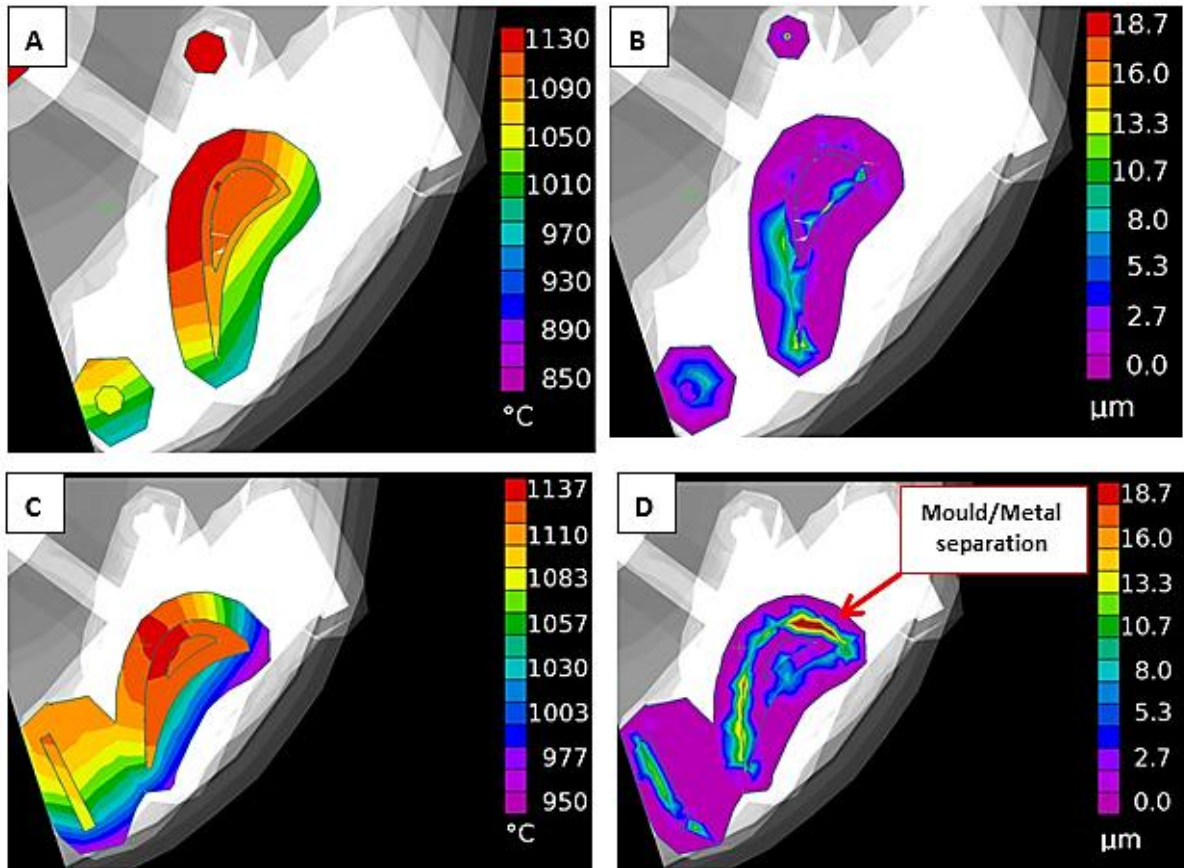


Figure 3.24 Temperature and displacement contour plots calculated using ProCAST™ for the bottom section (a-b) and for the top section (c-d) at 1100°C.

In both Figure 3.23 and Figure 3.24, (a) and (b) refer to the bottom section whilst (c) and (d) refer to the top section. In both Figures, the temperature plots show that a significant temperature gradient occurs over the thickness of the mould, ranging from 100-200°C, and that there is also a temperature gradient of up to 40°C across the solid blade. The calculated gap width between mould and metal is larger at higher solidification heights and doubles in magnitude at 900°C compared to 1100°C, with a maximum gap width of 40 µm predicted in the top section at 900°C.

The gap width is also shown to be greater along the convex portion of the aerofoil, when compared with the concave surface, which is where surface scale is seen to form. In Figure 3.24(d) the mould-metal separation is nearly uniform across the entire

surface perimeter. The severity of the mould-metal separation is dependent on the assumptions made in calculations, but nevertheless semi-quantitative aspects of the separation are clearly illustrated by these results, namely that:

- a) Mould-metal separation occurs to a greater extent on the upper, convex portion of the blade surface. This agrees with the spatial location of surface scale.
- b) There exists a large temperature gradient across the mould and metal of up to 40°C which will exacerbate the differential thermal contraction.

During cooling, after solidification, the metal separates from the mould wall owing to the differential thermal contraction. This separation occurs in the solid-state and the degree of contraction is dependent on the constraints imposed by the geometry of the turbine blade as well as the interaction between the mould and the metal at the mould-metal interface. There will also be mechanisms in each material, such as creep and fracture that will act to relieve the strain imparted by the contraction.

There is an increasing gap width at the convex surface of the aerofoil and with increasing solidification height. In the unscaled region, there exists an intimate contact between the mould Prime-coat, the Al_2O_3 mould-metal reaction layer and the metal substrate but with increasing solidification height there is a clear de-bonding observed between the mould and metal expressed in terms of gap width (Figure 3.24). In these calculations the mould is only assumed to deform elastically, so there is a continuous build-up of stress within the ceramic. Once the stress exceeds a critical threshold, the ceramic mould fractures and this is observed in practice within the foundry. Following

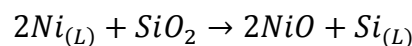
fracture, thereafter the metal will be able to detach easily from the mould without any constraint.

In the scaled region (upper portion of the aerofoil) where mould-metal contraction dominates and the metal contracts from the mould, the Al₂O₃ mould-metal reaction layer is present on the mating Prime-coat that is retained on the mould. The detachment of this “protective” Al₂O₃ layer from the surface of the aerofoil during contraction would then render the bare metal surface susceptible to subsequent oxidation. This is what happens on the scaled region as the casting keeps cooling during withdrawal from the furnace and this forms the basis of the discussion in the next section.

3.4.3 Surface Scale Formation

3.4.3.1 Thermodynamic analysis

In the scaled region of the aerofoil there is the presence of a dual-layered oxide ((Ni,Co)O upper layer with an Al, Cr rich sub-layer) instead of the Al₂O₃ seen in the unscaled regions. There is a sharp demarcation between the scaled and unscaled region (Figure 3.22) on the aerofoil and the scale oxide is ~0.5-1µm thick compared to ~2µm for the unscaled Al₂O₃. To show that these scale oxides are not the product of a mould-metal reaction, the same thermodynamic arguments as in Section 3.4.1 can be used. Considering a reaction between the liquid Ni and the SiO₂ to form NiO and Si:



$$\Delta G_{Reduction} = [\Delta G_{NiO}^0 - \Delta G_{SiO_2}^0] + RT \ln\left(\frac{a_{Si}}{a_{Ni}^2}\right) \quad \text{Equation 3.13}$$

Where ΔG_{NiO}^0 and $\Delta G_{SiO_2}^0$ can be obtained from the individual oxidation reactions (calculated using reference [121]) and the stoichiometry is taken into account. The activity of Ni, a_{Ni} , is assumed to be the mole fraction and the activity of Si, a_{Si} , is taken from Section 3.4.1 ($a_{Si} = 8 \times 10^{-6}$).

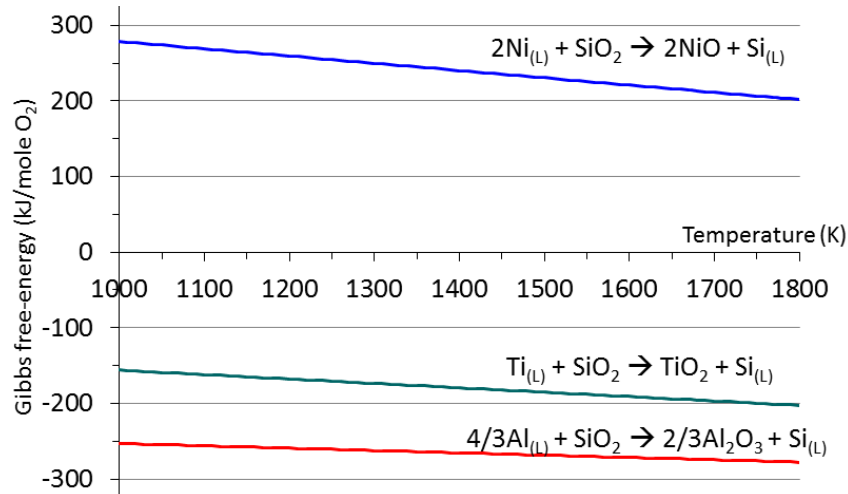


Figure 3.25 Gibbs free-energy for the reduction of SiO₂ by Al, Ni and Ti within the liquid alloy

The same analysis procedure can be applied for the reduction via titanium in the melt to form TiO₂. Figure 3.25 summarises the calculated free energies for the reduction of SiO₂ by Al, Ni and Ti and it is clear that the reduction of SiO₂ by Al is thermodynamically more favourable, as compared to that with Ti (since it is more negative). On the other hand, reduction of SiO₂ by Ni does not occur, since for the temperature range and silicon activity, ΔG is considerably greater than zero. Therefore, occurrence of a mould/metal reaction cannot account for the formation of NiO on the scaled portion of the aerofoil.

Rather than a mould-metal reaction, the surface scale oxides are instead a product of oxidation of the “bare” metal surface following the detachment of the Al₂O₃ reaction layer by differential mould-metal contraction. There are a number of oxidation studies of the SRR99 [122][123] and CMSX10K (variant of CMSX10N) alloys [124][125], which

provide good insight into the oxidation behaviour of these materials. However, the key difference is that these oxidation studies are performed under atmospheric conditions and for prolonged isothermal holds with the aim of assessing the alloys in-service oxidation resistance. However in the results presented in this Chapter, the oxygen partial pressure (P_{O_2}) in the casting furnace ($\sim 10^{-6}$ atm) and also the oxidation times are significantly lower than those used to assess in-service oxidation performance and this will in turn affect the oxide species produced.

Using the Gibbs free-energy of formation (Equation 3.14 [85]) there is, for each element, a unique partial pressure above which oxidation will occur. However, while the metal oxide can be assumed to be pure and solid (therefore activity, $a_{M_xO_y} = 1$), the alloying elements are in solid-solution and therefore, assuming Raoult's law, will be characterised by activities less than 1. These can be found from their mole fractions within the alloy (calculated in Table 3.4, page 94).

$$\Delta G_f = \Delta G^0 + RT \ln \left[\frac{a_{M_xO_y}^{2/y}}{a_M^{2x/y} \cdot P_{O_2}} \right] \quad \text{Equation 3.14}$$

For the oxidation reaction to be spontaneous, $\Delta G_f < 0$, whilst at equilibrium $\Delta G = 0$. The Ellingham diagram is a useful way of graphically representing under what conditions the oxidation reaction will occur by plotting the Gibbs free-energy change against temperature. This allows the direct comparison of various oxide reactions; the most stable being lowest on the diagram and having the lowest Gibbs free-energy of formation. It is also possible to find the partial pressure of oxygen that, at equilibrium, is equal to the dissociation pressure of the oxide, allowing the identification of likely oxidation reactions for any known P_{O_2} [86].

Figure 3.26 shows the Ellingham diagrams calculated for CMSX-4 and CMSX-10N, using Equation 2.12 and taking into account the elemental activities (Table 3.4) and the typical casting furnace P_{O_2} of 10^{-6} atm. Equilibrium partial pressure of oxygen is the pressure at which the driving force for oxidation is zero and is shown in Figure 3.27. When the partial pressure of oxygen is greater than the predicted equilibrium partial pressure, the free-energy change for the reaction is negative and there is a driving force for the reaction to take place and metal will be oxidized.

It is clear that, below 1450-1500°C, all the oxides are thermodynamically stable with Al_2O_3 the most stable, followed by TiO_2 , Ta_2O_5 , Cr_2O_3 , WO_2 , CoO/NiO respectively. It is apparent that the evolution in Cobalt content from CMSX-4 to CMSX-10N (9.5-3.1wt%) has reversed the order of most thermodynamically stable oxide, in favour of NiO in CMSX-10N.

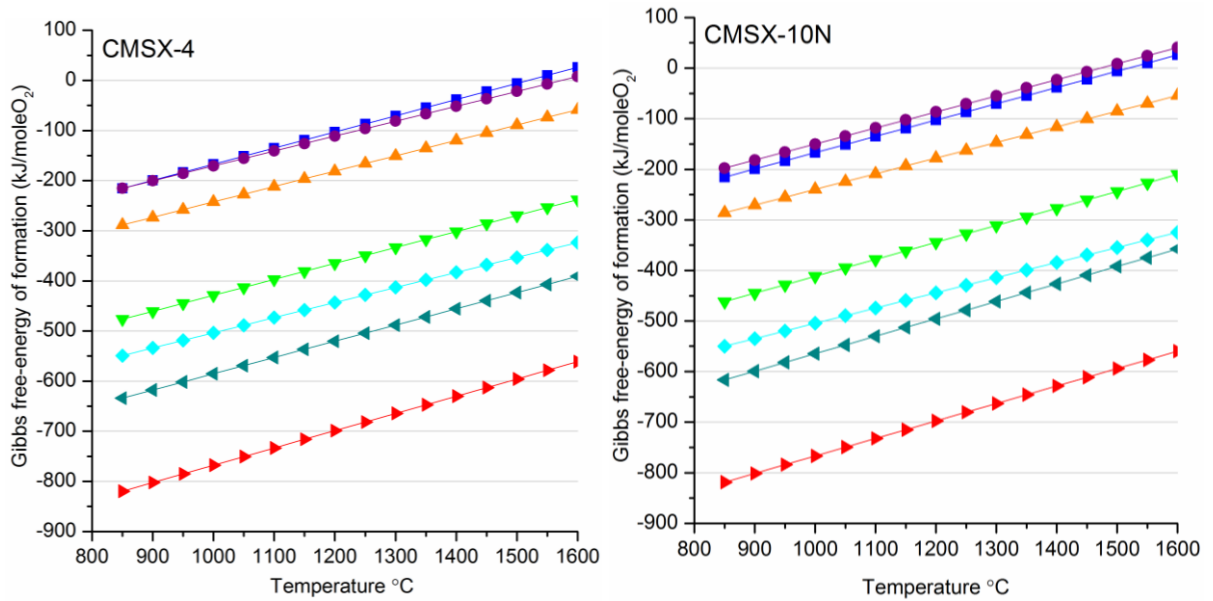


Figure 3.26 Calculated Ellingham diagrams for CMSX-4 and -10N (Legend in Figure 3.27) [126]

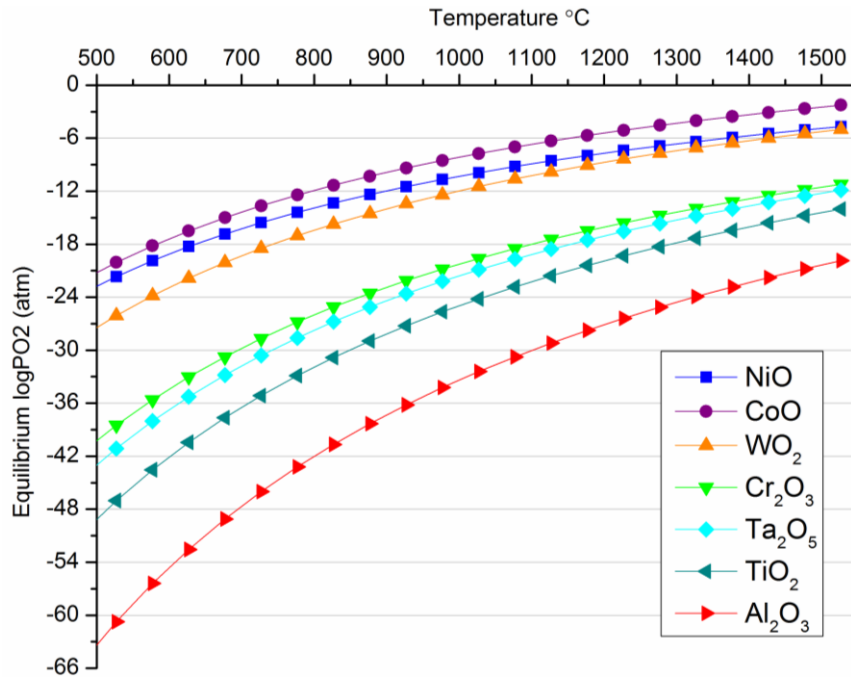


Figure 3.27 Equilibrium partial pressure of oxygen versus temperature for CMSX-4 NB: Same as CMSX-10N

The effect of oxygen partial pressure is shown in Figure 3.27. The typical casting furnace P_{O_2} of 10^{-6} atm is highlighted on the vertical scale and it is clear that Al_2O_3 , TiO_2 , Cr_2O_3 and Ta_2O_5 can all form at the temperatures experienced during casting since they appear lower on the diagram than the equilibrium P_{O_2} of 10^{-6} atm. The formation of NiO , CoO and WO_2 however is dependent on the temperature since they all have P_{O_2} values above the 10^{-6} atm line until 1370, 1230 and 1430°C respectively.

These results show that the all of these oxides can form on the surface of the turbine blades, in the solid-state, since the Liquidus-Solidus temperatures for CMSX-4 and 10N are ~1423-1369°C and ~1382-1329°C respectively.

From this data it is clear that thermodynamic stability is not the only factor affecting the type of oxide species that form since there exists an outer (Ni,Co)O layer on top of a mixed subscale of the more thermodynamically stable oxide formers, Al and Cr. The growth kinetics of each oxide clearly plays an important role in the oxidation mechanism and will be discussed next.

3.4.3.2 Kinetic analysis of oxide formation

For both alloys, the surface scale oxide is around 1 micron thick and is predominantly composed of NiO. In oxidation studies of CMSX-10N variant alloys [124][125] similar observations were made. It has been shown in isothermal and cyclic oxidation studies, at or below 1000°C, that NiO is a fast growing, porous oxide (typically with small amounts of CoO in solution) found as the upper most oxide species, below which Al₂O₃ and/or Cr₂O₃ dominate after steady-state conditions are reached [127][128]. NiO is a non-stoichiometric oxide that exhibits p-type semiconductor behaviour, inducing growth through outward cation (M⁺ ions) migration due to a metal deficit crystal structure. This is evident by the way the NiO grows outward from the metal surface at the gas/oxide interface (Figure 3.28). Al₂O₃ on the other hand is highly stoichiometric and typically forms at the oxide/metal interface growing via the rate-controlling transport of O₂ ions through the oxide layer. However, it has been shown that its

growth can be controlled by the diffusion of Al [129] and that the oxide can be either an n-type or p-type semiconductor, depending on the local oxygen potential [130].

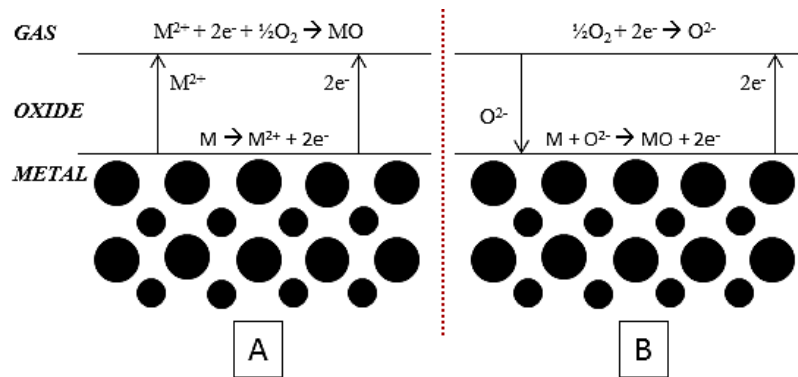


Figure 3.28 Ion and electron transport schematic for (a) cation diffusion controlled oxide film (e.g. NiO) and (b) anion diffusion controlled oxide film (e.g. Al₂O₃). Adapted from [131]

In the case of surface scale formation the oxidation is not steady-state (temperature is not isothermal and time is a few hours only) but is instead transient which corresponds to the initial period of rapid oxide growth prior to the establishment of steady-state conditions. Within this period (alloy dependent between 1-100hrs [111][127][132][133][134]) the observations are similar to the TEM/EDX experimental results in Section 2.5.4, i.e. the outer growth of (Ni,Co)O and a mixed subscale/spinel below.

The subscale is a product of solid-state reactions between oxide species and a reducing oxygen partial pressure due to the NiO layer acting as a diffusion barrier above. Isothermal and cyclic oxidation studies on various SX alloys (SRR99, CMSX-2 & 3 and DD32) at 800-1150°C have shown that this subscale is most likely composed of spinel phases (mineral of general formulation $A^{2+}B^{3+}_2O^{2-}_4$) such as Ni(Cr,Al,Co)₂O₄ as well as (Cr,Al)TaO₄ and (Cr,Al)₂O₃ [122][132][135][136]. Kear *et al* [137] investigated the transient oxidation of a Ni-15Cr-6Al alloy at 1000°C in 0.1 atm oxygen for up to 40 minutes isothermal hold. This work is important to discuss since the nature of the

transient oxidation process matches that occurring in the scaled regions during casting. Kear *et al* produced a schematic diagram of the transient oxidation process (Figure 3.29), within the first minute of oxidation a thin layer of oxide has already formed, composed of a spinel ($\text{Ni}(\text{Cr},\text{Al})_2\text{O}_4$) with small islands of NiO. Beneath the oxide layer, Cr oxidises to form small particles of Cr_2O_3 (Figure 3.29(a)). After 5mins oxygen diffusion within the oxide and the alloy favour the growth of the NiO which grows laterally over the spinel. At the same time Cr in the alloy diffuses to the oxide/alloy interface and continues to form Cr_2O_3 particles. As the oxide layer grows, the oxygen partial pressure at the oxide/alloy interface is reduced; therefore Al starts to preferentially oxidise at this interface (Figure 3.29(b)). These Al oxides initially are not $\alpha\text{-Al}_2\text{O}_3$, rather polymorphs with orthorhombic structure, e.g. χ and Υ phases, which subsequently transform into the stable $\alpha\text{-Al}_2\text{O}_3$ phase upon further oxidation. After 40mins, the distinct Cr_2O_3 particles have coalesced to form a continuous band of Cr_2O_3 with some Al_2O_3 in solution. Above this layer the growth of the NiO and spinel phases is retarded due to the Cr_2O_3 diffusion barrier below preventing fresh metal migrating to the oxide/air interface (Figure 3.29(c)). Continued oxidation past 40mins results in the formation of a continuous layer of $\alpha\text{-Al}_2\text{O}_3$ at the oxide/alloy interface, due to the decreased P_{O_2} , and after 20hours oxidation there was little evidence of the NiO/spinel phases remaining. These are either consumed by the oxides below or spalled/vaporized away.

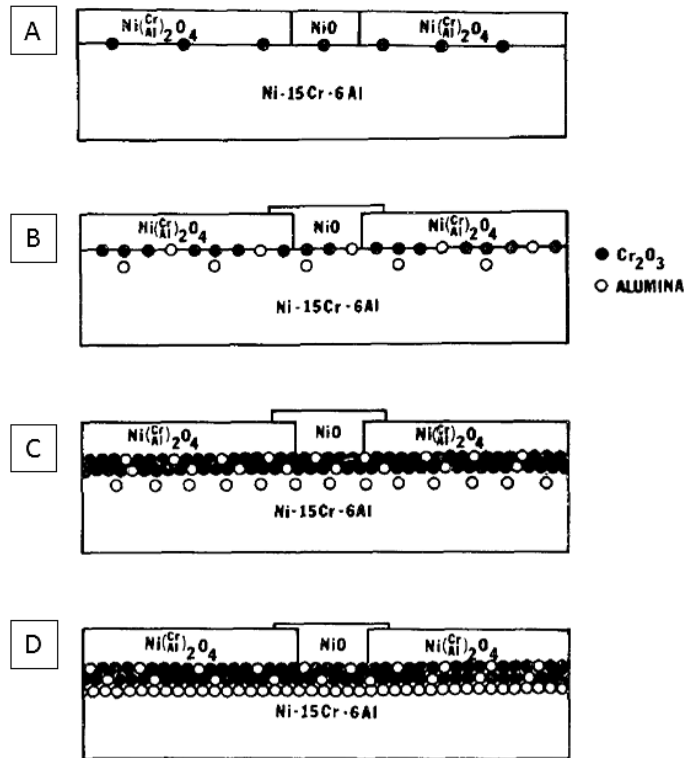


Figure 3.29 The transient oxidation process of a Ni-15Cr-6Al alloy at 1000°C in 0.1 atm oxygen [137]

Usually the formation of the NiO and subscale/spinel layers would have the effect of reducing the oxygen transport (P_{O_2}) to the alloy surface sufficiently to allow the preferential oxidation of Al_2O_3 . This is not seen in oxidation during casting meaning that there is insufficient time for the NiO and subscale below to become thick enough to allow the production of an Al_2O_3 layer and therefore steady-state conditions are not encountered. The typical withdrawal rate from the furnace hot-zone during directional solidification is $5 \times 10^{-5} \text{ms}^{-1}$, giving a time of ~ 5.56 hours to remove the whole casting/mould assembly from the hot-zone (assembly height $\sim 1\text{m}$). However, the temperature is constantly falling; therefore the actual oxidation time will likely be smaller than this. Using the evidence from Kear *et al* as a guideline, it seems likely that the total oxidation time is less than 1hr since the resultant scale oxide does not form a continuous Al_2O_3 layer.

3.5 A Model for Surface Scale Formation

The refined model for formation of surface scale is proposed in Figure 3.30, which is an evolution of the initial model proposed by Brewster [7]. It depicts the key stages of Surface Scale formation as follows (i) – (v):

- i. During casting and after pouring, the liquid metal is in intimate contact with the mould face-coat over the entire surface of the casting.
- ii. A mould-metal reaction of Al in the liquid reducing the SiO_2 in the face-coat results in the formation of a $\sim 2\mu\text{m}$ thick Al_2O_3 layer over the entire casting surface. Si is a by-product of this reaction that is dissolved in the liquid.
- iii. Upon cooling below the solidus temperature, mould-metal differential contraction occurs, resulting in key areas of the blade coming away from the mould wall. These areas are the upper, convex parts of the aerofoil and will become scaled.
- iv. The separation of mould and metal also removes the Al_2O_3 from the scaled regions surface, exposing a “bare” casting surface to the furnace atmosphere.
- v. Subsequently, transient oxidation occurs at the “bare” casting surface to form a multi-layered oxide scale, termed ‘Surface Scale’. The composition and thickness of this oxide scale is dependent on alloy composition and oxygen partial pressure/temperature within the furnace and at the oxide/alloy interface.
- vi. When the mould is separated from the casting, on the unscaled areas, small patches of remnant mould face-coat as well as the Al_2O_3 layer can be seen. In the scaled areas the surface is much smoother, absent from adhered mould

material and exhibits a patina of discolouration caused by the presence of surface scale oxides.

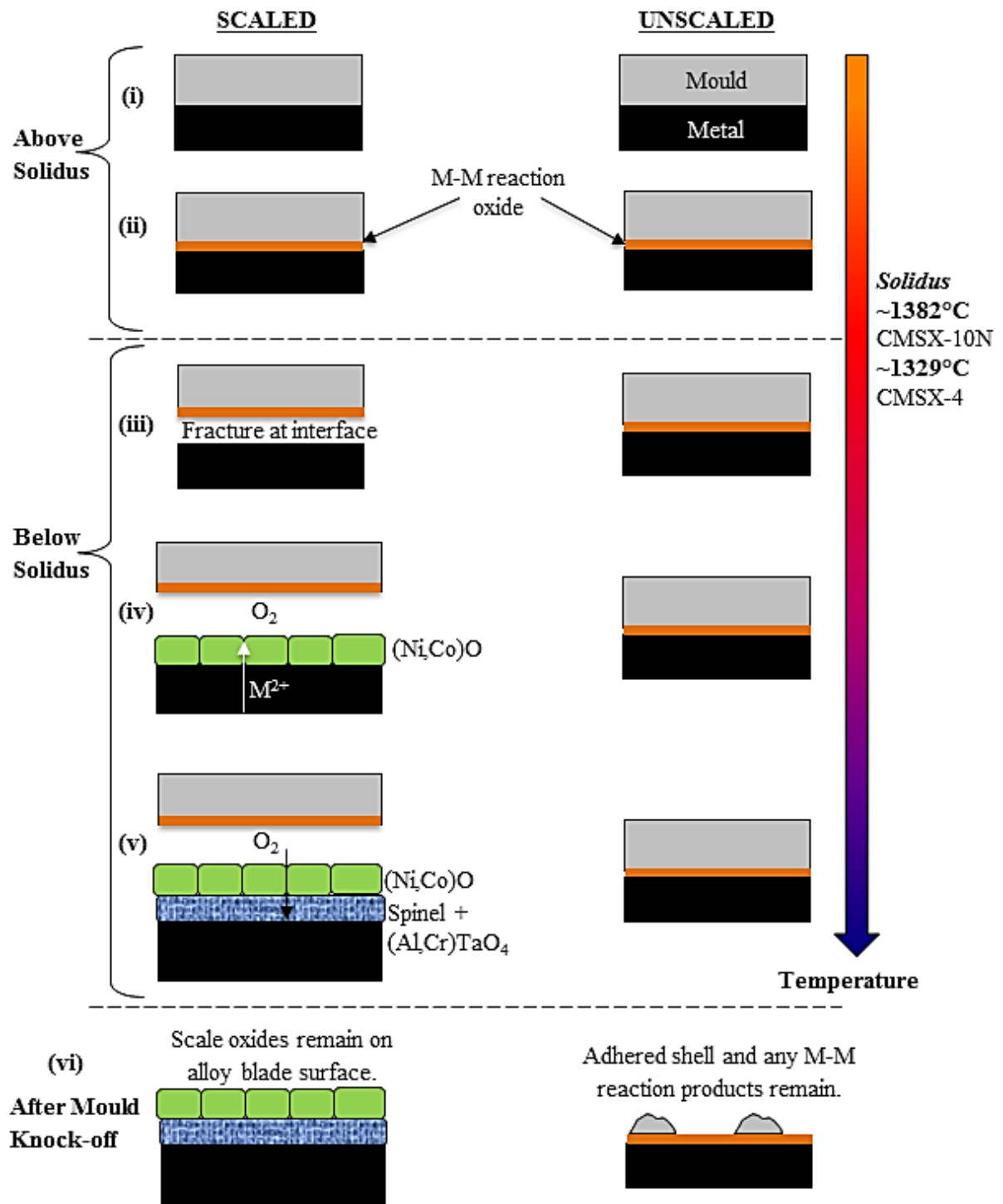


Figure 3.30 Schematic diagram of the model for the formation of surface scale during directional solidification (adapted from the original diagram by Brewster [7])

Chapter 4. Characterisation of the Surface Melt Blister formed during Heat-Treatment

4.1 Introduction

This Chapter aims to characterise the morphology and evolution of the surface defect known as ‘Surface Melting’ or ‘Surface Melt Blister/Wrinkle’ which occurs during heat-treatment of Nickel-based superalloy turbine blades, particularly those cast in single-crystal form. It is identified as an area of raised material on the aerofoil surface immediately after heat-treatment (Figure 4.1) that is 10’s of mm² in size. This defect is directly linked with surface scale, discussed in Chapter 3, because it is in the areas that previously exhibited surface scale that the melt blisters appear during subsequent heat-treatment. This melted and re-frozen layer has to be mechanically abraded before the components surface can be visually assessed for grain structure defects such as re-crystallisation, freckles and high-angled grain boundaries. It is also more likely that the blade will be scrapped due to excess material removal (resulting in exceeded dimensional tolerances) or if the part requires too many rework stages.

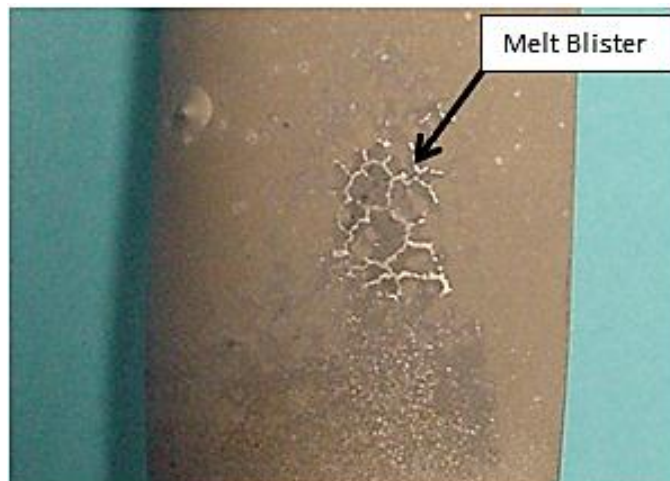


Figure 4.1 Surface wrinkle melt blister on the aerofoil of an IPTB cast from CMSX-10N [68]

During solutioning the alloy is heated to, and held at, a temperature above the γ' -solvus, within the γ phase-field (but below the solidus temperature), for a period of about 8-24 hours (in the case of CMSX-4 and CMSX-10N respectively). However, it has been observed that microstructural instability and localised melting can develop across certain regions of the aerofoil surface during solutioning, specifically in the areas that were scaled in the as-cast condition [7][77]. This is especially evident in the latest generation single-crystal (SX) superalloy, CMSX-10N (but also in CMSX-4) in part due to the narrow heat-treatment window between adequate γ phase homogenisation and incipient melting. A representative cross-sectional image of the melt blister microstructural instability is shown in Figure 4.2.

This Chapter therefore aims to investigate the surface melt blister morphology during heat-treatment by tracking the microstructural evolution of SX test-bars during solutioning and ageing and to answer the following key questions:

- a) Why does the microstructural instability only affect the previously scaled regions of the aerofoil and not the unscaled regions as well?
- b) What processes are occurring at the surface of the casting during solutioning and ageing heat-treatments that result in the microstructural instability?

With these answers it is hoped that proposals can be made that will mitigate the formation of the surface melt blister and thus improve production efficiency.



Figure 4.2 OM image of melt blister cross-section from a heat-treated SX turbine blade

4.2 Experimental Methods

The SX Nickel-based superalloy, CMSX-4, was considered extensively in this chapter due to its significant industrial importance and susceptibility to surface melt blisters. Nominal composition (wt.%) is given in Table 4.1. Single-crystal test-bars were chosen for the microstructural analysis due to their availability (turbine blades are notoriously difficult to request due to production requirements) and because they undergo the same processes simultaneously as the turbine blades.

Alloy	Al	Co	Cr	Ti	Mo	Ta	W	Re	Ni
CMSX-4	5.8	9.5	6.5	1.1	0.6	6.5	6.5	3	Bal

Table 4.1 Nominal composition (wt.%) of alloying elements

4.2.1 Investment Casting and Heat-Treatment

For this study, cylindrical test-bars (10mm OD x 60mm H) were cast using the methods described in Chapter 3 at the Precision Casting Facility (PCF), Rolls-Royce plc in Derby. The test-bars were subsequently heat-treated by standard industrial practices within the turbine blade heat-treatment furnaces (during standard production) at Bodycote plc. The heat-treatment includes a series of ramps and holds to a final solutioning temperature of 1312°C for 8 hours. During the ramp up stages of solutioning the furnace is under a vacuum of 10^{-3} mbar ($\sim 10^{-6}$ atm), beyond 1140°C Ar gas is introduced with a partial pressure of $P_{Ar} = 0.5$ mbar ($\sim 5 \times 10^{-4}$ atm). Following the isothermal hold at 1312°C the furnace is rapid gas fan quenched using Argon gas.

The test-bars were then aged at 1140°C for 2 hours at a vacuum level of 10^{-3} mbar before rapid gas fan quenching in Argon gas. After casting, prior to heat-treatment, the test-bars were grit blasted with Al_2O_3 media to remove all surface oxides (both surface

scale and the unscaled Al_2O_3). This is to ensure that the as-cast surface oxides and surface eutectic are removed prior to solutioning so as to discount their effect from the results.

In the case of the pre-oxidised test-bars, these were also grit-blast in the as-cast condition prior to being heat-treated using a laboratory furnace in atmospheric air at 1100°C for a maximum hold time of 4 hours and a ramp rate of 10Kmin^{-1} before being air-cooled. These were then solutioned as standard.

4.2.2 Optical Microscopy and Scanning Electron Microscopy (SEM)

Transverse aerofoil cross-sections were cut from the test-bars using a diamond tipped rotary bench saw before being mounted in conducting Bakelite resin and progressively polished with grit/SiC papers followed by a final $1/4\mu\text{m}$ diamond polish for metallographic examination. Where necessary, samples were etched with a Nimonic etchant of 50ml HNO_3 , 200ml HCl , 12.5g CuCl_2 and 12.5g FeCl_2 made up to 500ml with distilled water. For EBSD analysis the samples were mechano-chemically polished using the Vibromet at Rolls-Royce, Derby with $0.65\mu\text{m}$ colloidal silica for several hours.

Turbine blade surfaces were initially analysed with an Olympus BX51 optical microscope (OM) at various magnifications to select appropriate areas for further analysis. SEM/EDX was used to study the morphology and chemistry of the surface structure in greater detail than with OM. Back-scattered electron imaging (BSI) was performed, to enhance compositional contrast, at a typical working distance (WD) of 5mm, spot size 5 and an accelerating voltage of 15-20 kV. For EDX analysis the

accelerating voltage was varied between 15-20kV (in order to excite X-ray emission from the heavy refractory elements but reduce detector dead-time). EDX spectra were collected from a minimum of three different locations, within the area of interest, to check for consistency.

EBSD analysis of the near-surface regions of the heat-treated test-bars was conducted in order to assess its crystallographic orientation. Kikuchi patterns were collected using a Hikari EDAX camera and were indexed at a frame rate of 280 frames sec^{-1} according to Nickel structure files. Following this orientation, data was analysed using the EDAX software package.

4.3 Results

4.3.1 Microstructural Analysis of the Heat-Treated Surface

Before heat-treatment, the as-cast test-bars were examined under the microscope to ensure the surface is free of any remaining oxides or eutectic (some minimal inter-dendritic eutectic is present intersecting the surface, Figure 4.3).

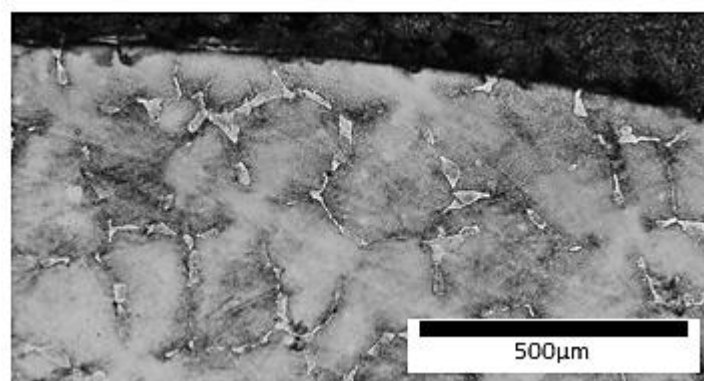


Figure 4.3 As-cast test-bar surface after grit-blasting. There is no remaining oxides or eutectic, except for small channels of inter-dendritic eutectic that intersects with the surface

Figure 4.4(a) shows an OM of the test-bar surface after solution and ageing heat-treatments and it can be seen that a significant surface microstructural instability has evolved at the surface that is $\sim 20\mu\text{m}$ thick and continuous around the entire test-bar perimeter. A corresponding back-scattered electron image (BSI) is shown in Figure 4.4(b) that focuses on the surface layer in more detail, whilst in Figure 4.5 the EDX spectra are shown from the key areas highlighted in Figure 4.4(b).

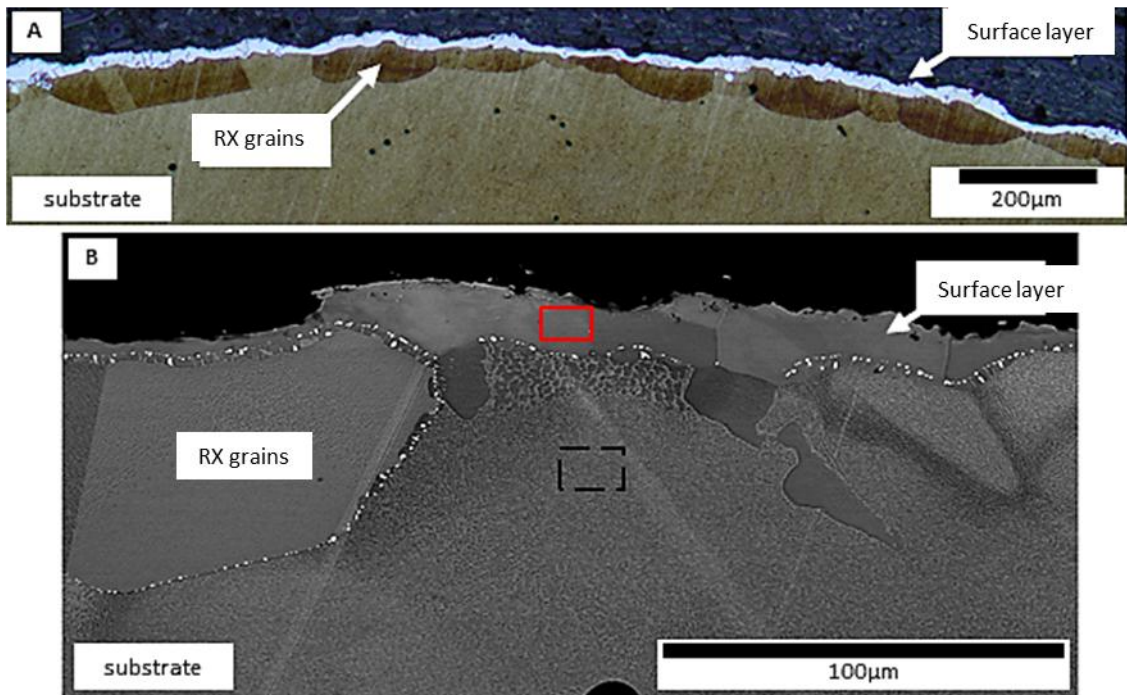


Figure 4.4 (a) OM image of the fully heat-treated test-bar surface with surface layer and (b) higher magnification BSI of the same surface area with EDX spectral locations highlighted for Figure 4.5

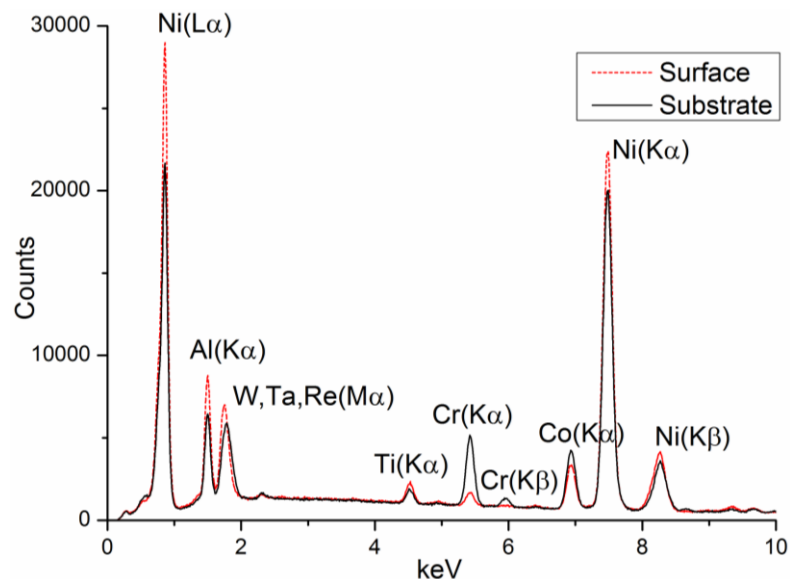


Figure 4.5 EDX spectra from the surface layer (red) and the substrate (black)

The EDX spectra (Figure 4.5) shows that the surface layer is composed of γ' since there is a reduction in the peak heights of the γ partitioning elements Cr and Co and an increase in Al+Ti, in comparison to the substrate spectrum. There is also enrichment of the refractory elements W, Ta and Re within the surface layer (these are indistinguishable using EDX due to their $M\alpha$ peak overlaps) as well as Ni. In many locations, recrystallized (RX) γ grains have nucleated and grown beneath the γ' surface layer into the substrate and at the boundary between these γ grains, the substrate and the γ' layer above, refractory-rich precipitates (TCP's) have nucleated (these appear bright white in the BSI). This can also be seen occasionally between adjacent γ grains. A closer examination of the γ' surface layer, as well as the interfaces between each γ grain and the surface layer is shown in Figure 4.6.

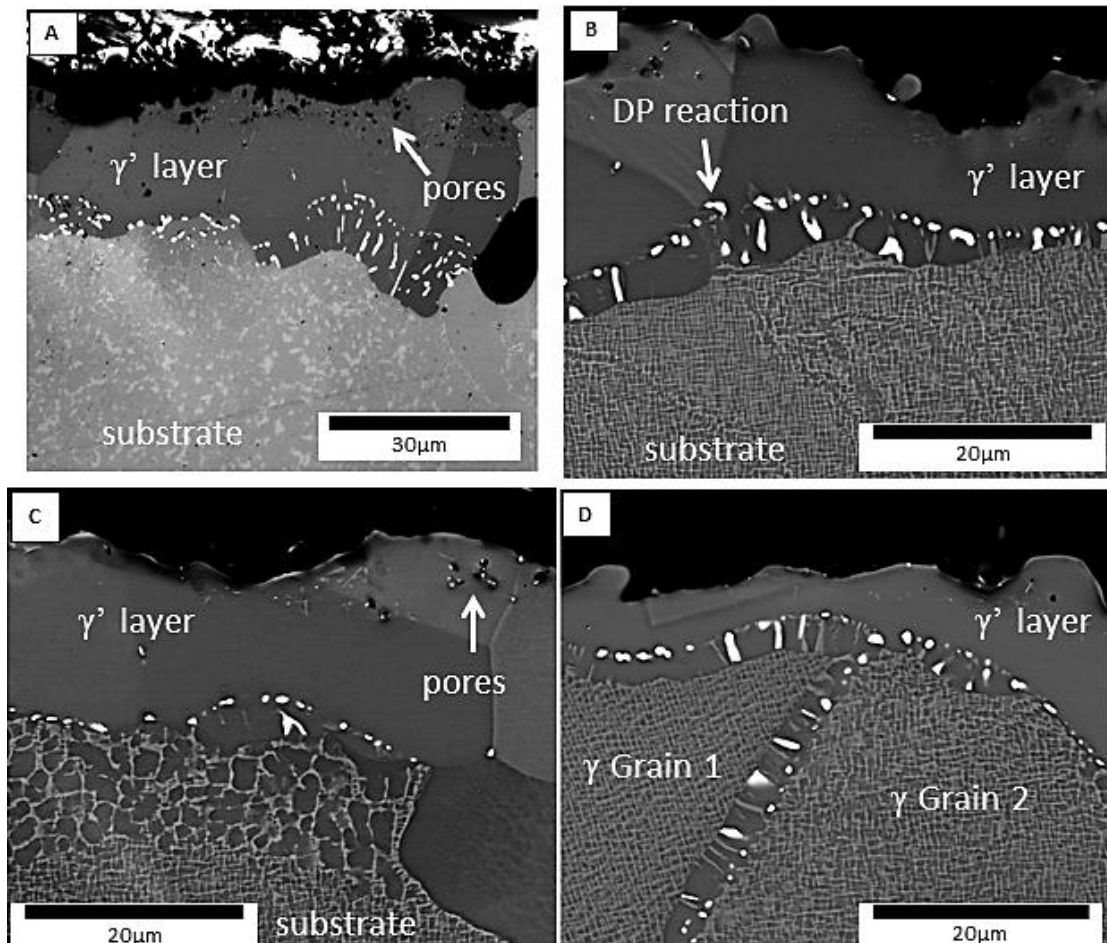


Figure 4.6 BSI's showing (a-b) close-up of the γ' surface layer porosity and DP reaction (c) γ' coarsening in the substrate adjacent to the γ' surface layer and (d) the interface with the γ' layer and γ RX grains below

From Figure 4.6(a) the presence of pores within the upper portion of the γ' surface layer are evident. In all figures there is evidence of discontinuous precipitation (DP) occurring between γ grains as well between the γ' the surface layer and the substrate. This DP reaction is characterised by the growth of TCP's and lamellar γ phase channels (Figure 4.6(d)). In Figure 4.6(c) the γ' precipitates in the substrate, adjacent to the γ' surface layer have coarsened and the similar contrast, in back-scatter mode, between the surface layer and the γ' precipitates in the grains below makes it clear that the surface layer is indeed γ' . The coarsening is an indicator of the diffusion and concentration of γ' formers (i.e. Al) towards the border with the γ' surface layer.

The RX γ grains contain blocky γ' precipitates, as is normal of the substrate, with a DP reaction occurring between each RX γ grain. It is also clear that these grains are polycrystalline, not single-crystal like the substrate below, however it is not clear whether the γ' surface layer is polycrystalline or SX. It was therefore decided to use EBSD analysis of this region to confirm the orientation of the surface layer and sub-grains.

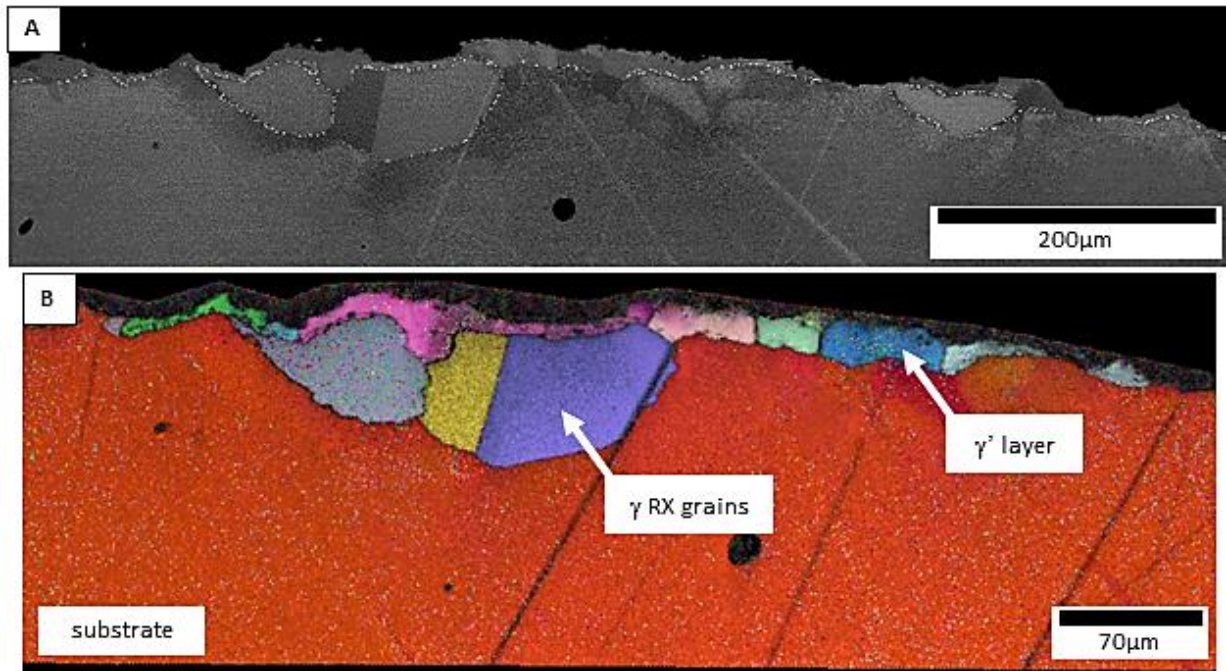


Figure 4.7 Crystallographic analysis of the surface region (a) BSI of γ' surface layer and RX γ grains and (b) EBSD derived inverse pole figure map of same area showing polycrystalline nature of the surface (where colour variation indicates different crystallographic orientations)

Figure 4.7(a) shows a BSI of the surface of the heat-treated test-bar, representative of the γ' surface layer + RX γ grains + TCP's morphology. In Figure 4.8(b) the corresponding EBSD derived inverse pole figure map is shown and from this it is clear to see that both the γ' surface layer and the RX γ sub-grains are polycrystalline whereas the substrate is SX.

In order to assess the change in surface morphology between solution and ageing heat-treatments some purely solutioned test-bars were analysed (un-aged) and these are shown in Figure 4.8. It is clear that in the purely solutioned state, the occurrence of both the γ' surface layer and the RX γ grains are evident whilst the DP reaction at the interfaces between γ grains, the γ' surface layer etc is missing. However there is evidence of the precipitation of needle-like discrete particles of TCP's at the γ' layer/substrate interfaces. In the RX γ grains the γ' phase has precipitated during quench with the small blocky morphology characteristic of the substrate whilst at the

grain boundaries, there is evidence of coarsening of these γ' precipitates due to the increased solubility of the boundary. Finally, it can be concluded that the DP reaction occurs during ageing and not during solutioning heat-treatment.

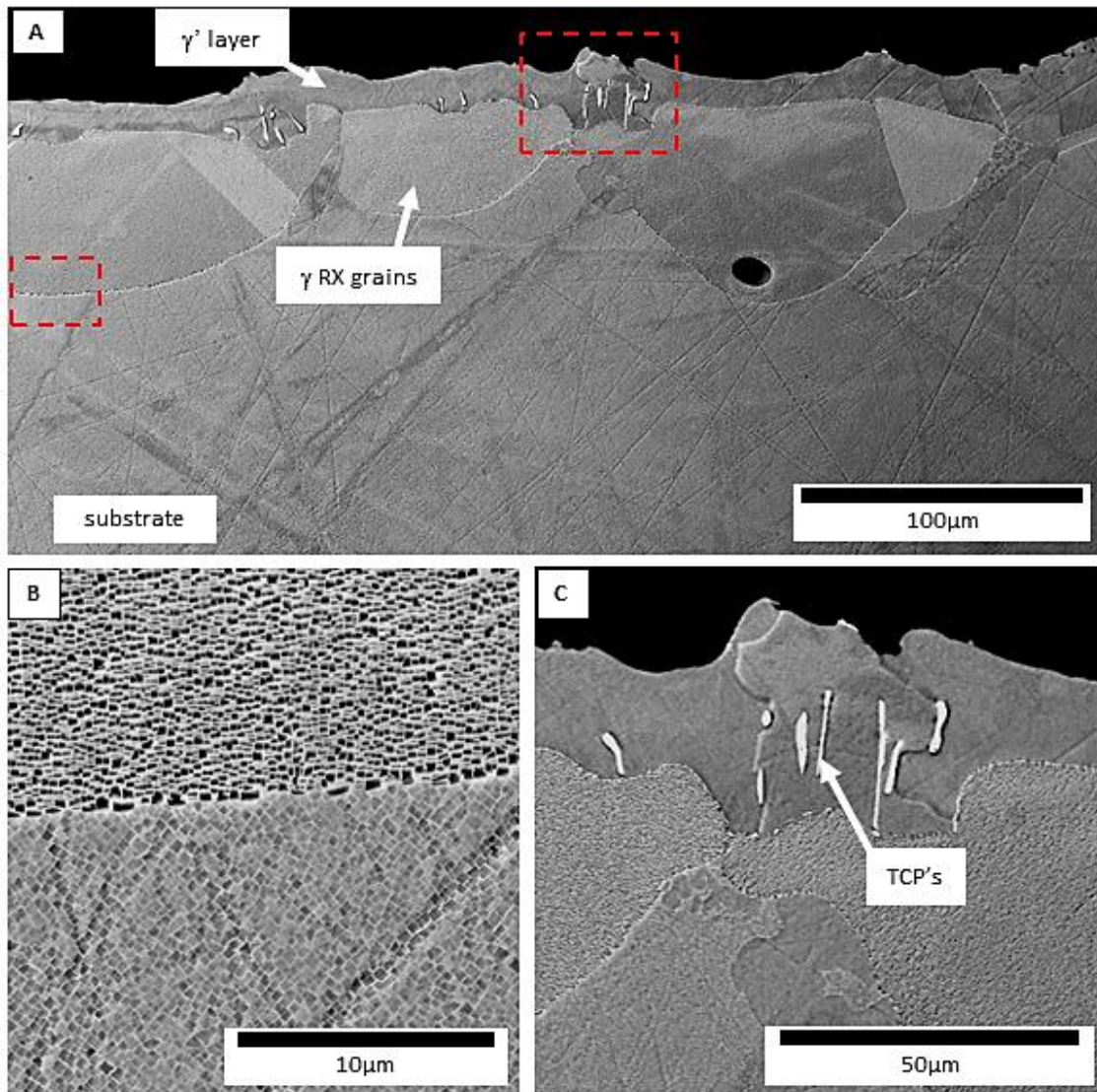


Figure 4.8(a) BSI of the solutioned test-bar with characteristic γ' surface layer and RX γ grains but no DP at interfaces (b) RX γ grain/substrate interface showing coarse γ' precipitates on the grain-boundary and an absence of DP (c) close-up of the γ' surface layer/ γ RX grain interface showing formation of some discrete TCP's

4.3.2 Microstructural Analysis of the Pre-Oxidised Test-Bars

In order to stabilise the γ' phase at the surface (to form the γ' surface layer), the γ phase stabilising elements must first be depleted (i.e. Ni, Cr and Co) in order to increase the ratio of γ' stabilising elements such as Al and Ta. In order to test this statement and to attempt to suppress the formation of the γ' surface layer, test-bars

were pre-oxidised in atmospheric air prior to solutioning and their surfaces were analysed after subsequent solutioning. Figure 4.9 shows that the surface of the pre-oxidised test-bar is covered in a thin ($\sim 1\mu\text{m}$) external layer of Al_2O_3 with internal oxidation occurring below. There is also an intermediate γ' precipitate free zone (PFZ) between the outer oxide and the substrate beneath that is $\sim 10\mu\text{m}$ in depth. The growth of the Al_2O_3 layer, and the PFZ below, effectively removes γ' forming Al from the surface region, stabilising the γ phase.

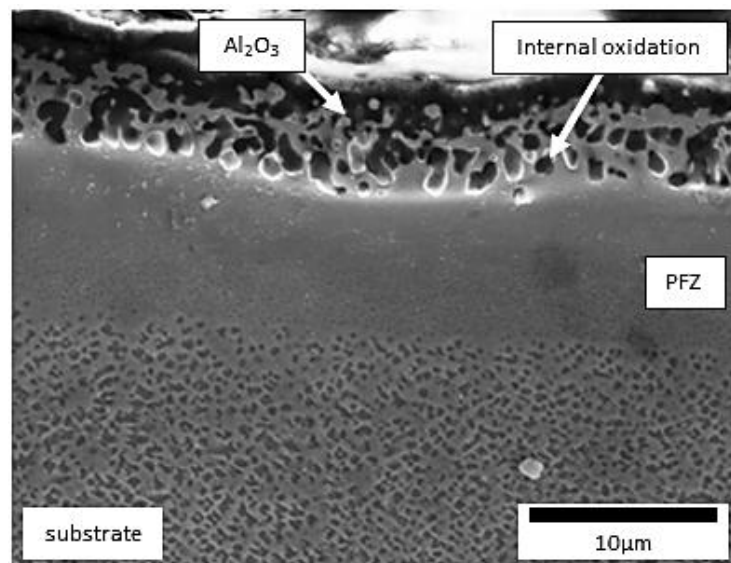


Figure 4.9 Pre-oxidised test-bar surface prior to subsequent solutioning with Al_2O_3 surface oxide (black)

The subsequently solutioned surface morphology is shown in Figure 4.10 and the first point to note is that the γ' surface layer has not formed, unlike in the standard case in Figure 4.4. The surface oxide layer of Al_2O_3 is clear to see in the BSI as a dark surface layer as well as small chains of internal oxidation. Finally, the recrystallized γ grains have formed into the substrate, as is to be expected due to the grit blasted nature of the test-bar surface prior to solutioning. In Figure 4.11 the three key areas of interest have been analysed using EDX, (i) the surface oxide, (ii) the near surface region and (iii) the substrate, in order to compare their composition. It is clear that the near surface region and the substrate have a similar composition and that therefore there is no γ'

surface layer or depletion of γ stabilising elements. From the BSI in Figure 4.10(b) it is clear that the precipitate free zone (PFZ) has disappeared in the solutioned state due to long-range diffusion of the γ' formers, e.g. Al, to the surface at the high temperatures and hold times experienced during solutioning. The surface oxide is also confirmed to be Al_2O_3 from the $\text{Al}(\text{K}\alpha)$ and $\text{O}(\text{K}\alpha)$ peak heights. This confirms that by pre-oxidising the test-bar surface, the formation of the γ' surface layer is precluded and that therefore, in order for its formation to proceed, significant alloy redistribution is required, particularly losses of Ni, Cr and Co.

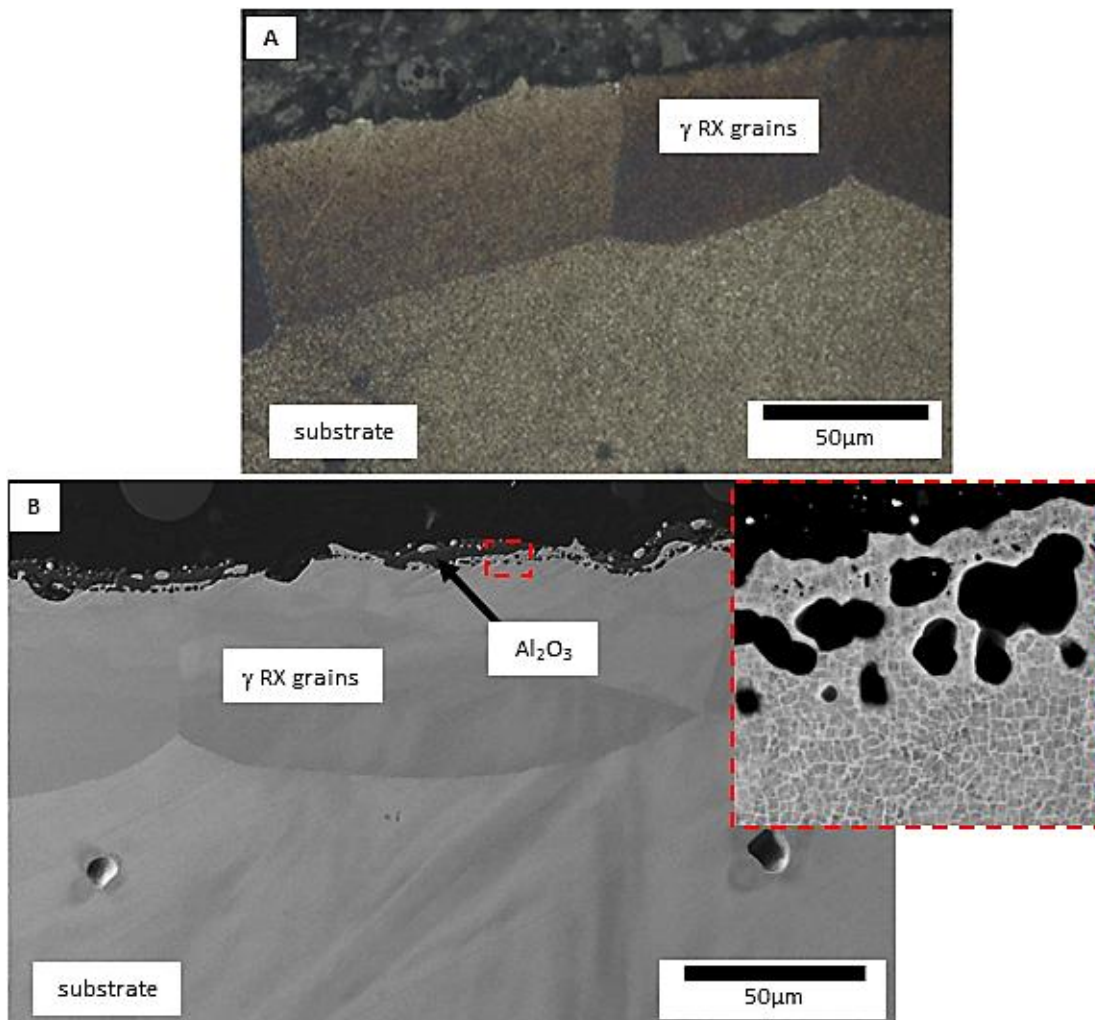


Figure 4.10 Pre-oxidised and solutioned test-bar surface (a) OM and (b) BSI of the surface morphology showing the outer Al_2O_3 layer (plus internal oxidation), RX γ grains and no γ' layer. Insert shows no PFZ below oxide

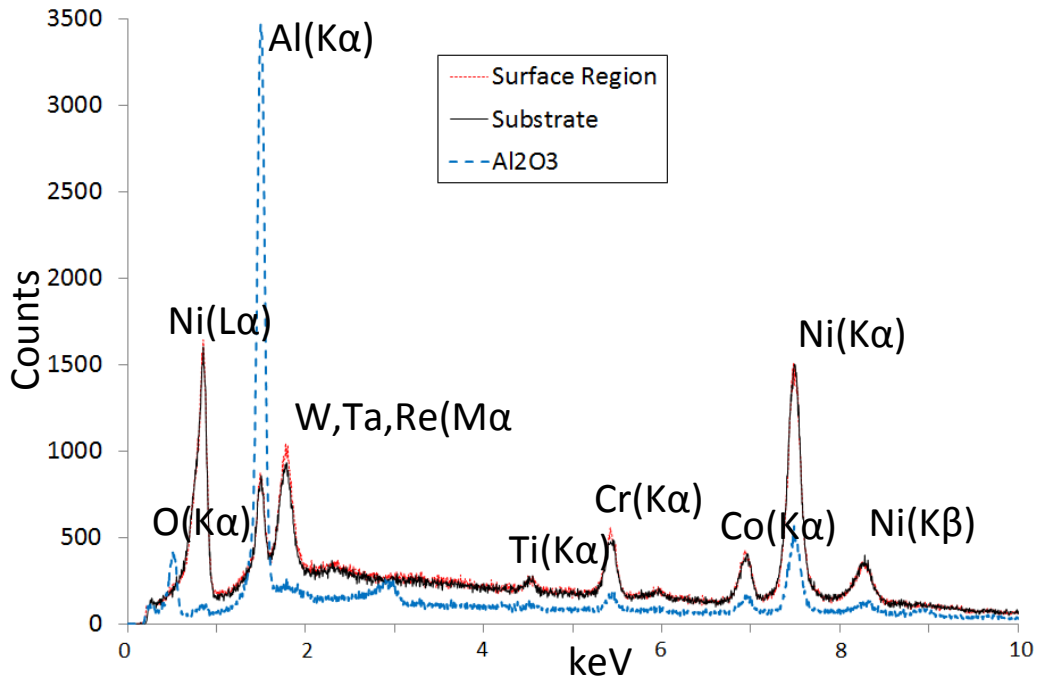


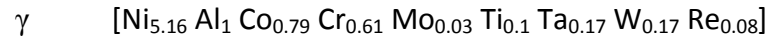
Figure 4.11 EDX spectra for the surface oxide layer, the γ RX grains and the substrate of the pre-oxidised and solutioned test-bar sample

4.4 Discussion

4.4.1 Stabilisation of the γ' Phase at the Surface during Solutioning

During solutioning the component is held at a temperature within the γ phase-field, which is high enough to dissolve the γ' phase, and homogenise the segregated microstructure via long-range volume diffusion. At the same time some surface oxidation occurs in the low- P_{O_2} heat-treatment environment, favouring the formation of the thermodynamically stable (but slow growing), Al_2O_3 . The typical thickness of this oxide layer in the post-solutioning state is observed as $\sim 1\text{-}2\mu\text{m}$ and by forming this oxide, Al is pulled from the near-surface region resulting in an Al depleted zone, the severity of which depends on the oxidation time, temperature, oxide growth rate and the rate of diffusion of Al to the surface. This generally acts to increase the stability of the γ phase at the near-surface region, however in the case of the results shown in this

Chapter the converse has been identified, with the increased stabilisation of the non-equilibrium γ' phase at the surface. In order to achieve this, significant re-distribution of solute is required in the near-surface region. From the nominal composition, the γ and γ' phases can be written as (normalised for Al):



A reduction in the Ni/Al ratio is thus required in order to stabilise the γ' phase, as well as redistribution of the solid-solution strengthening elements Cr, Co, W and Re which typically have a low solubility in γ' . Ni, Co and Cr are however characterised by relatively high vapour pressures and therefore the role of vaporisation (sublimation) must be considered. The equilibrium partial pressures for pure Ni, Co and Cr are calculated from the following expressions (thermodynamic data from [138]):

$$\log[P_{Ni}] \text{ atm} = 10.557 - \frac{22606}{T} - 0.8717 \log T \quad \text{Equation 4.1}$$

$$\log[P_{Cr}] \text{ atm} = 6.8 - \frac{20733}{T} + 0.4391 \log T - 0.4094 T^{-3} \quad \text{Equation 4.2}$$

$$\log[P_{Co}] \text{ atm} = 10.976 - \frac{22576}{T} - 1.028 \log T \quad \text{Equation 4.3}$$

However in the case of Nickel-based superalloys, these elements are not in their pure form but are rather part of a solid-solution (alloy) so they will have an associated reduction in their vapour pressures. In the case of solid-solutions, assuming ideal behaviour, then Raoult's law applies and therefore the partial pressure of each element in the solution is proportional to its mole fraction:

$$P_i = P_i^0 \cdot x_i \quad \text{Equation 4.4}$$

Where P_i is the vapour pressure of the species in solution, P_i^0 is the vapour pressure of the species in its standard, pure form and x_i is the mole fraction of the species in the alloy. The mole fraction adjusted vapour pressure variation with temperature is shown

for Ni, Co and Cr in Figure 4.12(a). The rate of evaporation into a vacuum is proportional to the vapour pressure and given by the Langmuir equation [139]:

$$E_i = \frac{P_i}{\sqrt{2\pi M_i RT}} \quad \text{Equation 4.5}$$

Where E_i is the number of moles of species i evaporated per m^2 per second, P_i is the vapour pressure of i in solution, M_i is the molecular weight of i and R and T are the gas constant and temperature respectively.

By combination of Equations 4.4 and 4.5 one can represent the evaporative rate of each element, within the alloy, for increasing temperature. This is shown in Figure 4.12(b) for the elements Ni, Co and Cr (adjusted for mole concentration according to Raoult's law).

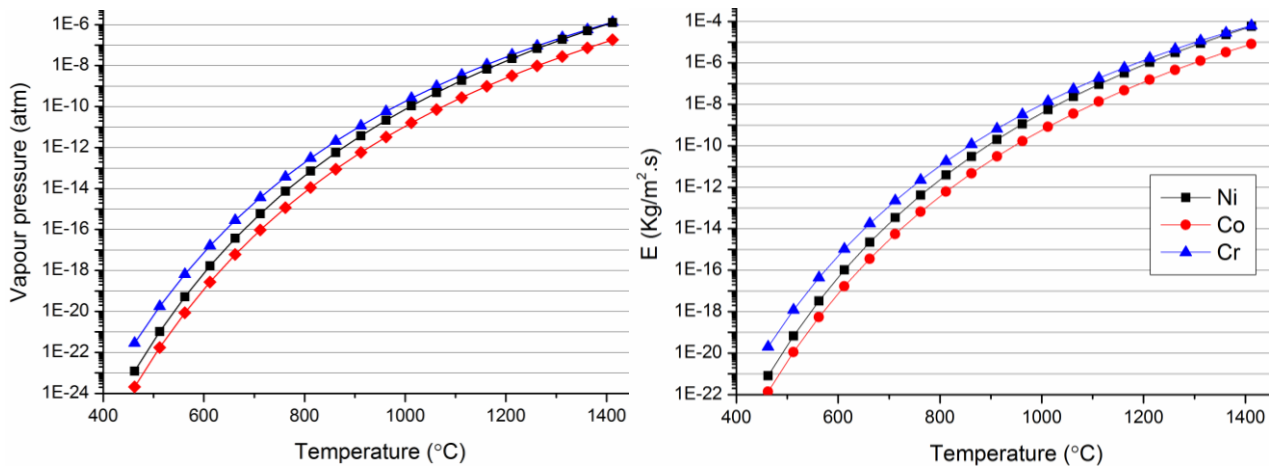


Figure 4.12(a) Vapour pressure vs. temperature plots for Ni, Co and Cr (b) Evaporative rate from the sample surface into vacuum using the Langmuir equation

From this figure it can be concluded that, below $\sim 800^\circ\text{C}$, the evaporative losses for Cr are at least one order of magnitude greater than those for Ni and Co at the same temperature. Above 800°C the vapour pressures, and associated evaporative losses, for Ni and Cr converge, becoming identical at $\sim 1400^\circ\text{C}$, however both remain larger than Co by one order of magnitude.

It is pertinent to this discussion that since the heat-treatment furnace atmosphere is not held at a perfect vacuum during solutioning, rather it is held at an Argon partial pressure of $P_{Ar} = 0.5\text{mBar}$ (10^{-4} atm), it is necessary to consider fractions of the total Langmuir loss. It is clear that Cr is the most susceptible element to evaporative mass loss, followed by Ni and finally Co is the least susceptible. This analysis shows that it is likely that significant amounts of Cr and Ni can be lost during solutioning to evaporation. It is however a first approximation to this problem and ignores other factors affecting surface mass loss such as oxidation and long-range diffusion within the alloy which is to be covered in greater detail in Chapter 5.

Evaporation of Cr and Ni from the surface of the solutioning test-bar would result in the necessary reduction in the Ni/Al ratio required to form the observed γ' surface layer, however at solutioning temperatures (1312°C in the case of CMSX-4); $\frac{T}{T_M} > 0.75$, volume diffusion is also predominant and must be considered as a competing factor to surface evaporation, acting to replenish the material lost to vaporisation.

As seen in Figure 4.7 the γ' surface layer is polycrystalline and not of the same orientation as the grain/substrate below it. It is also observed that, where they exist, the γ' surface layer grows into and consumes the RX γ grains. Where there are no RX γ grains the γ' surface layer grows into the substrate from the free-surface. This implies that the RX γ grains must form prior to the formation of the γ' surface layer and leaves the following question. If the RX γ grains have grown in a classical RX sense (due to the relief of plastic deformation from grit blasting) then these newly formed RX grains will subsequently be stress-free. What therefore is the driving force for the subsequent

growth of the polycrystalline γ' surface layer within them? This will be answered in the following sections which discuss the formation of the complete surface instability (both γ' surface layer and RX γ grains). Each stage will be discussed following the sequence in which they form during solution heat-treatment.

4.4.2 Discontinuous Cellular Recrystallization during Ramp-Up

The first stage to be discussed occurs during the initial ramp-up and pre-solutioning holds before the final solutioning hold is reached, typically lasting ~12 hours. During this period, prior to dissolution of the γ' phase, cellular recrystallization is seen to occur at the surface of highly-strained samples. Cellular recrystallization is a discontinuous precipitation process that occurs at and away from grain-boundaries in a super-saturated solid-solution and is a well-known phenomenon in Nickel-based superalloys that have seen large amounts of cold work imparted to their surface prior to solution heat-treatment [80]. Occurring at $T < \gamma'_{\text{solvus}}$ it is characterised by the migration of a grain-boundary into the strained matrix with a corresponding dissolution of γ' precipitates at the grain-boundary followed by the discontinuous re-precipitation of larger, blocky γ' precipitates and TCP phases, in the newly formed grain. It is therefore a grain-boundary diffusion controlled process, with the growth of the new γ' precipitates fed by solute from other dissolved γ' precipitates ahead of the grain-boundary [79]. The driving forces of this process are complex but elimination of internal strain energy (created by cold-work) is the major driving force for cellular RX, however super-saturation and grain-boundary diffusion are also contributing factors [25][140]. The movement of the advancing cellular RX grain-boundary is significantly retarded by the presence of coherent γ' precipitates in the strained matrix which must

be taken into solution (rather than the advancing boundary shearing the precipitates, which is less energetically favourable) before the boundary can progress further. This makes the growth kinetics of cellular RX significantly slower than for classical RX above the γ' solvus.

In single-crystal superalloys nucleation of cellular RX typically occurs at the energetically favourable free-surface, since there are no existing high-angled grain-boundaries to act as preferential nucleation sites. The free-surface also corresponds to the highest plastically deformed region due to cold-work; therefore the driving force for formation is highest. The moving grain-boundary is a high-angled grain-boundary that is highly disordered so therefore has a much higher local solubility and diffusivity associated with it, compared to the surrounding matrices. This allows the moving grain-boundary to become super-saturated in solute from the dissolved γ' ahead of it. The super-saturation of solute subsequently leads to decomposition of the single-phase behind the grain-boundary, resulting in the formation of γ lamellae within a γ' matrix. The γ lamellae form radially and perpendicular to the grain-boundary and are homogeneously distributed, branching occurs in order to maintain spacing between γ lamellae [140][141]. In the case of the latest generation Nickel-based superalloys (e.g. CMSX-4/10N) the fraction of TCP forming refractory elements W and Re is significant. Subsequently, during the cellular RX process, these elements preferentially form coarse TCP plates within the new RX grain governed by the equilibrium composition and their insolubility within the γ' matrix. It has been observed that these TCP plates constitute the Re/W-rich orthorhombic *P*-phase [142].

Although cellular RX has not been directly observed in these experiments it has been observed by D'Souza [143] in similar experiments on interrupted solutioning of CMSX-10N test-bars at 1288°C, the composition of which is similar to CMSX-4 (differing by a higher mole-fraction of refractory elements). It can be confidently concluded therefore that cellular RX would form during the ramp-up stages of the solutioning of CMSX-4 since all the necessary factors are present, i.e. highly strained surface and a composition that is susceptible to super-saturation and chemical instability. Compared to classical RX, the formation of cellular RX grains requires a significantly higher amount of cold work prior to solutioning [141]. This is easily the case of the test-bars analysed in this Chapter since they were aggressively grit blasted prior to solutioning however, in the case of production turbine blades, the surface strains are likely to be much lower since they are not grit-blast (the only imparted strain arising from interaction with the mould/core during casting and knock-off) and therefore the occurrence of cellular RX on ramp-up is unlikely.

4.4.3 Classical Strain-Induced Recrystallization

Classical recrystallization is the process by which stored internal strain-energy is relieved at high-temperatures by thermally activated dislocation movement, resulting in the production of new, virtually strain-free grains, of different orientation to the parent matrix from which they formed [81]. This process differs from cellular RX in that (a) it is purely driven by strain relief and (b) it does not involve super-saturation or discontinuous precipitation of new phases. Classical RX occurs most rapidly at temperatures above the γ' solvus, where the retardation effect of precipitate pinning is absent, and therefore the completion of RX is usually rapid (completed within

60mins) [80][144]. Due to the effect of grain-boundary pinning caused by γ' precipitates, the formation of RX grains initially starts in the dendrite cores where the finer γ' dissolves faster than the coarser γ' and γ/γ' eutectic within the inter-dendritic regions. As these are subsequently taken into solution, the RX grain-boundaries coalesce at the same final depth into the substrate where all the plastically deformed material is consumed (Figure 4.13) [80][81][145].

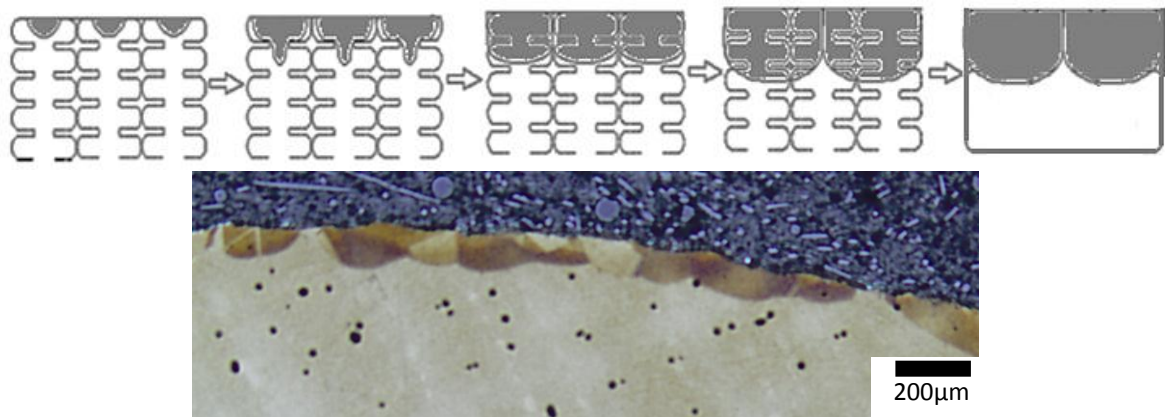


Figure 4.13(a) Schematic of the classical recrystallization process and final solutioned structure (adapted from [145]) (b) OM of the final solutioned surface with RX grains grown into the substrate

Bürgel *et al* [141] investigated the recrystallization behaviour of several SX Nickel-based superalloys and showed that the first new RX grain formed after only 1% plastic strain whilst plastic strains between 1-2% resulted in full recrystallization at the surface. This compares to the estimated strains of 2-3% imposed on the components surface due to interactions with the mould and core during casting. It was also shown that, in the area of RX nucleation, the γ' must be dissolved and that a free-surface must be available in order to overcome the high activation energy barrier (RX within dendrite cores is not observed so a free-surface is a definite requirement for RX).

In the case of the experiments in this Chapter, the grit-blasting of the as-cast surface imparts significant plastic deformation into the near-surface and this is evident by the

formation of classical RX γ grains during solutioning (Figure 4.8). The RX γ grains observed after solutioning are directly related to the cellular RX grains, formed during ramp-up, since it is these cellular RX grains that transform to pure γ phase upon $T > \gamma'_{\text{solvus}}$.

The discontinuously precipitated cellular RX grains, upon exceeding the γ'_{solvus} temperature, transform back to the stable equilibrium γ phase by solutioning the γ' and TCP phases and redistributing this solute via bulk diffusion. It is the remaining strain in the near-surface region (that was not consumed by the prior cellular RX) that is the driving force for the continued growth of the RX γ grains into the substrate. The RX γ grains subsequently precipitate the fine, cuboidal γ' phase during cooling, in an identical way to the rest of the substrate.

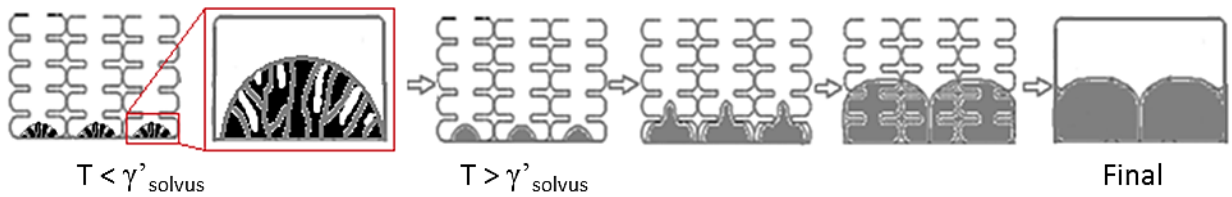


Figure 4.14 Schematic diagram showing sequence of cellular RX grain transformation to classical RX and its subsequent growth into the substrate during solutioning (γ' = black, γ = grey and TCPs = white)

4.4.4 Diffusion-Induced Recrystallization of the γ' Surface Layer

The formation of the larger, recrystallized γ grains has so far been discussed and is comprised of two stages, the initial formation of smaller cellular RX grains and subsequent formation and growth of the larger classical RX grains. These are however the product of plastic deformation imparted on the surface of the as-cast test-bars by grit blasting, and are therefore a well-known and explained surface defect within the casting industry. The subsequent formation of the smaller γ' surface layer is however more interesting in the context of heat-treatment since this has not been previously explained. Since this layer is seen to form within the RX γ grains (where they exist),

plastic-deformation cannot account for the driving-force of their growth since the RX grains are virtually strain-free by definition. Instead it seems likely that chemical potential, caused by a gradient in composition, is the main driving-force behind the nucleation and growth of the γ' surface layer.

As discussed already, there is competing elemental vaporisation and volume diffusion occurring in the near-surface region during solution heat-treatment, however it is important to note that these will only occur during solutioning since (a) the vapour pressures for Ni, Co and Cr are an order of magnitude lower at 1200°C compared to solutioning at 1312°C, implying the driving-force for vaporisation is significantly retarded at lower temperatures and (b) volume diffusion is temperature dependant and therefore only significant at higher temperatures. The combination of these two factors during solutioning provides a significant degree of solute diffusion and therefore the chemical driving-force needed for the nucleation and growth of the γ' surface layer via a diffusion-induced recrystallization (DIR) process.

DIR, and the related process of diffusion-induced grain-boundary migration (DIGBM), are solute diffusion controlled phenomena which leave an area of discontinuously different composition behind a moving grain-boundary caused by increased diffusion of solute along the grain-boundary compared to the grain interior [146]. The description of DIR/DIGBM is relatively simple and well understood however, the explanation of the driving-force(s) responsible for the grain-boundary motion (and in the case of DIR, the nucleation of new grains) is complex and a constant area of debate with conflicting proposals and evidence citing the effects of chemical potential (free-

energy of mixing) [146][147], coherency strain ahead of the moving grain-boundary [148][149] and grain-boundary Kirkendall effects [150][151] for example. The difference between DIGBM and DIR is that in the former case, existing grain-boundaries migrate due to solute diffusion along the boundaries leaving regions of different composition behind them whereas in the latter case, the process starts with the nucleation of new grains, of different composition, that subsequently grow in the same way as DIGBM. It has been shown that the nucleation of these new DIR grains can occur in poly-crystals as well as at the surface of single-crystals exposed to vapour, solid or liquid solute sources [146][152][153].

A schematic diagram in Figure 4.15 shows the typical microstructure before and after DIGBM annealing. The initial grain-boundary position is shown by the dotted line and the final position, due to DIGBM, is shown as the solid line. The area between these two lines is the swept region, which is alloyed with solute diffused along the boundaries. The shape of the migrated grain-boundaries is often observed to be S-shaped, growing into both adjacent grains and often increasing the total grain-boundary area whilst prolonged annealing results in the coalescence of the segments on each side of the initial grain-boundary. The distance each grain-boundary migrates is not wholly uniform throughout all boundaries, with some progressing further than others due to the degree of misorientation. Grain-boundary diffusivity and mobility are strongly affected by misorientation, with HAGB's much more mobile than LAGB's, therefore DIGBM is also strongly dependent on the degree of misorientation between grain-boundaries [153].

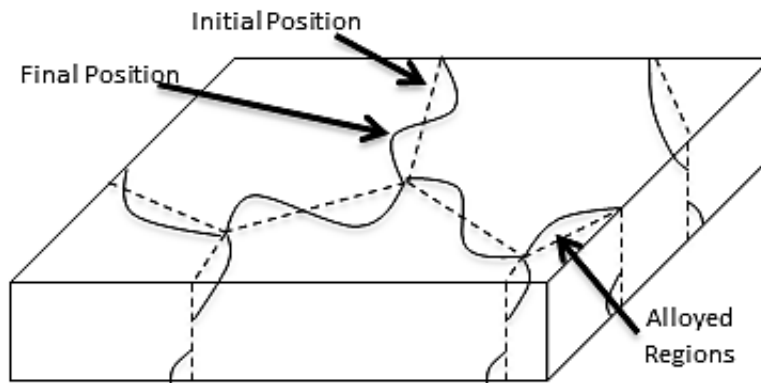


Figure 4.15 Schematic diagram of the microstructure of a polycrystalline material that has undergone DIGBM transformation. The initial grain-boundary location is shown by the dotted-line [adapted from [153]]

The effect of distance from the surface is also shown in Figure 4.15, as distance from the surface increases the lateral growth velocity reduces, before increasing again as the opposite face of the sample is approached. This was shown to be a result of the reduced concentration of solute with distance from the surface, thus the chemical potential for DIGBM is reduced and the grain-boundary lags behind below a certain depth from the surface [148]. In the case of the nucleation of new DIR grains, the lateral growth is also much quicker than the growth into the matrix, with grains rapidly impinging on each other before continued growth perpendicular to the surface.

As mentioned already, the explanations of the driving-force behind DIGBM and DIR is a controversial one but it is key to understanding the process and how it relates to the formation of the γ' surface layer seen after solutioning in this Chapter. In recent years there has been a general consensus that the main driving-force for DIGBM/DIR is the coupling of chemical potential with coherency stress energy during diffusion along grain-boundaries however, grain-boundary misorientation is also an influencing factor since it affects the diffusivity and mobility of the boundary, both of which effect solute diffusion [154]. Diffusional coherency strain arises due to changes in the lattice parameter with composition. As the solute diffuses along the grain-boundary due to

chemical potential, there is some lattice diffusion of the solute into the adjacent grain resulting in the creation of a stress-field within the first few atomic layers ahead of the grain-boundary and a net force pulling it forwards (Figure 4.16).

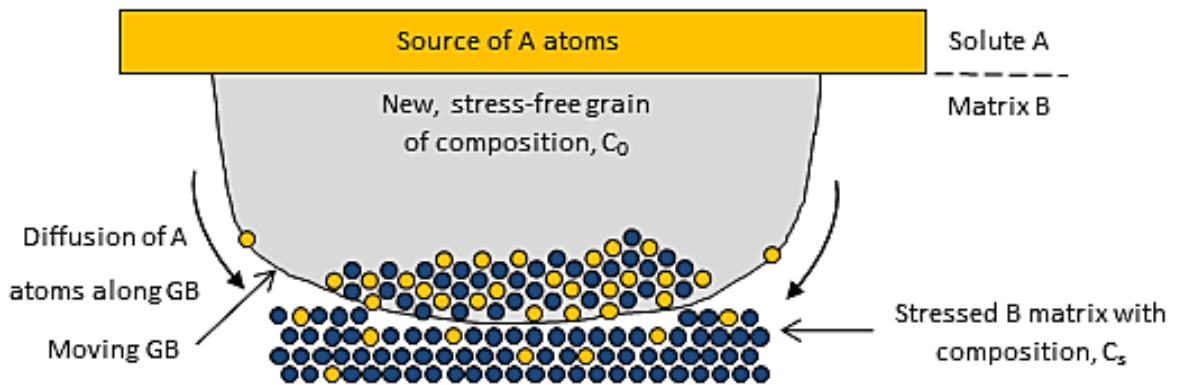


Figure 4.16 Diagram of the mechanism of DIGBM induced by grain-boundary diffusion of solute. A thin, inter-diffusion area exists ahead of the moving GB which is stressed due to size mismatch between A & B atoms (adapted from [155])

It has been shown [156][157][158] that the nucleation of DIR grains at the surface of a SX sample exposed to a suitable solute source occurs in a similar manner to the production of new grains during plastic deformation induced classical recrystallization, except that it is misfit strain from solute diffusion rather than cold-work that is the driving-force. The diffusion of solute creates lattice strain and therefore misfit dislocations which, given sufficient annealing temperature and time, rearrange to form new grain boundaries. The work by den Broeder [157] showed that the formation of DIR grains was only possible at higher temperatures and solute concentrations than for pure DIGBM, indicating that these are a pre-requisite in order to overcome the high nucleation energy associated with the formation of new grain-boundaries. Clearly therefore, in the case of the results presented in this Chapter, the solutioning at 1312°C for 8 hours is sufficiently hot/long enough to allow the nucleation of DIR grains.

It was initially believed that, since DIGBM is a grain-boundary diffusion controlled phenomenon, volume diffusion must be disabled in order for DIGBM/DIR to occur, however this has been shown not to be the case, in fact DIGBM has been observed in examples where volume diffusion is significant [159][160][161] and in fact the coherency strain model requires volume diffusion to be active in order to create a strained layer ahead of the grain-boundary. Clearly, at the solutioning temperatures involved in the heat-treatment of Nickel-based superalloys, the action of volume diffusion is enhanced (since this is the purpose of solutioning). Volume diffusion also acts to replenish the lost material evaporating from the surface, if the rate of mass loss from the surface was equal to that replenished via volume diffusion then it could be assumed that little or no chemical potential existed, and therefore DIR would not occur. Clearly this is not the case, therefore the mass loss due to evaporation must be greater than the mass replenished by volume diffusion, in order to account for the creation of the γ' surface layer.

The coherency strain model that drives DIGBM does not however suitably explain the driving-force for the formation of the γ' grains in the case of chemical potential arising from material evaporating from the surface. This is because, during evaporation, the diffusion of material is effectively occurring in reverse, removing material via grain-boundaries rather than supplying it. There is no reason therefore for solute atoms to be placed ahead of the migrating grain-boundary rather they should be going in the opposite direction, towards the surface. Instead, it is the difference in the rates of diffusion of elements that induces stress within the matrix [162][163][164] and provides the driving-force for the growth of the γ' grains by the Kirkendall effect. The

Kirkendall effect arises due to the non-reciprocal diffusion of elements and compensating diffusion of vacancies within the matrix in the presence of a chemical potential and has been previously advocated as an additional way to explain the driving-force behind DIGBM [165]. During substitutional diffusion, vacancies preferentially exchange with the faster diffusing atoms, resulting in a net vacancy flux from the slower diffusing atoms side to the faster (and the possible creation of porosity if the vacancies coalesce, see Figure 4.17(a)). They are also injected to, or eliminated from, the solid at vacancy sources and sinks in order to maintain their thermodynamic equilibrium mole fraction. Grain-boundaries and free-surfaces can act as both sources and sinks for vacancies during diffusion, with the region that is super-saturated in vacancies being compressed, due to vacancy elimination and the associated reduction in volume, whilst the region that is depleted of vacancies experiences tensile stresses [166]. In a constrained sample, i.e. a large bulk specimen, these stresses can be high enough to create dislocations and initiate recrystallization.

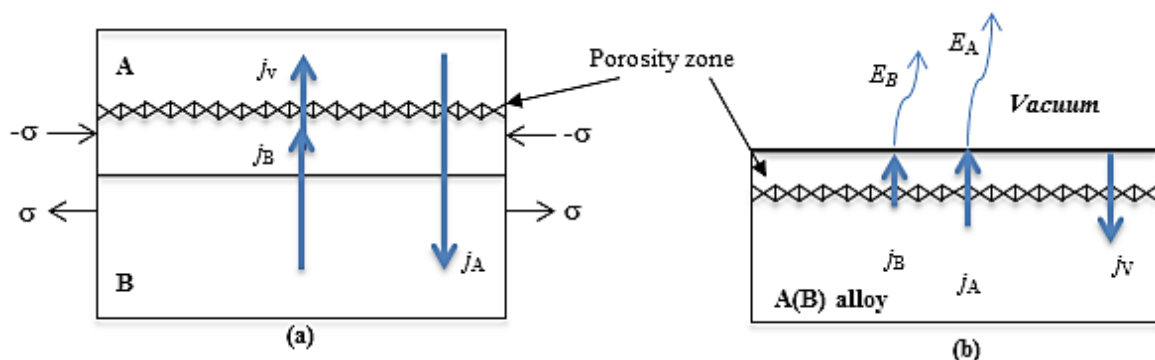


Figure 4.17 (a) Schematic representation of the Kirkendall effect. The diffusion coefficient of metal A is greater than for metal B resulting in the net flux of vacancies, j_v , towards metal A and the production of a porosity zone [adapted from [162]] (b) Representation of the diffusion and evaporation fluxes from the surface of an A(B) alloy in the presence of a vacuum. Both the diffusion coefficient and vapour pressure of A is greater than that for B

For the results presented in this Chapter, this mechanism of vacancy and atomic fluxes is made more complicated by the fact that it is not a simple binary diffusion-couple, but rather there is a net flux of atoms both out from the material surface (evaporation)

and towards the surface (volume diffusion), as well as an associated flux of vacancies into the substrate. This is represented in Figure 4.17(b) and is similar to the way in which inter-diffusion occurs between the bond-coat and thermally-grown oxide on Nickel-based superalloys, and the associated stresses that result [167][168]. The SEM analysis of the upper part of the γ' surface layer (Figure 4.6) has identified the existence of Kirkendall-like porosity. Clearly for the Nickel-based superalloys alloy, the large number of alloying elements, their varying diffusion coefficients and vapour pressures makes this scenario significantly more complex than a simple binary system. It is the stresses induced in the surface region during non-reciprocal diffusion, arising from competing surface evaporation and volume diffusion, which creates the driving-force for the recrystallization and growth of the γ' surface layer. At the same time it is the net loss of γ stabilising elements due to surface evaporation that results in the phase transformation to γ' and creates the chemical potential for diffusion, and hence recrystallization and growth, to occur.

Finally, there is also the competing process of oxidation to consider. During solutioning there is the selective oxidation of Al to form a surface layer of Al_2O_3 , which acts to deplete Al from the surface and prevent the formation of the γ' layer. However the growth kinetics of Al_2O_3 is very slow (made slower by the reduced P_{O_2} within the heat-treatment furnace) therefore there is an initial period where surface evaporation can occur at ease, with no oxide to act as a barrier. The results from the pre-oxidised sample showed that, by growing a dense barrier layer of Al_2O_3 prior to solutioning, the formation of the γ' layer can be precluded. This also shows that it is the evaporation of

material from the test-bar surface that is the root-cause of the formation of the polycrystalline γ' surface layer.

4.4.5 Discontinuous Precipitation during Subsequent Ageing

It is observed from the solutioned-only samples (Figure 4.8) that the characteristic discontinuous precipitation (DP) reaction between the γ RX grains, the γ' surface grains and the substrate is a product of the ageing heat-treatment. This is because discontinuous precipitation is a grain-boundary diffusion controlled process and therefore occurs at lower temperatures, where volume diffusion is either locked out or sufficiently retarded. The driving-force for DP reactions is typically solute super-saturation within the grain-boundary and therefore it can be concluded that the grain-boundaries of the γ RX grains as well as the γ' surface layer must be super-saturated in the quenched condition after solutioning. This adds further evidence to the arguments made in Section 4.4.4 where non-reciprocal diffusion during solutioning was the root-cause of the recrystallization and growth of the γ' surface layer. At the solutioning temperatures, volume diffusion is prevalent however, grain-boundary diffusion will also act as short-circuit pathways, enhancing the diffusion of material to the surface. When the test-bars are quenched at the end of solutioning, the solute is frozen into the grain-boundary and during subsequent ageing heat-treatments, results in the DP reaction. The DP reaction is a transformation of the equilibrium $\gamma_{\text{matrix}} + \gamma'$ phases into a $\gamma'_{\text{matrix}} + \gamma'_{\text{lamellae}} + \text{TCPs}$ and suggests that the grain-boundaries are super-saturated in γ' forming elements during solutioning. This is a logical conclusion since the volume diffusion coefficient of Al in Ni is the highest of all the alloying elements and therefore the grain-boundary diffusion coefficient would also be high.

4.5 Conclusions

Because the surface scale oxides are thin and porous they are non-protective and prone to spallation. During subsequent solution heat-treatment, the scaled surface of the casting is fully exposed to the furnace atmosphere which is held at vacuum on ramp-up and at low P_{O_2} during solutioning. This situation has been represented in this Chapter by the use of grit blasted test-bars, mimicking the exposed scale surface. During ramp-up, the plastic deformation that was imparted to the surface during grit-blasting causes recrystallization to occur, initially via cellular RX and upon exceeding the γ' solidus temperature, via classical RX. During this time oxidation of the surface will be extremely slow due to the high-vacuum (thus low P_{O_2}) level used during ramp-up. Upon reaching solutioning temperature and due to the relatively high vapour pressures of key γ phase stabilisers, Ni, Co and Cr, the surface region is destabilised resulting in the transformation of the equilibrium γ phase to the non-equilibrium γ' phase and the associated precipitation of TCPs. The nucleation and growth of the γ' surface grains is driven by the competing vaporisation of material and volume/grain-boundary diffusion giving rise to non-reciprocal diffusion and induced stresses due to the Kirkendall effect. It is this transformation of the surface to the γ' phase which constitutes the Surface Melt Blister defect.

At the same time as evaporation is occurring, selective oxidation of Al will occur, but at a significantly slower rate due to the low P_{O_2} , making the formation of a protective barrier against vaporisation a slow process. The outcomes of this investigation are that the current heat-treatment thinking is incomplete and that the effects of evaporation

during solutioning must be considered, in parallel to the effects of oxidation. The use of high vacuum and low- P_{O_2} heat-treatment atmospheres is clearly detrimental to the surface microstructure, in the same way as is excessive oxidation. The results from the pre-oxidation of the casting indicate that the prevention of evaporation, and therefore the formation of the γ' surface layer/surface melt blister, is achievable by the relatively easy method of pre-oxidising the as-cast component, in air, prior to solutioning and that this does not result in any discernible reduction in the volume fraction of the strengthening γ' phase after solutioning.

However, the degree of evaporation from the surface during solutioning has yet to be investigated in great detail. The microstructural evidence presented in this Chapter shows that evaporation is occurring and that it favours the formation of the γ' phase, therefore elements such as Ni, Co and Cr must be lost via evaporation to a greater extent than Al. It is the aim of the next Chapter to investigate the surface evaporation in more detail, including the resultant variations in thermodynamic phase stability and the analysis of condensate using cold-trap type experiments.

Chapter 5. Elemental Evaporation from the Scaled Casting

Surface during Solution Heat-Treatment

5.1 Introduction

As has been discussed in the previous Chapters, during casting of SX Nickel-based superalloys there is oxidation of the surface in areas where mould-metal separation has occurred which is defined as the 'Scaled' areas. The Surface Scale oxide has been shown to constitute a thin, porous oxide of predominantly NiO whilst the rest of the blade surface (defined as 'Unscaled') is covered in a thicker, dense layer of Al₂O₃, which is the product of a mould-metal reaction. These two types of oxides remain on the surface of the casting and during subsequent solution heat-treatment it is the scaled areas that exhibit the surface melting defect known as 'Melt Blisters'. In Chapter 4 the link between the scaled areas porous and unprotective NiO surface layer and the evaporative loss of γ phase stabilisers (namely Ni, Cr and Co) was shown to be the cause of the formation of the melt blister defect and its associated microstructural instabilities. In that Chapter it was assumed that, due to their relatively high vapour pressures into vacuum, it was the evaporation of only Ni, Cr and Co that was of concern, since it is observed that the surface transforms into the γ' phase. However, it must be noted that Al (the key γ' phase former) is characterised as also having a very high vapour pressure and therefore this must also be considered. This Chapter therefore focuses on examining the elemental evaporation in greater detail by using thermodynamic phase modelling software (Thermo-Calc) to examine the phase transformations that occur in response to key composition changes, brought about by

surface evaporation. Additionally, an experiment to trap and analyse the evaporated material, via a cold-trap type experiment, will also be discussed as this provides the key evidence that elemental surface evaporation is occurring during solution heat-treatment.

Evaporation (or sublimation) during heat-treatment of Nickel-based superalloys is a little known phenomenon and thus does not feature in the literature, however the effects of evaporation on oxidation resistance and growth kinetics has been studied extensively, most notably for the evaporation of Cr and its oxides during high-temperature operation. The decomposition of Cr_2O_3 to CrO_3 (which then evaporates) at high-temperatures, oxygen partial-pressures and gas flows has put a limit on the suitability of Cr_2O_3 protective oxide forming alloys to below 1000°C and lead to the introduction of Al_2O_3 forming superalloys for higher temperature applications [5][92][97][169][170]. In addition, the vapour pressures of pure inorganic substances (e.g. metals and their oxides) are well researched and listed in reference texts such as the following by Knacke *et al* and Alcock [126][138]. These were used extensively in this Chapter to approximate the mass loss of each element during solutioning.

5.2 Experimental Methods

As in the previous Chapters, the Nickel-based superalloy CMSX-4 was considered in this Chapter. The nominal composition in wt.% and mole fraction is given in Table 5.1.

CMSX-4	Al	Co	Cr	Ti	Mo	Ta	W	Re	Ni
wt.%	5.8	9.5	6.5	1.1	0.6	6.5	6.5	3	Bal
Mole fraction	0.13	0.1	0.08	0.01	0.004	0.02	0.02	0.01	0.63

Table 5.1 Nominal composition and mole fraction of alloying elements in the Nickel-based superalloy CMSX-4

5.2.1 Investment Casting and Heat-Treatment

For this study, identical cylindrical test-bars (10mm OD x 60mm H) from the previous Chapter were considered. These were cast using the methods described in Chapter 3 at the Precision Casting Facility, Rolls-Royce plc in Derby. As with the previous Chapter, after casting the test-bars were grit blasted with Al_2O_3 media to remove all surface oxides (both surface scale and the unscaled Al_2O_3).

These were subsequently solution heat-treated by standard industrial practices within the heat-treatment furnace at the University of Birmingham's School of Metallurgy and Materials (Figure 5.1(a)). The test-bars were positioned inside alumina crucibles in order to trap and condense the evaporated material on the surface of the crucible (Figure 5.1(b)). After ramping, the samples were solutioned at 1305°C for 8 hours and then rapid gas fan quenched using Argon gas. The solutioning temperature was reduced from the standard 1312°C to 1305°C due to concerns of over-heating the sample and incipiently melting the surface. During initial ramp up the furnace is held at a vacuum of 10^{-7} atm, beyond 1140°C the vacuum diffusion pump is switched off and Ar gas is continuously bled in with a partial pressure of $P_{\text{Ar}} = 10^{-4}$ atm.

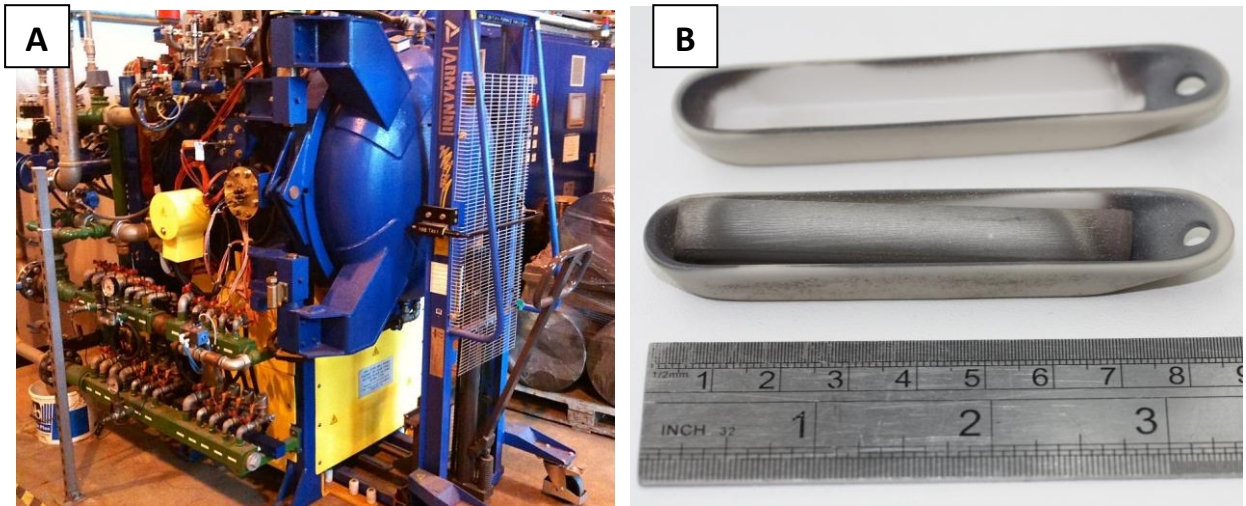


Figure 5.1 (a) University of Birmingham's solution heat-treatment furnace (b) solutioned test-bar inside the alumina crucibles used to trap the evaporated material on its interior surface, these were subsequently analysed

5.2.2 Scanning Electron Microscopy (SEM) and Focused Ion-Beam (FIB)

The as-cast test-bar surfaces were initially analysed with an Olympus BX51 optical microscope at various magnifications to ensure that the surface was free of any eutectic or oxides and that the γ' surface layer occurs during solutioning and not casting, this surface is shown in Figure 4.3. Transverse aerofoil cross-sections were cut using a diamond tipped rotary bench saw before being mounted in conducting Bakelite resin and progressively polished with grit/SiC papers followed by a final $1/4\mu\text{m}$ diamond polish for metallographic examination. Where necessary, samples were etched with a Nimonic etchant of 50ml HNO_3 , 200ml HCl , 12.5g CuCl_2 and 12.5g FeCl_2 made up to 500ml with distilled water.

SEM/EDX was performed to examine the surface of the solutioned test-bar to ensure that the γ' layer had evolved. Back-scattered electron imaging (BSI) and Secondary electron imaging (SEI) were performed at a working distance (WD) of 5mm, spot size 5 and an accelerating voltage of 15-20kV.

The Dual-beam SEM/FIB at the University of Loughborough was used to conduct microstructural and compositional analyses of the alumina boat surface. This system was used due to its ability to mill trenches in the sample surface, using the ion beam, to allow the examination of the surface cross-section and, coupled with the EDX detector, to produce elemental maps of the condensate deposits.

Where an SEM uses a beam of electrons, a FIB uses a beam of ions instead. The ion source is typically liquid metal gallium, surrounding a tungsten needle pointing towards a negatively charged aperture. By applying a large electric field ($> 10^8$ V/cm) to the wetted needle tip, the formation of a Taylor's cone (of radius ~ 10 nm) is achieved, from which field emission of the ions occurs. The ions are then accelerated, collimated and focused on to the sample by a series of apertures and electrostatic lenses in a similar manner to electron microscopes [171][172]. When the Ga ion beam leaves the beam column, it impacts the sample surface and sputters off ions or secondary electrons (as well as some neutral atoms), which can be used to form an image by rastering the beam across the sample.

In addition to forming an image, the FIB can be used to mill material away from the sample. At high beam currents the Ga ion beam will sputter a larger amount of material, allowing for precise milling of the sample surface whilst the addition of halogen gases, such as Cl_2 , to the near-surface can be used to enhance the etch rate. The FIB can conversely be used to deposit metal or insulators onto the sample surface

by a combination of a suitable deposit-carrying gas and the rastered ion beam. Typically a needle is manoeuvred close to the sample ($\sim 100\text{-}200\mu\text{m}$), through which a gas such as $\text{W}(\text{CO})_6$ (for W deposition) or $\text{C}_7\text{H}_{17}\text{Pt}$ (for Pt deposition) is injected. Where the gas and the ion beam interact on the sample surface, the gas decomposes, leaving a deposit on the surface and the by-product gas which is extracted via the vacuum pump [173].

The FIB operates at a beam voltage of 20kV and nominal current of 24nA. The EDX detector used was an EDAX Apollo XL Silicon Drift Detector (SDD) operating at a voltage of 10kV, current 2.3nA and WD of 5mm. The SEI were acquired at an operating voltage of 10kV to avoid charging/damage of the sample surface.

5.2.3 Thermo-Calc Phase Calculations

The CALculation of PHase Diagrams (CALPHAD) software package Thermo-Calc was used to determine the phase evolution at the surface of the test-bar during solutioning, assuming key values of elemental loss. The first stage was to estimate the elemental losses by using vapour pressure thermodynamic data [138], Raoult's law and the Langmuir equation [139][174], however this considers evaporation into vacuum but solutioning occurs under an Ar partial pressure atmosphere so percentages of the total Langmuir loss were considered to compensate (the following notation is used to express the percentage of total Langmuir loss, $X\% \text{Langmuir}$). From the microstructural analysis in Chapter 4, it can be concluded that the γ' surface layer is $\sim 20\mu\text{m}$ thick and therefore it is assumed for this study that the evaporative losses occur only from this

volume of surface material, allowing the total mass loss of each element from this volume to be calculated.

In order to simplify the calculations only Ni, Co and Cr evaporative losses were considered. These elements were chosen due to their relatively high vapour pressures and importance for the thermodynamic stability of the γ phase, i.e for the γ' phase to evolve these elements must be depleted. Likewise, aluminium losses were not considered due to the fact that the surface region is characterised as a transformation of $\gamma \rightarrow \gamma'$ and therefore it is only through the loss of Ni, Co and Cr that this can be achieved. The refractory elements are especially not considered in these calculations since their depletion does not cause a $\gamma \rightarrow \gamma'$ transformation and they are known to be very slow diffusers.

With the mass loss of each element estimated from the Langmuir equation, the composition of the surface layer is re-calculated and this is used as the starting point for the Thermo-Calc simulations. The Nickel-based superalloy Thermo-Calc database 'NiDat v7' was used and the equilibrium phase diagram calculated, plotting temperature on the x-axis and mole fraction of each stable phase on the y-axis, for each composition considered. The compositions considered are shown in Table 5.2 based on fractional losses of the total Langmuir loss to vacuum (Note: Cr losses were held at 0.5%Langmuir, due to the high vapour losses of Cr. Any higher percentages result in a negative mass within the 20 μ m surface layer).

Compositions (wt.%)	Ni	Al	Co	Cr	Ti	Mo	Ta	W	Re
Nominal	60.5	5.8	9.5	6.5	1.1	0.6	6.5	6.5	3
NiO+Cr ₂ O ₃ Losses	60.53	5.95	9.75	5.62	1.13	0.62	6.67	6.67	3.08
20%Langmuir	50.25	9.77	6.47	3.7	1.85	1.01	10.95	10.95	5.05
15%Langmuir	54.78	8.47	7.68	3.21	1.61	0.88	9.5	9.5	4.38
10%Langmuir	58.25	7.48	8.61	2.83	1.42	0.77	8.38	8.38	3.87
8%Langmuir	59.43	7.15	8.92	2.7	1.36	0.74	8.01	8.01	3.7
5%Langmuir	61.0	6.7	9.34	2.53	1.27	0.69	7.5	7.5	3.46

Table 5.2 Calculated compositions (wt.%) within 20 μ m surface layer following Ni and Co vapour losses of varying fractions of the total Langmuir loss to vacuum. Cr is maintained at 0.5%Langmuir. The composition due to mass losses of Ni and Cr to form oxides 0.5 μ m thick are also considered

For the compositions where liquid was predicted to occur at the solutioning temperature of 1312°C, the Scheil solidification model (i.e. no diffusion in the solid and complete mixing in the liquid) was used to simulate the quench process after solutioning of that liquid, in order to predict the final phase fractions. However, since freezing eventually terminates with a limited degree of back-diffusion of solute, phase fractions were taken when the remnant liquid fraction reaches 10%. The following steps were used to combine the equilibrium and Scheil condition predicted phase fractions:

- i. Calculate the equilibrium phase fractions at 1312°C using the composition in Table 5.2. Note down the mole fraction composition of each predicted phase.
- ii. Where there is liquid predicted, the liquid composition is modelled using the Scheil condition (to simulate quenching of this liquid). The phase fractions at 10% remaining liquid are noted down and a compensating multiplication factor is applied to bring the total to 1 (i.e. ignoring the 10% remaining liquid). An additional multiplication factor is then applied to each predicted phase to account for the initial liquid phase fraction calculated in part (i).

- iii. The equilibrium model is used to calculate the phase fractions upon cooling of each of the solid phases predicted in part (i). The temperature corresponding to the 10% remaining liquid in part (ii) is used as the temperature at which these phase fractions are taken. A multiplication factor is also applied to the predicted solid phases to account for the initial solid phase fractions predicted in part (i).
- iv. The calculated final equilibrium and scheil solid phases are all combined to give the quenched phase fractions (which total 100%).

For comparison with the vapour loss simulations, the mass losses of Ni and Cr due to the formation of their oxides (NiO and Cr₂O₃) during solutioning were also considered. This was achieved by calculating the masses of Ni and Cr within a NiO/Cr₂O₃ dual-oxide each of 0.5µm thickness (this is the thickness of the surface scale layer seen in Chapter 3) and re-calculating the composition within the 20µm surface layer using the same methodology as the vapour losses. Only Ni and Cr losses were considered in this scenario, all other elements remain as nominal composition. This composition is also shown in Table 5.2.

5.3 Results

5.3.1 SEM Analysis of the Solutioned Test-Bar Surface

The heat-treated test-bar surface was analysed to ensure that the γ' layer had evolved and to investigate the silvery deposits identified after solutioning at each end of the test-bar, adjacent to similar silvery deposits found on the end of the Al₂O₃ crucible (especially around the hole seen in Figure 5.2).

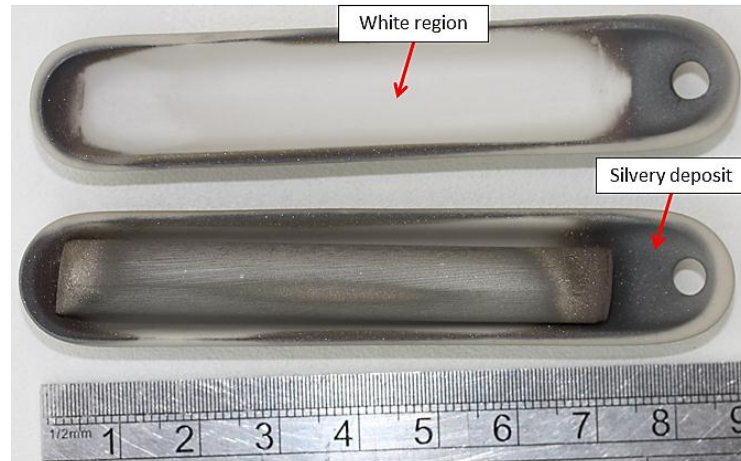


Figure 5.2 Image of the heat-treated test-bar sat inside the top half of the Al_2O_3 crucible. Around the crucible edges are silvery deposits whilst the rest of the crucible remains white

Centre-sections of the test-bar were cut and polished for OM examination (Figure 5.3) and these show that the γ' surface layer ($\sim 10\mu\text{m}$ thick) has evolved as expected during the solution heat-treatment, as have the γ RX grains (due to the grit-blasting).

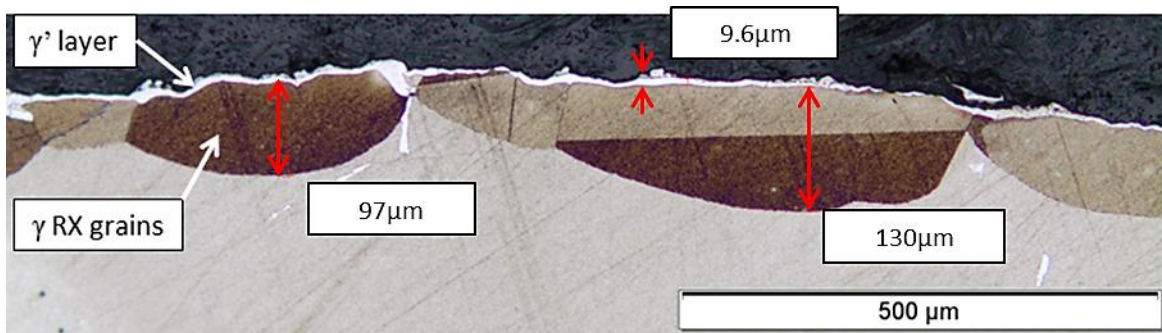


Figure 5.3 OM of the central portion of the solutioned test-bar surface. The evolution of the γ' surface layer is evident, as are the γ RX grains below

The end-sections of the test-bar were cut, polished and examined in a similar manner and the surface microstructure is drastically different. There is evidence of metallic deposits ($\sim 100\mu\text{m}$ thick) on the top of the test-bar surface and significant microstructural instability to a depth of $\sim 100\mu\text{m}$ below the original surface as a result of these deposits.

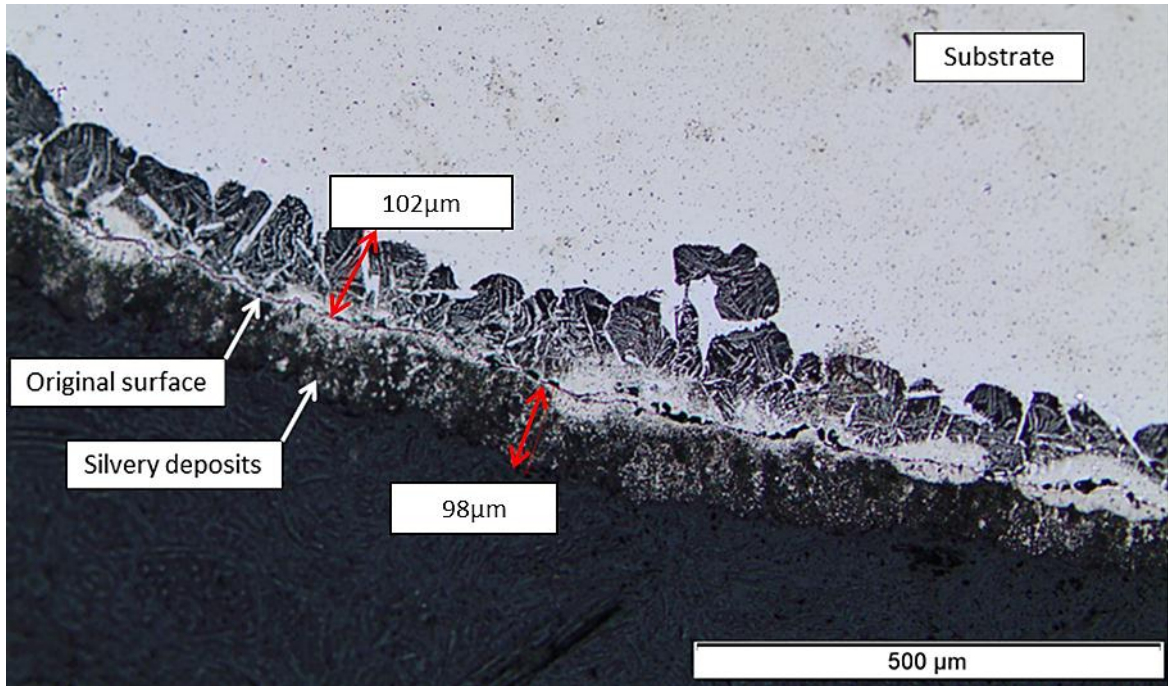


Figure 5.4 OM of the end of the solutioned test-bar. Cross-section shows the silvery deposits seen in Figure 5.2

SEM was subsequently used to investigate these surfaces in greater detail. The central portion of the solutioned test-bar surface is shown in Figure 5.5 and shows that this region is identical in nature to the γ' surface layer seen in the previous Chapter. It's thickness ranges from 10-20 μm and there are occasional, distinct particles of W,Re rich TCP phases, nucleating at the border with the γ RX grains below and growing into the γ' surface layer.

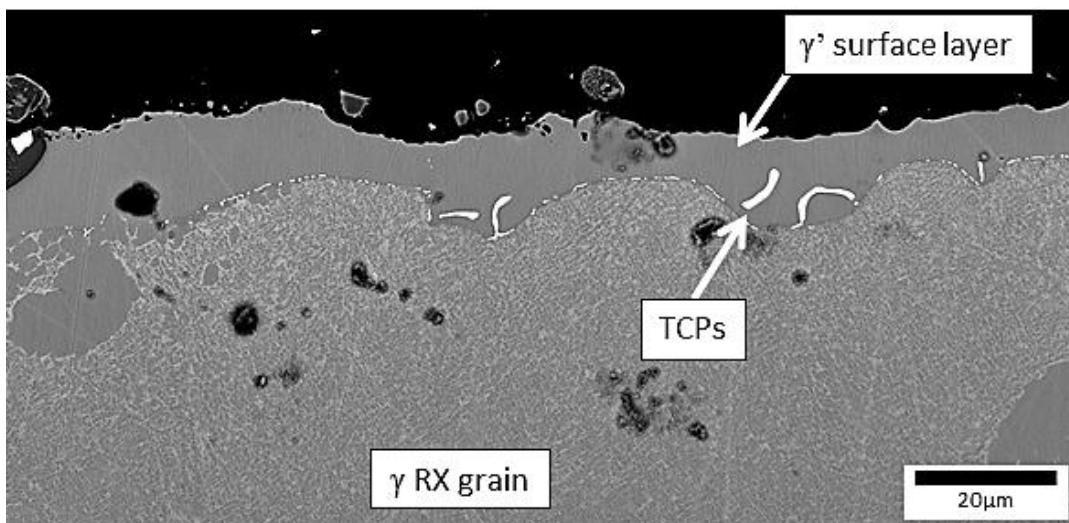


Figure 5.5 BSI of the central portion of the solutioned test-bar surface showing the typical γ' surface layer + TCPs and γ RX grains below

The silvery surface deposits found at the end of the test-bar were investigated using SEI and BSI coupled with EDX. The deposits form a continuous, thick $\sim 100\mu\text{m}$ layer around the perimeter of most of the test-bar as shown in Figure 5.6. The dark area above the deposit is found to be Al_2O_3 and can be seen in Figure 5.7 in black, growing between deposits.

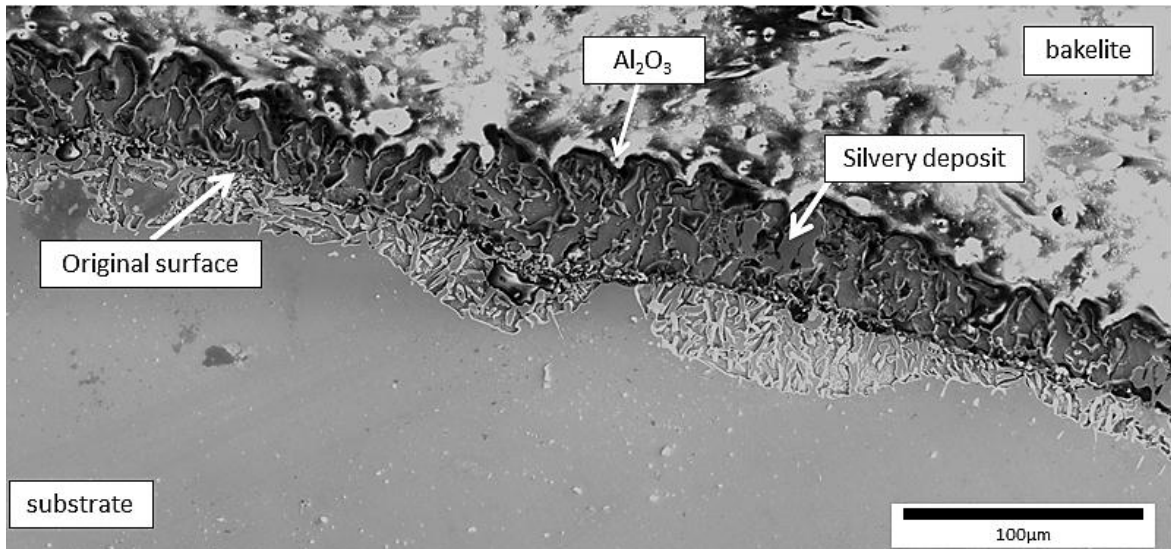


Figure 5.6 SEI of the end of the test-bar. Cross-section showing the silvery deposits above the original surface

However, in some areas the deposits are discontinuous and slightly thinner ($\sim 50\mu\text{m}$) and a γ' surface layer is evident below; this is shown in Figure 5.7 using Back-scatter to highlight the γ' layer. Using Backscattered imaging also makes the TCP precipitates stand-out (white) within this region. EDX spectra were collected from the upper silvery deposit and the bulk in Figure 5.7 for comparison and this is shown in Figure 5.8. This shows that the deposit is metallic in nature, with substantially higher amounts of Ni and Al than the bulk, and the lack of an oxygen peak confirms that this is not an oxide.

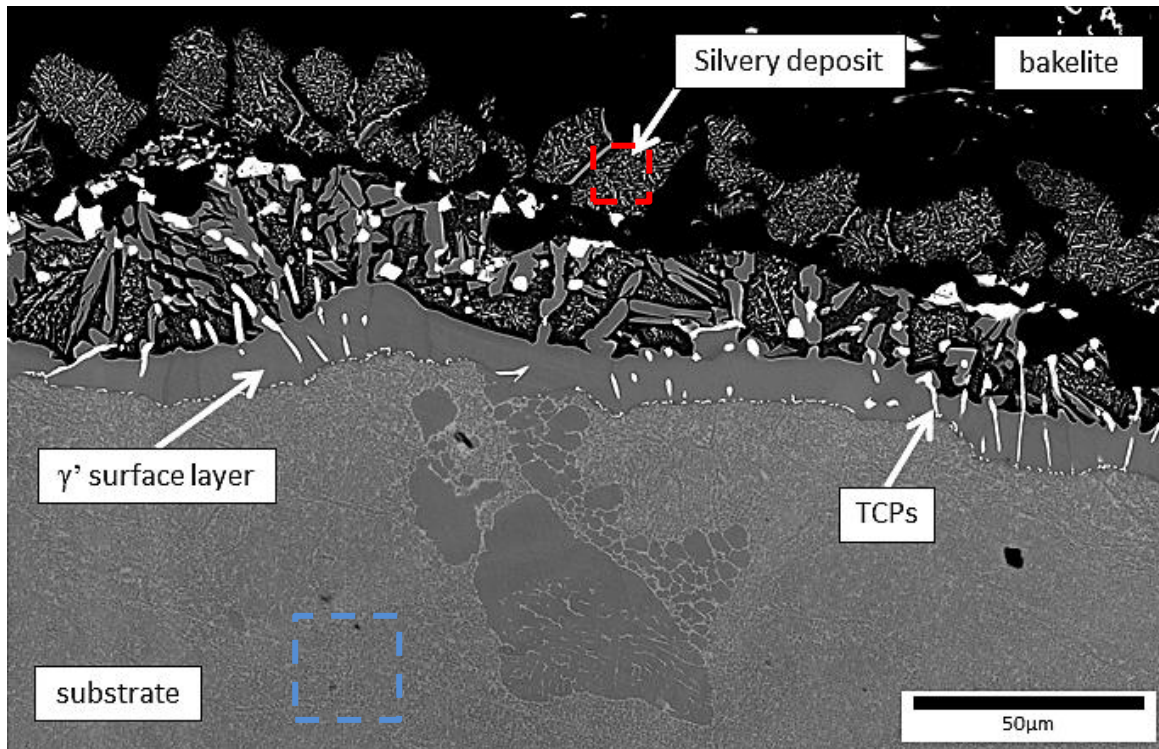


Figure 5.7 BSI of the end of the test-bar. Cross-section showing the silvery deposits above the γ' surface layer. EDX spectrum locals are highlighted by dotted line for Figure 5.8

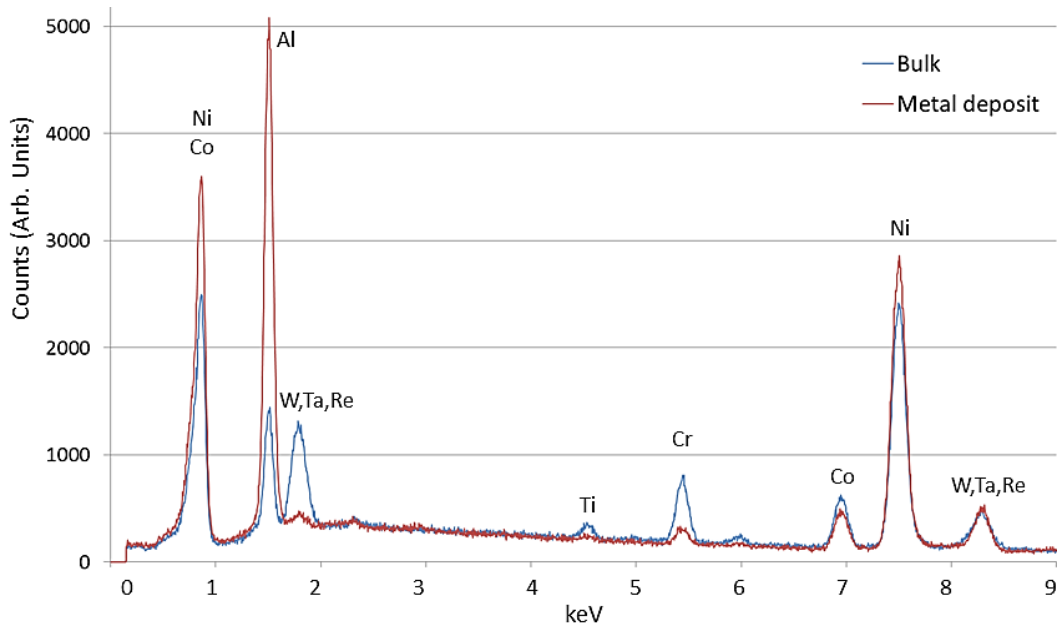


Figure 5.8 EDX spectra collected at 15kV from the upper silvery deposit and compared to the bulk

5.3.2 FIB/SEM Analysis of the Solutioned Alumina Crucible Surface

The heat-treated Al_2O_3 crucible is shown in Figure 5.2 with grey/silvery deposits evident over the surfaces near the hole and edges on both the top and bottom halves of the crucible. This is in contrast to the original crucible surfaces which are pure white.

The top and base of the crucibles have remained white throughout the heat-treatment. These two areas (grey and white) were analysed using the dual-beam FIB/SEM in order to look at the cross-section of each areas surface microstructure. Figure 5.9(a) is an SEI of the white area of the crucible and the surface is relatively smooth compared to the grey area shown in Figure 5.9(b). A close-up of the grey area is shown in Figure 5.10 and details the blocky, finer-grained nature of the surface microstructure. This equiaxed, polyhedral microstructure is characteristic of the high-temperature vapour deposition of metals [175].

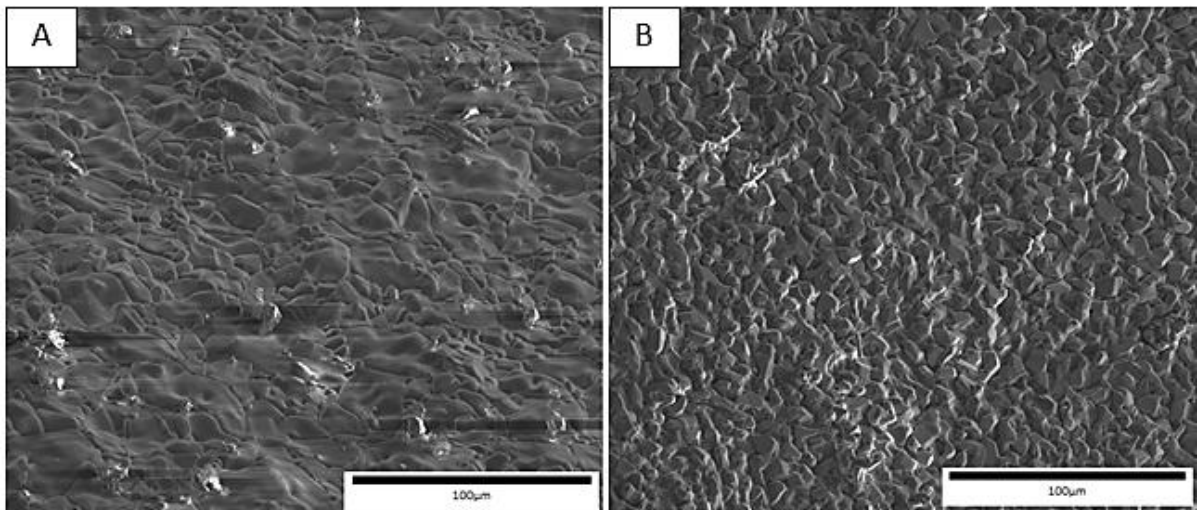


Figure 5.9 SEI of the heat-treated crucible surface (a) white area and (b) grey area

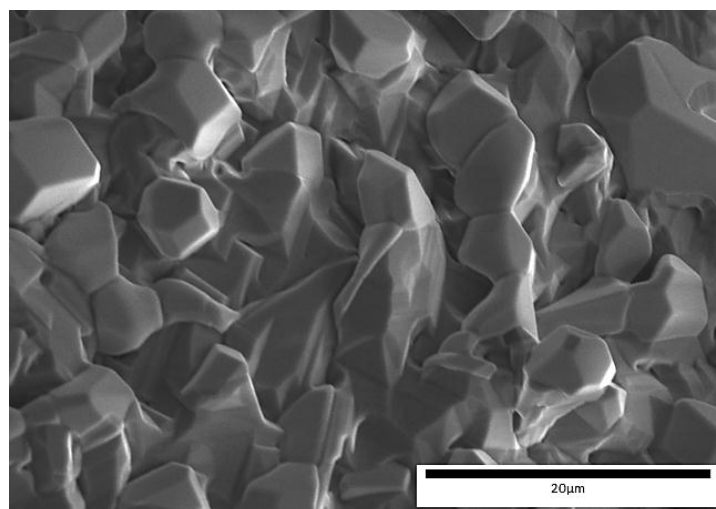


Figure 5.10 Close-up of the blocky deposits found in the grey area of the heat-treated crucible surface

A vertical trench was subsequently milled into the surface of the grey area using the Ga ion beam, the stage tilted to 52° and SEI performed of the milled cross-section. This is shown in Figure 5.11(a-b). The cross-section shows that the blocky grained surface microstructure is comprised of distinct particles that sit on top of the Al₂O₃ crucible substrate. (Note: (a) is an SEI conducted and 3kV and (b) is an SEI at 20kV to show that the band seen in (b) below the metal deposits is in fact a charging effect within the Al₂O₃ substrate as a result of the 20kV accelerating voltage).

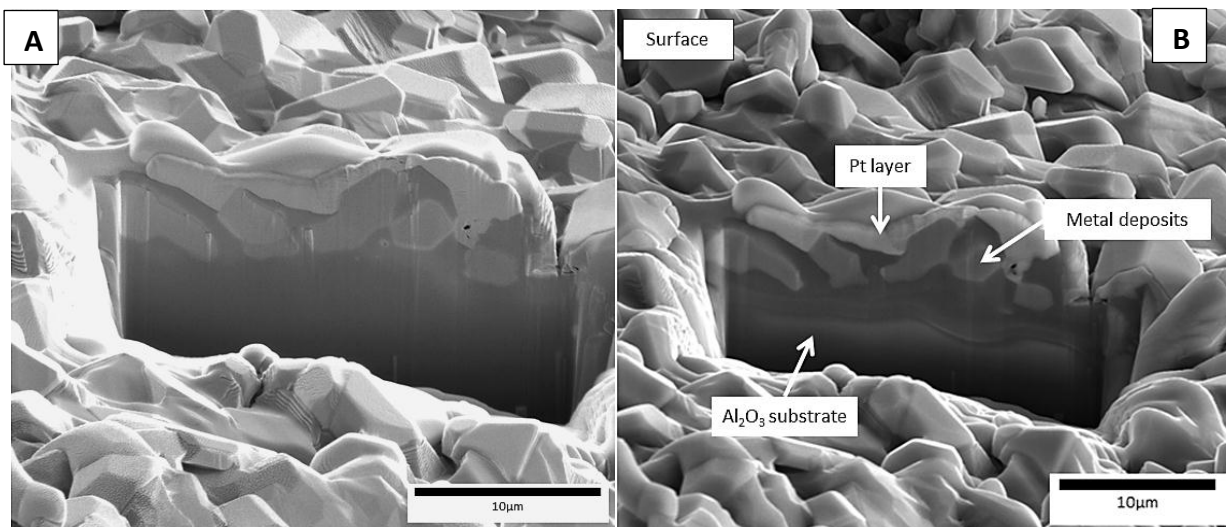


Figure 5.11 Grey area of the heat-treated crucible surface (a) 3kV and (b) 20kV SEI of the surface cross-section

Following the SEI, Ion beam imaging was performed as this gives contrast based on conductivity of the material and can therefore be used to distinguish between metallic and ceramic layers, this is shown in Figure 5.12.

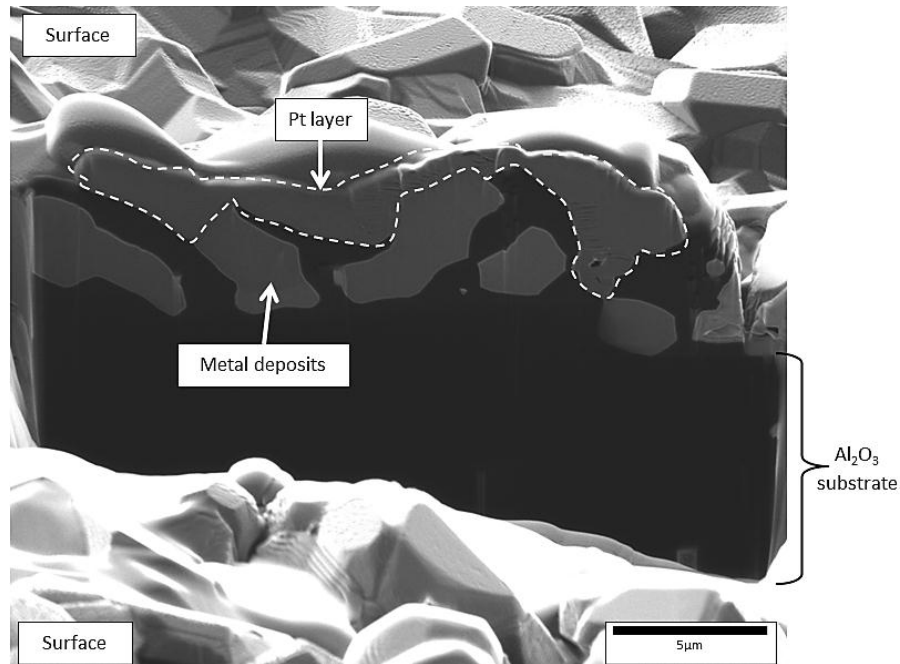


Figure 5.12 FIB image showing the milled cross-section face with metal deposits on top of the Al_2O_3 substrate

This image shows the Pt layer (highlighted by the dotted line for clarity) sitting on top of the blocky particles, which are in turn sitting on top of the Al_2O_3 substrate (which appears black). The particles are metallic in nature and appear embedded within the Al_2O_3 substrate. In order to ascertain the composition of these particles, and therefore gain insight on their provenance, EDX mapping was performed of the milled cross-section and these are shown in Figure 5.13(a-f) for the elements Al, Co, Ni, O and Pt. To complement the maps, spot spectra were collected from the interior of one of the blocky particles and from the Al_2O_3 surrounding it for comparison (Figure 5.14).

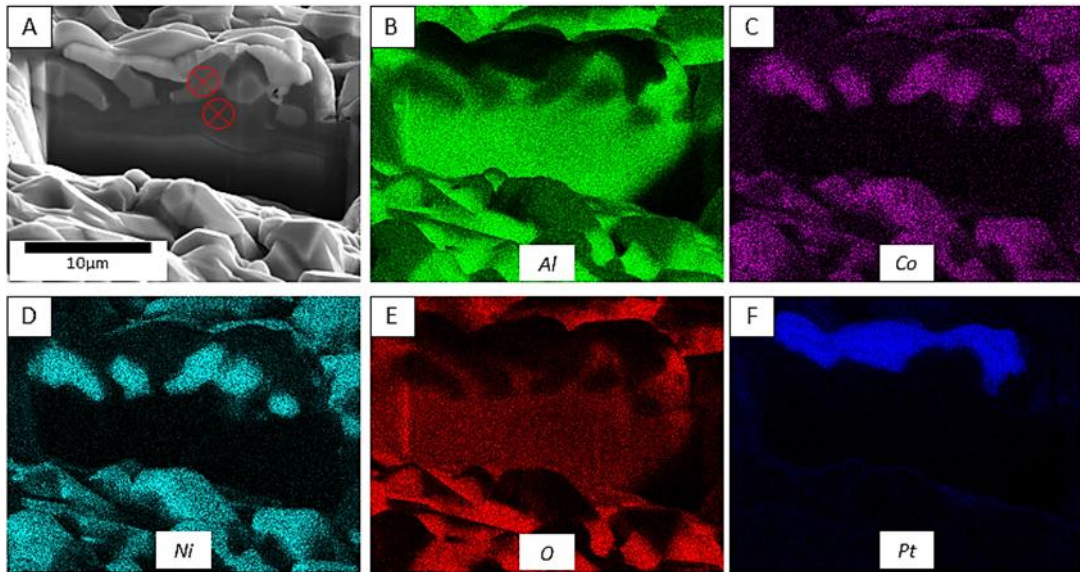


Figure 5.13 EDX 10kV maps of the grey area cross-section (a) 20kV SEI (b) Al (c) Co (d) Ni (e) O (f) Pt

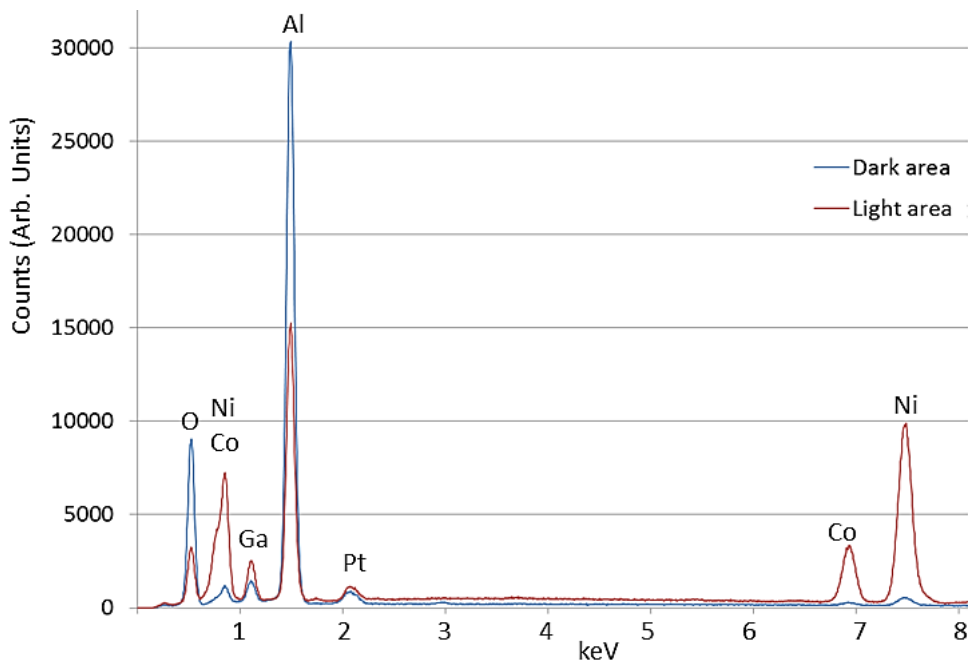


Figure 5.14 EDX point spectra (10kV) from the Ni,Co particles and the Al_2O_3 area surrounding them. Ga and Pt peaks are present due to contamination from the Ga ion beam and Pt deposit respectively

From the ion beam image in Figure 5.12 and the EDX maps/spectra it is possible to conclude that the particles are neither spalled oxide from the test-bar surface that have fallen onto the crucible during solution heat-treatment, nor are they simple oxides of Ni, Co or Al. The particles are strong in Ni and Co, with some trace of Al and O, and can only originate from the test-bar alloy therefore this provides the conclusive

evidence that evaporation occurs during solutioning from the un-protected surface (i.e. the scaled areas as opposed to the unscaled areas) of Nickel-based superalloys.

In contrast to the grey areas, the white portions of the crucible show no signs of collecting any metallic condensate. The SEI in Figure 5.15(a) shows the white surface area where the FIB was used to mill a trench whilst Figure 5.15(b) shows the ion beam image of that cross-section. The Pt deposit is clearly sitting above the dark Al_2O_3 with no condensates sandwiched between them.

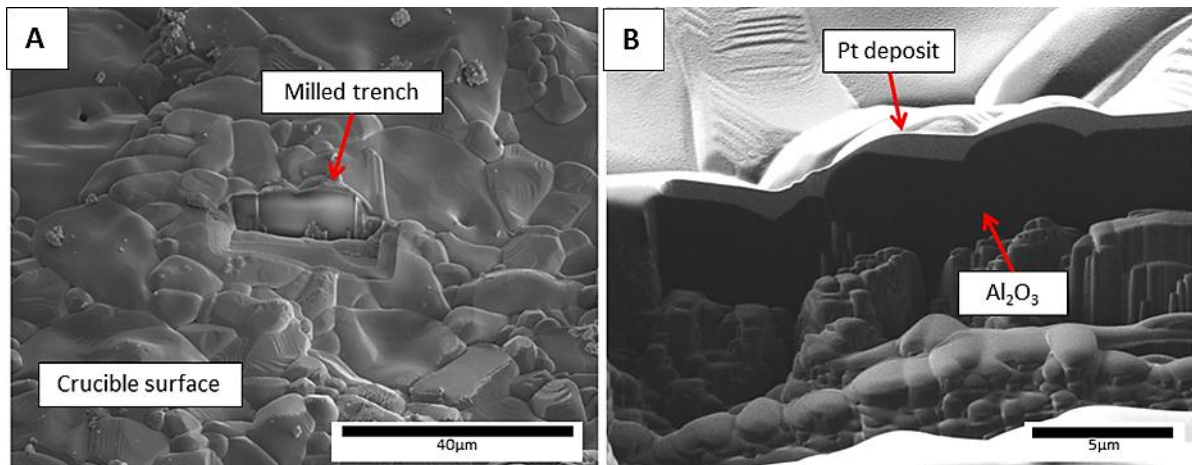


Figure 5.15 White area cross-section of the heat-treated crucible surface (a) 10kV SEI and (b) Ion beam image

5.3.3 Thermodynamic Modelling of the Surface Phase Instability

The phase evolution due to evaporative losses of Ni, Co and Cr was calculated in Thermo-Calc using the compositions in Table 5.2 and the calculated phase transition temperatures are shown below in Table 5.3.

Fractions of Langmuir loss	Nominal Composition	NiO + Cr_2O_3 losses	5% Ni,Co (0.5% Cr)	8% Ni,Co (0.5% Cr)	10% Ni,Co (0.5% Cr)	15% Ni,Co (0.5% Cr)	20% Ni,Co (0.5% Cr)
Liquidus °C	1369	1371	1374	1362	1382	1464	1559
Solidus °C	1329	1331	1331	1314	1298	1263	1241
γ' Solvus °C	1260	1276	1331	1329	1324	1311	1272

Table 5.3 Calculated transition temperatures using Thermo-Calc (Equilibrium condition) for fractions of Langmuir loss, as well as NiO+ Cr_2O_3 losses and nominal composition for comparison

The solutioning temperature of 1312°C corresponds to the γ phase region for the nominal composition, where γ' completely dissolves. This is shown in Table 5.3 however, it is clear that this is not the case for Ni,Co losses between 5 – 10% Langmuir (Cr 0.5% Langmuir) since the γ' solvus temperature is higher than 1312°C and there is between 26.4 – 44% γ' phase predicted at 1312°C. There is also a corresponding increase in the liquidus temperature and a decrease in the solidus, with incipient melting predicted above 8% Ni,Co Langmuir losses (corresponding to 0.04g and 0.006g respectively) and 0.5% Cr Langmuir loss (0.003g).

Fractions of Langmuir loss	Nominal Composition	NiO + Cr ₂ O ₃ losses	5% Ni,Co (0.5% Cr)	8% Ni,Co (0.5% Cr)	10% Ni,Co (0.5% Cr)	15% Ni,Co (0.5% Cr)	20% Ni,Co (0.5% Cr)
Phases at 1312°C (equilibrium condition)	γ (100%)	γ (100%)	γ (73.6%) γ' (26.4%)	γ (58%) γ' (41.2%) σ (8%)	Liquid (19%) γ' (44%) γ (35%) σ (2%)	Liquid (87%) γ' (11%) σ (2%)	Liquid (65.9%) NiAl (29.4%) σ (3.8%) BCC_A2 (0.9%)
Phases after quench (Scheil+Eqlb conditions)	n/a	n/a	n/a	n/a	At 1195°C γ' (79%) γ (17%) σ (2%) NiAl (1%) P (1%)	At 1214°C γ' (56.4%) γ (21.2%) NiAl (20%) σ (2.4%)	At 1173°C γ (24.8%) γ' (23%) NiAl (47%) σ (4.2%) BCC_A2 (1%)
Equilibrium phases for nominal composition of CMSX-4 alloy					At 1195°C γ (72%) γ' (28%)	At 1214°C γ (78%) γ' (22%)	At 1173°C γ (64.9%) γ' (34.8%) P (0.3%)

Table 5.4 Phases (mole %) calculated at 1312°C solution and after quench. Scheil condition applied to liquid fraction at 1312°C to ascertain final solidified phases. Nominal composition phases shown for comparison

From Table 5.4 the occurrence of incipient melting is clear as is the reduction in the fraction of the γ phase, with the gradual increase in the γ' phase fraction. However, as the Langmuir losses of Ni,Co exceed 10%, the liquid fraction becomes greater at the expense of the γ' phase. As a result of the enrichment of Al and the refractory

elements W, Ta and Re there is an increasing fraction of TCP phases (like the σ -phase) and the occurrence of NiAl and minor amounts of BCC_A2 (a disordered BCC phase [176]). It is the formation of the intermetallic TCP phases and NiAl that are responsible for the increase in the liquidus temperature due to their high melting points. The solidus temperature is conversely lowered due to the de-stabilisation of the γ phase.

Where liquid is predicted at 1312°C, the Scheil model was used to calculate the phase fractions that would evolve upon quenching and it is seen that with increasing losses of Ni and Co (and 0.5% Langmuir Cr) there is a greater fraction of TCP phases like P and σ , as well as NiAl and minor amounts of BCC_A2. The final fraction of the γ' phase is also typically higher than that predicted using the nominal composition, with significantly reduced fractions of the γ phase.

Upon quenching, it can be seen from the equilibrium phase diagrams in Figure 5.16(a-b) that those compositions with no predicted liquid phase at 1312°C (5% and 8% Ni,Co Langmuir loss) will precipitate out the γ' phase as well as minor amounts of TCPs (P and μ). These phase diagrams also show how the γ phase, in contrast to the γ' phase, becomes decreasingly stable at 1312°C eventually disappearing by 15% Langmuir loss.

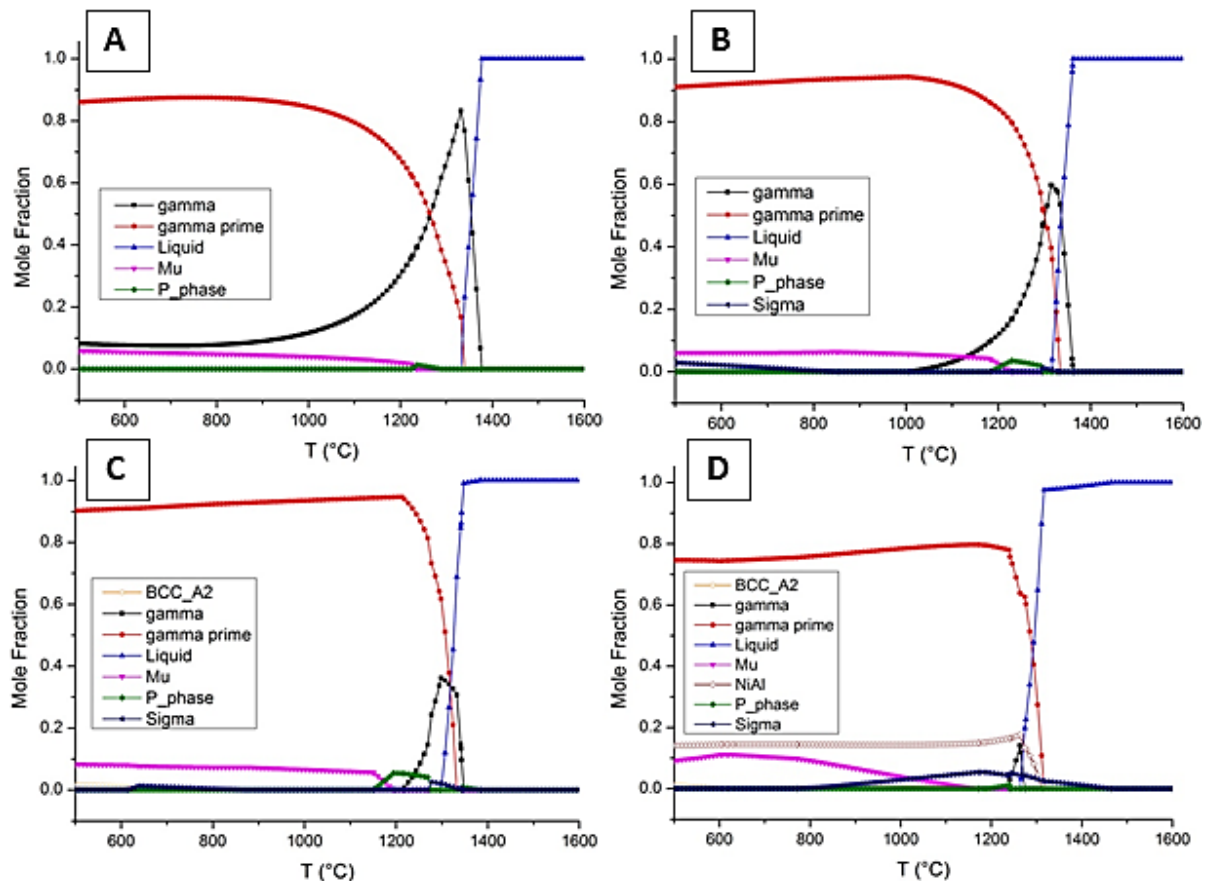


Figure 5.16 Phase evolution of the surface layer calculated using Thermo-Calc for elemental vapour losses (a) 5% Langmuir Ni, Co loss (b) 8% Langmuir Ni, Co loss (c) 10% Langmuir Ni, Co loss (d) 15% Langmuir Ni, Co loss. Cr losses are at 0.5% Langmuir in (a)-(d)

It is worth noting however that the existence of the NiAl or BCC_A2 phases are not observed in the microstructural analysis of the γ' surface layer. In the case of NiAl, this is most likely due to the assumption that only Ni, Co and Cr losses are considered and that diffusion interactions with the matrix are ignored, therefore the mass losses are likely not as severe as the scenario's above 10% Langmuir loss. In the case of BCC_A2, this phase is not typically observed in Nickel-based superalloys, and considering the low predicted fractions ($\sim 1\%$), this is likely due to instabilities in the Thermo-Calc predictions.

For comparison, the phase fractions at 1312°C as a result of the compositional changes due to the formation of a NiO/Cr₂O₃ dual-oxide layer (each 0.5 μ m thick) are also

shown in Table 5.4. The formation of the dual-oxide layer results in the depletion of 0.0049g of Ni and 0.0034g of Cr from the 20 μ m surface layer; which equates to 2.5% and 15.8% mass losses respectively. This emphasises that the mass losses due to oxidation of Ni and Cr are insufficient to produce any γ' surface layer, therefore this transformation is not an oxidation related process.

5.4 Discussion

5.4.1 Surface Evaporation during Solution Heat-Treatment

It has been shown in Chapter 4 that the vapour pressures of Ni, Cr and Co are relatively high (with Cr and Ni higher than Co) and that elemental vaporisation from the bare alloy surface is thermodynamically possible during solutioning. The phase evolution due to evaporative losses of γ stabilisers have been qualitatively modelled using Thermo-Calc in Section 5.3.3 and these results have shown that the γ' phase can be stabilised at solutioning temperatures following evaporation of Ni, Cr and Co. The observed microstructure of the solutioned test-bar surface corresponds to the phase fractions predicted at a net loss of ~8 – 10% Langmuir for Ni and Co and ~0.5% Langmuir for Cr. These Langmuir percentages correspond to net mass loss percentages of 20 – 25% (Ni), 19 – 22% (Co) and 14% (Cr) from within the 20 μ m surface layer. The maximum rate at which these elements can evaporate from the test-bar surface is given by the Langmuir equation for evaporation into a vacuum:

$$E_i = \frac{P_i}{\sqrt{2\pi M_i RT}} \quad \text{Equation 5.1}$$

Where E_i is the number of moles of species i evaporated per m^2 per second, P_i is the vapour pressure of i in solution, M_i is the molecular weight of i and R and T are the gas constant and temperature respectively.

The maximum Langmuir loss corresponds to evaporation into a high vacuum where the vapours that evolve from the surface are removed from the system (non-equilibrium conditions), for example via the vacuum pump. In this scenario, the corresponding rate of condensation is zero and subsequently the atmosphere above the surface cannot reach equilibrium conditions where the vapour becomes saturated and evaporative flux is equal to the condensation flux [177]. In the previous Chapter fractions of the total Langmuir loss were considered since the vacuum atmosphere used at Bodycote for heat-treatment is under a partial pressure of Ar and not a high vacuum. This means that the resulting evaporation rate will be lower than the ideal Langmuir value. However, whilst the diffusion pump is switched off at high temperatures, the vacuum pump remains on (with a constant bleed of Ar to maintain partial pressure) therefore the vapour species that evolve from the test-bar surface can be removed from the system therefore preventing the formation of a saturated vapour pressure and resulting in a higher evaporation rate.

Figure 5.17(a) shows the variation of mass loss rate (Langmuir loss) with temperature for Ni, Cr and Co whilst Figure 5.17(b) shows the fractions of the calculated Langmuir mass loss to vacuum from a test-bars cylindrical surface (10mm OD and 60mm in length) during the standard isothermal solutioning at 1312°C for 8 hours. As mentioned in Chapter 3, since the actual heat-treatment furnace is held under an Ar

partial pressure of $P_{Ar} = 10^{-4}$ atm it is necessary to consider fractions of the total Langmuir mass loss to vacuum.

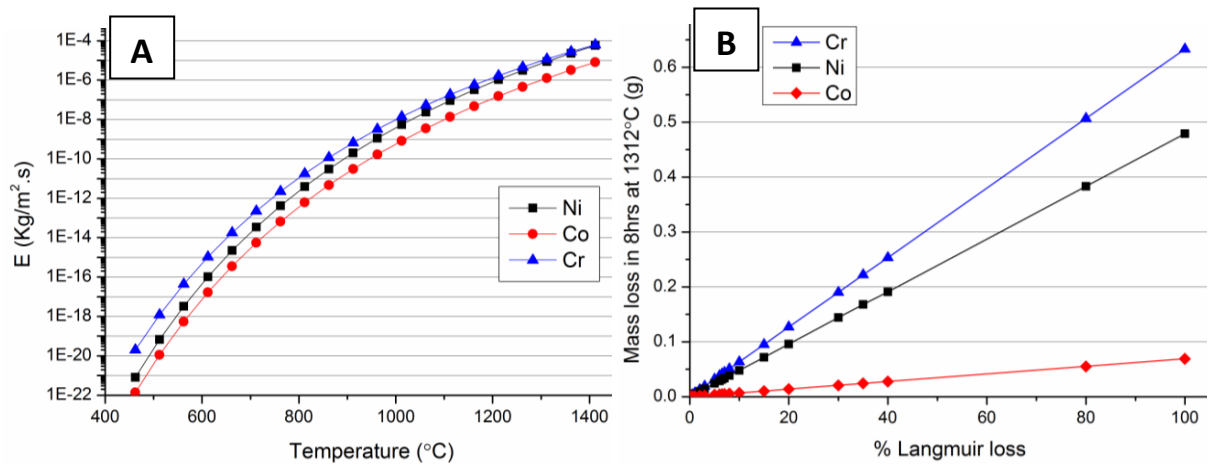


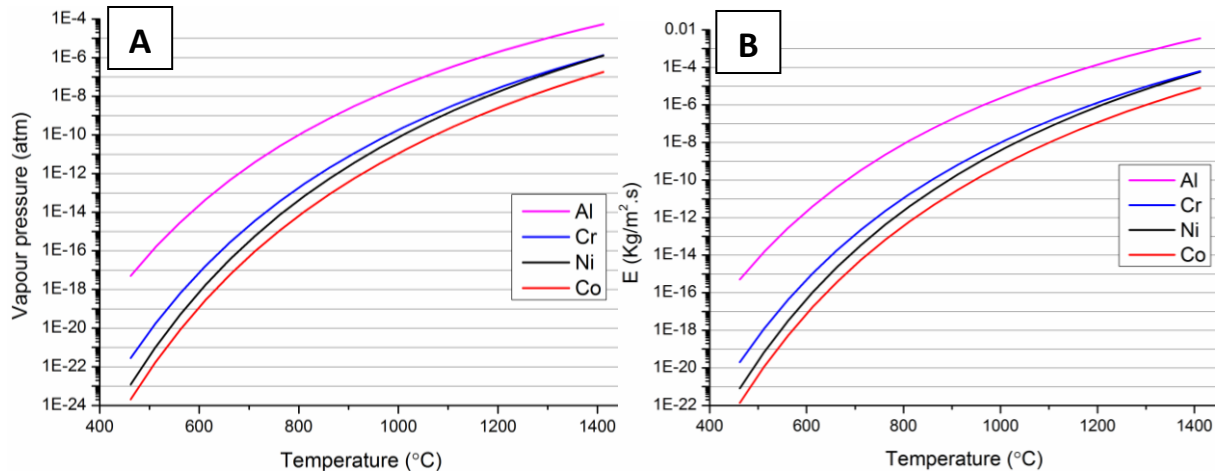
Figure 5.17(a) Langmuir evaporative rate into vacuum (b) Mass loss (g) of Ni, Cr and Co for different %'s of total Langmuir loss to vacuum (during 8 hours solution at 1312°C)

Figure 5.17 is adjusted for the mole fraction of each element within the CMSX-4 alloy (using Raoult's law) and it can therefore be concluded that whilst Cr is only present at 6.5wt.% within the alloy, it has the highest mass loss, due to its higher vapour pressure than Co and smaller atomic weight than Ni (since the vapour pressures of Ni and Cr are almost identical, the atomic mass term in Equation 5.1 is the only rate affecting term between them). However the evaporation of aluminium has been tacitly neglected in this discussion so far due to the fact that the surface layer transforms from γ to γ' , which requires an associated net increase in the Al to Ni ratio. Aluminium is however characterised as also having a relatively high vapour pressure which is described by the following Clausius-Clapeyron equation [138]:

$$\log[P_{Al}] \text{ atm} = 9.459 - \frac{17342}{T} - 0.7927\log T \quad \text{Equation 5.2}$$

Using Equation 5.2 (with the same data for Ni, Co and Cr taken from Chapter 4), the vapour pressures and evaporative rates of Al, Ni, Cr and Co are displayed in Figure 5.18(a) and (b) for comparison. This has been adjusted for the mole fraction of each element within the CMSX-4 alloy by application of Raoult's law. The strong

temperature dependence of the vapour pressure is clear to see, this is because the release of atoms from the solid (or liquid) phase to the gas is thermally activated. It is clear that aluminium's vapour pressure, and corresponding evaporative rate, is between 1 – 2 orders of magnitude higher than all the other metals at 1312°C. At lower temperatures the difference is even greater.



The mass loss to vacuum for Al can be added to those of Ni, Cr and Co to compare the effective rate of Al evaporation during solutioning of the CMSX-4 test-bars (Figure 5.19). This shows that the high vapour pressure of Al results in a significantly higher rate of loss to evaporation compared to Ni, Cr and Co.

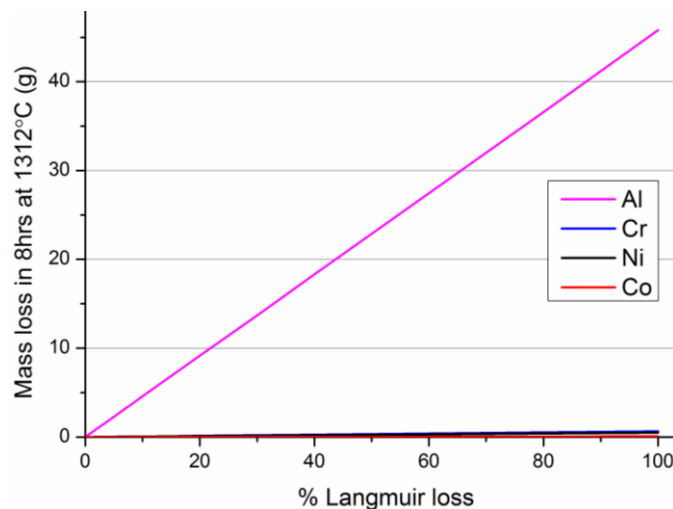


Figure 5.19 Mass losses (g) of Ni, Cr, Co and Al for different %s of total Langmuir loss to vacuum (during 8 hours solution at 1312°C)

The maximum calculated mass losses of Ni, Cr and Co are 0.5g, 0.63g and 0.07g respectively (shown clearly in Figure 5.17(b)) whilst the maximum mass loss of Al is calculated to be almost x100 that, 45.77g. This is a result of both a higher vapour pressure and a lower atomic weight, when compared to the other metals. Again, it must be emphasised that, whilst the mole fraction (and thus activity) has been accounted for, the heat-treatment furnace is not held at a perfect vacuum and therefore these values will be lower than that for 100% Langmuir loss.

An additional consideration is the difference between the ambient pressure (i.e. the pressure inside the heat-treatment furnace) and the vapour pressure of the material. Even though the vapour pressure is dependent only on the temperature (and substance), the rate of evaporation is increased by reducing the ambient pressure. This in effect reduces the number of collisions between the vapour molecules and the ambient gases, resulting in a lower probability of the vapour molecule losing energy through a collision and re-depositing on the surface in the condensed state. Therefore since the vapour pressure of Al at 1312°C ($\sim 10^{-5}$ atm) is much closer to the ambient furnace pressure of $\sim 10^{-4}$ atm (partial pressure of Ar) than Ni, Cr and Co ($\sim 10^{-7}$, 10^{-7} and 10^{-8} respectively) its evaporative rate will be comparatively lower. The resultant percentage reduction in the rate of evaporation has been estimated to be $\sim 2-4\%$ [139]. However, since the Al evaporative rate is significantly higher than those for Ni, Cr and Co it seems likely that there will also be a significant evaporative loss of Al. This raises the question, how can Al be enriched at the surface, to form the γ' surface layer, considering the much larger driving-force for vaporisation compared to Ni, Cr and Co?

5.4.2 Diffusion Interactions in the Near-Surface Region

It is clear from the microstructural analysis that the surface layer is comprised of the γ' phase and therefore it must be enriched in Al, with a concurrent reduction in Ni, Cr and Co. However, Al vapour losses are significantly higher than those for Ni, Cr and Co and so in order to form γ' , the diffusion of metal from the substrate must compensate for the discrepancies in the vapour losses. When metal losses occur in one area, in relation to another, diffusion will occur along that concentration gradient in order to replenish the lost material and homogenise the chemical composition. During surface vaporisation, metal is continuously drawn away from the component's near-surface region; in this manner there exists a composition gradient between the near-surface and the substrate/bulk. This drives the flow of metal atoms to achieve a state of chemical homogeneity. The magnitude of the concentration gradient does not affect the diffusivity; instead the diffusion coefficient is purely temperature and composition dependent [178].

In order for diffusion to occur, the temperature must be high enough to overcome to activation energy barrier to atomic motion. Atoms in a crystalline solid diffuse by vacancy or interstitial diffusion, depending on their atomic size. If the solute atoms are smaller than the matrix atoms then interstitial diffusion dominates, whereby the solute migrates via the 'gaps' between atomic planes, and the activation energy required is relatively low. If the solute atoms are of a comparable size, or larger than the matrix atoms then substitutional diffusion occurs via vacancies in the crystal lattice. This is the case for the majority of Nickel-based superalloys, where the solute elements are substitutional rather than interstitials. Vacancies are 'holes' in the lattice,

i.e. missing an atom, and as the atoms flow in one direction, the vacancies flow in the opposite. In the case of substitutional diffusion, the activation energy is much higher than that for interstitial diffusion and this difference arises due to the need for each atom to break the chemical bonds with its neighbour and 'squeeze' past to the vacancy site in order to migrate. The activation energy needed for an atom to diffuse is however significantly reduced at lattice sights with a high degree of disorder, such as at grain-boundaries, dislocations and at free-surfaces. The activation energy for substitutional diffusion is usually significantly higher than the energy of the atom in its original lattice site at room temperature and thus heat is needed in order for diffusion to occur. An Arrhenius equation is used to relate the temperature dependence of this process to the diffusion coefficient [178]:

$$D = D_0 \exp\left(\frac{-Q}{RT}\right) \quad \text{Equation 5.3}$$

Where D_0 is the diffusion coefficient at ∞ temperature and Q is the activation energy, both of which are dependent on composition, not temperature.

By rearranging Equation 5.3 it is possible to show the temperature dependence of D :

$$\ln D = \ln D_0 - \frac{Q}{RT} \left(\frac{1}{T}\right) \quad \text{Equation 5.4}$$

Which displays a straight line graph with a slope of $-Q/RT$ and an intercept of $\ln D_0$.

The typical diffusion coefficients of the alloying elements within the nickel matrix are shown in Figure 1.24(a) as a function of the inverse temperature. Likewise, in Figure 1.24(b) the self-diffusion coefficient of nickel within a SX nickel matrix is shown.

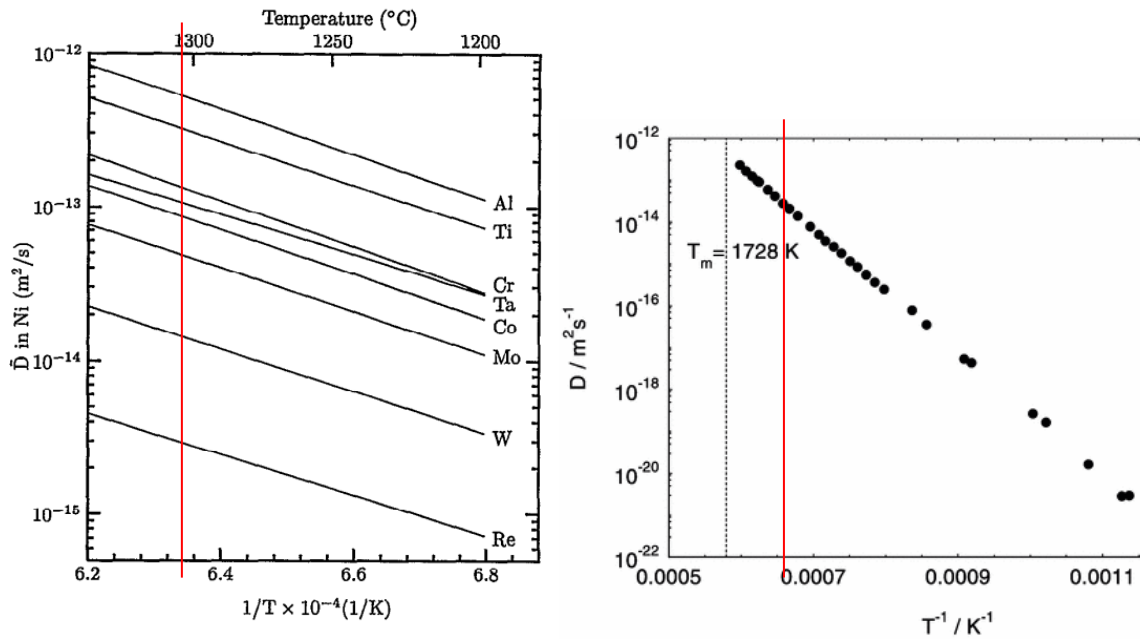


Figure 5.20(a) Diffusion rates of key alloying elements within pure Ni as a function of $1/T$ [54] (b) Self-diffusion rate of Ni within pure, SX Ni as a function of $1/T$ [179]. The solutioning temperature, 1312°C , is marked to highlight the relative diffusion coefficients acting to replenish metal evaporative losses

These diagrams graphically show that at the solutioning temperature of 1312°C the activation energy for diffusion is surpassed (since $T/T_m > 0.75$) and it can be seen that the diffusion coefficient of Al in nickel is the highest ($5 \times 10^{-12} \text{ m}^2/\text{s}$), followed by Cr ($\sim 9 \times 10^{-12} \text{ m}^2/\text{s}$) and Co ($1 \times 10^{-13} \text{ m}^2/\text{s}$). The self-diffusion of nickel is roughly the same as the diffusion coefficient of Co in nickel at 1312°C .

The effects of diffusion were ignored from the Thermo-Calc simulations for simplicity, since the formation of the γ' surface layer was already observed and therefore the net loss of metal must favour the depletion of the γ forming elements, Ni, Cr and Co. This estimation neglects the interaction of the γ' surface layer and the substrate, indeed it was already discussed in Chapter 3 that significant inter-diffusion of these two layers will occur and that this creates the driving-force for the growth of the γ' surface layer. However, as a first-approximation this serves to qualitatively show that the mass loss of key elements is a vital stage in the formation of the γ' surface layer.

The diffusion coefficient data for Al, Cr, Co and Ni within the SX Ni matrix indicates that the net loss (or enrichment) of metal in the near-surface region is a product of the inter-play between the evaporative rate, acting to remove material from the surface, and the diffusive rate that acts to replenish the lost material. Clearly therefore, it is the faster diffusivity of Al that prevents its depletion in the near-surface region, since it has already been shown that its evaporative rate is higher than those for Ni, Cr and Co.

5.4.3 Vapour Condensate Analysis

The thermodynamic considerations in the previous Section have shown that elemental evaporation from the test-bar surface occurs during solutioning, and that this results in the transformation of $\gamma \rightarrow \gamma'$ within the near-surface region. This is in agreement with the microstructural observations of the γ' surface layer that evolves during solutioning. However, during evaporation of a species there exists the concomitant condensation of that species which, at equilibrium in a closed system, has a rate equal to that of evaporation. In an open system however, the rate of evaporation can be much higher since the evaporated species is able to diffuse away and cannot subsequently condense back on to the surface. The Bodycote heat-treatment furnace can be described as an open-system, since during solutioning the atmosphere is held at an argon partial pressure of $\sim 10^{-4}$ atm with the vacuum pumps constantly evacuating the chamber. This means that the vapour species that evolve from the alloy surface will likely be removed from the furnace chamber and non-equilibrium conditions will govern. Additionally, the vapour species can condense on any part of the furnace or test-bar that may act as a 'cold-trap'. In order to experimentally observe and analyse

the evaporated material from the test-bar surface a simple cold-trap experiment was devised, utilising an Al_2O_3 crucible to surround the sample test-bar and trap and collect the condensed vapour species.

The condensate microstructural and compositional analysis clearly shows the deposition of metal vapour from the test-bar surface onto areas of the Al_2O_3 crucible near the join between top and bottom. This points towards the condensates forming as the vapour moves out of the loose-fitting crucible. However, whilst Ni and Co condensates were observed, there is a distinct lack of any Cr condensates. There is also no sign of metallic Al on the crucible (the only Al seemingly arising from the Al_2O_3 crucible itself) however the silvery deposits found on the ends of the test-bar are rich in metallic Al (as well as Ni and Co). The aluminium vapour is therefore predominantly condensing on the test-bar surface, rather than the crucible surface. These metallic deposits are not typically seen on standard heat-treatment experiments since the lack of a surrounding crucible allows the vapours to diffuse around the furnace and be removed via the vacuum pump, making their re-deposition onto the test-bar surface less likely.

These observations seem counter-intuitive given that Al and Cr have the highest vapour pressures (and evaporation rates) and Co has the lowest, they should contribute the highest amount to the condensates. This could be due to the oxidation of the Al and Cr vapour species, since the partial pressure of oxygen in the furnace is significantly lower than the $P_{Ar} = 10^{-4}$ atm, Ni and Co will not oxidise and the deposits remain as elemental Ni and Co. The lack of Cr is hard to explain on the other hand,

however the evaporation of Cr and its oxides, Cr_2O_3 and CrO_3 , above 1000°C is well-known [92][97][180][170] therefore any Cr vapour may remain in the gas state and be removed from the furnace, instead of condensing on the crucible. This possibility is heightened by the fact the crucible was not cooled in any way (it is at the same temperature as the alloy during solutioning) relying on condensing the vapour species by collisions of the saturated vapour phase with the Al_2O_3 crucible surface.

5.4.4 Oxidation during Solution Heat-Treatment

Oxidation of Al is a counter-acting process that occurs during solution heat-treatment, albeit at a slow rate. The oxidation of Al acts as a barrier to the formation of the γ' surface layer in two ways, (i) it depletes Al from the near-surface region, stabilising the γ phase and (ii) by forming a physical barrier to evaporation. The partial pressure of oxygen is minimised in the furnace via the use of a vacuum and subsequent Ar partial pressure however there will still be residual oxygen remaining, and this is sufficient to allow the formation of a thin ($1\text{-}2\mu\text{m}$) Al_2O_3 surface oxide layer [7]. A typical SEI and EDX mapping of the heat-treated test-bar surface is shown in Figure 5.21, highlighting the Al_2O_3 layer that evolves during solutioning.

The equilibrium P_{O_2} needed for Al_2O_3 formation at $1305\text{-}1312^\circ\text{C}$ is $\sim 10^{-24}$ atm whereas NiO, Cr_2O_3 and CoO require oxygen partial pressures of $\sim 10^{-6}$, $\sim 10^{-14}$ and $\sim 10^{-5}$ atm respectively (see Figure 5.22). These conditions prohibit the formation of NiO and CoO, however Thermo-Calc was used to conclusively show that, even if these oxides did form, the mass loss from the surface layer was insufficient to cause any microstructural instability.

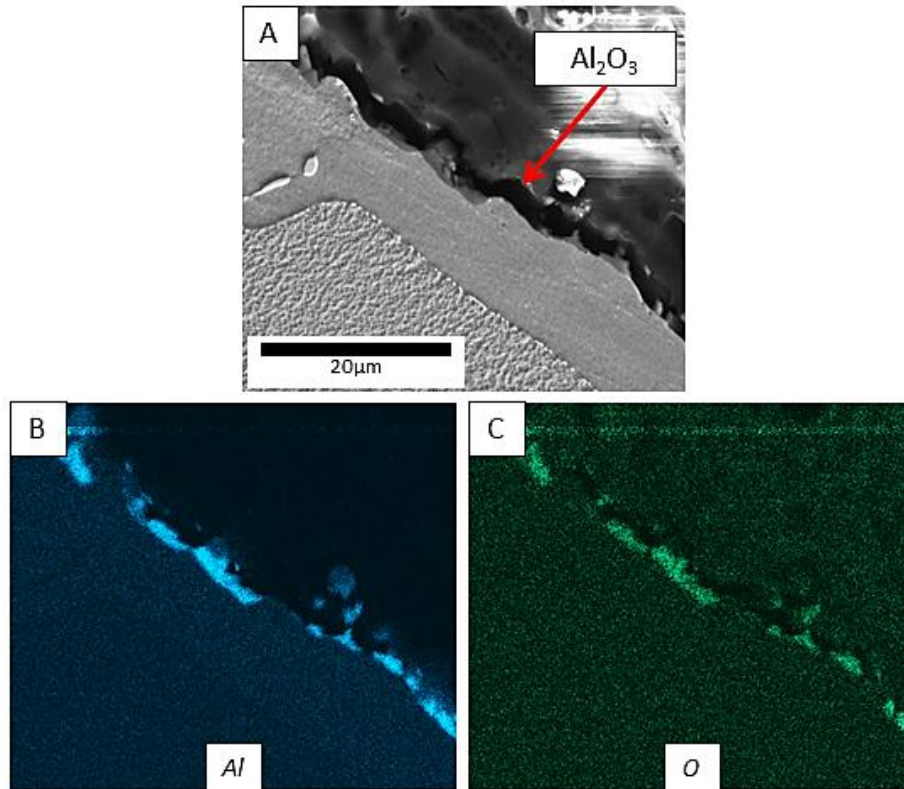


Figure 5.21 EDX mapping of the Al_2O_3 surface oxide formed during solution heat-treatment (a) SEI (b) Al and (c) O

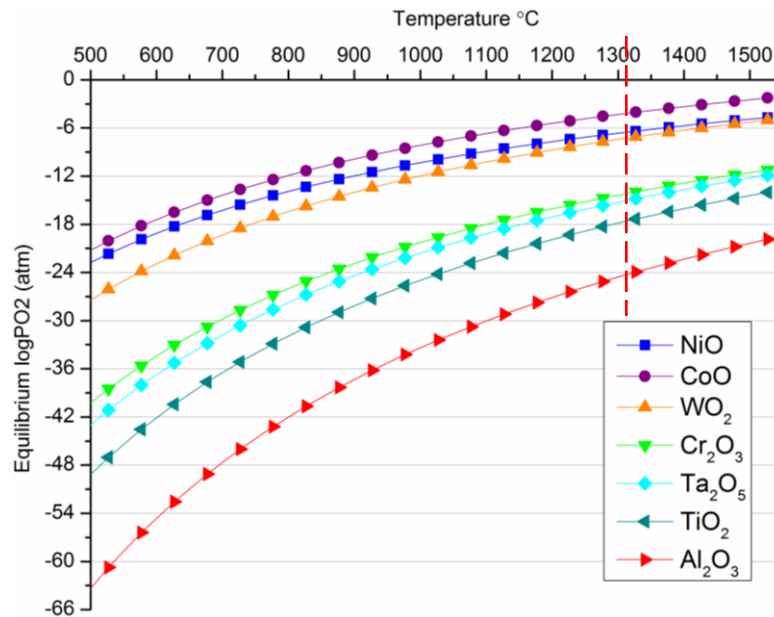


Figure 5.22 Calculated Ellingham diagram for the alloy CMSX-4 with solutioning temperature indicated by red line

Because the P_{O_2} required for Al_2O_3 formation decreases with increasing temperature, the formation at low temperatures will be prohibitively slow and therefore it is only upon reaching solutioning temperatures that the oxidation will precede at its maximum rate. This is an identical situation to surface evaporation, since this too is a

thermally activated process. The literature on the oxide growth kinetics of Nickel-based superalloys focuses on the 'in-air' response, since this is the most critical to the operation of the component, and the growth kinetics of Al_2O_3 , especially at such low P_{O_2} , is sparse. However oxidation experiments on superalloys in air have shown that the establishment of a protective Al_2O_3 layer typically takes many hours [111][122][132][133] and Kear *et al* [137] found that a continuous Al_2O_3 layer did not form before 40mins of oxidation at 1000°C in 0.1 atm of air. Clearly, in the case of solution heat-treatment with a significantly lower P_{O_2} , the growth kinetics of Al_2O_3 will be much slower, allowing the evaporation of elements to occur for a considerable amount of time.

Finally, the test-bars considered in this Chapter (and others) were grit blasted prior to solutioning, removing all oxides formed during casting. It is seen in Chapter 3 that Surface Scale oxides form on some areas of the casting surface, the rest of the surface being 'Unscaled' and populated by a micron thick Al_2O_3 layer. It is this Al_2O_3 layer in the unscaled regions that acts as an evaporation barrier during subsequent heat-treatment. In the scaled regions on the other hand, the oxides are a porous dual-oxide consisting of NiO and spinel phases which are readily spalled away and therefore do not provide an adequate evaporation barrier during heat-treatment. This is why the surface melt blister defects are only seen to occur in the scaled regions of the casting.

5.5 Conclusions

It has been shown that elemental vaporisation during solution heat-treatment can result in the transformation of the stable γ phase into the non-equilibrium γ' phase with associated TCP formation. As a first approximation to the problem, using the vapour pressures and evaporation rates for Ni, Cr and Co, the composition of a surface layer 20 μm thick was calculated and modelled using the software package ThermoCalc. Several fractions of the total Langmuir elemental loss to vacuum were considered and it was found that mass losses of 20 – 25% Ni, 14% Cr and 19 – 22% Co from the 20 μm surface layer corresponded to the observed microstructure of the γ' surface layer in Chapter 4. In these simulations it was assumed that there was no inter-diffusion between the γ' surface layer and the substrate in order to simplify the complex nature of the problem, this is therefore only a qualitative analysis. The inter-diffusion between the evolving γ' surface layer and the substrate was discussed and it is shown that Al is a fast diffuser at the solutioning temperature of 1312°C and can therefore replenish any surface vapour losses faster than Ni, Cr and Co, allowing the formation of the γ' phase at the surface.

The relationship between the surface scale casting defect and the heat-treatment surface melt blister defect is discussed and it is shown that the melt blisters form in the scaled regions due to the lack of a protective oxide barrier to evaporation during solutioning. In the unscaled regions (described in Chapter 3), a $\sim 2\mu\text{m}$ layer of Al_2O_3 already exists in the as-cast condition and therefore no evaporation can occur during solutioning, prohibiting the formation of a γ' surface layer.

Chapter 6. Exploring the use of Neutron Diffraction for Tracking the Formation of the γ' Surface Layer during Heat-Treatment

6.1 Introduction

As discussed in the previous Chapters, the formation and evolution of a γ' surface layer, and related morphologies, occurs during solution heat-treatment of single-crystal Nickel-based superalloys. This layer is the result of elemental vapour losses from the surface of the casting, governed by the individual elemental vapour pressures and the temperature/vacuum conditions within the heat-treatment furnace. The experiments conducted so far have yet to determine at what point during the heat-treatment cycle that the γ' surface layer forms (although it is likely to occur during solutioning rather than ramp-up due to the temperature dependence of the vapour pressures) and therefore it was decided to explore the use of Neutron Diffraction to investigate the formation of the γ' surface layer using *in-situ* solution heat-treatment at the Engin-X facility at the ISIS neutron source, Rutherford Appleton Laboratory, Didcot UK. Initial studies were performed using as-cast CMSX-10N test-bars however, due to excessive residual eutectic phases present within this as-cast alloy subsequent studies were performed using fully solutioned CMSX-4 test-bars. To complement the neutron diffraction analysis, optical microscopy and SEM was conducted to ascertain the start (as-received) and post-test surface morphologies.

6.2 Research on Neutron Diffraction in the Open Literature

The Engin-X neutron diffractometer at ISIS is a dedicated engineering apparatus, used extensively for the measurement of strain (and therefore stress) within crystalline solids by employing the materials atomic lattice planes as in-built strain gauges [181][182] but it can also be used to study the phase evolution of a solid by tracking the movement of diffraction peaks, associated with each phase, with temperature.

The development and processing of Nickel-based superalloys has benefited from the use of neutron diffraction (ND) techniques due to the ability to probe the atomic structure in detail, revealing material properties, such as lattice strain misfit [183][184][185], deformation mechanisms [186][187][188], and how to adequately characterise and relieve residual stresses to retain the optimum material strength [189][190][191]. The paper by Preuss *et al* [192] compared the microstructure, mechanical properties and residual stresses of three inertia friction welded Nickel-based superalloys, using the Engin-X neutron diffractometer to measure the radial, axial and hoop stresses generated by the welding process. It was shown that large axial and hoop stresses are produced near the welds in the as-welded condition, with the hoop direction experiencing larger tensile stresses than the axial. It was also shown that by employing a post-weld heat-treatment (PWHT), all three alloys could have their residual axial and radial stresses significantly reduced with the hoop stresses also being relieved, albeit to a lesser extent. The importance of choosing the correct PWHT temperature was highlighted, in order to maximise the stress relief and ensure the correct microstructure remains in the PWHT state.

Ma *et al* [193] used neutron diffraction with *in-situ* heating to investigate the change in misfit strain in a polycrystalline Nickel-based superalloy during heating to 900°C and during subsequent creep loading. The misfit strain was shown to decrease from 0.02% at room temperature to -0.17% at 900°C indicating that the alloy has a very low misfit between the γ and γ' phases at room temperature, with the γ' phase under slight compression within the γ matrix. The level of misfit decreased as temperature rose, generating significant stresses within the constituent phases, and the thermal expansion of the individual, constrained lattices was shown to be larger for the γ phase than the coherent γ' . The creep experiments showed that the [001] and [111] orientated grains within the polycrystalline structure pick up load whilst the [110] grains shed load due to the γ channels allowing easier passage for dislocations.

Coakley *et al* [194] used neutron diffraction to characterise the deformation of the Nickel-base superalloy CMSX-4 during tensile creep, with the focus on the differing responses of the γ and γ' phases on the micro-scale. *In-situ* creep tests were performed in the tertiary (900°C, 460MPa) and primary (650°C, 825MPa) creep regimes at the Engin-X diffractometer. The diffraction spectra collected contained the (300) and (100) γ' peaks and the (200) γ/γ' peak. The (200) composite peak was deconvoluted by assuming (i) the instrumental peak widths of both phases are equal, (ii) the Voight shape function of both peaks are equal and (iii) the (200) γ' position is given by $d_{(200)}^{\gamma'} = 0.5 * d_{(100)}^{\gamma'}$. It was also shown that the intensity ratio between the two phases in the (200) peak was given by $I_{(200)}^{\gamma} = 0.25 * I_{(200)}^{\gamma'}$. The peak widths were found to be contributed to by strain (i.e. dislocations), the initial sample mosaic spread

(i.e. how ordered the γ' precipitates are within the γ matrix) and the instrumental broadening. The lattice strain response in the two creep regimes was ultimately found to be distinct, indicating that the micro-mechanisms of deformation differ during primary and tertiary creep.

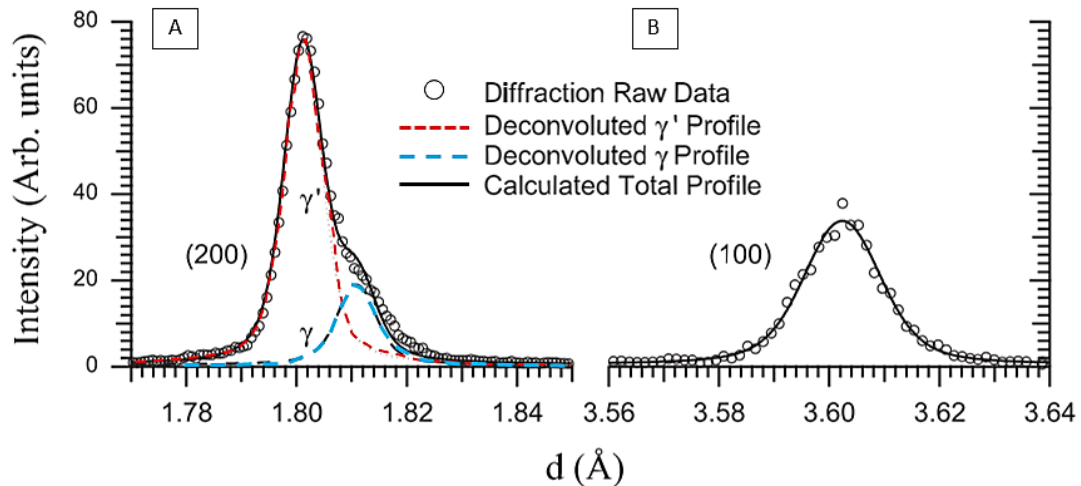


Figure 6.1 (200) γ/γ' peak de-convolution. (200) peak is constrained by the γ' (100) d-spacing (adapted from [194])

6.3 Experimental Methods

The as-cast Nickel-based superalloy CMSX-10N was initially considered in this chapter, with solutioned CMSX-4 test-bars eventually being investigated due to their homogenized composition and microstructure compared to the as-cast CMSX-10N.

Nominal composition (wt.%) is given in Table 6.1.

Alloy	Al	Co	Cr	Ti	Mo	Ta	W	Re	Ni
CMSX-4	5.8	9.5	6.5	1.1	0.6	6.5	6.5	3	Bal
CMSX-10N	5.9	3.1	1.6	0.1	0.45	8.5	5.5	6.8	Bal

Table 6.1 Nominal composition (wt.%) of alloying elements in the Ni-based superalloys CMSX-4 and CMSX-10N

6.3.1 Investment Casting and Heat-Treatment

For this study, cylindrical test-bars (10mm OD x 60mm H) were cast using the methods described in Chapter 3 at the Precision Casting Facility, Rolls-Royce plc in Derby. The as-cast CMSX-10N samples were subsequently grit blasted to remove any oxides or

surface eutectic formed during casting. The CMSX-4 samples were solution heat-treated by standard industrial practices within the turbine blade heat-treatment furnaces at Bodycote plc. Following solutioning, the test-bars were grit blasted with alumina media to remove any oxides or γ' surface layer that may have formed during the Bodycote heat-treatment.

6.3.2 Neutron Diffraction and *in-situ* Heat-Treatment

Neutron diffraction is a technique by which thermal or cold neutrons are accelerated towards a sample where they interact to give information on the atomic structure of the sample material. As charge-neutral particles, neutrons interact directly with the nucleus of the impacted atom, experiencing elastic scattering where the exiting neutrons have almost the same energy as the incident neutrons. Due to their charge neutrality, they are able to penetrate much further into solid matter (order of centimetres) making them an ideal medium for bulk sample analysis. This has led to the wide use of neutron diffraction as a method for the measurement of residual stresses in large engineering components [182].

The CMSX-10N and CMSX-4 test-bars were investigated at the ENGIN-X neutron strain scattering facility at ISIS, Didcot (Figure 6.2). This facility was used to analyse the microstructural evolution of the near-surface region during *in-situ* solution heat-treatment experiments. ENGIN-X is a time-of-flight (TOF) neutron diffractometer which records the diffracted neutrons from a pulsed proton spallation source and, assuming elastic collisions, defines the neutron wavelength as:

$$\lambda = \frac{h}{m(L_1+L_2)} t \quad \text{Equation 6.1}$$

Where h is Planck's constant, m is the neutron mass, $L_{1,2}$ are the primary and secondary flight paths and t is the time-of-flight.

The lattice (d) spacing of a crystalline solid is described in terms of an (hkl) family of lattice planes as given by Bragg's law, $\lambda_{hkl} = 2d_{hkl}\sin\theta_B$, which is therefore obtained from the TOF neutron spectrum from the position of the t_{hkl} peak by:

$$d_{hkl} = \frac{h}{2\sin\theta_B m(L_1 + L_2)} t_{hkl} \quad \text{Equation 6.2}$$

The lattice spacing gives the user insightful information on the phases present as well as the stress state of the crystal lattice by a simple application of $\varepsilon_{hkl} = (d_{hkl} - d_{hkl}^0)/d_{hkl}^0$ coupled with strain-free d^0 samples [181]. These are typically machined 'combs' of the sample material which relieves internal strains prior to measurement.

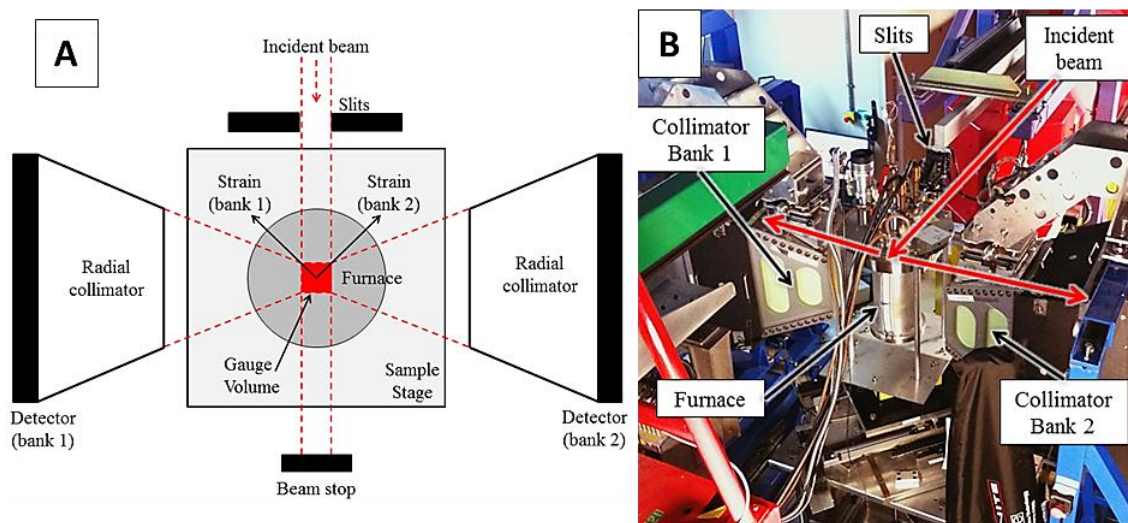


Figure 6.2 Engin-X neutron beam line experimental setup for *in-situ* heat-treatment. (a) Schematic diagram of experimental setup and gauge volume and (b) photo of experimental stage with furnace installed

The diffracted neutrons are recorded by two banks of ZnS scintillators at 90° each side of the sample, with vertical and horizontal coverage's of 21° and $\pm 15^\circ$ respectively.

For the as-cast CMSX-10N initial experiments a 2mm collimator was used with a jaw aperture of $2 \times 20\text{mm}$, giving a nominal gauge volume of 80 mm^3 . The nominal gauge volume is the volume of sample that is intersected by the incident neutron beam and the collimator coverage as defined by the incident beam slits and the diffracted beam

collimators; it therefore represents the measurement volume of material. For the solutioned CMSX-4 experiments the nominal gauge volume was modified to maximise the amount of near-surface material sampled. Therefore, a 3mm collimator was used with a jaw aperture of 3 x 20mm, giving a nominal gauge volume of 180mm³.

The samples were first scanned to ascertain the correct rotation of the test-bar single-crystal with respect to the detector banks so that the diffraction condition is satisfied. The heat-treatment furnace was subsequently installed and the test-bar was placed within the furnace at the base of the sample holder (Figure 6.3), so as to intersect with the neutron beam gauge volume at the same position and angle as without the furnace. The furnace was subsequently pumped down to a vacuum of $\sim 10^{-5}$ mbar ($\sim 10^{-8}$ atm) before heating could commence.

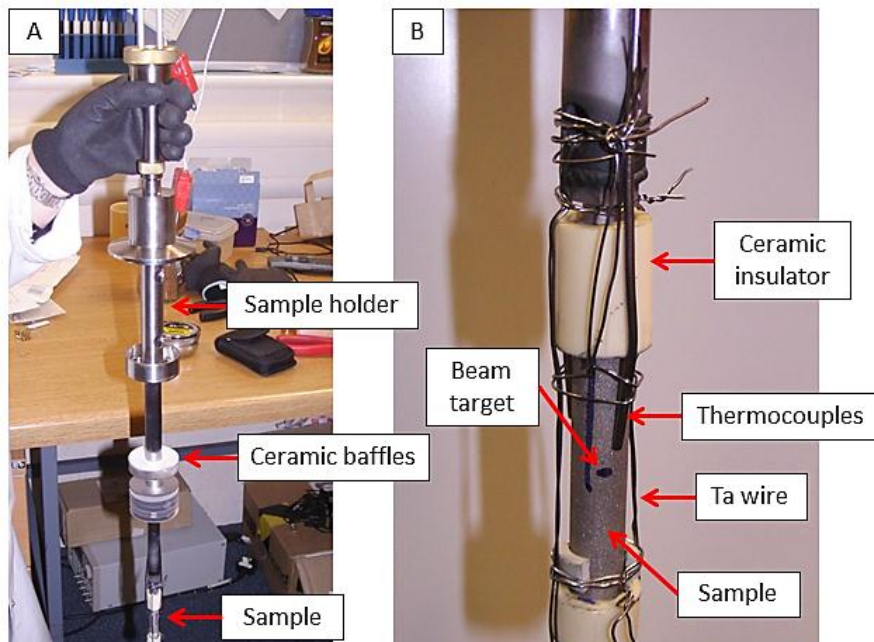


Figure 6.3 Sample holder layout. Sample is suspended at the bottom with Ta wire and insulated with Al₂O₃ ceramic. Thermocouples are placed against the sample to provide temperature feedback for the furnace control

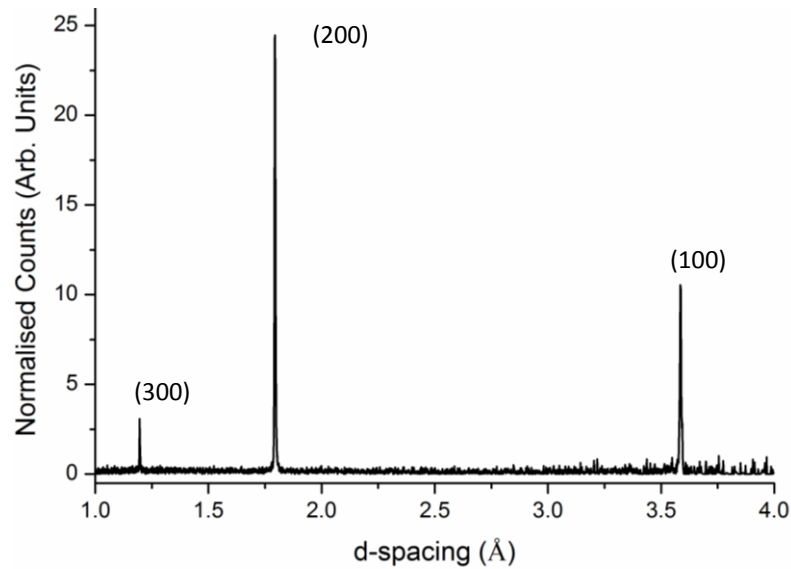


Figure 6.4 Diffraction spectra of a single-crystal test-bar obtained by TOF neutron diffraction

An example of a typical neutron diffraction spectrum is shown in Figure 6.4 where each peak is a diffraction condition for a particular lattice orientation. The diffraction pattern is comprised of the (300) and (100) superlattice reflections from the ordered $L1_2 \gamma'$ phase only, as well as the (200) doublet reflection from the combined γ/γ' phases. The misfit between γ and γ' is small so the two phases form a single, broad (200) peak. The peak heights are normalised neutron counts, with arbitrary units, that represent the volume of each phase interacted with.

Neutron diffraction (ND) spectra were collected in two positions, the middle of the sample (bulk) and the near-surface region, during *in-situ* heat-treatments of as-cast CMSX-10N and solutioned CMSX-4. For the near-surface measurements the sample stage was moved so that the gauge volume intersected only the top 1mm of the sample surface, with the rest of the gauge volume in vacuum (this does not contribute to the diffraction spectrum). This was done to capture as much surface volume as possible within the constraints of count time, neutron flux and collimator/jaw size. The heat-treatment consisted of various ramps before a final solution at 1305°C for 8 hours

and 1350°C for 25 hours for CMSX-4 and CMSX-10N respectively. These hold temperatures are slightly lower than the industry standard temperatures of 1312°C and 1363°C (respectively) due to concerns of overheating the samples caused by the inaccuracy of the thermocouples and the uniformity of the temperature gradient within the installed Engin-X furnace.

6.3.3 Optical Microscopy (OM) and Scanning Electron Microscopy (SEM)

Transverse test-bar cross-sections were cut using a diamond tipped rotary bench saw before being mounted in conducting Bakelite resin and progressively polished with grit/SiC papers followed by a final 1/4µm diamond polish for metallographic examination. Where necessary, samples were etched with a Nimonic etchant of 50ml HNO₃, 200ml HCl, 12.5g CuCl₂ and 12.5g FeCl₂ made up to 500ml with distilled water.

Test-bar surface cross-sections were initially analysed with an Olympus BX51 optical microscope at various magnifications to select appropriate areas for further SEM analysis. A FEI Sirion Field Emission Gun SEM (FEGSEM) was used operating at 15-20kV. Back-scattered electron imaging (BSI) and Secondary electron imaging (SEI) were performed at a working distance (WD) of 5mm and a spot size 5.

6.4 Results

6.4.1 Optical Microscopy and SEM of the As-Cast CMSX-10N and Solutioned CMSX-4 Test-bars

The initial surface of the as-cast CMSX-10N test-bars was first imaged using optical microscopy (OM) to confirm the starting microstructure, prior to ISIS *in-situ* heat-treatment. These test-bars were received in the as-cast and grit blasted state (so as to remove any surface oxides/eutectic formed during casting). Figure 6.5 shows the as-received surface condition from which the following observations can be made:

- i. There is a significant degree of micro-segregation within the microstructure. Large pools of eutectic can be seen in the inter-dendritic (IDP) regions.
- ii. The dendrites have grown to impinge on the surface with only small areas where the inter-dendritic eutectic has intersected the surface.
- iii. There is no evidence of any surface layer, neither γ' nor surface oxides. There is also no continuous layer of eutectic at the surface.

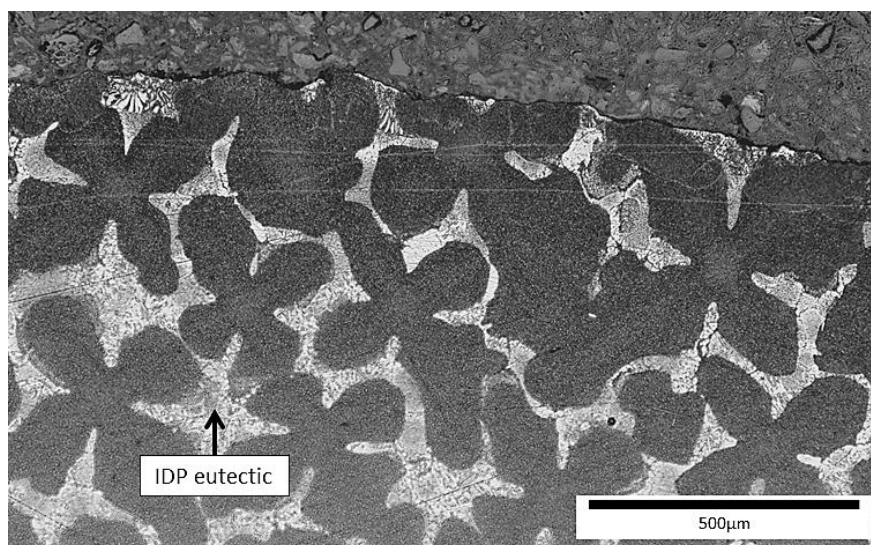


Figure 6.5 OM image of the as-received CMSX-10N test-bar surface

After the *in-situ* heat-treatment and neutron diffraction analysis at ISIS the microstructure was again investigated using OM and SEM and these are shown in Figure 6.6.

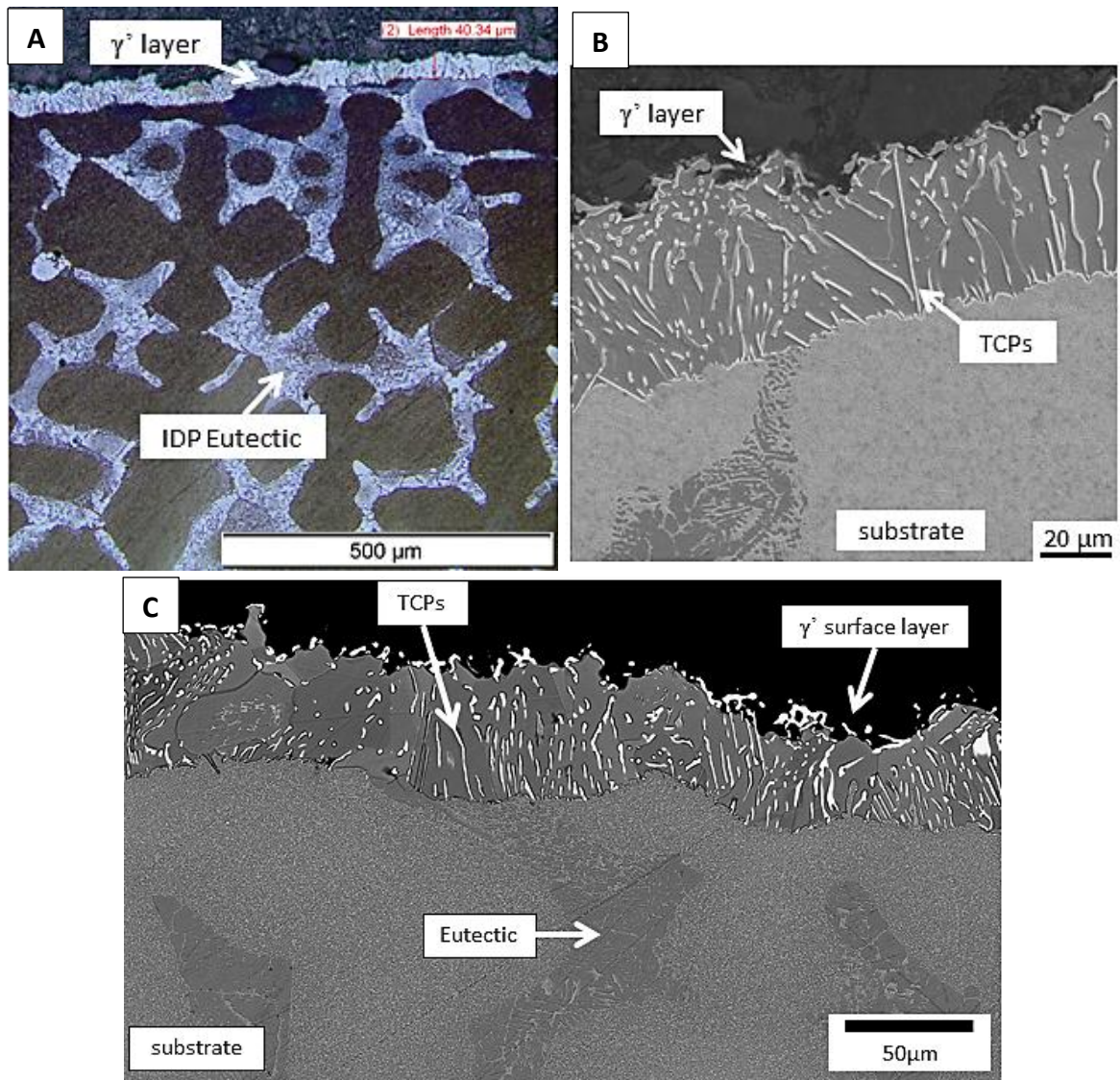


Figure 6.6 (a) OM image (b) SEI and (c) BSI of the ISIS tested CMSX-10N test bar surface. The γ' surface layer is shown in detail in (b) & (c). Of note are the TCP needles fanning out from the substrate within the γ' layer (white)

From these images the following observations about the surface region can be made:

- i. There remains a large degree of inter-dendritic eutectic after the ISIS 25 hour solution heat-treatment at 1350°C.

- ii. A γ' surface layer has evolved that is $\sim 40\text{-}50\mu\text{m}$ thick across the entire perimeter of the test-bar. This layer is populated with both needle-like and globular TCP phases, some of which fan out from the border with the substrate.
- iii. Whilst the γ' surface layer is continuous around the entire perimeter, the TCP phases within that layer are more concentrated above the dendrite arms and there is a distinct lack of TCPs growing out from the inter-dendritic regions (Figure 6.7). This is because the IDP eutectic rejects the TCP forming elements W and Re to the γ dendrite during solidification, therefore when the γ' surface layer grows into the IDP regions during solutioning, there is less W and Re and therefore less TCPs.

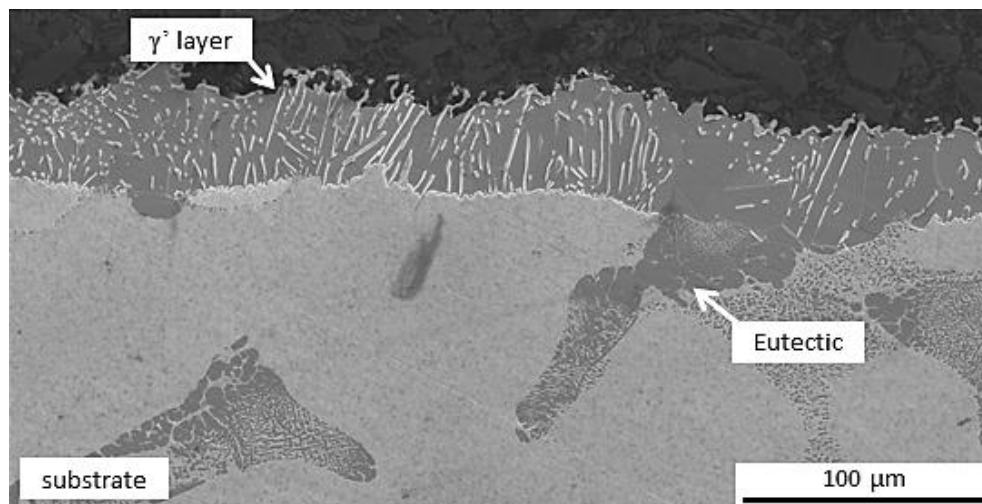


Figure 6.7 SEI of the ISIS tested CMSX-10N test bar surface detailing the lack of TCP phases within the γ' surface layer adjacent to the inter-dendritic eutectic region

The inter-dendritic regions are composed of a γ / γ' eutectic and due to the large amount of eutectic present within the as-cast CMSX-10N sample, the distinction of the γ' surface layer within the neutron diffraction spectra from the residual eutectic is impossible. It was therefore decided to repeat the experiment with solutioned CMSX-4 test-bars as this removes the problem of residual eutectic. The pre-solutioning at Bodycote removes any as-cast inter-dendritic eutectic and fully homogenises the

microstructure, whilst the CMSX-4 alloy has a lower fraction of as-cast eutectic and is less prone to post-solutioning residual eutectic due to its compositional differences to CMSX-10N (most importantly, the reduced refractory additions of W and Re).

The solutioned CMSX-4 test-bars were first grit blasted, after solutioning at Bodycote, to remove any γ' surface layer formed during this pre-solutioning. This means any detection of γ' during subsequent ISIS heat-treatment can be attributed to the formation of a new γ' surface layer (as well as the bulk γ' precipitates upon cooling below the γ' solvus temperature). In order to establish whether the grit-blast had successfully removed all remnant γ' phase from the surface the initial test-bar surface was investigated using optical microscopy (OM) and SEM. Figure 6.8 shows this surface is free of any γ' layer and that there are only re-crystallised γ grains remaining (from the prior solutioning). Any γ' layer seen after the ISIS heat-treatment is therefore a product of that heat-treatment.

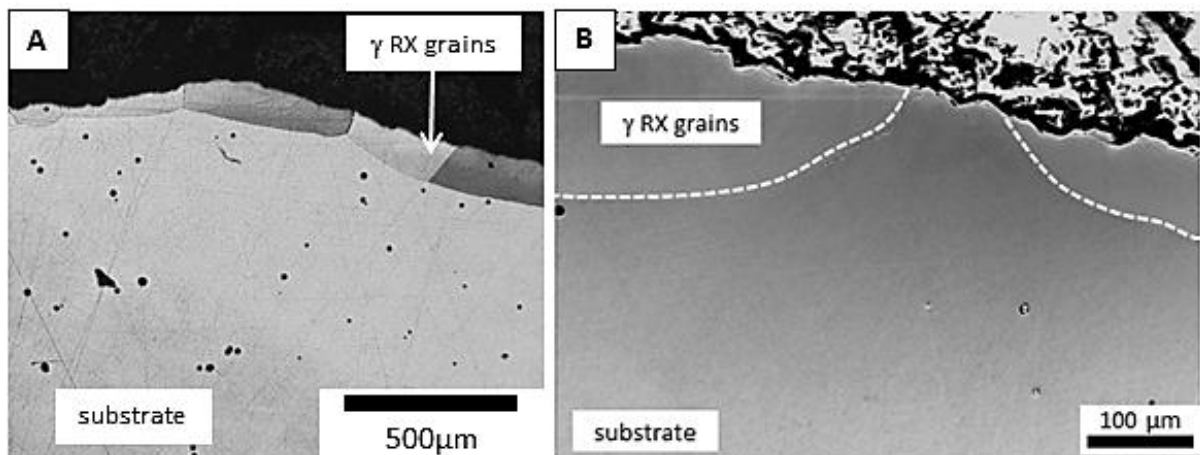


Figure 6.8 (a) OM and (b) SE images of the CMSX-4 test-bar surface prior to ISIS heat-treatment, showing the complete removal any remnant γ' surface layer. RX γ grains due to grit-blast/solutioning are highlighted in (b)

The OM and SEM surface analysis was repeated on the test-bar after the *in-situ* heat-treatment and analysis at ISIS and these results are shown in Figure 6.9 to Figure 6.10.

The formation of the surface γ' layer is apparent from the OM image in Figure 6.9 and it is $\sim 40\text{-}50\mu\text{m}$ across the entire perimeter of the test-bar. From the SE image in Figure 6.10 it is possible to see that the γ' surface layer is populated with TCP phases (appearing bright in SE) and that there are no remaining γ channels within the layer.

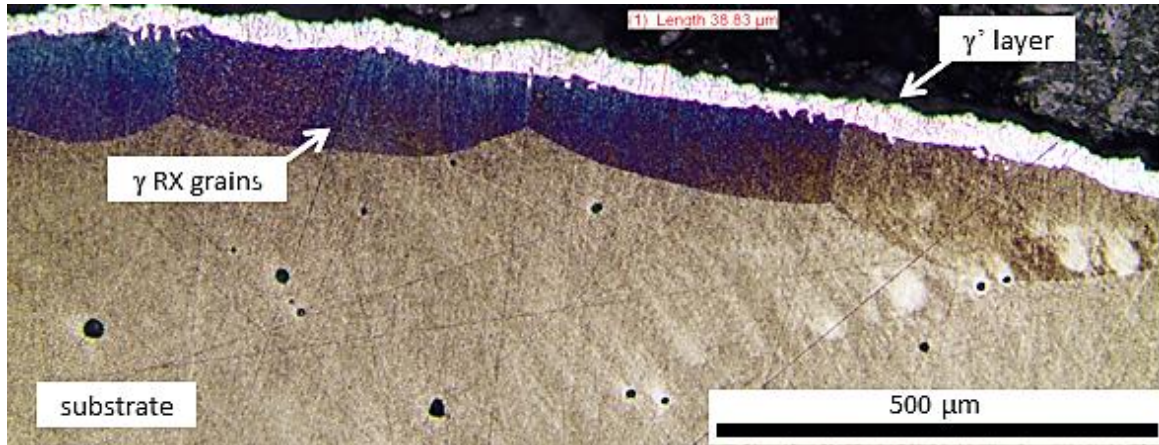


Figure 6.9 OM of the ISIS test-bar surface. The γ' surface layer is clearly visible in white above the γ RX grains

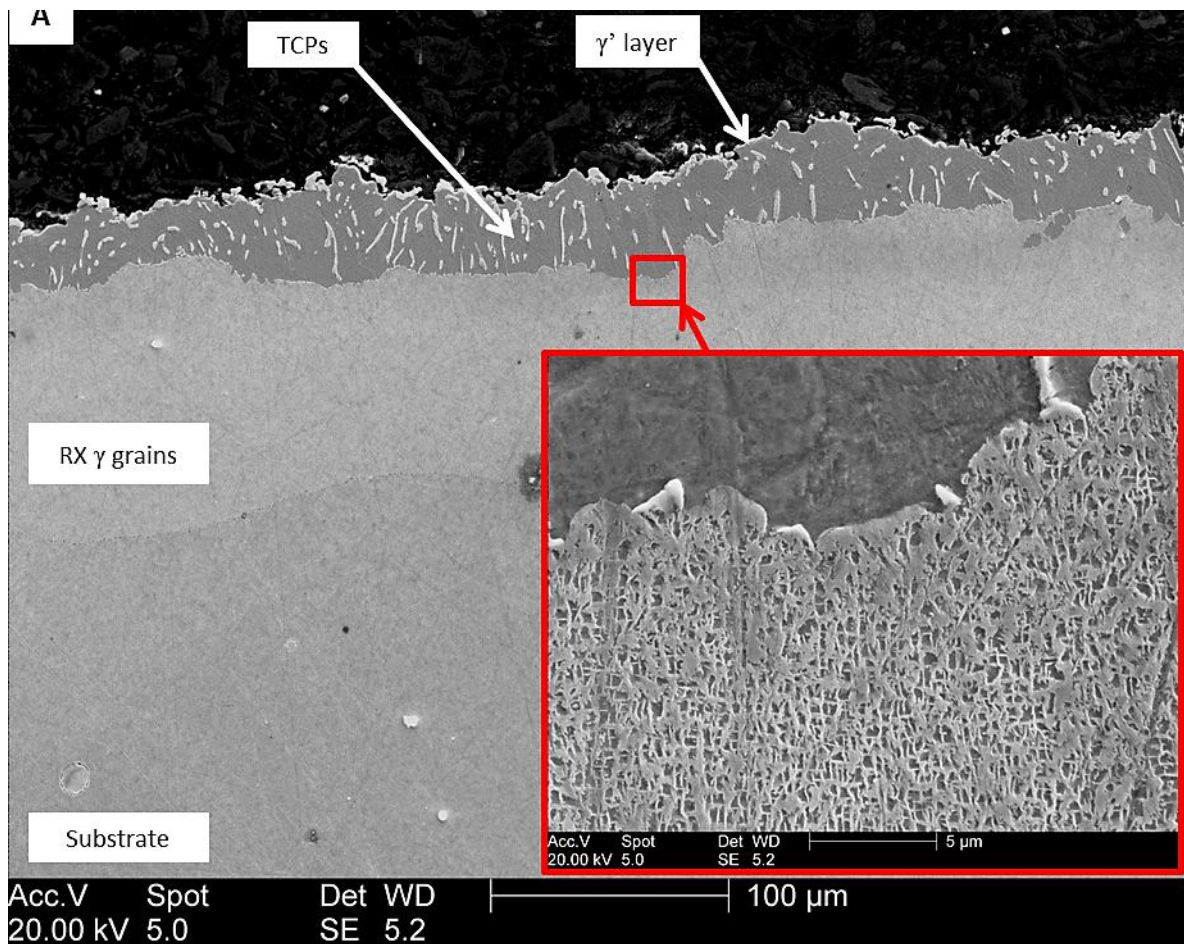


Figure 6.10 (a) SEM image of the ISIS solutioned test-bar surface and (b) close-up of the interface with the γ RX grain below. The γ' surface layer is clearly visible, as are the TCPs formed within this layer. Of note is the way the γ' layer has grown into the substrate, consuming the γ RX grains where possible

In some instances the γ' layer can be seen to have consumed the whole of the γ RX grain below, up to and arresting at the border with the substrate. This is visible because the plane in which the test-bar was cut (perpendicular to the surface) has intersected the plane in which the γ' layer has grown, which is not always the case (Figure 6.11(b)).

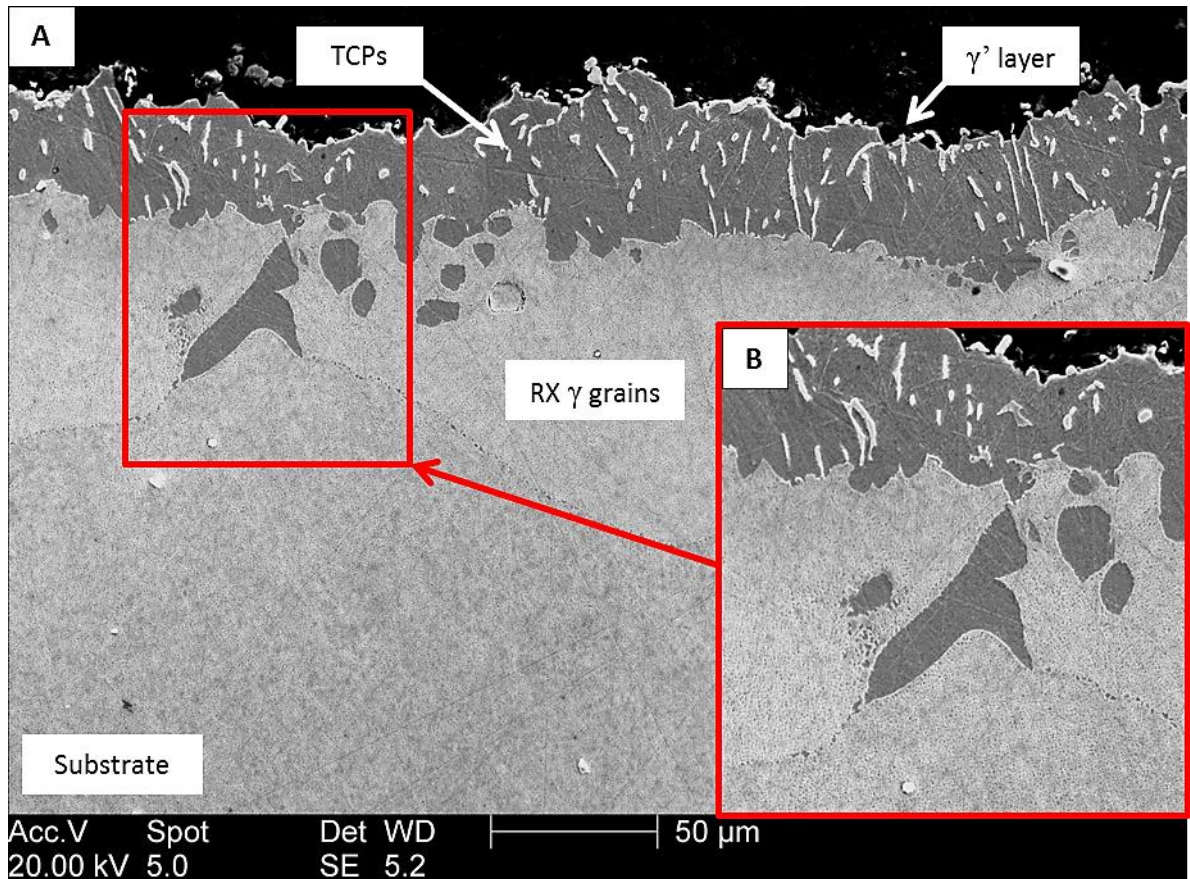


Figure 6.11 (a) SEM image of the ISIS solutioned test-bar surface and (b) close-up of an area where the γ' layer has consumed the RX γ grain up to the border with the substrate

The analysis of both test-bar surfaces shows that a γ' layer was grown during the neutron diffraction analysis experiments and that, in the case of the solutioned CMSX-4, there is no contribution from any previously grown γ' surface layer. It is also clear that the thickness of the γ' surface layer is greater than that seen after the standard industry solutioning at Bodycote, discussed in Chapter 4 ($\sim 40\mu\text{m}$ compared to $\sim 20\mu\text{m}$). This is further proof that elemental vapourisation is the cause of this surface instability

since the ISIS furnace uses a higher vacuum than Bodycote ($\sim 10^{-8}$ atm vacuum at ISIS compared to $\sim 10^{-4}$ atm partial pressure of Argon at Bodycote) that is constantly pumping and would therefore increase the rate of elemental loss to evaporation.

6.4.2 Neutron Diffraction Analysis of As-Cast CMSX-10N

In-situ heat-treatment of as-cast CMSX-10N alloy was carried out to ascertain the bulk phase transition temperatures and to ascertain whether the γ' surface layer can be distinguished. The room temperature bulk neutron diffraction (ND) spectra is shown in Figure 6.12; detailing the (200) γ/γ' peak and the (100) γ' peak.

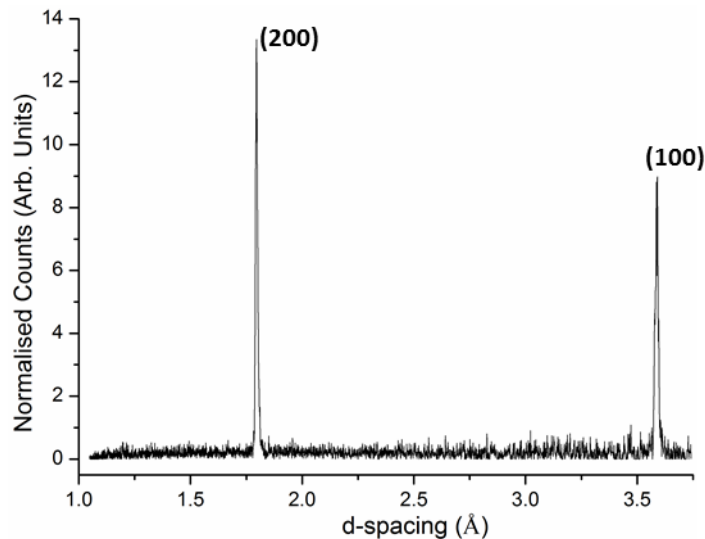


Figure 6.12 Room temperature ND spectra of the as-cast CMSX-10N bulk alloy

Following the room temperature measurements the *in-situ* heat-treatment was started, following a commercial CMSX-10N heat-treatment profile with a final solutioning temperature of 1350°C, and the dissolution of the (100) γ' peak was tracked. The bulk phase evolution is shown in Figure 6.13 from room temperature to 1350°C + 1 hour isothermal hold. The thermal expansion of the γ' crystal lattice is evident from the right-ward drift of the peak from $\sim 3.59\text{Å}$ to $\sim 3.66\text{Å}$ ($\Delta = 0.07\text{Å}$) and the gradual dissolution of the γ' phase can be identified by the reduction in peak height. At room temperature the peak height is 9 whilst at 1350°C this dropped to

below half that value, ~ 3 . After 1345°C there is however no change in the (100) peak height suggesting that the γ' phase is no longer dissolving. Of note is that the peak height is a measure of normalised neutron counts whose units are arbitrary. The greater the peak height however, the greater the volume of phase that is present.

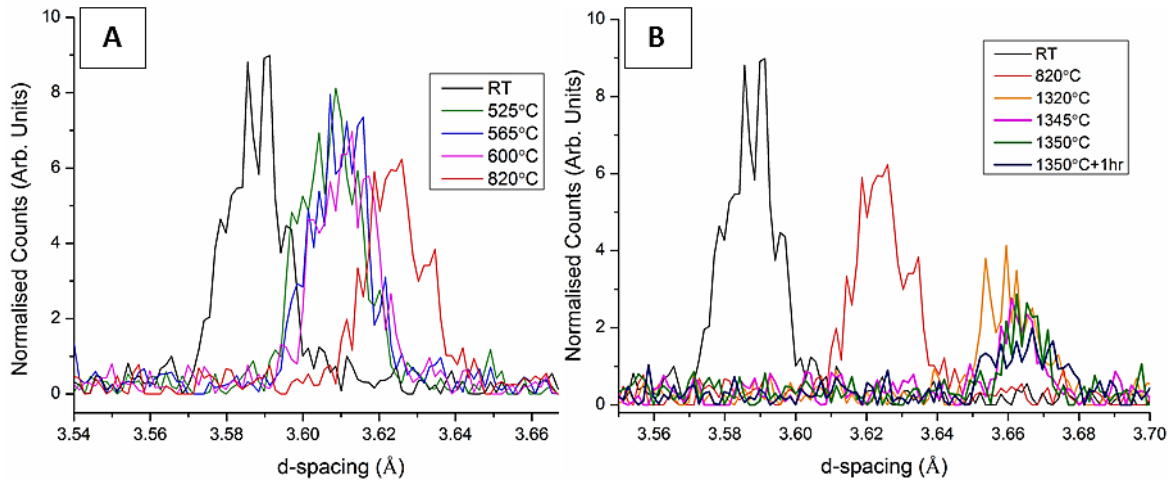


Figure 6.13 Dissolution of the (100) γ' peak from room temperature to $1350^\circ\text{C}+1\text{hr}$; (a) dissolution begins $\sim 525^\circ\text{C}$ (b) final stage of dissolution occurs $\sim 1345^\circ\text{C}$ after which dissolution of the γ' stops

The evolution of the γ/γ' (200) peak is shown in Figure 6.14 with a corresponding reduction in peak height as the γ' phase component is dissolved. Similar to the (100) peak, there is no change in peak height after 1320°C (the sudden increase at 1345°C is most likely an anomalous reading). The thermal expansion is also clear as the rightward movement of the peak from $\sim 1.78\text{Å}$ to $\sim 1.84\text{Å}$ ($\Delta = 0.04\text{Å}$).

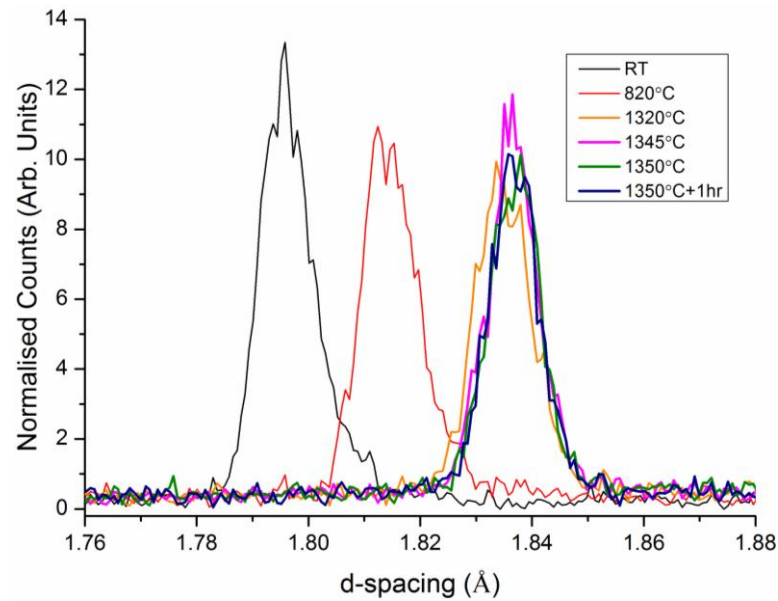


Figure 6.14 Dissolution of the (200) γ/γ' peak from room temperature to 1350°C+1hr

The neutron gauge volume was subsequently moved to the near-surface position after an isothermal hold of 18 hours at 1350°C and a diffraction spectra was collected which is shown in Figure 6.15. It is clear that there is still a significant amount of γ' phase remaining at the near-surface region after isothermal heat-treatment for 18 hrs since the (100) peak is clearly visible.

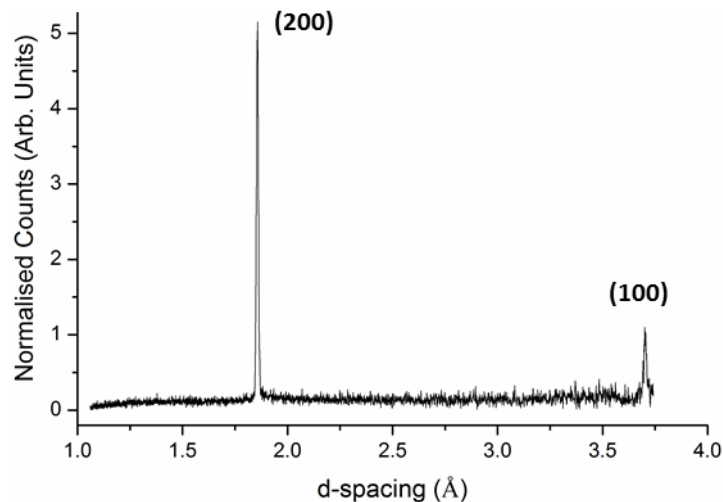


Figure 6.15 ND spectra from the near-surface region of as-cast CMSX-10N after heat-treatment at 1350°C for 18hrs

However, this cannot be confidently attributed to a γ' surface layer since there is a large amount of remnant inter-dendritic eutectic (γ/γ') in the post-test microstructure (see Figure 6.6). It was therefore decided to repeat the experiment using fully

solutioned CMSX-4 alloy test-bars with the aim of removing the inherent as-cast microstructural segregation (therefore removing any remnant inter-dendritic eutectic phases) and the measured (100) peak can thus be contributed solely to bulk γ' and/or the formation of the γ' surface layer.

6.4.3 Neutron Diffraction Analysis of Solutioned CMSX-4

6.4.3.1 Room temperature measurements

The first neutron diffraction (ND) spectra were collected at room temperature from the centre and surface regions as a reference for further measurements; these are shown in Figure 6.16 and Figure 6.17. All spectra were collected with the test-bar positioned within the heat-treatment furnace. The (300) and (100) γ' superlattice peaks are seen on the left and right of the normalised spectra (1.2\AA and 3.6\AA respectively), whilst the (200) γ/γ' peak (1.8\AA) is seen as the largest, central peak.

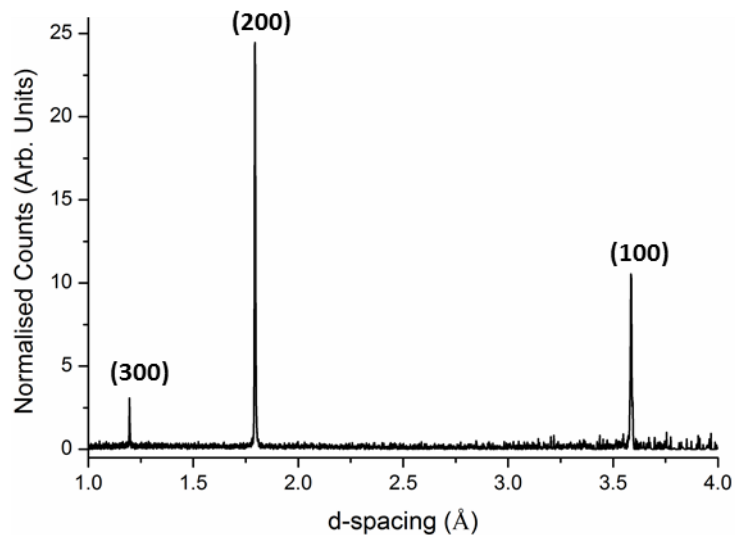


Figure 6.16 Room temperature ND spectra from the centre of the solutioned CMSX-4 test-bar

Figure 6.17(a) shows the spectrum collected from position 3, the surface measurement, and Figure 6.17(b) shows there is the addition of the (311), (220) and

(111) peaks at 1.08Å, 1.275Å and 2.08Å respectively within the lower end of this spectrum.

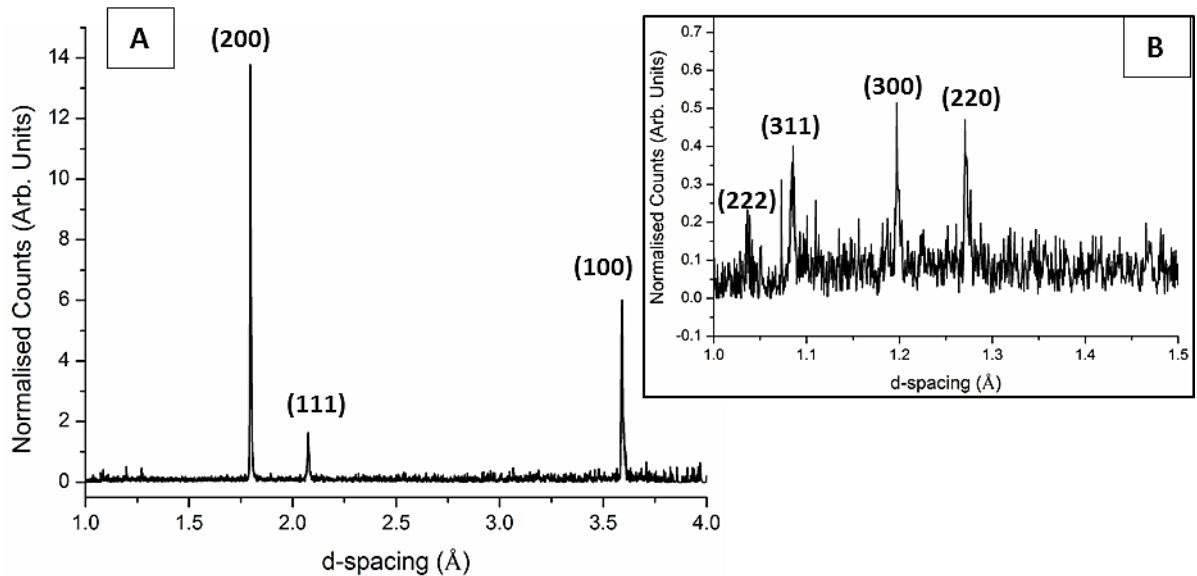


Figure 6.17 (a) Room temperature ND spectra from the surface of solutioned CMSX-4 (b) zoom of left-hand region

From Figure 6.8 and Figure 6.17 it is clear that these additional peaks are from the remnant re-crystallised (RX) γ grains present at the surface of the test-bars due to prior grit-blasting and solutioning at Bodycote.

6.4.3.2 *In-situ* heat-treatment – Dissolution of bulk γ'

The dissolution of bulk γ' during *in-situ* heat-treatment was investigated using the spectra from the middle of the test-bar. This allows conclusions to be made later as to whether a surface γ' layer is evolving at temperatures where the bulk γ' has dissolved. The dissolution of γ' is detected by analysing the reduction in the heights of the (100) and (200) peaks and when all the γ' is dissolved the (100) peak will disappear from the spectra.

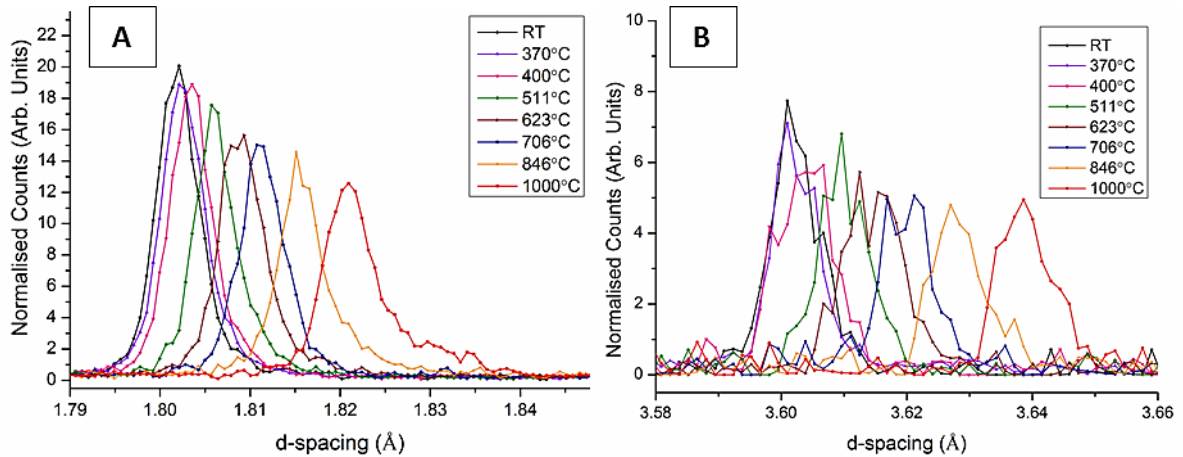


Figure 6.18 Dissolution of bulk γ' from room temperature to 1000°C; (a) (200) γ/γ' peak (b) (100) γ' peak

The dissolution of bulk γ' commences by 511°C, evident by the peak reduction in the (200) and (100) peaks (Figure 6.18). The dissolution progresses steadily until, at 1000°C, both peaks have lost of third of their size, showing that a considerable amount of γ' has dissolved.

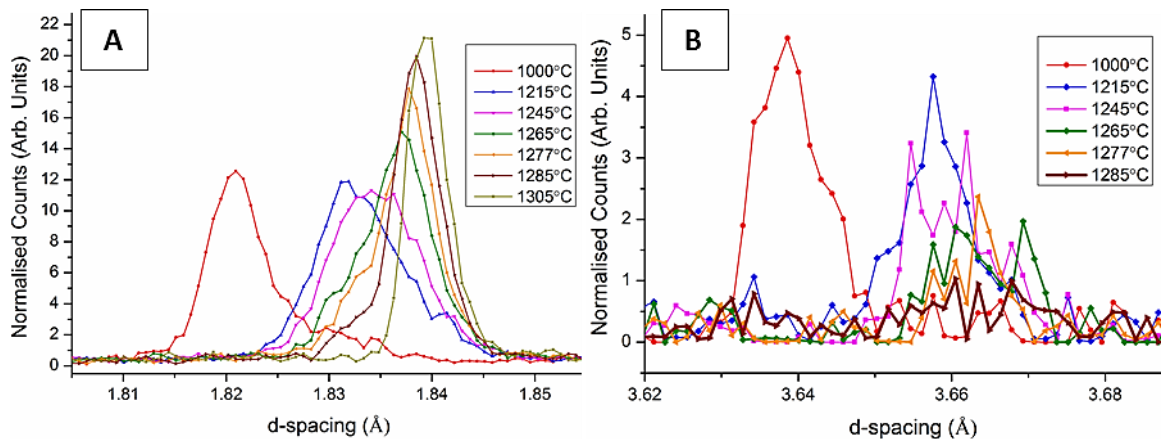


Figure 6.19 Final stages of bulk γ' dissolution; (a) (200) γ/γ' peak from 1000-1305°C (b) (100) γ' peak from 1000-1285°C, showing final dissolution at 1285°C

The final stages of γ' dissolution is shown in Figure 6.19. It can be seen in Figure 6.19(b) that all bulk γ' phase disappears by 1285°C whilst in Figure 6.19(a) the (200) peak can be seen to recover in size, after 1245°C, to a magnitude identical to which it started. These results also show that (100) γ' crystal lattice expands by 0.08Å between RT and 1285°C and the (200) γ/γ' expands by 0.04Å between RT and 1305°C. These values correspond to mismatch's of zero both at room temperature and at 1305°C (since $d=a/\sqrt{h^2+k^2+l^2}$).

6.4.3.3 In-situ heat-treatment – Formation of the γ' surface layer

In order to track the formation of the γ' surface layer the sample was moved to a position where the neutron beam would sample material from the top ~ 1 mm of test-bar perimeter (the remaining gauge volume is outside of the sample). The following figures present the (200) γ/γ' and (100) γ' ND spectra for this area from room temperature, through heat-treatment to isothermal hold at 1305°C for 7 hours. The dissolution of γ' from the near-surface is shown in Figure 6.20 from room temperature to 1000°C. The amount of γ' is not significantly reduced within this temperature range, in contrast to the bulk measurements above.

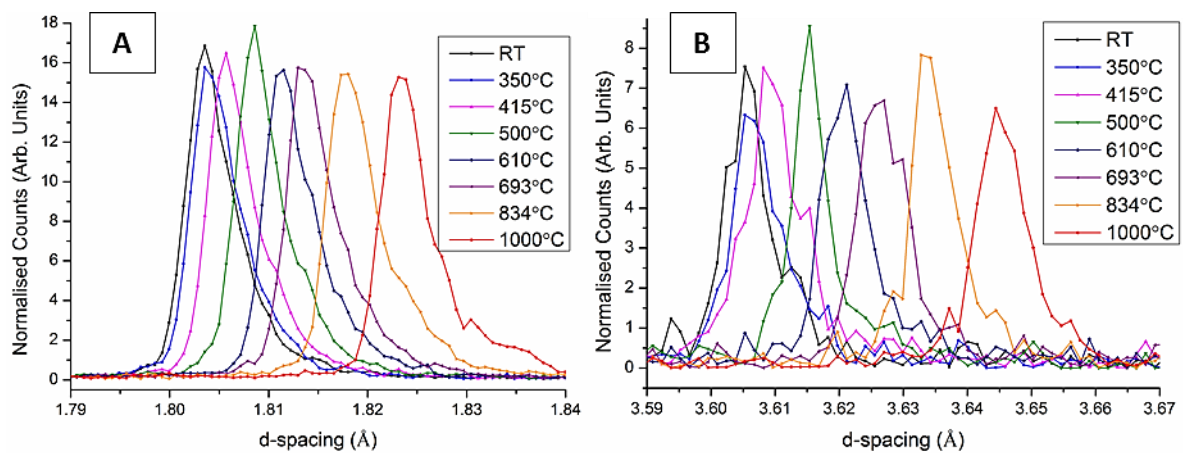


Figure 6.20 Dissolution of surface γ' from room temperature to 1000°C; (a) (200) γ/γ' peak (b) (100) γ' peak

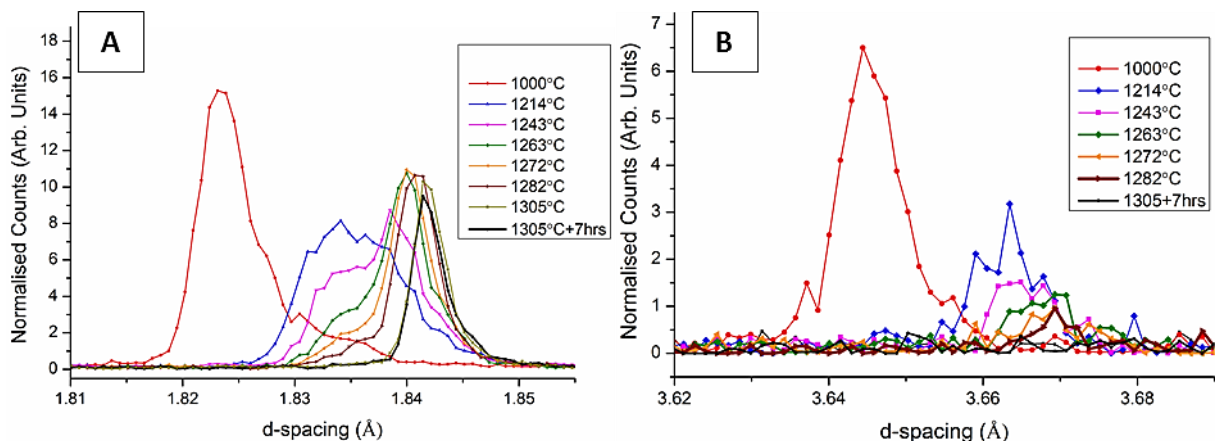


Figure 6.21 Final stages of surface γ' dissolution; (a) (200) γ/γ' peak from 1000-1305°C+7hr hold (b) (100) γ' peak from 1000-1305°C+7hr hold, final dissolution of γ' noted at 1289°C

Figure 6.21 details the final dissolution of γ' from 1000°C to 1305°C (and at the end of the 7 hour isothermal hold) which occurs at $\sim 1282^\circ\text{C}$ and agrees with the bulk γ' dissolution seen in Figure 6.19. In contrast to the bulk measurements, the (200) γ/γ' peak does not recover to its room temperature height as the temperature increases and the γ' dissolves.

The next figure details the evolution of the (100) peak through isothermal hold for a total of 8 hours. From the previous spectra, above 1289°C the (100) γ' peak should be located at $\sim 3.66\text{-}3.67\text{\AA}$.

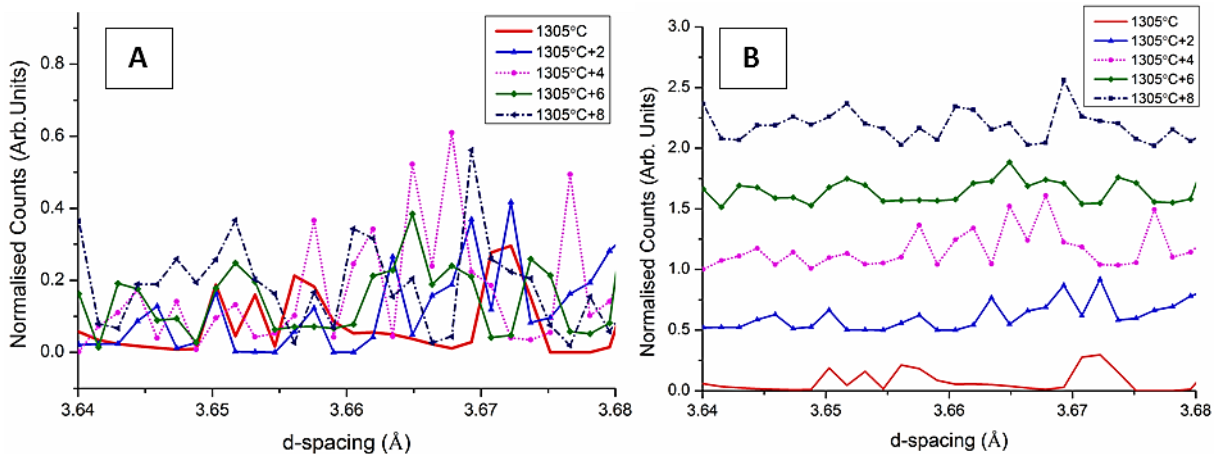


Figure 6.22 (a) Evolution of the (100) γ' peak through isothermal hold at 1305°C for 8 hours (b) Offset (+0.5) spectra

Figure 6.22(a) hints at the existence of a (100) γ' peak at $\sim 3.67\text{\AA}$ however when these spectra are analysed further, and offset to distinguish them more clearly, discerning a valid (100) peak becomes impossible (Figure 6.22(b)) due to the background noise.

The ND spectrum also contains the (300) γ' peak at $\sim 1.2\text{\AA}$, however this end of the spectrum has a lower signal to noise ratio than the (100) and (200) peaks, making identification much harder. Figure 6.23 shows the evolution of the (300) peak from room temperature to 1305°C , from which it is seen to disappear by 1281°C . The re-

crystallised grains are clear either side of the (300) peak at room temperature but become less so as temperature rises; the (220) remaining the clearest of the two at 1305°C.

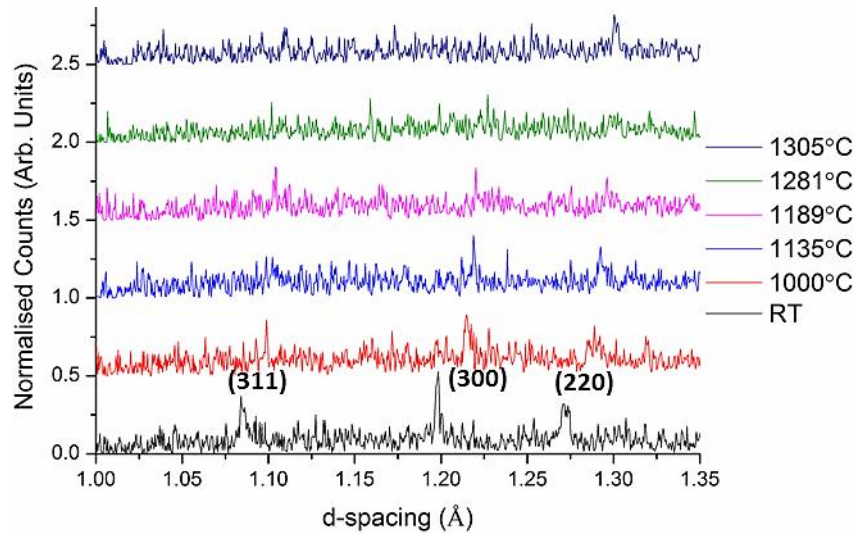


Figure 6.23 Offset (+0.5) spectra of the (300) and RX grain peaks showing evolution from room temperature to 1305°C

Figure 6.24 shows the peak evolution during the 8 hour isothermal hold and it is clear that no visible (300) γ' peak has evolved during this time; the only visible peak being the (220) RX grain at 1.3Å.

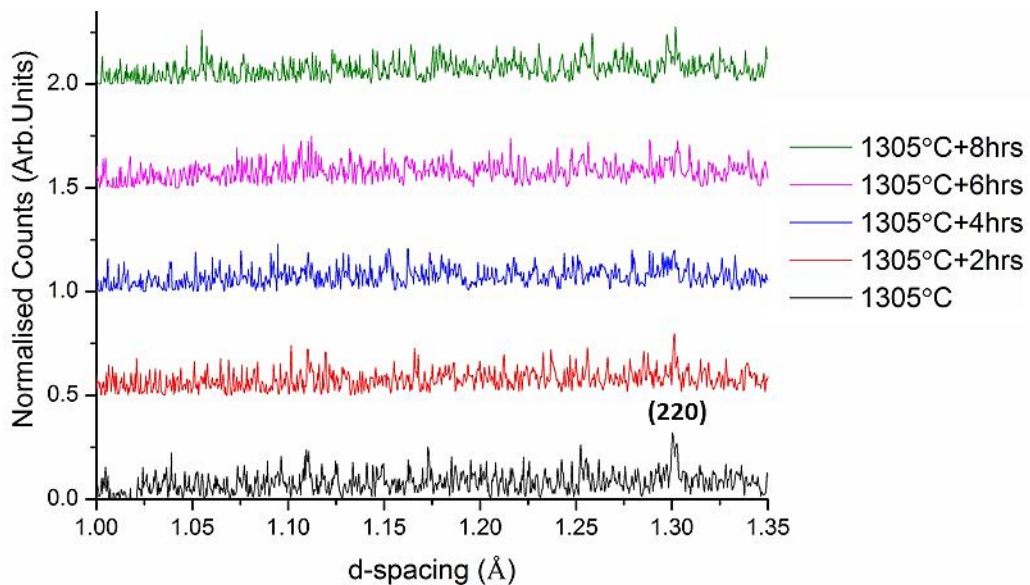


Figure 6.24 Offset (+0.5) spectra of the (300) and RX grain peaks showing evolution during 1305°C hold

Figure 6.25 shows the evolution during final cooling/quench, which was unfortunately too fast to measure spectra at the same temperature intervals as was done on heating.

It is however clear that the (300) γ' peak has reappeared by 1050°C, which is as expected from bulk γ' re-precipitating and not indicative of the formation of a γ' surface layer.

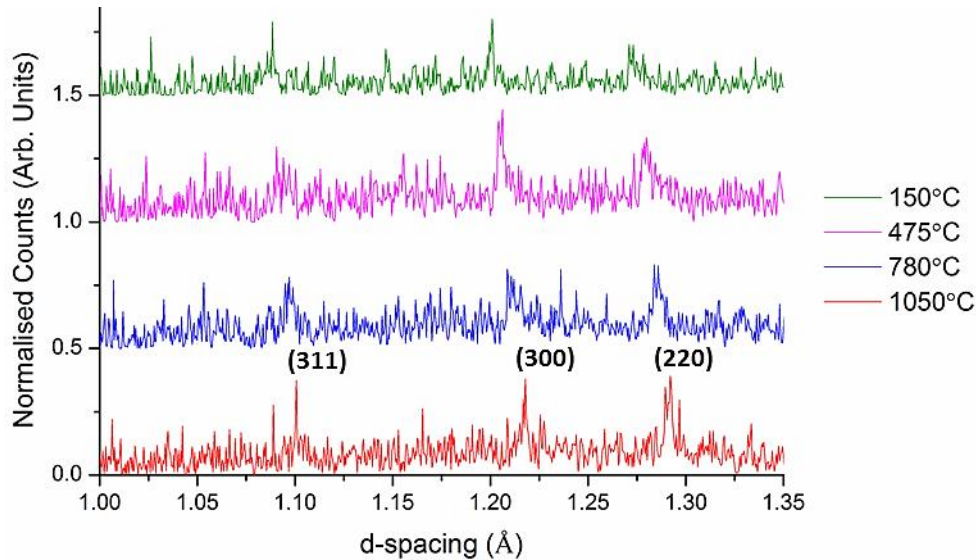


Figure 6.25 Offset (+0.5) spectra of the (300) and RX grain peaks showing evolution during cooling from 1305°C

6.5 Discussion

6.5.1 Microstructural Analysis

From the microstructural analyses of both the CMSX-10N and CMSX-4 test-bars it is seen that the γ' surface layer evolves during the ISIS heat-treatment experiment and that this layer is thicker than the γ' layer found on test-bars solutioned at Bodycote (see Chapter 4). The typical Bodycote γ' layer thickness is $\sim 20\mu\text{m}$, however the γ' layer is $\sim 40\text{--}50\mu\text{m}$ in the ISIS heat-treatment experiment. There is also a noticeable greater fraction of TCP phases within the γ' surface layer on the CMSX-10N alloy than for CMSX-4. This is due to the larger wt.% of refractory elements like Re and Ta (W is slightly lower by 1wt.%) in CMSX-10N and their insolubility within the γ' phase. Therefore as the γ' layer grows into the substrate, the refractory elements precipitate out as TCPs. This process is enhanced due to the low diffusivity of these elements,

particularly Re, within the Ni matrix [54]. It is also seen in Figure 6.11(b) that the γ' surface layer grows into, and consumes, the RX γ grains below. This is proof that the γ' surface layer forms after the RX grains and that the RX grains do not nucleate and grow from the γ' layer boundary. The advancing γ' layer is arrested at the existing RX grain boundary suggesting that there is insufficient energy remaining for the γ' layer to migrate the boundary, or to nucleate new grains.

The increased thickness of the γ' surface layer is an interesting observation and adds evidence to the conclusion that it is elemental evaporation that is the cause of its formation. In the Bodycote furnace, the chamber is pumped down to a vacuum of $\sim 10^{-7}$ atm up to a temperature of 1040°C, after which Ar is introduced to a partial pressure of $\sim 10^{-4}$ atm and the diffusion pumps are switched off (the vacuum pump remains on and Ar is bled in continuously to maintain the P_{Ar}). In comparison, the ISIS furnace is held at a vacuum of $\sim 10^{-8}$ atm throughout the entire experiment, with no Ar atmosphere, using a turbomolecular pump. This difference means that the vapours that evolve from the test-bar surface are removed from the ISIS furnace chamber, via the turbo pump, at a greater rate and the atmosphere does not reach an equilibrium saturated vapour state, where the rate of evaporation is equal to the rate of condensation (known as saturated vapour pressure). Instead, the evaporative rate to a vacuum, given by the Langmuir equation ($E_i = \frac{P_i}{\sqrt{2\pi M_i RT}}$), under equilibrium conditions describes the largest possible evaporation rate from the surface for a given temperature. Thus the fractions of the total Langmuir loss considered in Chapter 5 become higher in this scenario and the mass loss of material to evaporation in the ISIS

furnace is higher than that for the Bodycote furnace; consequently the γ' surface layer is thicker.

6.5.2 Neutron Diffraction Analysis

6.5.2.1 Gauge Volume Effects

In Section 6.3.2, the methodology for the neutron experiments was described and, in particular, the time-of-flight (TOF) neutron diffractometer and nominal gauge volumes were discussed. The nominal gauge volume (x, y, z mm³) is important, since this the user-defined variable key to achieving the desired sample volume and count-time / neutron intensity. The nominal gauge volume (NGV) does not however accurately describe the true, or instrument, gauge volume (IGV) since it does not consider the angular divergence of the neutron beam which gives rise to a penumbra (as shown in Figure 6.26). This penumbra results in a gradual decline in the contribution to the diffracted peak intensity from grains in the sample situated at the edge of the volume, and creates an associated blurred edge to the diffracted intensity profile [182].

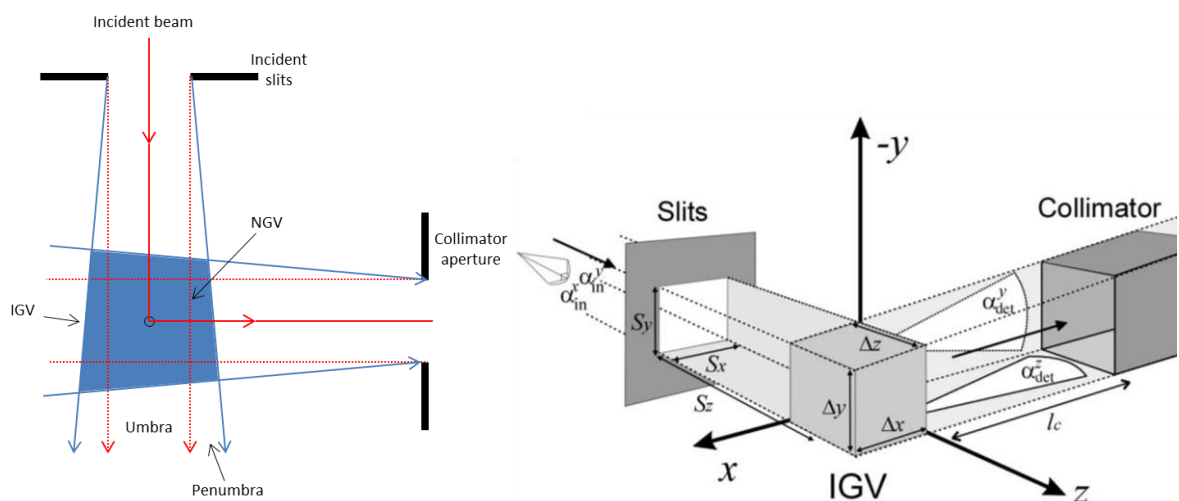


Figure 6.26 (a) Illustration of the Nominal Gauge Volume (red) and Instrument Gauge Volume (blue). (b) 3-dimensional illustration of the IGV arising from the scattering of the incident and diffracted neutron beams, defined by the scattering angle, $\alpha_{in,det}^{x,y,z}$ (adapted from [199])

The IGV is conventionally defined by a contour map, whose edge is taken to be that where the contributing diffracted intensity falls below a fraction of that in the centre. An example IGV contour map of the ENGIN-X diffractometer is shown in Figure 6.27 and perfectly illustrates the blurred edge of the IGV.

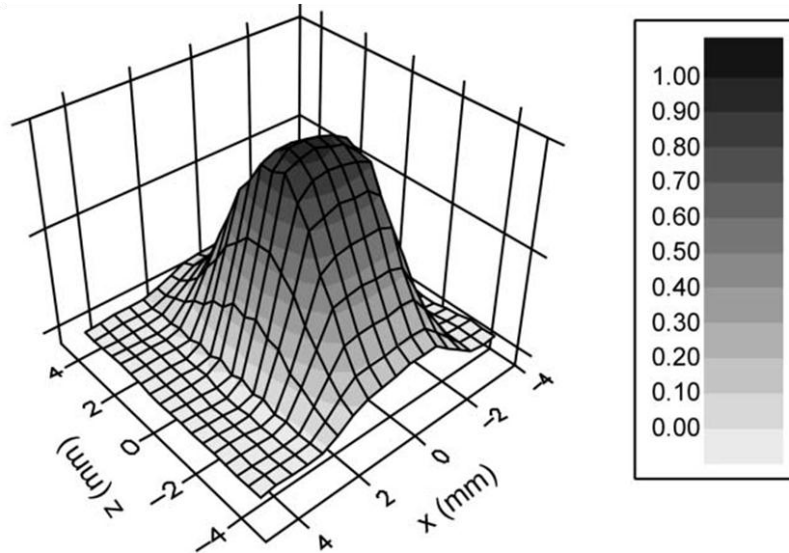


Figure 6.27 Example contour map of the ENGIN-X IGV taken from [199]. Measured by scanning a 0.25mm thin nylon thread across the horizontal plane (x,z)

The edge profile of the IGV is described by an error function, with a width defined by the beam divergence and slit distance, S_z , along the beam direction (see Figure 6.26(b)). The IGV is defined as a cuboid of dimensions $\delta V = \Delta x \Delta y \Delta z$, where Δx and Δy are given by the full-width-half-maximum (FWHM) of the incident beam profile and Δz is given by width of the intensity profile at the collimators [199].

For near-surface measurements, as in this Chapter, the IGV may only be partially filled by the sample; therefore the effective centroid of the IGV will differ from its geometric centre, since neutrons are only scattered from the partially filled volume (Figure 6.28 as a general case, and Figure 6.29 for the case of these experiments).

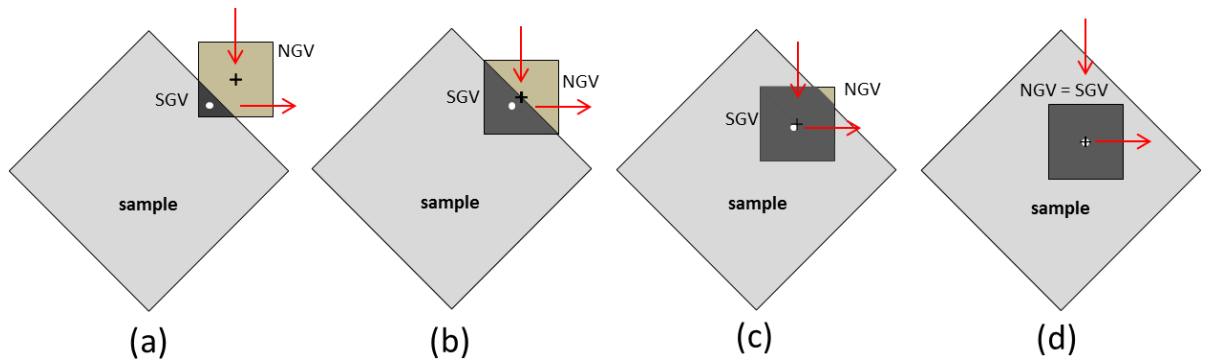


Figure 6.28 Illustration of SGV (dark) partially filling the nominal gauge volume (NGV) as the sample is translated into the NGV. The distance between the dot and the cross shows the variation in the geometric centroid of the SGV and NGV, resulting in a shift in the measured d -spacing's (illustration adapted from [182])

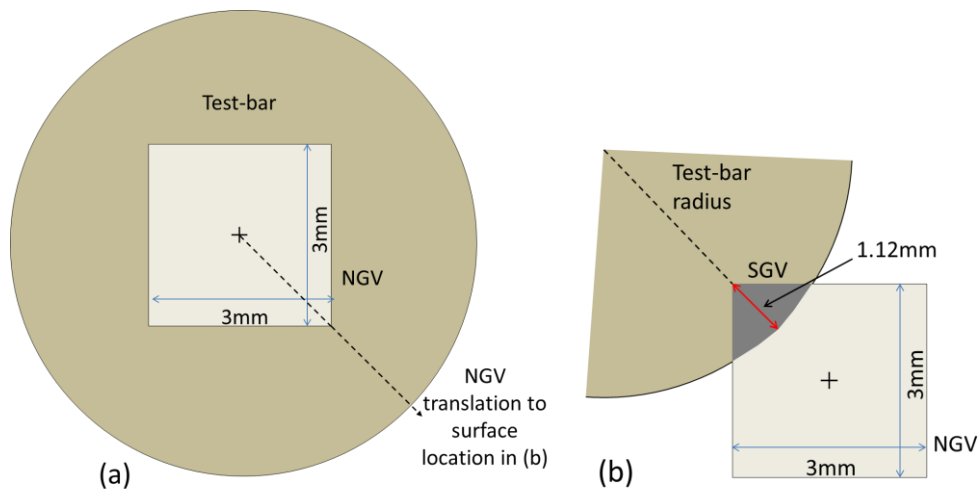


Figure 6.29 Schematic diagram of the two experimental positions used in this Chapter, (a) the bulk measurement position and (b) the surface measurement position, detailing the intersecting SGV with the test-bar radius

In addition, if there is significant attenuation of the neutrons across the gauge volume then an ‘effective’ or average-weighted centroid of the SGV must be given, taking into consideration the effects of partial filling of the IGV and beam attenuation; further complicating the displacement from the NGV geometric centroid. Even if the sample completely fills the gauge volume, beam attenuation can still result in an offset between the SGV centroid and that of the IGV [182] [200].

The offset of the geometric centroid means that, in addition to the position of the measurement being offset, the total neutron flight path length, L , and Bragg angle, θ ,

will also differ slightly. This combination will result in a corresponding variation in the measured peak d -spacing according to:

$$\frac{\Delta\tau}{\tau} = \frac{\Delta d}{d} + \frac{\Delta(L \sin \theta)}{L \sin \theta} \quad \text{Equation 6.3}$$

Where τ = the time-of-flight, d = d -spacing, L = path length, θ = Bragg angle.

The time-of-flight term, on the left hand-side, denotes the shift in the diffraction peak whilst the d -spacing and path length terms, on the right hand-side, denote the lattice-strain and pseudo-strain components, respectively. The pseudo-strain is the result of the partial filling of the gauge volume and the attenuation through the sample and must be accounted for, if accurate strain measurements are required [200]. In the case of the experiments in this Chapter, this is not necessary as the aim is to track the formation and dissolution of phases (the γ' phase in particular) by their corresponding peak heights. Therefore, knowledge of this pseudo-strain derived peak-shift is only required in order to accurately identify the correct phase peak position.

The effect of pseudo-strain due to partial filling of the IGV is evident when comparing the bulk and surface diffraction spectra for CMSX-4 (Figure 6.18 and Figure 6.20 respectively). The (200) and (100) peak positions for the bulk measurement in Figure 6.18 (at room temperature) are only very slightly shifted to the right of their nominal d -spacing's of 1.8\AA and 3.6\AA respectively. In comparison, the (200) and (100) peak positions for the surface measurement in Figure 6.20 shows a larger right-ward shift of $\sim 0.05\text{\AA}$ (although it is noted that this is not a considerably large shift).

As well as introducing a shift in the lattice spacing, the partial filling of the gauge volume also reduces the effective beam intensity. According to the paper by Santisteban *et al* [199] the shape of the ENGIN-X IGV beam intensity contour plot tails off from its maximum, to its minimum, over a distance of ~2mm (see Figure 6.27). Evidently, this means that when conducting the surface measurements in this Chapter the blurred nature of the gauge volume edge will result in lower beam intensities for the surface measurements, than for the bulk. To compensate for this, the count-time for each surface measurement was correspondingly increased to double that of the bulk measurements.

6.5.2.2 As-cast CMSX-10N

As-cast CMSX-10N test-bars were chosen as the initial experimental alloy due to its propensity to form the surface melt blister defect on turbine blades, as well as the γ' surface layer on test-bars. The aim of the experiment was to track the phase evolution, through the use of neutron diffraction, during *in-situ* solution heat-treatment and to identify the formation of the γ' surface layer via comparison with the bulk material.

The dissolution of bulk γ' begins at ~525°C and halves in intensity by 1320°C (it is worth noting that there is a +5°C increase in temperature between the start of each spectral collection and the end since the furnace is continuously heating). The final dissolution of γ' is not observed since the final isothermal hold temperature, 1350°C, and solution time were not sufficiently high enough to exceed the γ' solvus temperature and dissolve the large fraction of as-cast eutectic. This was due to initial concerns that the furnace used for these experiments would not be able to follow the standard heat-treatment profile to a high enough accuracy, or would overshoot

excessively, causing melting of the sample rather than the solid-state γ' formation. The origin of the detected γ' during solutioning can be seen to have contributions from the inter-dendritic eutectic and γ' precipitates within the dendrite arms, as well as the evolved γ' surface layer, in the post-test surface analysis (Figure 6.6), with the eutectic contributing a larger volume fraction. For this reason it was impossible to positively identify in the neutron diffraction spectra the formation of the γ' surface layer, despite confirmed knowledge of its formation.

Ordinarily there should be no detection of the γ' phase at the upper hold temperature, since it should have been taken into solution, and this therefore points to key experimental errors that were addressed for the next experiment, namely:

- The choice of solutioning temperature was not sufficiently high enough to take all the bulk γ' into solution. This is a consequence of the choice of alloy, and the fact that it is in the as-cast condition with a large fraction of residual eutectic.
- The 'heat-treatment window' (the temperature between the γ' solvus and incipient melting) is narrowed by using as-cast CMSX-10N compared to an alloy that has been solutioned to homogenise its microstructure. The micro-segregation is also more severe in CMSX-10N than compared to CMSX-4 due to the higher levels of refractory elements (such as W and Re) within its composition.

To address these issues we repeated the experiment using fully solutioned CMSX-4 alloy test-bars, removing any compositional segregation therefore there is no remnant eutectic, and the (100) peak can thus be contributed solely to bulk γ' and/or the γ' surface layer. We also increased the final hold solution temperature, closer to that

used in industry, to ensure that the bulk γ' is fully dissolved and removing its contribution to the spectra at high temperatures.

6.5.2.3 Solutioned CMSX-4

The solutioned CMSX-4 test-bar bulk spectra showed that the γ' started to dissolve at $\sim 511^\circ\text{C}$ and by 1000°C the volume of the γ' phase had reduced by roughly a third which is significantly below the γ'_{solvus} of $\sim 1289^\circ\text{C}$. Looking at the equilibrium phase diagram in Figure 6.30, the γ' phase room temperature fraction of $\sim 75\%$ remains at 500°C and gradually decreases to $\sim 65\%$ at 1000°C before rapidly dissolving with increasing temperature. Investigations into the dissolution of Nickel-based superalloys and CMSX-4 have shown that there is little change in the γ' volume fraction until $700\text{--}900^\circ\text{C}$ [195][196][197], therefore the detected decrease in the ND γ' peaks at 500°C suggests that the γ' precipitates dissolution can start below these temperatures. As the peak heights reduce, there is an associated peak broadening which is characteristic of the de-convoluted γ peak sitting to one side of the γ' peak [194] as well as the γ' precipitates becoming smaller. As the precipitates become smaller there are insufficient lattice planes to produce complete destructive interference either side of the Bragg angle and the result is a broadening peak [182]. Both the peak height reduction and the peak broadening indicate that the dissolution of the γ' phase is occurring and that this starts at a temperature of $\sim 511^\circ\text{C}$.

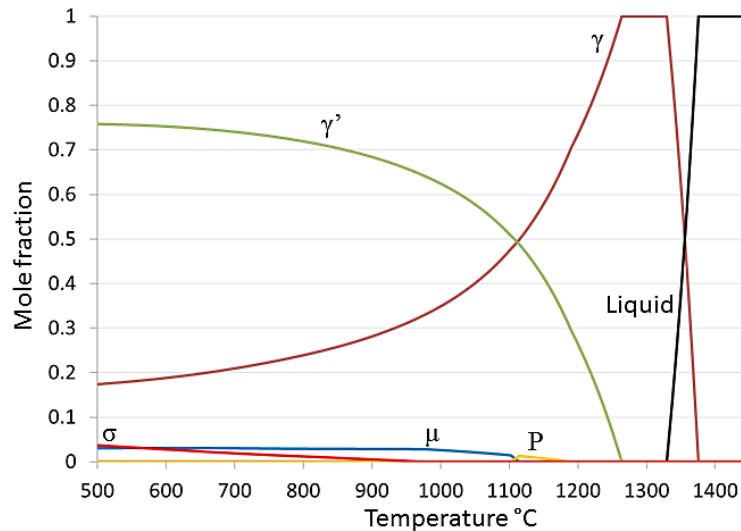


Figure 6.30 Calculated equilibrium phase diagram for CMSX-4 using Thermo-CALC

As the γ' phase dissolves, the (200) and (100) peak heights reduce. This is because the volume fraction of γ' is decreasing and therefore its contribution to the spectrum is also decreasing. However, as the γ' dissolves it is taken into the γ phase and therefore the γ volume fraction steadily increases (this is clearly visible in Figure 6.30). Since the (200) peak has contributions from both γ and γ' [194] the peak height steadily reduces on heating however, upon exceeding the γ'_{solvus} the (200) peak height begins to rise again until, at 1305°C, it has re-established its original room-temperature height. This shows that as the γ' phase dissolves, its solute is taken into the γ phase but this process takes time (since the solute needs to diffuse into the γ phase) and is not completed until reaching the solutioning temperature.

The surface ND spectra show a different evolution compared to the bulk spectra, however the (100) γ' peak is still seen to dissolve at the same temperature as the bulk at $\sim 1282^\circ\text{C}$ and not reappearing during solutioning. During the heating ramp-up to 1000°C both the (200) and (100) peak heights remain constant and do not decrease like in the bulk spectra. The cause of this apparent stabilization of the γ' phase at the

surface at temperatures below 1000°C is unknown as this cannot be due to the formation of the γ' surface layer since, at these temperatures, the vapour pressures (and hence evaporative rates) of the key γ phase stabilisers, Ni, Co and Cr, are prohibitively low (see Figure 6.31). These test-bars are also pre-solutioned so there can be no contribution from surface eutectic or inhomogeneous microstructure, like was seen in the as-cast CMSX-10N.

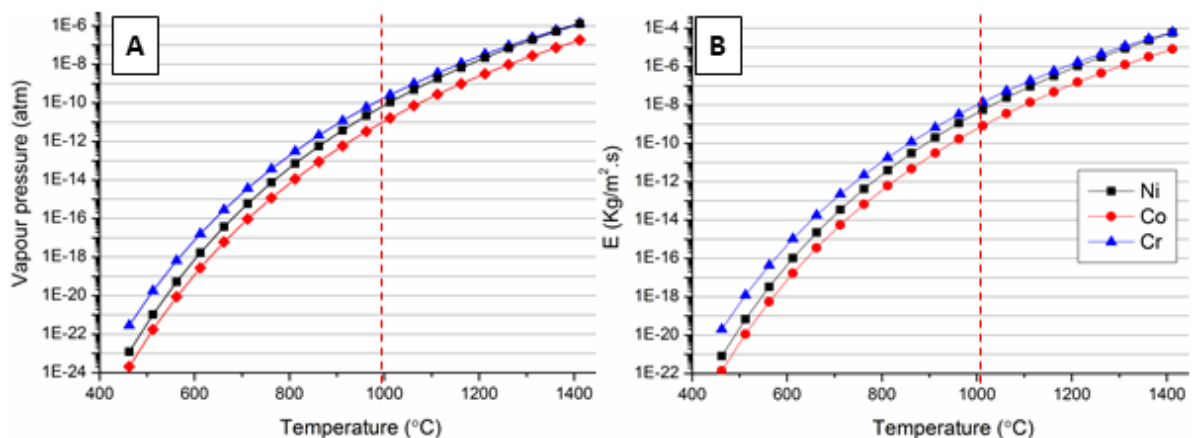


Figure 6.31(a) Vapour pressure vs. temperature plots for Ni, Co and Cr (b) Evaporative rate from the sample surface into vacuum using the Langmuir equation (taken from Chapter 4)

Upon further heating above 1000°C, the (200) peak starts to reduce in peak height and becomes broader (as for the bulk) and as the γ'_{solvus} is exceeded the (200) peak returns to a tall, thin shape. The height remains about a third lower than that at room-temperature however. It seems likely therefore that the volume of sample within the neutron beam gauge volume has reduced due to the uneven thermal expansion of the alloy and the very narrow slice of the surface intersected with the gauge volume. At 1305°C the only stable phase is γ and the full neutron spectrum shows no other peaks evolving that could explain the reduction in the (200) γ peak at high temperature.

6.6 Conclusions

The evolution of the γ' surface layer during *in-situ* solution heat-treatment has been investigated using neutron diffraction techniques at the ENGIN-X facility, UK. Although it was not possible to definitively observe the formation of the γ' surface layer it has been shown that the use of a continuous vacuum pump applied to the heat-treatment furnace during solutioning significantly increases the subsequent thickness of the γ' surface layer. It has also been shown that the γ' surface layer grows into, and consumes, the RX γ grains below, being arrested at the γ RX grain/substrate grain boundary.

The neutron diffraction spectra have shown that the dissolution of γ' within the bulk microstructure starts at $\sim 511^\circ\text{C}$ and at 1000°C there is a significant loss of γ' . The γ' solvus has been accurately tracked to $\sim 1282\text{--}5^\circ\text{C}$ (bulk and surface respectively) and it can be seen from the (200) peak shape evolution, between 1285°C – 1305°C , that the γ' solute is not re-distributed into the γ phase until reaching the solutioning temperature, 1305°C .

Significant differences are noted between the bulk and surface spectra between RT and 1000°C , as the (200) peak height does not decrease at the surface as opposed to the bulk. The cause of this is unknown, since it cannot be due to the formation of the γ' surface layer at these low temperatures. Above 1000°C the two regions show similar trends, with the γ' dissolving and the (200) peak height recovering. In order to further investigate the surface region in greater detail, it is suggested that synchrotron X-ray

diffraction techniques be employed. This high-resolution technique is ideally suited to analysing the surfaces of crystalline samples that do not require large beam penetration distances and can achieve beam sizes at the sample of $115 \times 210 \mu\text{m}$ [198]. With this beam size the percentage volume of the γ' surface layer within the total sampled volume will be larger than that achievable with neutron diffraction and therefore the detection of the γ' surface layer formation would be far easier. This will also allow the combined implementation of thermodynamic/kinetic modelling, using Thermo-Calc and DICTRA, of the surface transformation and greater understanding of the processes driving its formation.

Chapter 7. Overall Conclusions and Further Work

7.1 Conclusions

This research project has produced a systematic investigation into the formation mechanisms of the defects Surface Scale and Surface Melting, found on SX Nickel-based superalloy turbine blades. Focus has been put on achieving a complete understanding of the factors driving their formation during casting and heat-treatment in an effort to suggest methods by which to prevent their formation and thus improve the cost and production efficiency of these high-value components.

During casting, the formation of Surface Scale is particularly common and has been shown to be the result of a series of inter-related processes:

- (1) In the solid-state, the mould and metal experience differential thermal contractions due to their non-uniform thermal expansion coefficients resulting in the upper, convex areas of the casting separating from the mould wall.
- (2) The separation exposes the solid casting surface to the furnace atmosphere, which contains sufficient oxygen to initiate transient oxidation of the casting surface. The result is a dual oxide layer of predominantly NiO sitting above a sub-oxide spinel, which has a total thickness of 0.5-1 μ m. The nature of the Surface Scale is therefore alloy dependent; however the upper oxide is always seen to be NiO due to its fast growth kinetics.

In contrast, the areas that do not exhibit Surface Scale (Unscaled) remain in intimate contact with the mould wall for the duration of the casting process. After the mould is

removed the Unscaled surface is observed to be covered by a 1-2 μm thick Al_2O_3 layer and patches of adhered mould face-coat. It has been shown that during the initial stages of casting, above the Liquidus temperature, a mould-metal reaction occurs between aluminium in the melt and SiO_2 in the mould. The result is the dissolution of Si within the alloy and the production of the 1-2 μm thick Al_2O_3 layer at the casting surface. This process occurs over the entire casting surface, however when mould-metal separation occurs in the Scaled areas, the Al_2O_3 layer is stripped off the casting surface and remains on the mould face-coat.

It is suggested that to prevent the formation of Surface Scale an inert gas, such as Argon, be introduced into the casting furnace in order to sufficiently lower the oxygen partial pressure to prevent the formation of oxides, particularly Ni, Co and Cr oxides.

After subsequent heat-treatment it is observed that the Surface Melting defect only occurs within the regions that were Scaled. This spatial relationship has been shown to be a result of the as-cast surface condition and is directly linked to the oxides that are present in the Scaled and Unscaled regions. In the Unscaled regions the Al_2O_3 layer is sufficiently thick to act as a protective barrier to elemental vaporisation during subsequent solutioning. In contrast, the Scale oxides are thin, porous and non-protective and therefore during solutioning elemental evaporation of γ phase stabilisers occurs at the surface. The heat-treatment furnace is held at an initial vacuum of 10^{-7} atm until reaching 1040°C when Argon gas is introduced at a partial pressure of 10^{-4} atm. This environment is provided to prevent significant oxidation of the components during heat-treatment but this research has shown that this

environment is sufficient to induce significant levels of elemental evaporation from the component surface. The resultant change in surface chemistry causes the destabilisation of the γ phase at solutioning temperatures (where the γ' precipitates have been fully dissolved) and the transformation to the γ' phase plus TCPs.

The prevention of Surface Scale in the first instance is therefore insufficient to prevent the subsequent formation of Surface Melting, since it is the lack of a protective oxide that is the root-cause of this heat-treatment defect. Rather, pre-oxidation (in air) of the casting at 1100°C for 4 hours has been shown to produce an adequately thick Al_2O_3 layer in the Scaled regions to prevent elemental evaporation and thus the formation of Surface Melting, whilst at the same time retaining the optimum γ' distribution/morphology in the heat-treated condition.

To conclude, this research project has characterised two inter-related and highly significant surface defects observed on SX Nickel-based superalloys. The mechanisms of formation have been alluded to and the factors controlling them have been discussed. Finally, suggestions have been made to mitigate their formation and it is hoped that this can lead to a reassessment of current casting and heat-treatment methodologies.

7.2 Further Work

The mechanism of Surface Scale and Surface Melting defect formation, and their close link, has been shown. Based on these findings it is recommended that the following areas be explored further.

The introduction of Argon gas into the casting furnace is an effective method to prevent the formation of Surface Scale by reduction of the oxygen partial pressure within the furnace. This method is relatively easy to introduce since Argon gas is already employed with the Precision Casting Facility. However this method will not prevent the subsequent formation of Surface Melting since the Scaled surface will still remain exposed, with no protective oxide layer.

The design of new mould materials is a constant source of study, with emphasis on creating moulds with sufficient fired strength but that allow the unconstrained contraction of the metal component during cooling, whilst at the same time preventing any deleterious mould-metal reactions. It is suggested that, in order to prevent the formation of Surface Scale, moulds be designed and trialled with a built-in weak layer behind the face-coat, that allows the face-coat to remain adhered to the Scaled regions of the casting during thermal contraction. This would allow the Al_2O_3 surface layer to be retained on the Scaled surface and therefore prevent the exposure of the bare casting surface and resultant oxidation. The beneficial side-effect of this would be that the Scaled region would not experience any Surface Melting during solution heat-treatment, since the protective Al_2O_3 is retained on the surface.

The pre-oxidation experiment has shown that it is possible to prevent the Surface Melting defect by deliberately oxidising the casting surface in air, prior to solution heat-treatment. It is therefore suggested that trials be conducted to modify the current solution heat-treatment profile to include a pre-oxidation stage, potentially at

the 1040°C isothermal hold. By holding at this temperature, prior to the introduction of an Argon atmosphere, it would be possible to produce an Al₂O₃ layer whilst preventing the elemental evaporation experienced at higher temperatures. However, this will likely take more than the 4 hours experienced in the pre-oxidation trials since the residual oxygen partial pressure in the heat-treatment furnace is much lower. Care also needs to be taken to ensure that the adequate solutioning and γ' fraction/morphology is retained at the end of solutioning to maintain the optimum material properties.

The feasibility of all of these solutions need further study and industrial trials carried out in order to judge their effectiveness and economic viability before an effective solution can be implemented. However, it is hoped that this work will lead to the introduction of new production methods and the elimination of these defects.

Chapter 8. References

- [1] N. A. Cumpsty, *Jet Propulsion*, 2nd ed. Cambridge University Press, 2003.
- [2] J. Wickerson, *Hollistic Gas Turbine*. Rolls-Royce plc, 2010.
- [3] *The Jet Engine*, 5th ed. Rolls-Royce plc, 1996.
- [4] R. C. Reed, *The Superalloys: Fundamentals and Applications*, 1st ed. Cambridge University Press, 2006.
- [5] C. T. Sims, N. S. Stoloff, and W. C. Hagel, Eds., *Superalloys II: High Temperature Materials for Aerospace and Industrial Power*. New York: Wiley-Interscience, 1987.
- [6] M. J. Donachie and S. J. Donachie, *Superalloys: A Technical Guide*, 2nd ed. OH, USA: ASM International, 2002.
- [7] G. J. J. Brewster, "Solidification and heat-treatment related defects in single crystal nickel-base superalloys," Fitzwilliam College, Cambridge, 2009.
- [8] I. Edmonds, "The oxidation properties of uncoated and coated fourth generation nickel-based superalloys," University of Birmingham, 2009.
- [9] R. J. Christensen, D. M. Lipkin, and D. R. Clarke, "Nondestructive evaluation of the oxidation stresses through thermal barrier coatings using Cr³⁺ piezospectroscopy," *Applied Physics Letters*, vol. 69, no. 24, pp. 3754–3756, 1996.
- [10] M. Ganesan, "Homogenisation of single crystal superalloys: Experimental investigation and numerical modelling," Imperial College, London, 2003.
- [11] J. W. Schultz and H. F. Merrick, "Constitution of the Ni-Cr-Fe System From 0 to 40 Pct Fe Including Some Effects of Ti, Al, Si, and Nb," *Metallurgical Transactions*, vol. 3, no. September, pp. 2479–2483, 1972.
- [12] J. Tien and T. Caulfield, *Superalloys, supercomposites and superceramics*. San Diego: Academic Press Inc, 1989.
- [13] N. Warnken, D. Ma, M. Mathes, and I. Steinbach, "Investigation of eutectic island formation in SX superalloys," *Materials Science and Engineering: A*, vol. 413–414, pp. 267–271, Dec. 2005.
- [14] U. R. Kattner, "The thermodynamic modeling of multicomponent phase equilibria," *JOM*, vol. 49, no. 12, pp. 14–19, Dec. 1997.

- [15] P. Caron and T. Khan, "Evolution of Ni-based superalloys for single crystal gas turbine blade applications," *Aerospace Science and Technology*, vol. 3, no. 8, pp. 513–523, Dec. 1999.
- [16] P. Caron and T. Khan, "Improvement of Creep strength in a nickel-base single-crystal superalloy by heat treatment," *Materials Science and Engineering*, vol. 61, no. 2, pp. 173–184, 1983.
- [17] R. A. Hobbs, S. Tin, and C. M. F. Rae, "Solidification characteristics of advanced Nickel-base single crystal superalloys," *Superalloys 2004*, pp. 819–825, 2004.
- [18] S. Yang, "Effect of Ti and Ta on the oxidation of a complex superalloy," *Oxidation of Metals*, vol. 15, no. 5–6, pp. 375–397, 1981.
- [19] G. Brewster, H. B. Dong, N. R. Green, and N. D'Souza, "Surface Segregation during Directional Solidification of Ni-Base Superalloys," *Metallurgical and Materials Transactions B*, vol. 39, no. 1, pp. 87–93, Jan. 2008.
- [20] A. Heckl, S. Neumeier, S. Cenanovic, M. Göken, and R. F. Singer, "Reasons for the enhanced phase stability of Ru-containing nickel-based superalloys," *Acta Materialia*, vol. 59, no. 17, pp. 6563–6573, Oct. 2011.
- [21] S. Tin and T. M. Pollock, "Phase instabilities and carbon additions in single-crystal nickel-base superalloys," *Materials Science and Engineering: A*, vol. 348, no. 1–2, pp. 111–121, May 2003.
- [22] R. Dorolia, D. Lahrman, and R. Field, "Formation of Topologically Closed Packed Phases in Nickel-Base Single Crystal Superalloys," *Superalloys 1988*, pp. 255–264, 1988.
- [23] C. M. F. Rae, M. S. Hook, and R. C. Reed, "The effect of TCP morphology on the development of aluminide coated superalloys," *Materials Science and Engineering: A*, vol. 396, no. 1–2, pp. 231–239, Apr. 2005.
- [24] A. Suzuki and C. M. F. Rae, "Secondary Reaction Zone Formations in coated Ni-base Single Crystal Superalloys," *Journal of Physics: Conference Series*, vol. 165, p. 012002, May 2009.
- [25] W. Walston, J. Schaeffer, and W. Murphy, "A new type of microstructural instability in superalloys-SRZ," *Superalloys 1996*, pp. 9–18, 1996.
- [26] O. Lavigne, C. Ramusat, and S. Drawin, "Relationships between microstructural instabilities and mechanical behaviour in new generation nickel-based single crystal superalloys," *Superalloys*, pp. 667–675, 2004.
- [27] B. J. Pearcey, B. H. Kear, and R. W. Smashey, "Correlation of structure with properties in a directionally solidified nickel-base superalloy," *Transactions of the American Society of Metals*, vol. 60, pp. 634–643, 1967.

- [28] T. M. Pollock and A. S. Argon, "Creep resistance of CMSX-3 nickel base superalloy single crystals," *Acta Metallurgica et Materialia*, vol. 40, no. 1, pp. 1–30, 1992.
- [29] A. Vattré, B. Devincere, and A. Roos, "Dislocation dynamics simulations of precipitation hardening in Ni-based superalloys with high γ' volume fraction," *Intermetallics*, vol. 17, no. 12, pp. 988–994, Dec. 2009.
- [30] B. Kear and J. Oblak, "Deformation modes in γ' precipitation hardened Nickel-base alloys," *Journal de Physique Colloques*, vol. 35, no. 12, pp. 35–45, 1974.
- [31] D. Hull and D. J. Bacon, *Introduction to dislocations*, 4th ed. Oxford: Butterworth-Heinemann, 2001.
- [32] F. L. Versnyder and S. M. E, "The development of columnar grain and single crystal high temperature materials through directional solidification," *Materials Science and Engineering*, vol. 6, pp. 212–247, 1970.
- [33] A. Wagner, B. A. Shollock, and M. McLean, "Grain structure development in directional solidification of nickel-base superalloys," *Materials Science and Engineering: A*, vol. 374, no. 1–2, pp. 270–279, Jun. 2004.
- [34] S. Jones and C. Yuan, "Advances in shell moulding for investment casting," *Journal of Materials Processing Technology*, vol. 135, no. 2–3, pp. 258–265, 2003.
- [35] M. Gell and D. N. Duhl, "The development of single crystal superalloy turbine blades," *Superalloys 1980*, pp. 205–214, 1980.
- [36] M. J. Goulette, P. D. Spilling, and R. P. Arthey, "Cost Effective Single Crystals," *Superalloys 1984*, pp. 167–176, 1984.
- [37] H. Dai, "A Study of Solidification Structure Evolution during Investment Casting of Ni-based Superalloy for Aero-Engine Turbine Blades," University of Leicester, 2008.
- [38] Y. Z. Zhou, A. Volek, and N. R. Green, "Mechanism of competitive grain growth in directional solidification of a nickel-base superalloy," *Acta Materialia*, vol. 56, no. 11, pp. 2631–2637, Jun. 2008.
- [39] N. Stanford, "Seeding of single crystal superalloys—role of seed melt-back on casting defects," *Scripta Materialia*, vol. 50, no. 1, pp. 159–163, Jan. 2004.
- [40] W. Kurz and D. J. Fisher, *Fundamentals of Solidification*. Aedermannsdorf, Switzerland: Trans Tech SA, 1984.
- [41] G. J. Davies, *Solidification and casting*. Barking, UK: Applied Science Publishers LTD, 1973.

- [42] T. Pollock and W. Murphy, "The breakdown of single-crystal solidification in high refractory nickel-base alloys," *Metallurgical and Materials Transactions A*, vol. 27, no. April, pp. 1081–1094, 1996.
- [43] R. M. Kearsey, J. C. Beddoes, P. Jones, and P. Au, "Compositional design considerations for microsegregation in single crystal superalloy systems," *Intermetallics*, vol. 12, no. 7–9, pp. 903–910, Jul. 2004.
- [44] M. McLean, *Directionally solidified materials for high temperature service*. London: The Metals Society, 1983.
- [45] C. Walter, B. Hallstedt, and N. Warnken, "Simulation of the solidification of CMSX-4," *Materials Science and Engineering: A*, vol. 397, no. 1–2, pp. 385–390, Apr. 2005.
- [46] N. D'Souza, M. Lekstrom, and H. B. Dong, "An analysis of measurement of solute segregation in Ni-base superalloys using X-ray spectroscopy," *Materials Science and Engineering: A*, vol. 490, no. 1–2, pp. 258–265, Aug. 2008.
- [47] J. Campbell, *Castings*, 2nd ed. Oxford: Butterworth-Heinemann, 2003.
- [48] S. R. Hegde, R. M. Kearsey, and J. Beddoes, "Design of solutionizing heat treatments for an experimental single crystal superalloy," *Superalloys 2008*, pp. 301–310, 2008.
- [49] G. E. Fuchs, "Solution heat treatment response of a third generation single crystal Ni-base superalloy," *Materials Science and Engineering: A*, vol. 300, no. 1–2, pp. 52–60, Feb. 2001.
- [50] P. Jablonski and C. Cowen, "Homogenizing a Nickel-Based Superalloy: Thermodynamic and Kinetic Simulation and Experimental Results," *Metallurgical and Materials Transactions B*, vol. 40B, pp. 182–186, 2009.
- [51] M. Ganesan, D. Dye, and P. Lee, "A technique for characterizing microsegregation in multicomponent alloys and its application to single-crystal superalloy castings," *Metallurgical and Materials Transactions A*, vol. 36, no. August, 2005.
- [52] B. C. Wilson, J. A. Hickman, and G. E. Fuchs, "The effect of solution heat treatment on a single-crystal Ni-based superalloy," *JOM*, vol. 55, no. 3, pp. 35–40, Mar. 2003.
- [53] G. Erickson, "A new, third-generation, single-crystal, casting superalloy," *JOM*, vol. 47, no. 4, pp. 36–39, 1995.
- [54] M. S. A. Karunaratne, D. C. Cox, P. Carter, and R. C. Reed, "Modelling of the Microsegregation in CMSX-4 Superalloy and its Homogenisation during Heat Treatment," *Superalloys 2000*, pp. 263–272, 2000.

- [55] K. Takechi, "Influence of secondary precipitates and crystallographic orientation on the strength of single crystals of a Ni-based superalloy," *Metallurgical and Materials Transactions A*, vol. 30, no. May, 1999.
- [56] M. Durand-Charre, *The microstructure of superalloys*. USA: CRC Press, 1997.
- [57] X. L. Yang, H. B. Dong, W. Wang, and P. D. Lee, "Microscale simulation of stray grain formation in investment cast turbine blades," *Materials Science and Engineering: A*, vol. 386, no. 1–2, pp. 129–139, Nov. 2004.
- [58] Y. Zhou, "Formation of stray grains during directional solidification of a nickel-based superalloy," *Scripta Materialia*, vol. 65, no. 4, pp. 281–284, Aug. 2011.
- [59] S. Tin, "Carbon additions and grain defect formation in directionally solidified nickel-base superalloys," University of Michigan, 2001.
- [60] T. Pollock and S. Tin, "Nickel-based superalloys for advanced turbine engines: chemistry, microstructure and properties," *Journal of propulsion and power*, vol. 22, no. 2, pp. 361–374, 2006.
- [61] J. Zhang and R. F. Singer, "Hot tearing of nickel-based superalloys during directional solidification," *Acta Materialia*, vol. 50, no. 7, pp. 1869–1879, Apr. 2002.
- [62] J. E. Doherty, B. H. Kear, and A. F. Giamei, "On the origin of the ductility enhancement in Hf-doped Mar-M200 (Ductility enhancement in directionally solidified Ni base Mar-M200 alloy by Hf additions increasing gamma-gamma prime eutectic)," *Journal of Metals*, vol. 23, pp. 59–62, 1971.
- [63] K. Heck, R. Blackford, and R. Singer, "Castability of directionally solidified nickel base superalloys," *Materials science and ...*, vol. 15, no. February, pp. 213–220, 1999.
- [64] Y. Zhu, J. Radavich, Z. Zheng, X. Ning, and L. Lou, "The development and long-time structural stability of a low segregation Hf free superalloy--DZ 125 L," *Superalloys 2000*, pp. 329–339, 2000.
- [65] D. Lin, S. Huang, and C. Sun, "A Hafnium-Free Directionally Solidified Nickel-Base Superalloy," *Superalloys 1988*, pp. 345–354, 1988.
- [66] J. Rösler, M. Konter, and C. Tönnies, "On the Castability of Corrosion Resistant DS-Superalloys," *Superalloys 1996*, pp. 515–522, 1996.
- [67] J. Grindley, "Investigation into the causes of surface melting on heat-treated single crystal turbine blades made from Nickel-based superalloys," Rolls-Royce plc, Derby, 2005.

- [68] T. Jackson and R. Simkins, "Investigation into the cause of surface melting on heat-treated turbine blades at the PCF, Derby," Rolls-Royce plc, Derby, 2003.
- [69] J. R. Mihalisin, J. Corrigan, M. Launsbach, E. Leonard, R. Baker, and B. Griffin, "Some effects of carbon in the production of single crystal superalloy castings," *Superalloys 2004*, pp. 795–800, 2004.
- [70] J. R. Mihalisin, J. Corrigan, R. Baker, E. Leonard, and J. L. Vandersluis, "Clean single crystal Nickel base superalloy," 55497651996.
- [71] H. Frye, M. Yasrebit, and D. H. Sturgis, "Basic ceramic considerations for lost wax processing of high melting alloys," *2000 Platinum Day Symposium*, vol. 8, 2000.
- [72] P. N. Whateley, "Defects in Steel Investment Castings," Aston University, 1991.
- [73] M. Kim, S. Sung, and Y. Kim, "Microstructure, metal-mold reaction and fluidity of investment cast-TiAl alloys," *Materials Transactions*, vol. 45, no. 2, pp. 536–541, 2004.
- [74] C. Cingi, "Mold-metal reactions in magnesium investment castings," Helsinki University of Technology, 2006.
- [75] M. F. X. Gigliotti and C. Greskovich, "Furnace atmosphere effects on casting of eutectic superalloys," *Metallurgical Transactions A*, vol. 11, no. 2, pp. 319–322, 1980.
- [76] T. S. Piwonka, "Reactions at the mold/metal interface in investment castings," in *Investment Casting Institute, 42nd Annual Technical Meeting*, 1994.
- [77] N. D'Souza, G. J. Brewster, H. B. Dong, and G. D. West, "Incipient surface melting and secondary reaction zone formation during heat-treatment of a 3rd generation Ni-base superalloy, CMSX10N," *Metallurgical and Materials Transactions A*, no. (Under Review).
- [78] C. Panwisawas, H. Mathur, J.-C. Gebelin, D. Putman, C. M. F. Rae, and R. C. Reed, "Prediction of recrystallization in investment cast single-crystal superalloys," *Acta Materialia*, vol. 61, no. 1, pp. 51–66, Jan. 2013.
- [79] A. Porter and B. Ralph, "The recrystallization of nickel-base superalloys," *Journal of Materials Science*, pp. 707–713, 1981.
- [80] S. Bond and J. Martin, "Surface recrystallization in a single crystal nickel-based superalloy," *Journal of materials science*, vol. 19, pp. 3867–3872, 1984.
- [81] J. Meng, T. Jin, X. Sun, and Z. Hu, "Surface recrystallization of a single crystal nickel-base superalloy," *International Journal of Minerals, Metallurgy, and Materials*, vol. 18, no. 2, pp. 197–202, May 2011.

- [82] C. Y. Jo, H. Y. Cho, and H. M. Kim, "Effect of recrystallisation on microstructural evolution and mechanical properties of single crystal nickel base superalloy CMSX-2 Part 1-Microstructural evolution during recrystallisation of single crystal," *Materials science and technology*, vol. 19, no. December, pp. 1665–1670, 2003.
- [83] R. Doherty, "Role of interfaces in kinetics of internal shape changes," *Metal Science*, vol. 16, no. January, pp. 1–13, 1982.
- [84] B. Ralph, "Grain growth," *Materials Science and Technology*, vol. 6, no. November, pp. 1139–1144, 1990.
- [85] N. Birks and G. H. Meier, *Introduction to high temperature oxidation of metals*. London: Edward Arnold Ltd, 1983.
- [86] D. R. Gaskell, *Introduction to metallurgical thermodynamics*. McGraw-Hill, 1973.
- [87] S. Bose, *High temperature coatings and oxidation*. Oxford, UK: Butterworth-Heinemann, 2011.
- [88] C. Liu, A.-M. Huntz, and J.-L. Lebrun, "Origin and development of residual stresses in the Ni-NiO system: in-situ studies at high temperature by X-ray diffraction," *Materials Science and Engineering: A*, vol. 160, no. 1, pp. 113–126, 1993.
- [89] H. E. Evans, "Stress effects in high temperature oxidation of metals," *International Materials Reviews*, vol. 40, no. 1, pp. 1–40, 1995.
- [90] A. S. Khanna, *Introduction to high temperature oxidation and corrosion*. OH, USA: ASM International, 2002.
- [91] R. T. Grimley, R. P. Burns, and M. G. Inghram, "Thermodynamics of the vaporization of Cr₂O₃: Dissociation energies of CrO, CrO₂ and CrO₃," *Journal of Chemical Physics*, vol. 34, pp. 664–668, 1960.
- [92] C. S. Tedmon, "The Effect of Oxide Volatilization on the Oxidation Kinetics of Cr and Fe-Cr Alloys," *Journal of The Electrochemical Society*, vol. 113, no. 8, pp. 766–768, Aug. 1966.
- [93] B. Gorr, V. Trindade, S. Burk, H.-J. Christ, M. Klauke, D. Mukherji, and J. Rösler, "Oxidation Behaviour of Model Cobalt-Rhenium Alloys During Short-Term Exposure to Laboratory Air at Elevated Temperature," *Oxidation of Metals*, vol. 71, no. 3–4, pp. 157–172, Jan. 2009.
- [94] K. Kawagishi, H. Harada, A. Sato, A. Sato, and T. Kobayashi, "The oxidation properties of fourth generation single-crystal nickel-based superalloys," *Jom*, vol. 58, no. 1, pp. 43–46, Jan. 2006.

- [95] E. A. Gulbransen, K. F. Andrew, and F. A. Brassart, "Oxidation of Molybdenum 550° to 1700°C," *Journal of The Electrochemical Society*, vol. 110, p. 952, 1963.
- [96] E. A. Gulbransen and G. H. Meier, "Mechanisms of oxidation and hot corrosion of metals and alloys at temperatures of 1150 to 1450K under flow," in *Proc. of 10th Materials Research Symposium*, 1979, pp. 1639–1682.
- [97] E. A. Gulbransen and S. A. Jansson, in *Heterogeneous kinetics at elevated temperatures*. New York: Plenum Press, 1970.
- [98] A. Heckl, R. Rettig, and R. F. Singer, "Solidification Characteristics and Segregation Behavior of Nickel-Base Superalloys in Dependence on Different Rhenium and Ruthenium Contents," *Metallurgical and Materials Transactions A*, vol. 41, no. 1, pp. 202–211, Oct. 2009.
- [99] N. D'Souza, R. Beanland, C. Hayward, and H. B. Dong, "Accuracy of composition measurement using X-ray spectroscopy in precipitate-strengthened alloys: Application to Ni-base superalloys," *Acta Materialia*, vol. 59, no. 3, pp. 1003–1013, Feb. 2011.
- [100] H. J. Dai, J. C. Gebelin, M. Newell, R. C. Reed, N. D'Souza, P. D. Brown, and H. B. Dong, "Grain Selection during Solidification in Spiral Grain Selector," *Superalloys 2008 (Eleventh International Symposium)*, no. c, pp. 367–374, 2008.
- [101] A. F. Giamei and D. L. Anton, "Rhenium Additions to a Ni-Base Superalloy : Effects on Microstructure," vol. 16, no. November 1985, pp. 1997–2005, 1997.
- [102] J. Goldstein, *Scanning Electron Microscopy and X-Ray Microanalysis*, 3rd ed. Kluwer Academic/Plenum Publishers, 2003.
- [103] D. Briggs and J. T. Grant, *Surface Analysis by Auger and X-ray Photoelectron spectroscopy*. UK: IM Publications, 2003.
- [104] G. W. Critchlow, "Instrumental techniques for the surface analysis of materials," *Transactions of the Institute of Metal Finishing*, vol. 74, no. 6, pp. 108–114, 1996.
- [105] F. Settle, *Handbook of instrumental techniques for analytical chemistry*. Prentice Hall PTR, 1997, pp. 791–808.
- [106] A. Carlson, "Auger effect," *Wikipedia*, 2007. [Online]. Available: http://en.wikipedia.org/wiki/Auger_effect. [Accessed: 09-Jul-2013].
- [107] S. J. Pennycook, A. R. Lupini, M. Varela, A. Borisevich, Y. Peng, M. P. Oxley, K. Benthem, and M. F. Chisholm, "Scanning Transmission Electron Microscopy for Nanostructure Characterization," in *Scanning Microscopy for Nanotechnology SE - 6*, W. Zhou and Z. Wang, Eds. Springer New York, 2007, pp. 152–191.

- [108] D. B. Williams and C. B. Carter, *Transmission Electron Microscopy I*. New York: Springer, 1996.
- [109] S. Hashimoto, C. Tanaka, A. Murata, and T. Sakurada, "Formulation for XPS Spectral Change of oxides by Ar Ion Bombardment: Application of the Formulation to Ta₂O₅ system," *Journal of Surface Analysis*, vol. 13, pp. 14–18, 2006.
- [110] N. Donkov and A. Zykova, "Tantalum pentoxide ceramic coatings deposition on Ti4Al6V substrates for biomedical applications," *Problems of Atomic ...*, vol. 17, pp. 131–133, 2011.
- [111] C. T. Liu, J. Ma, and X. F. Sun, "Oxidation behavior of a single-crystal Ni-base superalloy between 900 and 1000°C in air," *Journal of Alloys and Compounds*, vol. 491, no. 1–2, pp. 522–526, Feb. 2010.
- [112] A. Sato, J. J. Moverare, M. Hasselqvist, and R. C. Reed, "On the Mechanical Behavior of a New Single-Crystal Superalloy for Industrial Gas Turbine Applications," *Metallurgical and Materials Transactions A*, vol. 43, no. 7, pp. 2302–2315, Jan. 2012.
- [113] L. Huang, X. Sun, H. Guan, and Z. Hu, "Oxidation behavior of a single-crystal Ni-base superalloy in air at 900, 1000 and 1100 C," *Tribology Letters*, vol. 23, no. 1, pp. 15–22, 2006.
- [114] R. J. Blattner, "Solid phase reduction of SiO₂ in the presence of an Al layer," *Journal of Vacuum Science and Technology*, vol. 20, no. 3, pp. 320–323, Mar. 1982.
- [115] W. Wolbach and S. Bryan, "Optimization of chemical reactions between alumina/silica fibres and aluminium-magnesium alloys during composite processing," *Journal of materials ...*, vol. 32, pp. 1953–1961, 1997.
- [116] A. E. Standage and M. S. Gani, "Reaction Between Vitreous Silica and Molten Aluminum," *Journal of the American Ceramic Society*, vol. 50, no. 2, pp. 101–105, 1967.
- [117] K. Prabripulaloong and M. R. Piggott, "Reduction of SiO₂ by Molten Al," *Journal of the American Ceramic Society*, vol. 56, no. 4, pp. 184–185, 1973.
- [118] L. Tarrant, "Formulation and development of ceramic mould materials for investment casting," University of Birmingham, 2012.
- [119] D. Putman, "duncan.putman@rolls-royce.com." Rolls-Royce plc, Derby, 2013.
- [120] P. A. Jennings, "Foundaries satellite VeriCAST. Phase I simple blade casting trials and thermal history generation-Final report," 1996.

- [121] H. Li and G. Selvaduray, "Ellingham Diagram Web Project," 2013. [Online]. Available: <http://www.engr.sjsu.edu/ellingham/>. [Accessed: 09-Jul-2013].
- [122] M. Gobel, A. Rahmel, and M. Schtze, "The isothermal-oxidation behaviour of several Nickel-base single-crystal superalloys with and without coatings," *Oxidation of Metals*, vol. 39, pp. 231–261, 1993.
- [123] M. Gobel, A. Rahmel, and M. Schutze, "The cyclic-oxidation behaviour of several Nickel-base single-crystal superalloys with and without coatings," *Oxidation of metals*, vol. 41, pp. 271–300, 1994.
- [124] A. Akhtar, M. Hook, and R. Reed, "On the oxidation of the third-generation single-crystal superalloy CMSX-10," *Metallurgical and Materials Transactions A*, vol. 36, no. November, 2005.
- [125] C. M. Younes, G. C. Allen, and J. A. Nicholson, "High temperature oxidation behaviour of single crystal superalloys RR3000 and CMSX-4," *Corrosion Engineering, Science and Technology*, vol. 42, no. 1. pp. 80–88.
- [126] O. Knacke, O. Kubaschewski, and K. Hesselmann, *Thermochemical properties of inorganic substances I & II*, 2nd ed., no. v. 2. Berlin: Springer-Verlag, 1991.
- [127] M. Li, X. Sun, J. Li, Z. Zhang, and T. Jin, "Oxidation Behavior of a Single-Crystal Ni-Base Superalloy in Air. I: At 800 and 900 C," *Oxidation of Metals*, vol. 59, no. June, pp. 591–605, 2003.
- [128] A. S. Suzuki, K. Kawagishi, T. Yokokawa, H. Harada, and T. Kobayashi, "A New Oxide Morphology Map: Initial Oxidation Behavior of Ni-Base Single-Crystal Superalloys," *Metallurgical and Materials Transactions A*, vol. 43, no. 1, pp. 155–162, Jul. 2011.
- [129] M. Gall, A. M. Huntz, B. Lesage, C. Monty, and J. Bernardini, "Self-diffusion in α -Al₂O₃ and growth rate of alumina scales formed by oxidation: effect of Y₂O₃ doping," *Journal of Materials Science*, vol. 30, no. 1, pp. 201–211, 1995.
- [130] A. H. Heuer, D. B. Hovis, J. L. Smialek, and B. Gleeson, "Alumina Scale Formation: A New Perspective," *Journal of the American Ceramic Society*, vol. 94, pp. s146–s153, 2011.
- [131] A. Atkinson, "Transport processes during the growth of oxide films at elevated temperature," *Reviews of Modern Physics*, vol. 57, no. 2, pp. 437–470, Apr. 1985.
- [132] L. Huang, X. F. Sun, H. R. Guan, and Z. Q. Hu, "Effect of rhenium addition on isothermal oxidation behavior of single-crystal Ni-based superalloy," *Surface and Coatings Technology*, vol. 200, no. 24, pp. 6863–6870, Aug. 2006.

- [133] C. S. Giggins and F. S. Pettit, "Oxidation of Ni-Cr-Al Alloys Between 1000° and 1200°C," *Journal of The Electrochemical Society*, vol. 118, no. 11, p. 1782, 1971.
- [134] A. Sato, Y. L. Chiu, and R. C. Reed, "Oxidation of nickel-based single-crystal superalloys for industrial gas turbine applications," *Acta Materialia*, vol. 59, no. 1, pp. 225–240, Jan. 2011.
- [135] Y. Wu, X. W. Li, G. M. Song, Y. M. Wang, and T. Narita, "Improvement of the Oxidation Resistance of the Single-Crystal Ni-Based TMS-82+ Superalloy by Ni–Al Coatings with/without the Diffusion Barrier," *Oxidation of Metals*, vol. 74, no. 5–6, pp. 287–303, Sep. 2010.
- [136] A. Akhtar, S. Hegde, and R. C. Reed, "The oxidation of single-crystal nickel-based superalloys," *Jom*, vol. 58, no. 1, pp. 37–42, Jan. 2006.
- [137] B. H. Kear, F. S. Pettit, D. E. Fornwalt, and L. P. Lemaire, "On the transient oxidation of a Ni-15Cr-6Al alloy," *Oxidation of Metals*, vol. 3, no. 6, pp. 557–569, Nov. 1971.
- [138] C. Alcock, V. Itkin, and M. Horrigan, "Vapour pressure equations for the metallic elements: 298–2500K," *Canadian Metallurgical Quarterly*, vol. 23, no. 3, pp. 309–313, 1984.
- [139] A. Powell, U. Pal, J. Van Den Avyle, B. Damkroger, and J. Szekely, "Analysis of multicomponent evaporation in electron beam melting and refining of titanium alloys," ... *Materials Transactions B*, vol. 28B, no. December, pp. 1227–1239, 1997.
- [140] J. Oblak and W. Owczarski, "Cellular recrystallization in a Nickel-base superalloy," *Transactions of the Metallurgical Society of AIME*, vol. 242, no. August, pp. 1563–1568, 1968.
- [141] R. Bürgel, P. Portella, and J. Preuhs, "Recrystallization in single crystals of nickel base superalloys," *Superalloys 2000*, p. 49076, 2000.
- [142] J. Nystrom, T. Pollock, W. . Murphy, and A. Garg, "Discontinuous cellular precipitation in a high-refractory nickel-base superalloy," *Metallurgical and Materials ...*, vol. 28, no. December, pp. 2443–2452, 1997.
- [143] N. D'Souza, "Neil.Dsouza@Rolls-Royce.com." Rolls-Royce plc, Derby, 2013.
- [144] D. C. Cox, B. Roebuck, C. M. F. Rae, and R. C. Reed, "Recrystallisation of single crystal superalloy CMSX-4," *Materials Science and Technology*, vol. 19, no. 4, pp. 440–446, Apr. 2003.
- [145] B. Zhang, C. Liu, Y. He, C. Tao, and X. Lu, "Recrystallization of SRR99 single-crystal superalloy: Kinetics and microstructural evolution," *Rare Metals*, vol. 29, no. 3, pp. 312–316, May 2010.

- [146] M. Hillert and G. R. Purdy, "Chemically induced grain boundary migration," *Acta Metallurgica*, vol. 26, no. 2, pp. 333–340, Feb. 1978.
- [147] M. Kajihara and W. Gust, "Driving force for grain boundary migration during alloying by DIGM and DIR in binary systems," *Scripta Materialia*, vol. 38, no. 11, pp. 1621–1627, 1998.
- [148] L. Chongmo and M. Hillert, "Diffusion induced grain boundary migration in Cu-Zn," *Acta Metallurgica*, vol. 30, no. 6, pp. 1133–1145, Jun. 1982.
- [149] D. Yoon, "Chemically induced interface migration in solids," *Annual Review of Materials Science*, vol. 19, pp. 43–58, 1989.
- [150] R. W. Balluffi and J. W. Cahn, "Mechanism for diffusion induced grain boundary migration," *Acta Metallurgica*, vol. 29, no. 3, pp. 493–500, Mar. 1981.
- [151] R. A. Fournelle, "On the thermodynamic driving force for diffusion-induced grain boundary migration, discontinuous precipitation and liquid film migration in binary alloys," *Materials Science and Engineering: A*, vol. 138, no. 1, pp. 133–145, May 1991.
- [152] V. Y. Doo and R. W. Balluffi, "Structural changes in single crystal copper-alpha brass diffusion couples," *Acta Metallurgica*, vol. 6, no. 6, pp. 428–438, Jun. 1958.
- [153] D. Gupta and P. S. Ho, *Diffusion phenomena in thin films and microelectronic materials*. USA: Noyes Publications, 1988.
- [154] L. Liang and A. H. King, "Diffusion induced grain boundary migration in the zinc-cadmium system," *Acta Materialia*, vol. 44, no. 7, pp. 2983–2998, Jul. 1996.
- [155] S. M. Eich, M. Kasprzak, A. Gusak, and G. Schmitz, "On the mechanism of diffusion-induced recrystallization: Comparison between experiment and molecular dynamics simulations," *Acta Materialia*, vol. 60, no. 8, pp. 3469–3479, May 2012.
- [156] Y. K. Paek, H. Y. Lee, and S. J. L. Kang, "Diffusion induced recrystallization in alumina," *Journal of the European Ceramic Society*, vol. 24, no. 4, pp. 613–618, Apr. 2004.
- [157] F. Den Broeder, "Diffusion-induced grain boundary migration and recrystallization, exemplified by the system Cu₂Zn," *Thin Solid Films*, vol. 124, pp. 135–148, 1985.
- [158] K. W. Chae, C. S. Hwang, D. Y. Kim, and S. J. Cho, "Diffusion induced recrystallization of TiC," *Acta Materialia*, vol. 44, no. 5, pp. 1793–1799, May 1996.

- [159] F. J. A. den Broeder and S. Nakahara, "Diffusion induced grain boundary migration and recrystallization in the Cu-Ni system," *Scripta Metallurgica*, vol. 17, no. 3, pp. 399–404, Mar. 1983.
- [160] K. Tashiro and G. R. Purdy, "The role of volume diffusion in DIGM, a reappraisal," *Scripta Metallurgica*, vol. 17, no. 4, pp. 455–458, Apr. 1983.
- [161] S. M. Schwarz, B. W. Kempshall, and L. a. Giannuzzi, "Effects of diffusion induced recrystallization on volume diffusion in the copper-nickel system," *Acta Materialia*, vol. 51, no. 10, pp. 2765–2776, Jun. 2003.
- [162] D. Stevens and G. Powell, "Diffusion-induced stresses and plastic deformation," *Metallurgical Transactions A*, vol. 8, no. 10, pp. 1531–1541, 1977.
- [163] I. Daruka, I. Szabo, and D. Beke, "Diffusion-induced bending of thin sheet couples: Theory and experiments in Ti-Zr system," *Acta materialia*, vol. 44, no. 12, pp. 4981–4993, 1996.
- [164] D. L. Beke, G. Opposits, and I. a. Szabó, "Diffusion-induced stresses," *AIP Conference Proceedings*, vol. 491, pp. 77–88, 1999.
- [165] D. Liu, W. A. Miller, and K. T. Aust, "Diffusion Induced Recrystallization in Nickel-Copper Diffusion Couples," *Defect and Diffusion Forum*, vol. 66–69, pp. 735–748, 1989.
- [166] H. C. Yu, A. Van der Ven, and K. Thornton, "Theory of grain boundary diffusion induced by the Kirkendall effect," *Applied Physics Letters*, vol. 93, no. 9, p. 091908, 2008.
- [167] Z. Suo, D. V. Kubair, A. G. Evans, D. R. Clarke, and V. K. Tolpygo, "Stresses induced in alloys by selective oxidation," *Acta Materialia*, vol. 51, no. 4, pp. 959–974, Feb. 2003.
- [168] M. Caliez, F. Feyel, S. Kruch, and J.-L. Chaboche, "Oxidation induced stress fields in an EB-PVD thermal barrier coating," *Surface and Coatings Technology*, vol. 157, no. 2–3, pp. 103–110, Aug. 2002.
- [169] H. Asteman, J. Svensson, and L. Johansson, "Evidence for Chromium Evaporation Influencing the Oxidation of 304L : The Effect of Temperature and Flow Rate," vol. 57, no. April, 2002.
- [170] D. Caplan and M. Cohen, "The volatilization of chromium oxide," *Journal of The Electrochemical Society*, vol. 108, no. 5, pp. 438–441, 1961.
- [171] J. Orloff, M. Utlaut, and L. Swanson, *High Resolution Focused Ion Beams*. New York: Plenum Publishers, 2003.

- [172] R. M. Langford and a. K. Petford-Long, "Preparation of transmission electron microscopy cross-section specimens using focused ion beam milling," *Journal of Vacuum Science & Technology A: Vacuum, Surfaces, and Films*, vol. 19, no. 5, p. 2186, 2001.
- [173] L. A. Giannuzzi and F. A. Stevie, "A review of focused ion beam milling techniques for TEM specimen preparation," *Micron*, vol. 30, no. 3, pp. 197–204, Jun. 1999.
- [174] D. Price, "Volatilisation, evaporation and vapour pressure studies using a thermobalance," *Journal of thermal analysis and calorimetry*, vol. 64, pp. 315–322, 2001.
- [175] B. A. Movchan and A. V. Demchishin, "Study of the structure and properties of thick vacuum condensates of Nickel, Titanium, Tungsten, Aluminium Oxide and Zirconium Dioxide," *Physics of Metals and Metallurgy*, vol. 28, no. 4, pp. 83–90, 1969.
- [176] Thermo-Calc, "TCNI6 - TCS Ni-based Superalloys Database, Version 6.0." 2012.
- [177] A. Chambers, *Modern Vacuum Physics*. USA: Chapman and Hall/CRC, 2005.
- [178] P. Shewmon, *Diffusion in Solids*. Warrendale, PA, USA: TMS, 1989.
- [179] H. Mehrer, "Self-diffusion in Metals," in in *Diffusion in Solids SE - 17*, vol. 155, M. Cardona, P. Fulde, K. von Klitzing, H. J. Queisser, R. Merlin, and H. Stormer, Eds. Springer Berlin Heidelberg, 2007, pp. 297–312.
- [180] K. C. Wang, L. H. Dreger, V. V. Dadape, and J. L. Margrave, "Sublimation of Cr₂O₃ at High Temperatures," *Journal of the American Ceramic Society*, vol. 43, pp. 509–510, 1960.
- [181] J. R. Santisteban, L. Edwards, A. Steuwer, and P. J. Withers, "Time-of-flight neutron transmission diffraction," *Journal of Applied Crystallography*, vol. 34, pp. 289–297, 2001.
- [182] T. Hutchings, P. J. Withers, T. M. Holden, and T. Lorentzen, *Introduction to the Characterization of Residual Stress by Neutron Diffraction*. Taylor & Francis, 2005.
- [183] D. Q. Wang, S. S. Babu, E. A. Payzant, P. G. Radaelli, and A. C. Hannon, "In-situ characterization of γ/γ' lattice stability in a Nickel-base superalloy by neutron diffraction," *Metallurgical and Materials Transactions A*, vol. 32, pp. 1551–1552, 2001.
- [184] R. Gilles, D. Mukherji, D. M. Töbrens, P. Strunz, B. Barbier, J. Rösler, and H. Fuess, "Neutron, X-ray and electron diffraction measurements for the

- determination of γ/γ' lattice misfit in Ni-base superalloys," *Applied Physics A*, vol. 74, pp. 1446–1448, 2002.
- [185] D. Dye, J. Coakley, V. a. Vorontsov, H. J. Stone, and R. B. Rogge, "Elastic moduli and load partitioning in a single-crystal nickel superalloy," *Scripta Materialia*, vol. 61, no. 2, pp. 109–112, Jul. 2009.
- [186] M. Preuss, J. Quinta da Fonseca, B. Grant, E. Knoche, R. Moat, and M. Daymond, "The effect of γ' particle size on the deformation mechanism in an advanced polycrystalline nickel-base superalloy," *Superalloys 2008*, pp. 405–414, 2008.
- [187] B. M. B. Grant, E. M. Francis, J. Quinta da Fonseca, M. R. Daymond, and M. Preuss, "Deformation behaviour of an advanced nickel-based superalloy studied by neutron diffraction and electron microscopy," *Acta Materialia*, vol. 60, no. 19, pp. 6829–6841, Nov. 2012.
- [188] Y. Lu, S. Ma, and B. S. Majumdar, "Elastic Microstrains during Tension and Creep of Superalloys: Results from In Situ Neutron Diffraction," *Superalloys 2008 (Eleventh International Symposium)*, pp. 553–562, 2008.
- [189] D. Dye, K. T. Conlon, P. D. Lee, R. B. Rogge, and R. C. Reed, "Welding of Single Crystal Superalloy CMSX-4: Experiments and Modeling," *Superalloys 2004 (Tenth International Symposium)*, pp. 485–491, 2004.
- [190] D. Dye, K. Conlon, and R. Reed, "Characterization and modeling of quenching-induced residual stresses in the nickel-based superalloy IN718," *Metallurgical and Materials Transactions A*, vol. 35, no. June, pp. 1703–1713, 2004.
- [191] M. Jensen, D. Dye, and K. James, "Residual stresses in a welded superalloy disc: characterization using synchrotron diffraction and numerical process modeling," ... *Materials Transactions A*, vol. 33, no. September, pp. 2921–2931, 2002.
- [192] M. Preuss, P. J. Withers, and G. J. Baxter, "A comparison of inertia friction welds in three nickel base superalloys," *Materials Science and Engineering: A*, vol. 437, no. 1, pp. 38–45, Nov. 2006.
- [193] S. Ma, D. Brown, M. A. M. Bourke, M. R. Daymond, and B. S. Majumdar, "Microstrain evolution during creep of a high volume fraction superalloy," *Materials Science and Engineering: A*, vol. 399, no. 1–2, pp. 141–153, Jun. 2005.
- [194] J. Coakley, R. C. Reed, J. L. W. Warwick, K. M. Rahman, and D. Dye, "Lattice strain evolution during creep in single-crystal superalloys," *Acta Materialia*, vol. 60, no. 6–7, pp. 2729–2738, Apr. 2012.
- [195] B. Roebuck, D. Cox, and R. Reed, "The temperature dependence of γ' volume fraction in a Ni-based single crystal superalloy from resistivity measurements," *Scripta materialia*, vol. 44, pp. 917–921, 2001.

- [196] M. M. Attallah, H. Terasaki, R. J. Moat, S. E. Bray, Y. Komizo, and M. Preuss, "In-Situ observation of primary γ' melting in Ni-base superalloy using confocal laser scanning microscopy," *Materials Characterization*, vol. 62, no. 8, pp. 760–767, Aug. 2011.
- [197] A. Royer, P. Bastie, and M. Veron, "In situ determination of γ' phase volume fraction and of relations between lattice parameters and precipitate morphology in Ni-based single crystal superalloy," *Acta Materialia*, vol. 46, no. 15, pp. 5357–5368, Sep. 1998.
- [198] "Diamond - I07 Beamline Guide," 2012. [Online]. Available: <http://www.diamond.ac.uk/Home/Beamlines/I07/beamline.html>. [Accessed: 17-Jul-2013].
- [199] J. R. Santisteban, M. R. Daymond, J. A. James, and L. Edwards, "ENGIN-X: a third-generation neutron strain scanner," *Journal of Applied Crystallography*, vol. 39, pp. 812-825, Oct. 2006.
- [200] S. R. Creek, J. R. Santisteban, and L. Edwards, "Modelling pseudo-strain effects induced in strain measurement using time-of-flight neutron diffraction," *Report FRG/2005/02/08*, The Open University, Milton Keynes, UK, 2005.